The University Of Sheffield.

Multidisciplinary Optimisation of High Pressure Turbine Blade Tips

Luka Vincekovic

A thesis submitted in partial fulfilment of the requirements for the degree of

Doctor of Philosophy

The University of Sheffield

Faculty of Engineering

Department of Mechanical Engineering

Submission Date

July 2022

This thesis is dedicated to everyone whose support and guidance brought me to this moment. With a humble heart, I say thank you.

Acknowledgements

Firstly, I would like to thank my supervisor, Professor Ning Qin, who gave me the opportunity to commit to this work. His suggestions, advice, and the discussions we shared always pushed me further, enabling me to see many things more clearly. I particularly appreciate the trust and freedom he gave me while delivering this work, and for that, I am truly thankful.

I would also like to thank Dr Shahrokh Shahpar, my mentor at Rolls-Royce, who was always there for me with his immense industrial and scientific experience. The practical support of him and his team meant a great deal to me, especially throughout the period of remote working.

I also want to thank Rolls-Royce for providing me with tools to carry out this work and for supporting me towards publishing in conferences and journals.

I must not forget to acknowledge the European Union's Horizon 2020 research and innovation programme from which this project received funding (Grant Agreement No 769025). This gave me the opportunity to work in the MADELEINE project alongside many research partners from the industry and academia. Through those collaborations, I learned a great amount across different fields and beyond the scope of my work. Partners inside the MADELEINE project have always shown great commitment that served to benefit everyone involved. I thank them for their support and advice.

I want to express my huge gratitude to my friends and colleagues at the University of Sheffield. Without the fellows from the aerodynamics group, former and present residents of RD-14, and the colleagues from the Fluids lab, I wouldn't be the engineer and researcher I am today. Thank you for all the support, lovely discussions, and being there for me.

Finally, I want to thank my family and friends from the bottom of my heart. Without their constant support, this task would be way more

difficult. Thank you for all the conversations, long calls, visits, and being the best stress relief one could possibly imagine. I will never forget that. Thank you.

List of publications

Conference papers

- L. Vincekovic, A. John, N. Qin & S. Shahpar, "*Exploring Topology Optimisation of High Pressure Turbine Blade Tips*" ASME Turbo Expo 2020: Turbomachinery Technical Conference and Exposition, American Society of Mechanical Engineers, 2020
- L. Vincekovic, N. Qin & S. Shahpar, "*Multidisciplinary Optimisation of High Pressure Turbine Blade Tip With Turbine Inlet Capacity and Stage Reaction Constraints*" AIAA AVIATION 2021 Forum

Journal papers

- L. Vincekovic, A. John, N. Qin & S. Shahpar, "*Exploring Topology Optimisation of High Pressure Turbine Blade Tips*" ASME Journal of Turbomachinery, July 2022; 144(7)

Abstract

High pressure turbines are characterised by increasing turbine entry temperatures and unshrouded rotor blades, resulting in thermal stresses at the turbine blades due to elevated heat load. Removal of the shroud improves turbine performance by allowing over tip leakage flow driven by the turbine propulsive pressure gradient. This thesis discusses the multidisciplinary optimisation of high pressure turbine blade tips, where both heat load and turbine performance are assessed simultaneously.

Optimising winglet tips, the thesis shows that by using a locally corrected heat transfer coefficient, good representation of heat load can be achieved taking into account the change of local flow with wall temperature. Focusing on the tip leakage, performance losses are identified, and their changes are analysed for a set of selected winglet tips. It is presented that winglet tips have a great potential for increasing the stage efficiency through the tip leakage mass flow and shearing losses reduction.

By utilising a design space defined through the use of the radial basis function surfaces, the thesis demonstrates that both topology and in-topology shape optimisation can be simultaneously performed. Because of the non-linearity of the design space, conventional gradient based methods are shown to struggle regressing a design space and finding an optimum. To resolve that, approach using subdivision of design space has been examined. Novel response surface method that uses artificial neural networks is also successfully applied to this kind of a design space. Finally, the thesis provides results of genetic based optimisation and Pareto front has been generated and analysed. Discussion shows that treating a turbine tip optimisation as a topology problem can significantly increase the range of a potential improvement, both aerodynamically and in the terms of heat load.

Contents

List of Figures

List of Tables

Nomenclature

Names and abbreviations

2D	Two Dimensional
3D	Three Dimensional
ADS	Active Design Subspaces
ANN	Artificial Neural Network
ARMOGA	Adaptive Range MultiObjective Genetic Algorithm
CAD	Computer Aided Design
CFD	Computational Fluid Dynamics
CFL	Courant-Friedrichs-Lewy
CV	Corner Vortex
DOE	Design Of Experiments
DR	Dimension Reduction
FEA	Finite Element Analysis
HL	Hidden Layers
HP	High Pressure
HSLC	High Speed Linear Cascade
HTC	Heat Transfer Coefficient
IP	Intermediate Pressure
LE	Leading Edge
MAE	Mean Average Error
MAM	Multipoint Approximation Method
MSE	Mean Square Error
MUSCL	Monotone Upstream centered Scheme for Conservation Laws
NSGA	Non-Sorting Genetic Algorithm
Nu	Nusselt Number
OTL	Over Tip Leakage
OTLV	Over Tip Leakage Vortex
PADRAM	Parametric Design and Rapid Meshing
Pr	Prandtl Number
PS	Pressure Side
PV	Passage Vortex
RANS	Reynolds averaged Navier-Stokes
RBF	Radial Basis Function
Re	Reynolds Number
RMSE	Root Mean Square Error

RS	Response Surface
SCV	Scrapping Vortex
SS	Suction Side
SST	Shear Stress Transport
stl	stereolithography
TE	Trailing Edge
TET	Turbine Entry Temperature
TR	Temperature Ratio

Subscripts

0	total
ad	adiabatic wall
ax	axial
is	isentropic
p	at constant pressure
t	turbulent
w	wall
r	rotor

Latin Symbols

B_j	Set of boundary faces
C	Blade chord
C_j	Convective part of a residual
D	Destruction term
D_j	Dissipative part of a residual
E	Energy
F	Convective and diffusive terms sum
f	Objective function
F_1	Blending function
F_2	Blending function
h	Enthalpy
h_0	Heat transfer coefficient constant
h_1	Heat transfer coefficient correction
k	Kinetic energy
k_t	Thermal conductivity
$\dot{m}$	Mass flow
M	Mach number
p	Pressure
P	Production term
q	Heat flux
Q	Variables vector
Q_j	Solution at a time step
R	Specific gas constant
R^2	Coefficient of correlation
R_j	Residual at a time step

s	Entropy
S	Magnitude of vorticity
$\tilde{S}$	Modified vorticity
S_{ij}	Mean strain rate tensor
t	Time
T	Temperature
u	x-velocity component
v	y-velocity component
V	Measure of control volume
w	z-velocity component
W	Work

Greek Symbols

α	Weighing factor
γ	Specific heat capacity ratio
η	Efficiency
Λ	Turbine stage reaction
μ	Dynamic viscosity
$\tilde{\nu}$	Spalart-Allmaras variable
ν	Kinematic viscosity
ρ	Density
τ	Friction forces tensor
ϕ	Instantaneous variable
Φ	Turbine inlet capacity
ω	Specific turbulent dissipation rate
Ω	Vorticity magnitude
ψ	Rotor skew angle

Chapter 1

Introduction

1.1 Background

1.1.1 Gas turbine cycle

Gas turbines are often used for power generation or as propulsion systems for aeronautical or naval applications. An example can be seen in Figure 1.1, which shows a cut view of a new generation of Rolls-Royce's high-bypass ratio Ultrafan engine. This engine is a three-shaft design, meaning it operates through multi-stage compression and expansion.

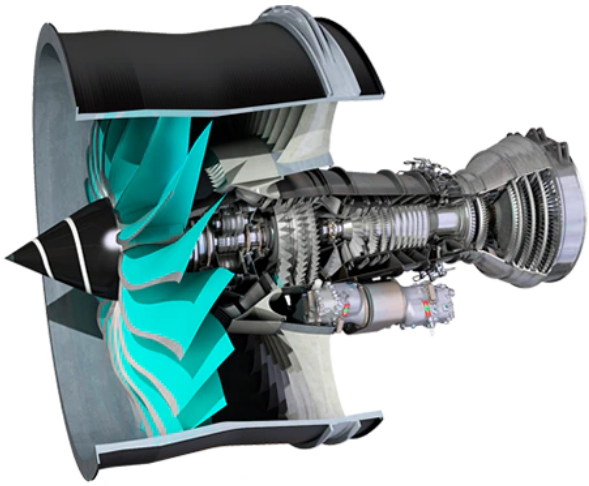

Figure 1.1: Rolls-Royce Ultrafan engine [1]

The operating principle of a gas turbine engine follows the Brayton cycle, as presented in Figure 1.2 in the form of a T-s diagram. In an ideal Brayton cycle, air is compressed in a compressor (1-2), then sent to the combustor, where it is mixed with fuel and ignited (2-3). The ideal Brayton cycle assumes constant pressure combustion.

Finally, hot gases are then expanded in the turbine (3-4). In an ideal cycle, compression and expansion are assumed to be isentropic, resulting in no entropy increase. A representative of a real Brayton cycle, considering irreversible compression and expansion with some entropy generated, is shown as compression 1-2' and expansion 3-4', assuming no pressure loss in the combustor.

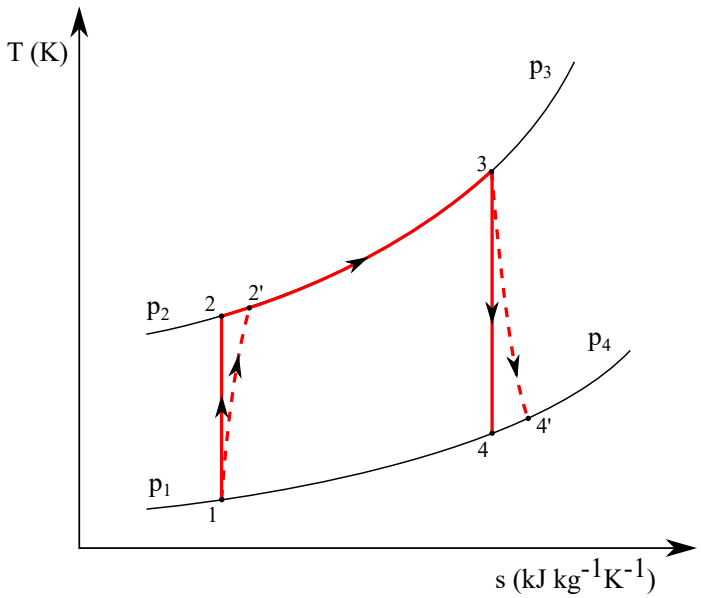

Figure 1.2: Gas turbine cycle

The efficiency and specific work output of a gas turbine cycle are a function of the compressor pressure ratio p_2/p_1, the maximum cycle temperature T_3, and the efficiencies corresponding to the compression and expansion processes (see Saravanamuttoo et al. [2]). This means that for a given pressure ratio p_2/p_1, the higher the temperature entering the turbine (3-4), the higher the overall cycle efficiency.

Efforts to increase the gas turbine cycle efficiency include increasing both the compressor pressure ratio p_2/p_1 and the turbine entry temperature T_3. The trend of increasing turbine entry temperature since the introduction of gas turbine engines is shown in Figure 1.3. During this period, the turbine entry temperature has increased by approximately 700 K due to improvements in turbine materials and cooling technologies. As a result of this increase, high-pressure turbines in gas turbine engines, located just after the combustor, are now operating with turbine inlet temperatures that far exceed the turbine blade material melting temperatures. This has been achieved through the use of thermal barrier coatings and advanced blade cooling techniques, highlighting the complexity and importance of accurately predicting blade heat loads.

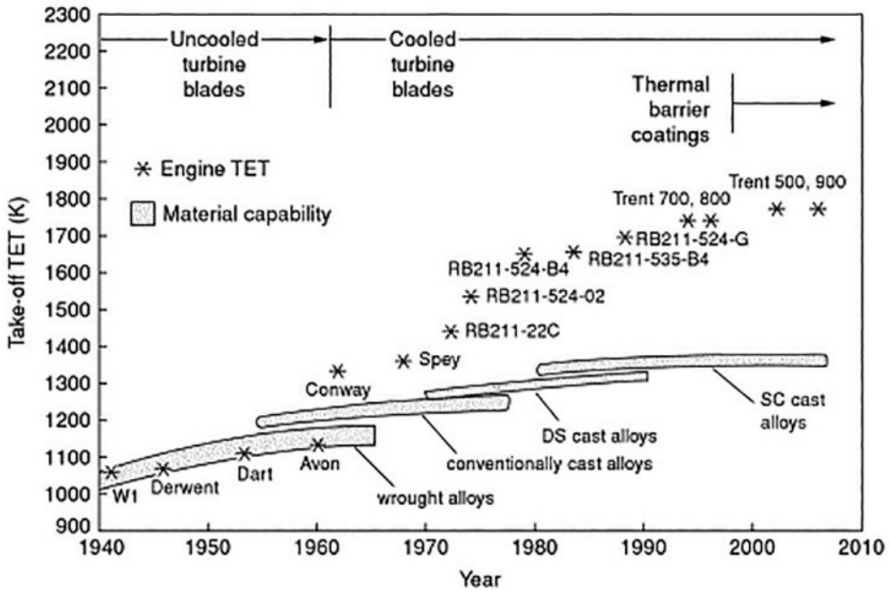

Figure 1.3: Trend in increase of turbine entry temperature (TET) [3]

1.1.2 Turbine properties

1.1.2.1 Turbine efficiency

Turbines are designed to convert the energy of the working fluid into useful work at the turbine output shaft. The performance of this process is measured by the overall turbine efficiency, which is defined as the ratio of the mechanical energy available at the turbine shaft to the energy of the working fluid at the turbine inlet. This definition takes into account all the mechanical losses that occur as the turbine operates, such as friction in the bearings and seals.

For a turbine blade designer, a more important indicator of the turbine's performance is the isentropic efficiency. This is defined as the ratio of the actual work produced to the ideal (isentropic) work produced. The actual work produced is visible in Figure 1.2 as expansion 3-4', while the ideal (isentropic) work produced is represented as expansion 3-4. The total-to-total isentropic efficiency, considering expansion that is both adiabatic and reversible, is presented in Equation 1.1.

$$\eta_{is} = \frac{W_{actual}}{W_{ideal}} = \frac{h_{03} - h_{04'}}{h_{03} - h_{04}} \tag{1.1}$$

If the operating fluid is assumed to be a perfect gas with negligible variations in specific heat capacity, c_p, the total enthalpy change can be expressed as $\Delta h_0 = c_p \Delta T_0$. The isentropic efficiency can then be expressed as the ratio of the actual

total temperature change to the isentropic total temperature change, as shown in Equation 1.2.

$$\eta_{is} = \frac{T_{03} - T_{04'}}{T_{03} - T_{04}} \tag{1.2}$$

1.1.2.2 Turbine Inlet Capacity

When the design of a turbine datum is altered, for example in the case of optimisation, it is important for the designer to make a fair comparison of the new design with the datum. This requires evaluating certain design changes at the same operating points of the turbine. To define the operating point of a turbine stage, with the assumption of constant rotational speed and inlet and outlet conditions, turbine inlet capacity and stage reaction are used.

Turbine inlet capacity, also known as the mass flow coefficient in some literature, provides information about the mass flow passing through the turbine stage. It is expressed in Equation 1.3 and is considered the most important turbine parameter according to Povey et al. [4]. Inaccurate performance evaluation and unmatched stages can occur if the turbine inlet capacity is not matched.

$$\Phi = \frac{\dot{m}_{0_{stage}} \sqrt{T_{0_{stage\ inlet}}}}{p_{0_{stage\ inlet}}} \tag{1.3}$$

In this equation, $\dot{m}_0$ represents the mass flow passing through a turbine stage, T_0 is the total temperature at the inlet of the turbine stage, and p_0 is the total pressure at the inlet.

When the inlet capacity of a single turbine stage is fixed, choking of the turbine occurs when the ratio of the total pressures at the inlet and outlet exceeds approximately 2. Choking can occur in either the stator throat area or at the turbine outlet, with the former being more common (as noted in Dixon and Hall's work [5] and Saravanamuttoo et al. [2]).

1.1.2.3 Turbine Stage Reaction

Turbine stage reaction, or degree of reaction, is a turbine parameter that expresses the fraction of stage expansion that takes place in the rotor. It is calculated as the ratio of the static enthalpy change in the rotor to the static enthalpy change across the entire turbine stage, as shown in Equation 1.4.

$$\Lambda = \frac{h_{rotor\ inlet} - h_{rotor\ outlet}}{h_{stage\ inlet} - h_{stage\ outlet}} \tag{1.4}$$

Turbines with a reaction of 0 % are called "impulse turbines," while turbines with expansion in both the stator and rotor are called "action turbines." A typical value of gas turbine stage reaction is around 50 %, which implies symmetrical velocity triangles and similar blade shapes for both the stator and rotor blades (see Dixon and Hall [5]).

When the design of a turbine rotor blade is altered, it is important to keep the turbine stage reaction close to the datum values. If the stage reaction of one turbine stage is changed, it affects all downstream stages, resulting in either underexpansion or overexpansion in later turbine stages. Every turbine stage in a gas turbine engine powers a specific compression stage, which requires a predetermined power. Keeping the turbine stage reaction unchanged helps to keep that power constant. Additionally, components of the gas turbine engine that transmit power are carefully designed for the nominal power, and a change in stage reaction could result in component failure.

1.2 Loss mechanisms in a turbine stage

Main sources of losses in the turbine stage are caused by viscous effects in boundary layers, mixing processes, shock waves, and heat transfer across blades and endwalls. The principles behind each loss source can be investigated independently, but they often have strong interactions. According to Denton [6], losses in the turbine stage can be divided based on their causes into:

- Profile losses
- Secondary flows
- Cavity losses.

1.2.1 Profile losses

1.2.1.1 Boundary layer

Boundary layer loss in a turbine stage occurs due to skin friction at the airfoil surface, starting at the leading edge stagnation point. As the flow advances from the leading edge, the boundary layer grows until the transition point, when it naturally turns from laminar to turbulent flow. According to Hoheisel et al. [7], two factors affect the boundary layer transition behaviour: the pressure gradient on the blade surface and the freestream turbulence.

As the turbine's function is to turn the flow, strong pressure gradients cause the laminar boundary layer to be mostly present on the blade pressure side, and the transition occurs at the blade suction side. Therefore, from the perspective of a turbine designer, it is desirable to find velocity distributions that would keep the boundary layer laminar as far downstream as possible. A separated boundary layer near the trailing edge on the blade suction side is depicted in Figure 1.4.

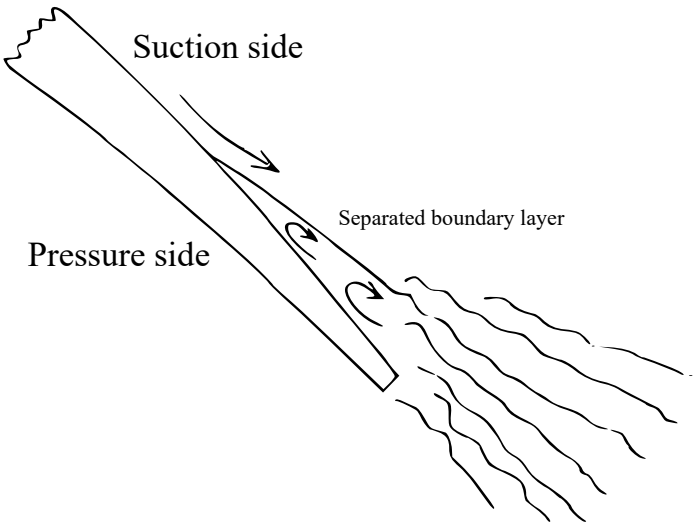

Figure 1.4: Separated boundary layer near trailing edge and downstream mixing

As mentioned previously, the high pressure turbine is located just after the combustor. The combustion process is characterised by a highly turbulent flow, which enhances mixing, and therefore, the working fluid fed into the high pressure turbine has a large freestream turbulence. According to Kopriva et al. [8], freestream turbulence impacts the boundary layer, which, in turn, impacts downstream wake mixing. This means that to correctly predict the blade boundary layer behaviour, the freestream turbulence must be taken into account. Furthermore, an accurate boundary layer prediction is important for both the turbine aerodynamic performance and the heat transfer, which also includes the tip leakage behaviour. In the case of blades with film cooling, the early boundary layer transition can also be triggered by the cooling flow interfering with the main flow [9].

1.2.1.2 Trailing edge wake

Trailing edge loss occurs due to the joining of pressure side and suction side flows, and according to Denton [6], it can account for up to a third of the overall profile loss. According to Xu and Denton [10], trailing edge loss increases linearly with

the trailing edge thickness. It is desirable to keep the trailing edge thickness small, but because trailing edges are prone to increased heat load, they are often made thick to accommodate the cooling system. In these cases, trailing edge loss becomes extremely important for cooled blades. In some turbines, up to 70 % of profile loss has been recorded. Downstream of the trailing edge, the difference in pressure side and suction side flow velocities causes a thin layer of increased friction, known as the wake. The trailing edge wake is a highly unsteady region where the blunt trailing edges form shed vortices. Melzer and Pullan [11] state that vortex shedding is a dominant mechanism for generating trailing edge loss, and shock waves have been observed at Mach numbers between 0.5 and 1. For a detailed explanation of the unsteady trailing edge wake behavior, see Sieverding et al. [12].

1.2.1.3 Shock waves

Shock waves in turbine passages occur due to the acceleration of the flow to supersonic conditions at the blade suction side and at the blade trailing edge. According to Denton [6], shocks at the blade suction side are oblique, with a small pressure rise causing little direct loss. However, shock waves forming at the blade suction side cause intense viscous dissipation in the separated trailing edge region, which may become the largest loss source in the entire turbine.

1.2.2 Secondary flows

Secondary flows in the turbine stage occur close to the endwalls as passage, horseshoe, and corner vortices, and as a tip leakage vortex in the rotor tip (radial) gap. They cause the flow in a turbine to be fully three-dimensional and can occupy a significant portion of the overall loss. Secondary flows are depicted in Figures 1.5 and 1.6.

1.2.2.1 Passage vortex

As flow enters the turbine stage, a boundary layer forms near the endwalls. Decelerated fluid near the endwalls is turned by the stator vane, causing a passage vortex to form. The magnitude of the vortex depends on the thickness of the boundary layer and the angle of turning of the flow. The passage vortex affects the angle of the exit flow through phenomena known as under-turning and over-turning. Over-turning refers to an exit flow angle greater than the stator vane turning angle, while under-turning refers to the opposite.

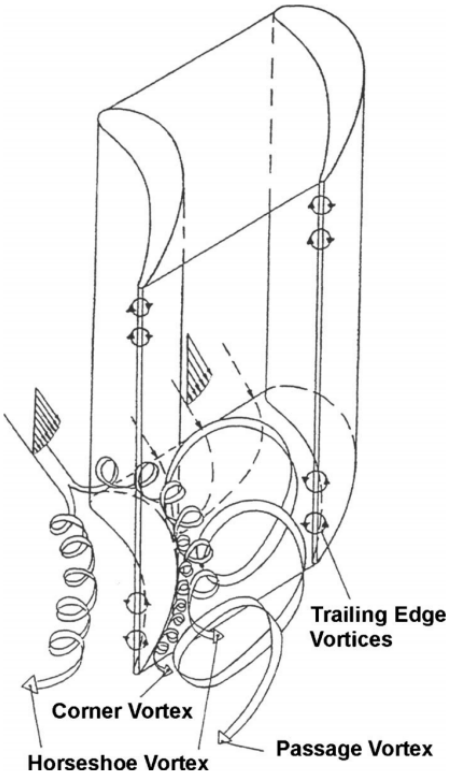

Figure 1.5: Passage, horseshoe and corner vortices [13]

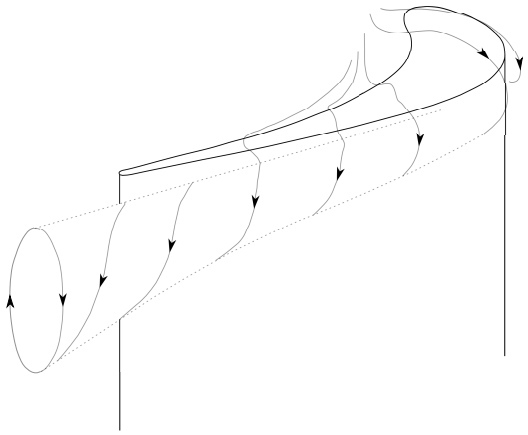

Figure 1.6: Schematics of the tip leakage vortex

1.2.2.2 Horseshoe vortex

A horseshoe vortex is formed when a boundary layer flow rolls around a cylindrical shape, such as a blade. As it originates from the blade leading edge, the horseshoe vortex has a significant influence on the blade heat transfer around the leading edge region. As it passes the leading edge, it is divided into the pressure side leg and the suction side leg. The pressure side leg of the horseshoe vortex has the same direction of rotation as the passage vortex, and as they merge, the passage vortex pulls the pressure side leg of the horseshoe vortex towards the suction side of the blade. The suction side leg of the horseshoe vortex is pushed by the passage vortex into the corner between the late suction side and the endwall, forming the corner vortex.

1.2.2.3 Over tip leakage vortex

Tip leakage flow originates from the axial turbine rotor due to the necessity of a physical gap between the rotating blade and the stationary casing. The strong pressure gradient between the blade pressure side and the blade suction side causes part of the passage flow to escape through the tip gap. This is illustrated in Figure 1.6. The

angular momentum from the stator blade is passed on to the passage flow entering the rotor domain, causing it to be turned by the rotor blade. However, some of the flow that passes through the tip gap is not deflected as intended and exits at a different angle, resulting in the formation of the over-tip leakage vortex. This vortex causes significant aerodynamic losses due to viscous effects, and its magnitude depends on the amount of leaked flow and the mismatch angle between the leaked flow and the main passage flow. Pátý and Lavagnoli [14] explained the vortex for flat and various squealer tips.

1.2.3 Cavity losses

The rotor blade is positioned inside the turbine on a rotor disk, between the two stationary stator vanes, as shown in Figure 1.7. As the rotor disk rotates, a gap must exist between the two adjacent stator vane mountings. These gaps are part of the larger cavities known as the upstream and downstream cavities. The air in these cavities is stationary on one side (next to the stator vane mounting) and moving on the other (next to the rotor disk), which causes torque drag on the rotor disk. Additionally, due to the existence of gaps between the stationary and moving shrouds, ingestion of hot gas into the upstream and downstream cavities is possible. This can result in severe problems with the rotor disk, and to prevent this, the air inside the cavities is at a higher pressure compared to the hot gas main flow. This causes some air to flow through the cavity gaps and into the turbine stage passage, interacting with the main flow and causing additional losses.

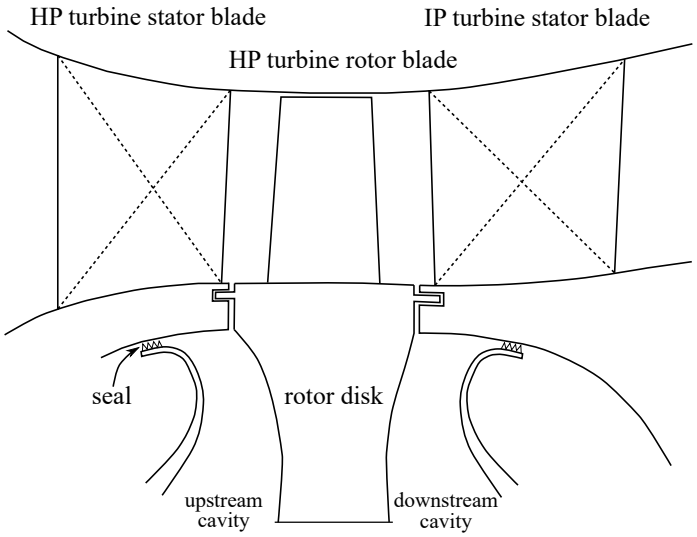

Figure 1.7: Meridional view of high pressure turbine with intermediate pressure stator blade and upstream and downstream cavities

1.3 Literature study of over tip leakage flow

In previous sections, the concept of turbine stage losses was briefly introduced. The focus of this thesis is to examine one of these losses, the over tip leakage flow in unshrouded turbine rotors, and a literature study was conducted in that field.

To accurately estimate the potential of the methodology and the performance of a specific design, a comprehensive understanding of all aspects associated with the over tip leakage flow is necessary. Therefore, the literature review is structured as follows.

Section 1.3.2 explains early experimental work on understanding the basics of tip gap aerodynamics, primarily studies that focused on the behaviour of flat tip blades in a linear cascade. Section 1.3.3 presents experimental work on the tip gap heat transfer, with an emphasis on early work that dealt with the fundamental features of the tip gap flow.

After covering the established fundamentals of blade tip aerodynamics and heat transfer, numerical investigations are presented. These include studies of different tip shapes, their advantages and disadvantages, and a brief overview of state-of-the-art numerical models.

Finally, a review of tip optimisations is provided, with a focus on flow around different types of tips and ways of modelling their features.

1.3.1 Introduction to tip shapes

Common turbine tip shapes, as shown in Figure 1.8, can be divided into flat, winglet, squealer, and a combination of winglet and squealer tips. Winglet tips are characterised by circumferential tip extensions, which can partially or fully encircle the tip edge, referred to as overhangs. Squealer tips are created by extending the tip area in a radial direction, rather than circumferentially like winglets, forming squealer rims or walls (both terms are used in literature). The area fully or partially enclosed by the squealer rims is known as the squealer cavity. Winglet squealers, as their name suggests, are a combination of both winglet and squealer features, attempting to harness the best of both.

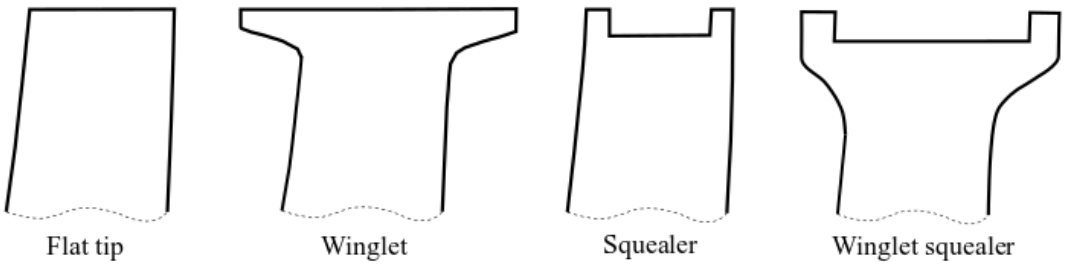

Figure 1.8: Common turbine tip shapes

For easier understanding of the next section in this literature review, a brief explanation of the main working principle behind each of the flat, winglet, and squealer tip shapes is presented next.

1.3.1.1 Flat tip

Flat tips are no longer a viable option for modern unshrouded turbine rotors. They serve mostly as a benchmark due to their lower performance compared to squealers and winglets. Still, despite their limited use, it is important to understand the physics of the leakage flow over flat tips, which is shown in Figure 1.9.

When the flow enters the tip gap, it separates over the pressure side tip edge and creates a separation vortex, also known as a recirculation bubble. The tip leakage flow gets compressed over the vortex and as it passes, it impacts the tip surface, creating a heat transfer hotspot. The area where the tip leakage flow impacts the tip surface is indicated with a red circle in Figure 1.9. As the flow continues towards the suction side, the tip leakage flow creates a boundary layer over the tip edge, effectively reducing the nominal tip gap, a phenomenon known as *vena contracta*. Finally, the tip leakage flow exits the tip gap, rolling into a tip leakage vortex whose size depends on the velocity, direction, and angle of the tip leakage flow.

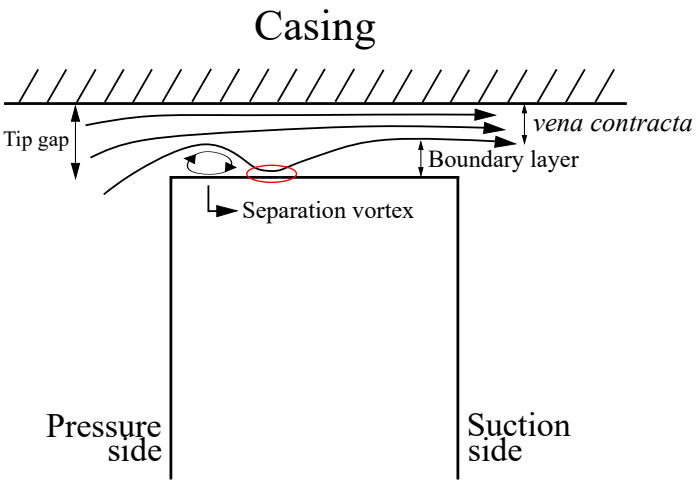

Figure 1.9: Flow over flat tip

1.3.1.2 Winglet tip

Tip leakage flow over a winglet tip resembles the flow over a flat tip, as depicted in Figure 1.10. As the flow enters the tip gap on the pressure side tip edge, a separation vortex is created. Its size is influenced by the size of the pressure side winglet overhang. Part of the tip gap flow contracts over the separation vortex and impinges on the winglet tip surface, causing a hotspot stripe. A larger separation vortex usually results in a more significant impingement effect. As the tip leakage flow moves toward the suction side, it develops a boundary layer, similar to the flat tip, leading to a *vena contracta* effect. One advantage of the winglet tip over a flat tip is that its tip is wider, causing the boundary layer to grow over a larger distance, effectively closing the tip gap more. This enhances the *vena contracta* effect and blocks more of the leakage flow. Another benefit of winglet tips is that since the leakage flow has to travel a greater distance between the pressure and suction sides, it aligns more with the main passage flow, resulting in a lower angle mismatch between the leakage and the main passage flow, and thus, fewer shearing losses. This is the clear advantage of adding winglet overhangs.

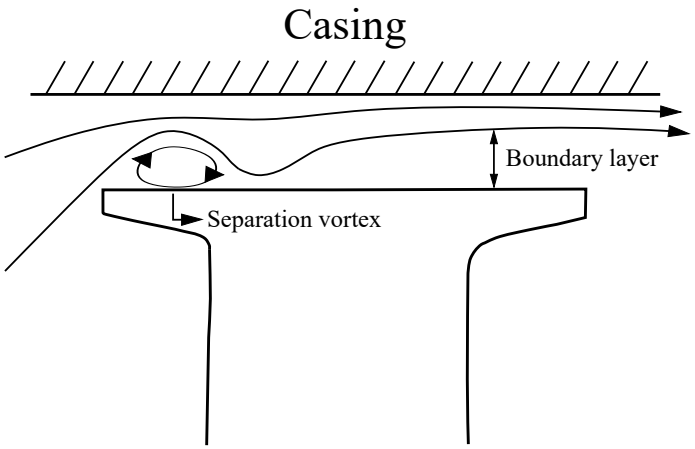

Figure 1.10: Flow over winglet tip

1.3.1.3 Squealer tip

Tip leakage flow over squealer tips is explained in Figure 1.11. The features of this flow largely depend on the width of the tip, and three different tips are shown. Before going into the specifics of each, it is important to fully understand the specifics of squealer tip flow, and to explain the counter rotation of the casing.

Counter rotating casing

In the absolute frame of reference, as seen by a bystander, the turbine rotor blades rotate and the casing is stationary. However, since the whole rotor domain, including the blades, rotates in the absolute frame, the blades only experience the flow around them without feeling the rotation of the turbine. In other words, in numerical simulations, the rotation of the turbine can be neglected, and the blades can be assumed to be stationary with only the flow around them moving. This is called the relative frame of reference, which is subtracted from the absolute frame of reference by the rotational velocity of the rotor domain. In this case, neglecting the rotation of the turbine needs to be taken into account by introducing the counter rotating casing. This means that the casing is set to move from the suction side to the pressure side within the relative frame of reference, as shown in Figure 1.11a.

Flow over different squealer tips

The flow over a wide squealer tip is shown in Figure 1.11a. As the flow separates over the pressure side tip edge, it compresses and then passes over the pressure side squealer rim, trying to expand and fill the squealer cavity. This flow can be assumed to split into two parts. One part fills the squealer cavity and, depending on its size,

impinges on the bottom. The other part stays in the upper region of the squealer cavity and is entrained into a scraping vortex (SCV) by the counter rotating casing. The two corners between the squealer cavity floor and the pressure side and suction side rims are filled with two vortices: the pressure side corner vortex (PSCV) and the suction side corner vortex (SSCV). The pressure side and suction side corner vortices have the same clockwise rotation, while the scraping vortex rotates counterclockwise. Depending on the dimensions of the squealer, all three vortices can coexist in the squealer cavity, making the squealer tip act as a labyrinth seal, blocking the leakage flow.

In the case of a narrower squealer cavity, the size of the three vortices can vary, and the suction side corner vortex can become smaller or disappear, as shown in Figure 1.11b. In such cases, the labyrinth seal effect results in weaker tip leakage blockage than with a wide squealer.

In the case of a narrow squealer tip, the squealer cavity is typically filled with only one cavity vortex (CV). The flow passing over it generally behaves like in the case of a flat tip, but the *vena contracta* effect is often not present as the cavity vortex accelerates the boundary layer. Depending on the design of the squealer, the flow can separate over both the pressure side and suction side rims, but narrow squealers generally have poor performance in terms of tip leakage blockage. This is a common occurrence at the aft portion of the blade near the trailing edge, where the blade becomes thinner. To address this issue, squealer tips are frequently modified by adding a winglet overhang or incorporating openings into the squealer rims.

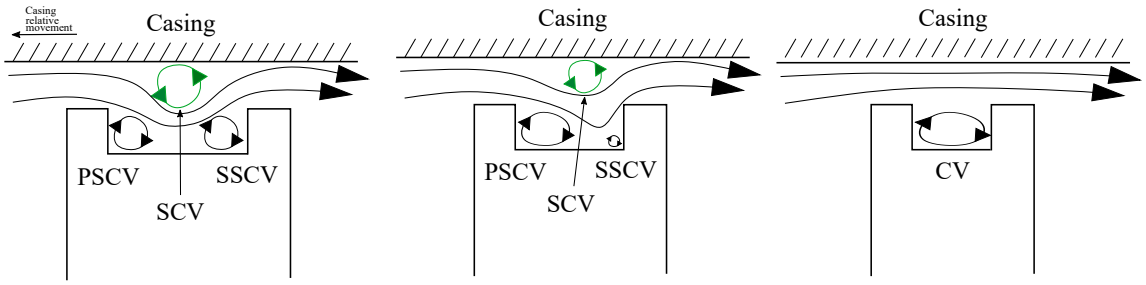

(a) Wide squealer tip (b) Semi-wide squealer tip (c) Narrow squealer tip

Figure 1.11: Flow over squealer tip

1.3.2 Tip gap aerodynamics

Some of the earliest detailed investigations of tip leakage flow were conducted on experimental linear cascade setups. A study by Bindon [15] quantified the tip leakage losses for different tip gap sizes and identified three main sources of losses: internal

gap loss, suction side corner mixing loss and casing endwall boundary layer loss. Bindon noted that the tip leakage loss was more related to separation rather than the quantity of leakage flow, and suggested the study of new streamlined blade tips to minimise entropy generation and maximise flow turning.

Moore and Tilton [16] focused on the effect of the tip gap entry flow separation and downstream mixing on static pressure across the tip. They presented correlations for the pressure rise in the tip gap and local heat transfer rates for low Mach number flow. However, they emphasised that unshrouded turbine tips in practice operate in a transonic leakage flow regime, meaning that the leakage flow and associated heat transfer must be studied in a compressible regime.

Heyes et al. [17] experimentally studied the performance of a flat tip, pressure side squealer, and suction side squealer in a linear cascade using one dimensional flow models. They examined flow separation at the tip gap entry and used the concept of flow discharge coefficient to quantify losses. To lower the discharge coefficient and tip gap losses, they found that sharp edges around the tip were important for forming a separation vortex at the tip edge.

Denton [6] provided a comprehensive summary of over tip leakage flow, explaining the flow regimes for different blade thicknesses (as shown in Figure 1.12). He noted that flow entering the tip gap and separating over the pressure side edge contracts to a jet. If the blade thickness was greater than four times the tip gap, the jet mixed out in the tip gap, resulting in increased entropy and static pressure (as shown in the upper part of Figure 1.12). In the case of thin blades (where the blade thickness was less than 2.5 times the tip gap), the separated over tip leakage flow was unlikely to reattach on the blade surface, exiting the tip gap with greater momentum (as shown in the lower part of Figure 1.12).

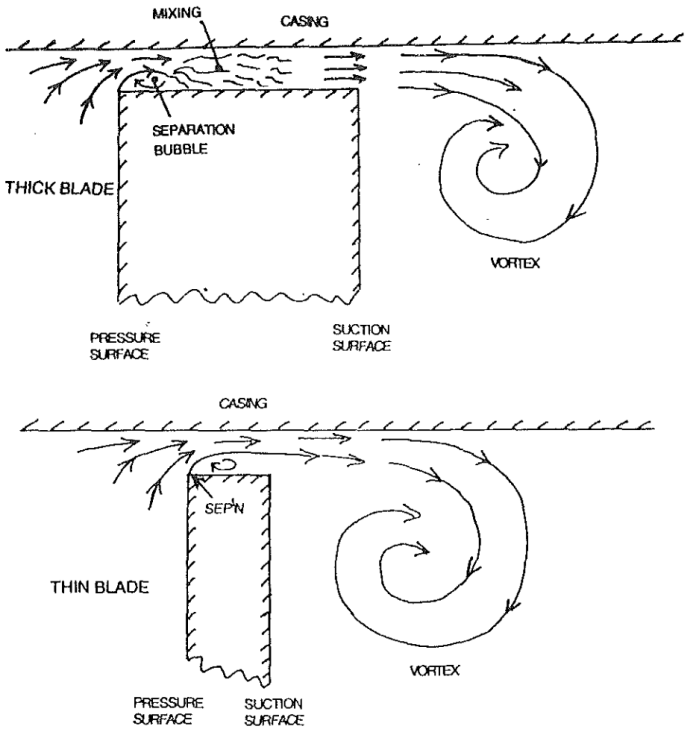

Figure 1.12: Tip gap flow over thick and thin blades [6]

Yaras and Sjolander [18] performed measurements of the tip gap flow in a linear cascade that included the counter-rotation of the casing in the relative domain by using a moving belt. As a result of the moving casing effect, they found a considerable decrease in the leakage mass flow. The core tip gap flow velocity also decreased due to the reduction in the over tip leakage flow driving pressure difference. In the second part of their study [19], Yaras et al. investigated the effect of the relative moving casing downstream of the tip gap. They found that when the effect of the relative moving casing was included, the strength of the tip leakage vortex significantly decreased, and a scrapping vortex formed. Both vortices acted as a tip leakage blockage at the blade suction side, reducing the pressure difference that drove the leakage flow. All of these findings showed the importance of including the relative casing movement in tip leakage studies, which was often neglected in earlier linear cascade studies.

1.3.3 Tip gap heat transfer

Moore et al. [20] conducted an investigation of the flow through a 2D tip gap geometry, using laminar flow calculations. The study covered a range of tip gap Reynolds numbers and revealed that flow separation occurred at the tip gap entry for higher

Reynolds numbers, with a recirculation zone close to the tip edge identified. The authors focused on the heat transfer in the recirculation region around the tip edge and found that the heat transfer coefficient could be up to 1.85 times higher than in the downstream region where the tip leakage flow had fully developed. They also stated that the temperature of the pressure side edge of an uncooled blade could approach the blade melting temperature, highlighting that tip gap heat transfer is a local issue that can create hotspots.

Chyu et al. [21] studied the flow over a squealer-like tip using a linear cascade, taking into account the effect of relative casing movement. They observed pressure side edge recirculation and cavity separations, but found that the counter rotating casing had little effect on the average tip heat transfer. In terms of the squealer geometry, the authors found that the average tip heat transfer coefficient decreased as the squealer cavity depth increased, for a constant leakage flow rate. They also noted that a too deep squealer cavity was undesirable as it increased the flow resistance while only providing a small increase in overall tip area, suggesting the existence of an optimal squealer cavity depth.

Bunker et al. [22] carried out a detailed heat transfer study of a high pressure turbine blade tip using a high speed linear cascade. The study examined the effects of different tip geometries (e.g. flat tips with sharp and rounded edges), tip gaps, and turbulence intensities. The results indicated that the tip gap heat transfer levels increased with the increase of tip gap, turbulence intensity, and rounding of the tip edge.

Azad et al. [23] conducted a similar study, focusing on the heat transfer of a flat tip for different tip gaps and turbulence intensities. They found that the highest heat transfer occurred at the pressure side portion of the leading edge and along the pressure side, decreasing across the tip towards the suction side. This is illustrated in Figure 1.13. Following the findings of Bunker et al. [22], Azad et al. also found that larger tip gaps led to increased tip heat transfer, due to an increase in the amount of leakage flow. Additionally, increasing turbulence intensity led to an increase in tip heat transfer along the flow path.

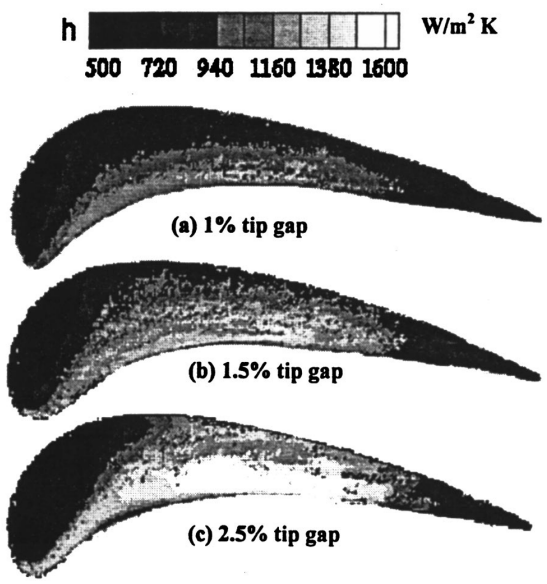

Figure 1.13: Heat transfer coefficient on flat tips with different tip gaps and turbulence intensity of 6.1% [23]

The heat load on turbine flat tips was investigated by Jackson et al. [24] for two different tip gaps, both experimentally and numerically, including and neglecting the effect of casing shear (counter rotation of the casing). Interestingly, without the casing shear, a smaller tip gap caused a decrease in the heat load, mostly due to the drop in the heat transfer coefficient. When casing shear was included, heat transfer was more dependent on the heat transfer-driving adiabatic wall temperature. The authors concluded the study by emphasising the importance of including the effect of counter rotating casing in all tip investigations.

Maffulli and He [25] investigated the effects of non-adiabatic wall temperature conditions on the heat transfer coefficient and the turbine passage flow for a stator passage of a high pressure turbine. By changing the wall temperature condition, they found differences in secondary flows, trailing edge shock positions, and heat transfer coefficients. The authors focused their study on finding a consistent heat transfer prediction and stated that, since changes in flow were found not only in magnitude, but also in position, the heat transfer relationship between different wall conditions had to be non-linear. As a result, they suggested a 3-point non-linear method for heat transfer calculation in which, with additional CFD simulation, a more consistent prediction of the heat transfer coefficient could be achieved. With the introduction of additional CFD simulation, instead of previously obtaining the heat transfer coefficient by scaling it between two temperatures, this new method

accounted for all flow differences caused by different wall temperature conditions. This allowed for correcting the heat transfer coefficient data on a local level, increasing the accuracy and stability of heat transfer coefficient predictions.

Zhang and He [26] followed the findings of Maffulli and He [25] and investigated how the over tip leakage flow aerodynamics was affected by the wall temperature condition. They performed studies for different wall temperature conditions for flat and winglet tips and concluded that, similar to the case of a 3D turbine passage flow, the wall temperature condition changed the aerodynamics of the over tip leakage flow. In particular, with different wall temperature conditions, they found differences in the tip static pressures, shock positions, tip leakage mass flows, and magnitudes of the heat transfer coefficient. An example of the change in tip leakage mass flow for two different temperature conditions over a flat tip is shown in Figure 1.14, where the x-axis shows the position along the suction side edge and the y-axis is normalised mass flow. Zhang and He also showed that these phenomena were not just amplified, but also shifted in position. They suggested that scaling the heat transfer data from cold experiments to real engine conditions was not sufficient since it would only resolve the magnitude, but not the shift of the phenomena position. To resolve this, they successfully applied the non-linear heat transfer coefficient correction method from Maffulli and He [25] to the case of the winglet tip and found a much improved prediction of the heat transfer coefficient. In conclusion, the authors highlighted the importance of this method for a consistent heat transfer coefficient calculation when turbine designers use loosely coupled CFD and FEA methods.

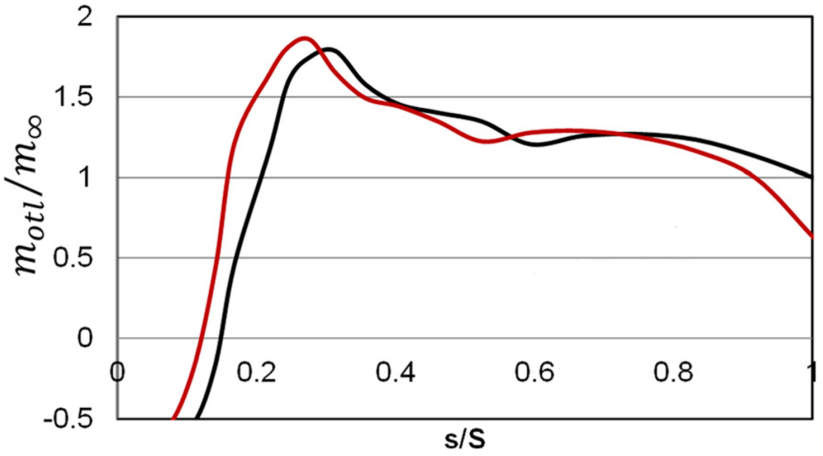

Figure 1.14: Changes in over tip leakage mass flow over flat tip for two different wall temperature conditions [26]

1.3.4 Tip shapes

As the studies that include different tip shapes are often interconnected or done together, the next part of the literature review will present them all together.

Ameri et al. [27] conducted a numerical study comparing two squealer tips with different cavity depths to a flat tip blade. They found that the heat transfer on the squealer tip is usually governed by two vortices: the pressure side squealer rim corner vortex and the cavity vortex that forms in the middle of the cavity. The highest heat transfer was found on the suction side rim, where the over tip leakage flow exits the tip region. The authors found no significant difference in efficiency between the investigated squealers and the flat tip of the same tip gap, although the mass flow rate of the squealer tip gap decreased by 14 %.

Newton et al. [28] conducted an experimental and numerical study of the flat tip, a full perimeter squealer, and a squealer with a rim only on the suction side of the tip. For the flat tip, the authors stated that the over tip leakage flow was characterised by separation over the leading edge and pressure side edges, creating a recirculation bubble before the flow reattached to the tip surface. The highest heat transfer was found in this area. They also reported that the over tip leakage vortex impinged on the blade's suction side, resulting in increased heat transfer. This area expanded as the tip gap increased, due to the stronger over tip leakage vortex. The authors found that the use of squealers eliminated the high heat transfer region associated with the leading edge and pressure side separation and reattachment, but high heat transfer was found on the squealer cavity floor, corresponding to the area of flow impingement after it contracts over the squealer rim.

Key and Arts [29] conducted a similar study comparing the squealer and flat tips at different tip gaps. Their conclusions regarding the separation bubbles at the flat and squealer tips were consistent with the findings of Newton et al. [28]. However, in contrast to Ameri et al. [27], Key and Arts [29] reported lower aerodynamic losses for the squealer tips, regardless of the tip gap, possibly due to decreased mixing losses in the tip gap, resulting from the lower tip leakage flow velocities.

Lee and Lee [30] focused their experimental study on suction side squealer tips with varying rim heights. They found that the total pressure loss coefficient decreased with increasing squealer rim height, but was still higher than the pressure side rim squealer from a previous study. Additionally, the over tip leakage vortex in the case of a suction side squealer was found to be larger than the pressure side squealer, resulting in higher over tip leakage loss. Based on their findings, it can be concluded that a

squealer tip with only a pressure side rim has a better aerodynamic performance than a squealer tip with only a suction side rim.

Du et al. [31] conducted a numerical study of the aerothermal performance of flat and different multi-cavity squealer turbine tip designs. The numerical model consisted of a fully structured multi-block mesh for both the stator and rotor domains, and RANS equations were solved using the standard k-ω turbulence model. The numerical model was validated using experimentally obtained heat transfer coefficient contours on the tip surface. The study included different squealer designs with cavities created by adding rims perpendicular to the blade camber line. All squealer designs were found to produce less leakage mass flow compared to the flat tip, with leakage mass flow increasing with the number of squealer cavities. In other words, a simple full perimeter squealer had better performance than all other squealers with perpendicular rims. The same pattern was found for the total pressure loss. Therefore, it can be concluded that adding perpendicular rims to squealers deteriorates their performance.

Mischo et al. [32] conducted an interesting study of a novel squealer geometry, comparing a simple full perimeter squealer to a novel squealer with full perimeter squealer rims of variable width. They focused on heat transfer improvements and, after explaining the flow over a simple squealer involving the formation of three counter-rotating vortices, they proposed a new squealer design. In general, as the relative movement of the casing causes the casing boundary layer to roll up into a scraping vortex, it increases the area of heat transfer by rubbing on the squealer cavity floor. Mischo et al. attempted to eliminate this effect by thickening the suction side of the squealer rim, effectively reducing the width of the squealer cavity and giving the scraping vortex less room to form. This led to a decrease in the overall tip heat load by 13 % compared to the flat tip and by 7 % compared to the simple squealer.

A numerical study of the effect of squealer tip shape and endwall motion on heat transfer was conducted by Krishnababu et al. [33, 34]. The numerical model was validated against experiments using different turbulence models and it was found that the k-ω SST turbulence model gave the best agreement with the experimental data. The authors found that there was an overprediction of heat transfer at the leading edge separation region and a slight underprediction of the overall tip heat transfer, which they attributed to excessive clipping on the overproduction of turbulent kinetic energy. Two squealer geometries were investigated: a full perimeter squealer and a suction side rim squealer. Both were found to decrease the average heat transfer area compared to a flat tip. The full perimeter squealer had a lower leakage flow rate

compared to the flat tip, while the suction side squealer had a higher leakage flow rate.

Schabowski and Hodson [35] conducted an experimental and numerical study of winglets, squealers, and their combination. They identified three main methods for reducing tip leakage flow loss. The addition of pressure side and suction side winglet overhangs which reduced the tip leakage driving pressure difference, the use of squealer rims that split the tip leakage flow into two parts and the use of thin squealer rims that prevented flow reattachment on the tip surface which lowered discharge coefficients.

Senel et al. [36] performed an extensive numerical study of squealer rim width and height on a high pressure turbine rotor, focusing on both aerodynamic performance and tip heat transfer. The numerical model was built using a fully structured multi-block mesh and a grid sensitivity study was performed. The mesh was gradually refined while maintaining y+ values of around 1. The turbulence was modelled using the k-ω SST turbulence model with RANS equations. The authors provided a detailed description of the tip gap vortical flow and its role in preventing tip leakage. They found that increasing the rim height and decreasing the rim width resulted in larger cavity vortices and reduced leakage flow, but also increased blockage. For a constant rim height, a wider rim increased the amount of leakage flow. The results on rim height were somewhat contrary to the findings of Chyu et al. [21], who found that a deeper squealer cavity led to a larger leakage flow. The study by Senel et al. showed that the highest heat transfer was found on the suction side of the squealer rim, where the majority of the leakage flow leaves the cavity. The overall heat transfer was found to increase with the increase of rim width. The squealer cavity floor was subjected to less heat load as the cavity became deeper, indicating a trade-off between aerodynamic performance and heat load in terms of squealer cavity depth.

A very interesting study on different squealer tips, highlighting the importance of squealer openings, was conducted by Kim et al. [37]. The squealers were created by hand, placing the rims at different locations around the tip's edge. In total, six additional squealer tips with openings were examined, apart from the full perimeter simple squealer, for aerothermal performance. The authors stated that squealers with suction side rims had lower total pressure loss coefficients when compared to squealers without suction side rims. The reason for this was that the suction side rim suppressed the development of cavity vortices, resulting in a reduced pressure loss. Furthermore, the authors found that the squealers with leading and trailing edge openings had the smallest total pressure losses, despite having the largest amount of tip leakage flow. This was because the leading edge opening caused the tip leakage flow to enter

the cavity with lower velocity and prevented the formation of a boundary layer that would have developed into a passage vortex. Regarding thermal performance, the authors stated that tips with leading edge openings had lower heat loads as there was no separated flow over the leading edge rim, which would have impinged on the cavity floor and caused oblique shocks in the tip region. Finally, the authors made an important statement that tip performance is about tuning the leakage flow and not necessarily preventing it.

Coull et al. [38] investigated the flow features and heat transfer of different winglets through a winglet overhang parametric study. The largest efficiency improvements were found for full perimeter winglets featuring overhangs all around the tip. However, due to their large area, these tips had the highest heat load increase compared to the flat tip. Winglets with overhangs only at the front portion of the blade's suction side brought substantial efficiency increase, either with no decrease or with a small decrease, in the overall heat load. Winglet tips also decreased the heat load at the aft portion of the blade's suction side, below the tip, by pushing the over tip leakage and passage vortices away from the blade. In the case of the flat tip, this region was subjected to higher heat loads as a result of the tip leakage flow and passage vortices rubbing. The authors concluded that the winglet tip improvements were a result of lower viscous losses, particularly by injecting the tip leakage flow into the region of higher pressure, aligning the tip flow more towards the main passage flow, and reducing the interaction between the over tip leakage and the passage vortex.

Cheon and Lee [39] investigated a combination of winglet and squealer tips. The authors found that adding a winglet to a full perimeter squealer led to a 5.8 % reduction in the total pressure loss coefficient. This was caused by better flow turning and larger flow slowdown areas. Interestingly, the total pressure loss coefficient was found to decrease with the winglet overhang size.

A combination of different pressure side winglet overhangs and squealer tips was also investigated by Yan et al. [40]. The authors stated that removing the pressure side rim or adding the pressure side winglet overhang both eliminated heat transfer hotspots in the leading edge area of the squealer cavity, compared to the simple squealer. Also, with the same modifications, the area averaged heat transfer coefficient on the tip could be reduced by approximately 10 %. The authors also performed a study of winglet coverage on the pressure side, starting from the trailing edge. It was found that the lowest area averaged tip heat transfer was achieved when the winglet overhang stretched only through the second portion of the pressure side, towards the trailing edge.

Zhang and He [41] investigated the transonic tip flow conditions, focusing on the effect of tip choking by varying flow conditions for a blade in the engine representative case. It was found that choked tip flow neglected the importance of the pressure gradient that usually drives the tip leakage flow. In other words, tip choking worked detrimentally for the amount of tip leakage flow as it reached the maximum. The authors also explained that with an increase in the blade passage exit Mach number, the tip leakage loss reduced as part of the overall passage loss.

Zhang et al. [42] carried out a study of the transonic tip gap flow conditions and their effect on tip heat transfer. It was found that in the front portion of the tip, where the flow was subsonic, the tip experienced higher heat transfer compared to the aft area of the tip, where the flow was mostly supersonic. In the area of supersonic flow, a series of oblique shock waves were found to originate at the tip pressure side edge. Impingements of these shocks caused stripes of increased heat transfer across the tip. O'Dowd et al. [43] took a similar approach in their experimental and numerical study of the aerothermal performance of a winglet tip with cavities under transonic conditions. They found that at the front part of the tip flow, it was mostly subsonic, reaching supersonic conditions as it developed down the tip. Similarly, to the study by Zhang et al. [42], supersonic flow resulted in a series of oblique shocks, resulting in increased heat transfer level stripes. The effect of moving casing was also included and showed that it had a significant impact on the prediction of supersonic flow regions, highlighting the importance of considering it when studying heat transfer.

Zou et al. [44] conducted an interesting numerical study on simple squealers and squealers with pressure side rims inclined outward. They focused on examining the heat transfer hotspots in the tip region and casing. Like the findings from Zhang et al. [42], the authors stated that the heat transfer inside the squealer cavity can be divided into two regions. In the front part of the cavity, the heat transfer was usually governed by the hot temperature gas flowing through the seal-like squealer structure, forming oblique shocks. In the middle of the cavity, the heat transfer was mostly governed by the scraping vortex rubbing against the squealer cavity floor, causing a hotspot. The authors also stated that the suction side of the squealer was subjected to a much higher heat load compared to the pressure side, mainly due to different squealer cavity vortices leaving the tip region, which aligns with the findings from Senel et al. [36].

Zhang and He [45] first investigated the tip shaping to create a variable tip gap height across the tip, exploring its potential in managing the tip heat load. Following the findings from Zhang et al. [42], they shaped the tip to accelerate the flow in the

front part of the tip where subsonic flow usually causes a higher heat load, giving it a converging-diverging shape across the tip. This resulted in the removal of the stripe of increased heat transfer at the tip's leading edge region. Through their CFD model, they found that the main driving mechanism of this flow behaviour was the reduction of local turbulence in the transonic flow area, as a result of tip shaping.

Building on previous studies that showed the importance of the transonic tip flow on heat transfer, De Maesschalck et al. [46] investigated the aerothermal performance of contoured tip shapes compared to conventional geometries, such as flat and squealer tips. The contoured geometries were created by combining a series of 2D tip profiles at different axial locations, following the tip chord line. Results showed that aerodynamic and heat load focused contoured shapes, through the use of local flow acceleration, decreased the heat transfer level compared to the flat tip. However, a contoured tip design focused on reducing the tip heat load was found to increase the heat load on the blade's suction side due to the tip leakage vortex rubbing.

1.3.5 Tip optimisation

Optimisation of 2D contoured tips was carried out by De Maesschalck et al. [47]. In their study, they focused on profiling the tip cross sections by minimising both aerodynamic loss and tip heat transfer. The optimisation was performed using an in-house evolutionary algorithm optimiser that was initialised with a set of design of experiments (DOEs). The numerical model was built and solved using RANS equations coupled with the k-ω SST turbulence model. Parametrisation was done using a set of parameters that defined a Bezier curve shaping the tip. Due to the nature of the optimisation, where large geometry differences were explored, an unstructured automatic mesh was used with a special focus on satisfying the y+ condition. Different flow conditions were investigated, and it was found that tip shapes that performed better in subsonic flow were not the optimum choice for supersonic flow conditions. Aerodynamic loss production in subsonic flow mainly depended on the amount of tip leakage flow, and its improvement was focused on closing the tip gap. In subsonic flow, placing a shallow dent close to the pressure side edge was found to increase the size of the pressure side edge recirculation bubble, narrowing the effective tip gap by enhancing the *vena contracta* effect. In supersonic flow, the optimum aerodynamic shape was found to be identical to the nominal flat tip with sharp edges. The optimum heat transfer shapes in subsonic and supersonic flow followed the findings from the study by Zhang and He [45], where the optimum subsonic flow tip had a converging shape and the supersonic flow tip had a diverging nozzle shape.

Caloni et al. [48] conducted a multidisciplinary optimisation of winglet squealer tips, focusing on aerodynamic efficiency and blade heat load. They utilised a surrogate model in the form of a Kriging response surface approach, coupled with a genetic algorithm, to iteratively improve the response surface prediction until it converged with predictions from CFD simulations. This resulted in the creation of a Pareto front that demonstrated the trade-off between efficiency and heat load. The analysed optimum shapes featured openings at the leading edge and trailing edge suction side, aligning with the findings of the best performing tips from Kim et al. [37]. The results showed that larger winglet overhangs increased the overall heat load on the tip by up to 15 %, but decreased the heat load on the blade suction side. Tips that improved efficiency by 0.5 % to 1 % were also found, with a corresponding small increase in heat load.

De Maesschalck et al. [49] carried out an aerothermal optimisation of carved (contoured) and squealer-like tip geometries, developing two different optimisation parametrisations. Carved tips were generated using a similar approach as in the study by Maesschalck et al. [47]. Squealer-like tip geometries from the other optimisation were generated following the principles of topology optimisation, in which, according to the authors, almost every possible rim-cavity layout was allowed to be generated. Both optimisations used in-house optimisation codes, which were initialised with a set of design of experiments. Afterwards, differential evolution optimisers were used. In both optimisations, after Pareto fronts of two objectives were generated, the best-performing designs were selected, and another design of experiments was generated in a Pareto front region to repopulate regions with the most promising designs. A CFD model was built for a whole turbine stage using a mixing plane between the stator and rotor domains. RANS equations were paired with a k-ω SST turbulence model, and an unstructured automatic mesh was generated for every rotor blade tip in question. The carved shape optimisation showed great potential for reducing the tip heat load by using the converging-diverging shape analogy for subsonic and supersonic flow conditions, albeit with an efficiency penalty. The results of the squealer-like optimisation showed that the new tip geometry definitions have great potential for exploring the flow features of unconventional tip shapes with better aerothermal performance than simple squealers and flat tips. Squealer designs with 0.2 % efficiency increase over simple squealers with no additional heat load were found.

Andreoli et al. [50] conducted an aerothermal topology optimisation of turbine tips. In this study, the squealer tip shapes were defined by modifying the Bezier surface through a set of control points. The Bezier surface was cut at a fixed height

to produce a description of squealer lines, which were then mapped onto the tip and extruded into squealer rims. The optimiser used was a genetic algorithm, and a Pareto front of efficiency and integrated heat flux was presented. The CFD model was built following the same analogy as De Maesschalck et al. [49]. This optimisation approach showed great potential for creating novel squealer shapes that feature an arbitrary number of squealer rims with possible openings in completely flexible locations. The optimum efficiency and heat flux tips were analysed and reverse engineered, and it was shown that this definition of the design space allowed for the testing of various squealer configurations, and the best operating principles were selected from the optimum designs. These operating principles can then be applied to new tip designs.

The work of Andreoli et al. [50] was continued in a study by De Maesschalck et al. [51]. In this study, a methodology for optimising not only the squealer tip topology but also the topology of tip cooling was included. The methodology was developed by cleverly defining the arbitrary location, amount, and size of the tip cooling holes, and it simultaneously investigated both the aerothermal performance and cooling effectiveness. As in previous studies of squealer designs, the best performing designs were found to have leading edge and late suction side squealer rim openings. These tips were later investigated further in another optimisation with a limited design space for additional performance and cooling effectiveness. The study confirmed the best performing tip topologies in terms of efficiency and also identified novel cooling hole arrangements that allowed for maintaining aerodynamic efficiency benefits while further reducing blade metal temperatures.

Baert et al. [52] also performed a high complexity design space optimisation on low pressure turbine blades. This study is interesting because a high complexity design space consisting of 350 parameters was optimised using a surrogate model based approach. Focusing on turbine aerodynamic performance, the authors stated that they managed to optimise both global and local flow characteristics, resulting in an efficiency increase of up to 0.5 %. Despite the size of the design space, an efficient data mining process enabled the use of the infill method for increasing surrogate model accuracy. As a result, the improvement in turbine efficiency achieved was beyond expectations and achieved with modest computational resources, as the sample size was only five times the number of design parameters.

1.4 Identified research gaps

In the previous section, physics of the over tip leakage flow has been presented for the different tip designs. It has been shown that nowadays, common turbine tip shapes are understood enough to find a direction where to seek for the additional improvements. Through the literature study on various tip designs, it can be concluded that the most promising state of the art design is a combination of winglet and squealer tip with squealer rim openings. Different researchers have proved this, but there is no unique design which works in all cases. Because the potential improvements in each examined tip design arise from the very local flow features that are result of very fine geometry changes, it is hard to predict how will a certain design behave from the beginning. Also, each design is very dependant on the flow in question, which is again turbine case defined. All this can lead us to conclusion that designer of a state of the art turbine tip has to do some back and forth investigations to make sure every bit of tip performance is found. All of this asks for the new methods and designs for the control of the tip leakage flow.

As shown in the literature study, squealer tips have been thoroughly researched. Different parametric studies and optimisations have been performed and two main directions can be identified. Earlier work was about starting from a simple full perimeter squealer which was then modified by adding or removing portions of the squealer rims by hand to investigate their potential. Since the potential of opening the squealer rims and varying the squealer cavity width and depth has been proven, newer work mostly dealt with investigating squealer tips in much more flexible definition of squealer rims. Instead of using predetermined position of squealer rims, researchers like De Maesschalck et al. [49], Andreoli et al. [50] and De Maesschalck et al. [51] developed methods for arbitrary squealer rims creation. This has shown to be a big jump when it comes to the exploring of the squealer tips potential. Nevertheless, some gaps are still visible. This kind of parametrisation can often be very costly in the number of parameters. This can either make an optimisation quite lengthy and even cause issues with the optimisation convergence. Recent state of the art work mostly focused on developing new optimisation parametrisation but little work had been done on improving the latest existing ones.

Furthermore, using flexible parametrisation with a large number of parameters so far meant using evolutionary and genetic algorithms and running optimisations using large amount of computational power, a resource whose use is worth minimising. Even when having large computational resources, topology optimisation has been proven

as difficult to converge. Baert et al. [52] addressed this issue and showed a lot of hidden potential. Still, a lot of effort is needed in making optimisers quicker and more efficient.

Previous research on winglet tips showed that their geometry and operating principle are much simpler than in the case of squealer tips. Therefore, they are less researched. Apart from their operating principle and its effect on the aerodynamic performance, literature study showed that the most crucial thing about winglet tips is the heat load which almost always increases due to the extra tip wetted surface. As to winglet's aerodynamic efficiency and heat load relationship, some of the best work done in this area is the winglet tip parametric study performed on a linear cascade by Coull et al. [38]. In that work, an efficient winglet tip parametrisation method has been presented and interdependence of efficiency and heat load has been given for a whole range of winglet tips for the case of a linear cascade. Still, no work has been done on the aerothermal optimisation of winglet tips in a real turbine stage.

In many recent work on tip optimisation, both aerodynamic efficiency and heat load were taken into account. Between the two, efficiency is easier to define. Heat load, on the other hand, can be defined differently. Through the literature study, in most of the work done on turbine blade tips, heat load was calculated directly from the wall heat flux and integrated. Wall heat flux was obtained by imposing an uniform wall temperature condition whose average resembled the real life temperature ratio against the turbine inlet temperature. This information is valuable but it does not provide much for the later work on a specific design. Also, real life turbine blades do not operate having a uniform wall temperature. Since Maffulli and He [25] showed that the wall temperature condition affects the flow, it can be concluded that calculating the heat load by imposing a uniform wall temperature clearly introduces an error. In the optimisation context, little has been done to assess the different heat transfer modelling effect on the outcome of the optimisation.

Lastly, the importance of turbine inlet capacity and stage reaction has been briefly given in the introduction. Despite these two turbine properties being one of the crucial for turbine performance, they are very often neglected in the literature. To the author's knowledge, very few researchers included turbine inlet capacity and stage reaction in their studies, especially when designing a turbine tip. One exception known to the author is the study by Shahpar et al. [53].

1.5 Aim and objectives of present work

The overall aim of this work is to present a methodology for designing a novel high pressure turbine tip. As mentioned in the previous section, research shows that the state of the art turbine tip is a combination of winglet and squealer properties. To develop a methodology for designing a novel high pressure turbine tip, this work addresses objectives that ultimately lead to aerothermal topology optimisation.

One of the objectives is to define a thermal load model that does not assume a constant blade surface, as this work deals with both aerodynamic and thermal assessments of turbine tips.

It has been emphasised in previous sections that the inclusion of turbine inlet capacity and stage reaction is important but often ignored. This work aims to include turbine inlet capacity and stage reaction in the design of a new tip.

Recent research shows that novel parametrisation methods for squealer geometry have a clear advantage over the designs of simple squealers. However, these parametrisations often come with increased computational costs due to a higher number of parameters. One of the objectives of this work was to see if similar parametrisations could be defined using a smaller number of parameters.

Dealing with a large number of parameters is often very challenging for an optimiser, especially in a non-linear design space such as the design space of the novel squealer optimisation presented in the literature study. Therefore, this work aims to propose a novel optimisation approach that creates an efficient workflow for optimising in a non-linear design space.

To evaluate the potential benefits of a winglet tip in a turbine stage and its aerothermal trade-off, which can later be used in combination with a squealer tip, this work aims to perform a winglet aerodynamic and aerothermal optimisation.

Finally, the objective of this work is to perform aerothermal squealer tip optimisation using a novel squealer tip parametrisation approach and a thermal load definition.

1.6 Outline of the thesis

In the next Chapter, the computational methodology is presented. It includes all the methods for building the computational model, starting with the presentation of the computational methods and the flow solver and its equations. Then, the optimisation

tools are described, followed by an explanation of the geometry parametrisation and different optimisation techniques.

With the computational methods explained, Chapter 3 focuses on the actual computational model. It starts with the presentation of the model evaluation, explaining the ways of calculating the model's properties that will be used as inputs for the optimiser. Then, the model is verified through a mesh verification study, and validated with two research cases. The effect of the turbulence model and the assessment of heat load are also discussed.

With the model verified and validated, optimisations were carried out next. In Chapter 4, the winglet tip optimisation with the methods for constraining the turbine mass flow and the stage expansion are presented, along with the results of both aerodynamic and aerothermal optimisations, which are analysed.

Chapter 5 covers the topology optimisation, which is carried out in several stages. Using different definitions of the design space, different ranges and complexities of topologies are optimised for both aerodynamics and aerothermal performance. The results of different optimisation techniques are also explained.

Finally, in Chapter 6, the most important conclusions are summarised and future work is discussed.

Chapter 2

Computational methodology

To study the various tip shapes, a Computational Fluid Dynamics (CFD) model is utilised. To optimise the tip shapes, various optimisation approaches are employed. This chapter begins by explaining the fundamentals of the CFD model, including the related equations and mesh, followed by an overview of the optimisation tools used in this study.

2.1 Flow solver

The flow solver used in this work is Hydra, which is an in-house code for CFD simulations developed by Rolls-Royce [54]. Hydra is an unstructured, edge based solver, with flow variables stored at cell vertices. It employs a second order upwind discretisation scheme and a five stage Runge-Kutta scheme for pseudo time stepping. The convergence process is accelerated by the use of a multi-grid element-collapsing algorithm, which is critical for generating CFD solutions in a timely manner that is suitable for effective optimisation [55].

2.1.1 Governing equations

The governing equations are the 3D unsteady compressible Navier-Stokes equations given as

$$\frac{\partial Q}{\partial t} + \nabla \cdot F = 0 \tag{2.1}$$

where Q represents the variables vector and F represents the sum of convective and diffusive terms. The variables vector and x-direction convective and diffusive terms are

$$Q = \begin{bmatrix} \rho \\ \rho u \\ \rho v \\ \rho w \\ \rho E \end{bmatrix} \tag{2.2}$$

$$F_x = \begin{bmatrix} \rho u \\ \rho u^2 + p - \tau_{xx} \\ \rho uv - \tau_{yx} \\ \rho vw - \tau_{zx} \\ u(\rho E + p) - u\tau_{xx} - v\tau_{yx} - w\tau_{zx} - k_T \frac{\partial T}{\partial x} \end{bmatrix} \tag{2.3}$$

$$F_y = \begin{bmatrix} \rho v \\ \rho uv + p - \tau_{xy} \\ \rho v^2 + p - \tau_{yy} \\ \rho vw - \tau_{zy} \\ v(\rho E + p) - u\tau_{xy} - v\tau_{yy} - w\tau_{zy} - k_T \frac{\partial T}{\partial y} \end{bmatrix} \tag{2.4}$$

$$F_z = \begin{bmatrix} \rho w \\ \rho uw - \tau_{xz} \\ \rho vw - \tau_{yz} \\ \rho w^2 - \tau_{zz} \\ w(\rho E + p) - u\tau_{xz} - v\tau_{yz} - w\tau_{zz} - k_T \frac{\partial T}{\partial z} \end{bmatrix} \tag{2.5}$$

where ρ is density, E is energy, p is pressure, τ is the friction forces tensor and k_T is the thermal conductivity. To close the set of equations, equation for state of perfect gas is needed.

$$p = \rho RT \tag{2.6}$$

2.1.2 Reynolds Averaged Navier-Stokes (RANS) equations

Solving the Navier-Stokes equations iteratively in space and time, after discretising them, is a complex and computationally demanding process. Even with these efforts, these equations often require many approximations and not all systems can be solved. To address this, numerical techniques that involve mathematical approximations are employed. The goal is to speed up the solution process while still retaining enough accuracy to gain useful insights into the flow in question.

In this work, time averaged Reynolds Averaged Navier-Stokes (RANS) equations are used. These equations are a simplified form of the general Navier-Stokes equations and work by decomposing the instantaneous flow variables into mean and fluctuating values, expressed as $\phi = \overline{\phi} + \phi'$. This process is known as a Reynolds decomposition [56]. The continuity and Reynolds averaged Navier-Stokes equations can be written as

$$\frac{\partial \rho}{\partial t} + \frac{\partial (\rho \overline{u}_i)}{\partial x_i} = 0 \tag{2.7}$$

$$\frac{\partial \rho \overline{u}_i}{\partial t} + \frac{\partial \rho \overline{u}_i \overline{u}_j}{\partial x_j} = -\frac{\partial \overline{p}}{\partial x_i} + \frac{\partial}{\partial x_j}\left(\mu \frac{\partial \overline{u}_i}{\partial x_j} - \rho \overline{u_i{}' u_j{}'}\right) \tag{2.8}$$

where the term $\rho \overline{v_i{}' v_j{}'}$ is known as the Reynolds stress tensor, τ_{ij}. The Reynolds stress tensor is a symmetric tensor that represents the additional stress due to turbulence (the fluctuating component of velocity), thereby introducing six new unknown variables. To close the equation system of 11 variables and 5 equations, a model for the Reynolds stresses is required. This is referred to as the closure problem.

In this work, two models were used to address this issue: the Spalart-Allmaras and the k-ω SST turbulence models. Both of these models employ the Boussinesq assumption, introducing the turbulent (or eddy) viscosity μ_t to model the unknown Reynolds stresses. In these turbulence models, the Reynolds stresses are expressed as

$$\tau_{ij} = 2\mu_t S_{ij} - \frac{2}{3}\rho k \delta_{ij} \tag{2.9}$$

where S_{ij} is mean strain rate tensor and k is the turbulent kinetic energy.

2.1.3 Turbulence modelling

2.1.3.1 Spalart-Allmaras turbulence model

Spalart-Allmaras turbulence model is a one equation turbulence model introduced by Spalart and Allmaras [57]. It assumes that turbulent kinetic energy is negligible, meaning only turbulent viscosity has to be found. Turbulent kinematic viscosity ν_t is expressed as

$$\nu_t = \tilde{\nu} f_{v1}, \qquad f_{v1} = \frac{\chi^3}{\chi^3 + c_{v1}^3}, \qquad \chi = \frac{\tilde{\nu}}{\nu} \tag{2.10}$$

where $\tilde{\nu}$ is the Spalart-Allmaras working variable. Its transport equation is

$$\frac{\partial \tilde{\nu}}{\partial t} + \frac{\partial u_j \tilde{\nu}}{\partial x_j} = P - D + T + \frac{1}{\sigma}\left[\nabla \cdot ((\nu + \tilde{\nu})\nabla\tilde{\nu}) + c_{b2}(\nabla\tilde{\nu})^2\right] \tag{2.11}$$

where P, D and T are the production, destruction and trip terms. They are given as

$$P = c_{b1}(1 - f_{t2})\tilde{S}\tilde{\nu}, \quad D = \left(c_{w1}f_w - \frac{c_{b1}}{\kappa^2}f_{t2}\right)\left[\frac{\tilde{\nu}}{d}\right]^2, \quad T = f_{t1}(\Delta u)^2 \tag{2.12}$$

where $\tilde{S}$ is modified vorticity. Trip term T is used for triggering the transition of the flow at a specified location. In this work, this is set to zero as the transition is not considered. Modified vorticity is given as

$$\tilde{S} = S + \frac{\tilde{\nu}}{\kappa^2 d^2} f_{v2}, \quad f_{v2} = 1 - \frac{\chi}{1 + \chi f_{v1}},$$
$$f_w = g\left[\frac{1 + c_{w3}^6}{g^6 + c_{w3}^6}\right]^{1/6}, \quad g = r + c_{w2}(r^6 - r), \quad r = min\left(\frac{\tilde{\nu}}{\tilde{S}\kappa^2 d^2}, r_{lim}\right) \tag{2.13}$$

where S is the magnitude of vorticity.

Empirical constant used in Spalart-Allmaras model are summarised in Table 2.1.

2.1.3.2 k-ω SST turbulence model

The k-ω SST turbulence model, proposed by Menter [58, 59], is a two-equation turbulence model in which the transported variables to be determined are the turbulence kinetic energy k and the specific turbulent dissipation rate ω. This turbulence model is a good choice for both low-Re and high-Re number flows as its k-ω formulation makes it usable in the highly viscous sublayers near the wall and its shear stress transport (SST) formulation in the freestream.

Transport equation for kinetic energy is given as

$$\frac{\partial(\rho k)}{\partial t} + \frac{\partial(\rho u_j k)}{\partial x_j} = P - \beta^* \rho k\omega + \frac{\partial}{\partial x_j}\left[(\mu + \sigma_k \mu_t)\frac{\partial k}{\partial x_j}\right] \tag{2.14}$$

and the transport equation for turbulent dissipation rate as

$$\frac{\partial(\rho\omega)}{\partial t} + \frac{\partial(\rho u_j \omega)}{\partial x_j} = \frac{\gamma}{\nu_t}P - \beta\rho\omega^2 + \frac{\partial}{\partial x_j}\left[(\mu + \sigma_\omega \mu_t)\frac{\partial \omega}{\partial x_j}\right] + 2(1 - F_1)\frac{\rho\sigma_{\omega 2}}{\omega}\frac{\partial k}{\partial x_j}\frac{\partial \omega}{\partial x_j} \tag{2.15}$$

Constant	Value
c_{b1}	0.1355
c_{b2}	0.622
c_{w1}	$\frac{c_{b1}}{\kappa^2} + \frac{1 + c_{b2}}{\sigma}$
c_{w2}	0.3
c_{w3}	2
c_{v1}	7.1
κ	0.41
σ	2/3
r_{lim}	10
d	distance to the nearest wall

Table 2.1: Spalart-Allmaras model constants

where P is production term and F_1 and F_2 are the blending functions. They are given as

$$P = \tau_{ij} \frac{\partial u_i}{\partial x_j}, \tag{2.16}$$

$$F_1 = \tanh(arg_1^4), \tag{2.17}$$

and

$$F_2 = \tanh(arg_2^2) \tag{2.18}$$

where arg_1 and arg_2 are given as

$$arg_1 = min\left[max\left(\frac{\sqrt{k}}{\beta^* \omega d}, \frac{500\nu}{d^2\omega}\right), \frac{4\rho\sigma_{\omega 2}k}{CD_{k\omega}d^2}\right] \tag{2.19}$$

$$arg_2 = max\left(2\frac{\sqrt{k}}{\beta^* \omega d}, \frac{500\nu}{d^2\omega}\right) \tag{2.20}$$

Constant	Value
γ_1	$\frac{\beta_1}{\beta^*} - \frac{\sigma_{\omega 1}\kappa^2}{\sqrt{\beta^*}}$
γ_2	$\frac{\beta_2}{\beta^*} - \frac{\sigma_{\omega 2}\kappa^2}{\sqrt{\beta^*}}$
σ_{k1}	0.85
σ_{k2}	1.0
$\sigma_{\omega 1}$	0.5
$\sigma_{\omega 2}$	0.856
β_1	0.075
β_2	0.0828
β^*	0.09
κ	0.41
a_1	0.31

Table 2.2: k-ω SST model constants

where d is distance to the nearest wall. $CD_{k\omega}$ is given as

$$CD_{k\omega} = max\left(2\rho\sigma_{\omega 2}\frac{1}{\omega}\frac{\partial}{\partial x_j}\frac{\partial \omega}{\partial x_j}, 10^{-20}\right) \tag{2.21}$$

and turbulent eddy viscosity is given as

$$\mu_t = \frac{\rho a_1 k}{max(a_1\omega, \Omega F_2)} \tag{2.22}$$

where Ω is the vorticity magnitude.
Model constants are given in Table 2.2.

2.1.4 Discretisation of RANS equations

2.1.4.1 Spatial discretisation

Spatial discretisation of RANS equations is presented next. The equations are taken from Moinier [60]. To begin, 3D compressible RANS equations are given in more concise way as

$$\frac{\partial \mathcal{Q}}{\partial t} + \nabla . \mathcal{F}(\mathcal{Q}, \nabla \mathcal{Q}) = \mathcal{S}(\mathcal{Q}, \nabla \mathcal{Q}) \tag{2.23}$$

where $\mathcal{Q}(\mathbf{x})$ is the vector of conserved variables $(\rho, \rho u, \rho v, \rho w, \rho E)^T$. $\mathcal{F}(\mathcal{Q}, \nabla \mathcal{Q})$ is the total flux and the source term $\mathcal{S}$ is in the form $(0, 0, 0, 0, 0, 0)^T$.

Using the finite volume approach, the Navier-Stokes equation 2.23 is integrated over the control volume. Next, the divergence theorem (also known as the Gauss theorem) is applied. It states that the outward flux of a vector field through a closed surface is equal to the volume integral of the divergence over the region inside the closed surface. In other words, the overall change within the control volume is equal to the sum of what passes through the volume's surfaces. After the application of the divergence theorem, it gives the expression

$$\mathcal{R}_j = \frac{1}{V_j} \Big(\oint_{\partial V_j} \mathcal{F}(\mathbf{n}, \mathcal{Q}, \nabla \mathcal{Q}) ds - \int_{V_j} \mathcal{S}(\mathcal{Q}, \nabla \mathcal{Q}) dv \Big) = 0, \quad \forall j \tag{2.24}$$

where $\mathcal{R}_j$ is the residual, which represents the imbalance of conservation inside the control volume, and V_j is the measure of the control volume associated with index j.

Hydra uses a cell-vertex scheme with median-dual control volumes. This way, the flow variables are stored at the computational mesh vertices and control volumes are constructed around each mesh vertex, connecting the centroids of the surrounding elements and edge-midpoints, as shown in Figure 2.1.

The flux integration in Equation 2.24 is performed by approximating the dual control volume surface area vectors ($\mathbf{n}$). These vectors represent the directional contributions of each control volume surface to the overall control volume surface area. The control surface area vectors are anti-symmetric, meaning the contribution of a surface appears with opposite signs on opposite faces of the control volume, ensuring conservation. The integration of the fluxes can therefore be approximated by summation as

$$\oint_{\partial V_j} \mathcal{F}(\mathbf{n}, \mathcal{Q}, \nabla \mathcal{Q}) ds \approx \sum_{i \in E_j} \mathcal{F}(\mathbf{n}_{ij}, \mathcal{Q}, \nabla \mathcal{Q})|_{x = \frac{1}{2}(x_i + x_j)} \Delta s_{ij} \tag{2.25}$$

where E_j is the set of all nodes connected to node j via an edge, $\mathbf{n}_{ij}$ is a unit vector and Δs_{ij} is an area in 3D associated with the edge connecting nodes i and j.

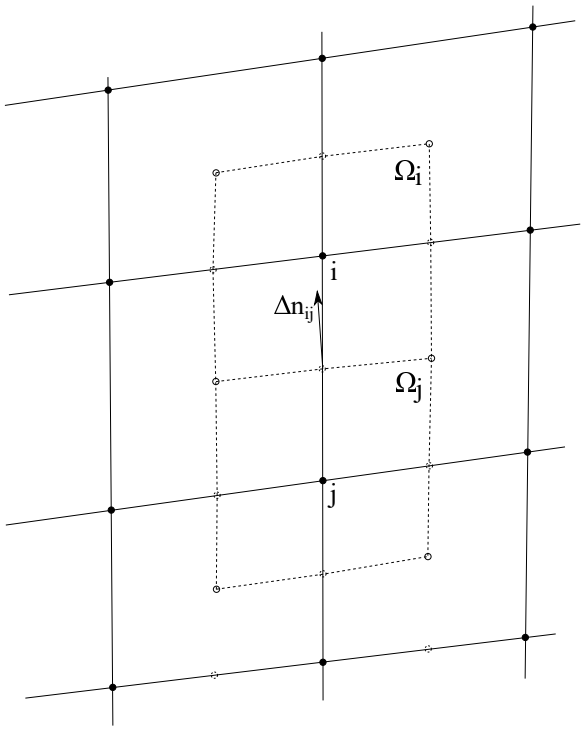

Figure 2.1: Control volumes built around mesh nodes

Regarding the nodes the boundary, extra terms from boundary faces are added and the approximation of the fluxes is written as

$$\oint_{\partial V_j} \mathcal{F}(\mathbf{n},,)ds \approx \sum_{i \in E_j} \mathcal{F}(\mathbf{n}_{ij},,)|_{x=\frac{1}{2}(x_i+x_j)} \Delta s_{ij} + \sum_{k \in B_j} \mathcal{F}(\mathbf{n}_k,,)|_{x_j} \Delta s_k \tag{2.26}$$

where B_j is the set of boundary faces associated with node j, $\mathbf{n}_k$ is the corresponding normal and Δs_k is the area. The closure of control volumes implies that

$$\sum_{i \in E_j} \mathbf{n}_{ij} \Delta s_{ij} + \sum_{k \in B_j} \mathbf{n}_k \Delta s_k = 0. \tag{2.27}$$

With that, the discrete equivalent to Equation 2.24 becomes

$$R_j = \frac{1}{V_j} \Big(\sum_{i \in E_j} F_{ij} \Delta s_{ij} + \sum_{k \in B_j} F_k \Delta s_k - S_j V_j \Big) \quad \forall j \tag{2.28}$$

where F_{ij} is the numerical flux in the direction $\mathbf{n}_{ij}$ associated with an antisymmetric edge (i, j), and F_k is the numerical flux associated with the boundary face k.

Lastly, to complete the discretisation, discrete flux functions need to be defined. Since the flux $\mathcal{F}$ can be split into inviscid and viscous part as

$$\mathcal{F}(\mathbf{n}, \mathcal{Q}, \nabla\mathcal{Q}) = \mathcal{F}^I(\mathbf{n}, \mathcal{Q}) + \mathcal{F}^V(\mathbf{n}, \mathcal{Q}, \nabla\mathcal{Q}), \tag{2.29}$$

for any unit normal $\mathbf{n}$, the discrete approximation F of $\mathcal{F}$ will have inviscid and viscous part. There are presented more in detail in the next sections.

2.1.4.2 Inviscid fluxes

The scheme used by Hydra, described next, is inspired by the monotone upstream-centered scheme for conservation laws (MUSCL) approach. In this approach, a functional representation of the conserved variable Q is used within each control volume to solve a Riemann problem at the interface between control volumes. The inviscid flux at the interface of a control volume is calculated using a second order scheme based on the flux-differencing method developed by Roe [61]. This combines central differencing of the non-linear inviscid fluxes with numerical smoothing based on one-dimensional characteristic variables. The inviscid flux at the interface between nodes i and j is given as

$$F^I_{ij} = \frac{1}{2}\big(\mathcal{F}^I_{ij}(Q^+) + \mathcal{F}^I_{ij}(Q^-) - |A_{ij}|(Q^+ - Q^-)\big) \tag{2.30}$$

where $\mathcal{F}_{ij} = \mathcal{F}(\mathbf{n}_{ij}, ,)$ and $A_{ij} = \partial\mathcal{F}^I/\partial\mathcal{Q}$ [60]. To avoid the expensive reconstruction of Q^+ and Q^-, Equation 2.30 is approximated as

$$F^I_{ij} = \frac{1}{2}\big(\mathcal{F}^I_{ij}(Q_i) + \mathcal{F}^I_{ij}(Q_j) - |A_{ij}|(Q^+ - Q^-)\big). \tag{2.31}$$

This way, flux terms are now expressed using nodal variables which allows for easier interpretation of the central difference method with numerical smoothing. Numerical smoothing, given as $|A_{ij}|(Q^+ - Q^-)$, is modified next. For that, the approach by Luo et al. [62] is used in which variable values Q_{j+} and Q_{i-} are constructed at equidistance spaced points along a straight line. This gives numerical smoothing expressed as

$$|A_{ij}|(Q^+ - Q^-) = \frac{1}{2}(1-\kappa)|A_{ij}|\Big[\big(\frac{1}{2}Q_{j+} - Q_j + \frac{1}{2}Q_i\big) - \big(\frac{1}{2}Q_j - Q_i + \frac{1}{2}Q_{i-}\big)\Big] \tag{2.32}$$

where $\kappa \in [0,1]$ represents a one-parameter family of second order schemes for a one-dimensional uniform mesh, with exception of $\kappa = 1/3$ being a third order scheme [60].

Inviscid flux is then given as

$$F_{ij}^{I} = \frac{1}{2}\Big(\mathcal{F}_{ij}^{I}(Q_i) + \mathcal{F}_{ij}^{I}(Q_j) - \frac{1}{2}(1-\kappa)|A_{ij}|\big(L_j(Q) - L_j(Q)\big)\Big) \tag{2.33}$$

where L is an undivided pseudo-Laplacian with a negative central unit coefficient, a modification to the pseudo-Laplacian is required as it only preserves a linear solution. To achieve this, a linear preserving form of the Laplacian L_j^{lp} is used in such a way that the numerical smoothing part of Equation 2.31 is switched off if the flow behavior is linear, as described in Moinier's work [63]. More information on the modification to the pseudo-Laplacian can be found in Moinier's PhD thesis [60].

In order to achieve monotonic resolution in areas where the flow is characterised by steep interior layers, such as shocks and shear layers, while maintaining accuracy where the solution is smooth, an additional treatment of the inviscid flux is necessary. The artificial dissipation term is therefore a non-linear blend of second and fourth-order differences, with a limiter introduced so that smoothing reverts to first order characteristic upwinding at shocks. The formulation from Jameson [64] and Crumpton et al. [65] is used

$$F_{ij}^{I} = \frac{1}{2}\Big(\mathcal{F}_{ij}^{I}(Q_i) + \mathcal{F}_{ij}^{I}(Q_j) - |A_{ij}|\Big(-\frac{1}{3}(1-\psi)\big(\hat{L}_j^{lp}(Q) - \hat{L}_i^{lp}(Q)\big) + \psi(Q_i - Q_j)\Big)\Big) \tag{2.34}$$

where

$$\psi = min\Big(\epsilon^2\left|\frac{p_j - p_i}{p_i + p_j}\right|^2, 1\Big). \tag{2.35}$$

Here, ϵ is user defined constant with a value of 8 and p is the static pressure at the corresponding node [60].

2.1.4.3 Viscous fluxes

The viscous fluxes are approximated halfway along each edge. The integration rule around each volume, as described in Equation 2.24, is then used, resulting in a consistent finite volume treatment of both the inviscid and viscous terms. For that,

∇Q needs to be approximated at the midpoint of each edge. The gradients of the flow variables can be estimated using the existing edge weights at the nodes. The approximation at the midpoint is calculated by a straightforward average as

$$\overline{\nabla Q_{ij}} = \frac{1}{2}(\nabla Q_i + \nabla Q_j). \tag{2.36}$$

Equation 2.36 is the average of two central differences and as such, it does not damp high frequency modes. In the case of inviscid flux, a numerical dissipation term was used to address this issue, but this is insufficient when viscous terms dominate, such as in the boundary layer. To address this issue, the component of ∇Q in the direction along the edge is replaced by a simple difference along the edge as

$$\nabla Q_{ij} = \overline{\nabla Q_{ij}} - \Big(\nabla Q_{ij} \cdot \Delta \mathbf{s_{ij}} - \frac{(Q_i - Q_j)}{|\mathbf{x_i} - \mathbf{x_j}|}\Big)\Delta \mathbf{s_{ij}} \tag{2.37}$$

where

$$\Delta \mathbf{s_{ij}} = \frac{\mathbf{x_i} - \mathbf{x_j}}{|\mathbf{x_i} - \mathbf{x_j}|}. \tag{2.38}$$

This formulation dampens the high frequency error nodes as in the boundary layer, it is the simple differences along the shortest edges that contribute to the dominant viscous flux terms [60].

2.1.4.4 Temporal discretisation

Time integration in Hydra is done through explicit 5-step Runge-Kutta scheme by Martinelli [66]. The solution at the time step Q_j^n is a linear combination of the solution at previous time step Q_j^{n-1} and all the precomputed time steps. This is given as

$$\begin{aligned} Q_j^{(0)} &= Q_j^n \\ Q_j^{(k)} &= Q_j^n - \alpha_k \Delta t_j R_j^{(k-1)}, \qquad\qquad k = 1, ..., 5 \\ Q_j^{(n+1)} &= Q_j^{(5)} \end{aligned} \tag{2.39}$$

where α_k is a constant, Δt_j is the time step and $R_j^{(k-1)}$ is the residual than can be expressed as

k	α_k	β_k
1	¼	1
2	⅙	0
3	⅜	14⁄25
4	½	0
5	1	11⁄25

Table 2.3: Constants used for 5-step Runge-Kutta time stepping

$$R_j^{(k-1)} = C_j(Q_j^{(k-1)}) - B_j^{(k-1)}$$
$$B_j^{(k-1)} = \beta_k D_j(Q_j^{(k-1)}) + (1-\beta_k)B_j^{(k-2)} \tag{2.40}$$

where term $C_j(Q_j^{(k-1)})$ represents the convective part of the residual, $D_j(Q_j^{(k-1)})$ is the dissipative part and β_k is a constant. Values of α_k and β_k are given in Table 2.3. Time step Δt_j is calculated in each cell using the CFL (Courant-Friedrichs-Lewy) number as

$$\frac{1}{\Delta t_j} = \frac{1}{CFL} max\left(\frac{1}{\Delta t_j^I}, \frac{\epsilon^V}{\Delta t_j^V}\right) \tag{2.41}$$

where I denotes inviscid and V viscous time step.

2.1.5 Boundary conditions

In the CFD model, boundary conditions are defined at mesh nodes that coincide with the boundaries of the physical domain being solved. Before solving the flow equations presented earlier, the flux contribution of the boundary conditions must be added to the boundary mesh nodes. In this study, a single stage of a high pressure turbine was modelled, including both the stator and rotor domains. The boundary conditions used in the model are briefly described below.

2.1.5.1 Pressure inlet

The inlet boundary condition used in this study was a subsonic pressure inlet, which defined the total temperature and total pressure, as well as specifying the turbulence quantities and flow direction. The turbulence quantities specified depend on the

turbulence model used. For the Spalart-Allmaras turbulence model, it requires specifying the Spalart-Allmaras working variable $\tilde{\nu}$. For the k-ω SST turbulence model, the values of turbulent kinetic energy k and the specific turbulent dissipation rate w must be specified. Specifying the flow direction involves defining the radial flow angle (known as the pitch angle) and the tangential flow angle (known as the swirl angle) explained in Figure 2.2.

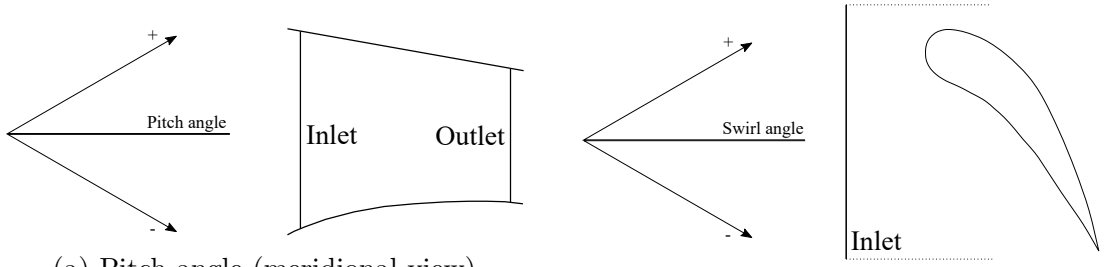

(a) Pitch angle (meridional view)

(b) Swirl angle (view from above)

Figure 2.2: Pitch and swirl angles

2.1.5.2 Pressure outlet

Outlet boundary condition used in this work was the pressure outlet, which specified the radial static pressure distribution, as was measured in the experiment, and later used in numerical model by Chana and Jones [67].

2.1.5.3 Wall

The walls of the geometry in question were specified as viscous walls with a no-slip condition. The no-slip viscous condition means that the fluid velocity at the wall is set to zero. The temperature wall condition used in this work included both adiabatic and isothermal walls. The adiabatic wall assumes no heat flux, meaning there is no additional energy flux going into the control volume around the node at the wall. In the case of the isothermal wall, an energy flux at the wall control volume is added to the energy equation.

2.1.5.4 Periodic

The periodic boundary condition is commonly used in turbomachinery modelling to describe the repeating flow around the annulus. The periodic boundary condition in Hydra assumes conformal mesh nodes at both upper and lower periodic boundaries. That means a specific node at one periodic boundary has the same flow solution as its pair on the other periodic boundary.

2.1.5.5 Mixing plane for stage interface coupling

In the case of rotating flows, such as the turbine flow modelled in this work, it is necessary to define the flow in relation to the rotating frame of reference [68]. Since this work involves modelling a single turbine stage, consisting of both the stationary (stator) and rotational (rotor) domains, the rotor domain was modelled as the moving system with a constant angular velocity. This approach necessitates a special definition of the interface between the stationary and rotational domains. For coupling the two domains of the turbine stage, the mixing plane was used.

The mixing plane, introduced by Denton and Singh [69], is an interface coupling approach for steady turbomachinery simulations that connects the outflow from the stationary domain to the inflow of the downstream rotating domain or vice versa. It involves radially averaging the flow properties, using the radial average values as inputs to the downstream domain. This removes the non-uniformities of flow phenomena, such as blade wakes, vortices, and shock waves. Neglecting the unsteadiness can impact the flow solution, but for RANS simulations, these differences are acceptable considering the computational cost [70]. This is particularly important for computationally expensive optimisation studies, where hundreds of CFD runs are often required. Therefore, the mixing plane interface approach remains state-of-the-art for optimisation studies of whole stages in the turbomachinery environment [53, 71, 72].

2.2 Mesh generation tools

In this study, two mesh generation approaches and tools were used. For the study of regular airfoil shaped tips, a structured mesh was employed. On the other hand, irregularly shaped tips in the form of squealers with different rim placements and openings were meshed using an unstructured, octree based approach. The two approaches are presented in more detail in the next sections.

2.2.1 PADRAM structured meshing

The structured meshing approach is a preferable option in the study of complex flows, as it provides a more accurate and stable CFD solution using an efficient approach. It involves dissecting the geometry in question into a number of blocks that follow the geometry outlines. This way, geometry features are described using regular hexahedrons, giving a higher quality mesh.

In this work, structured meshing was done in PADRAM, Rolls-Royce's in-house tool for geometry parametrisation and mesh generation. Amongst other applications, PADRAM is capable of producing high-quality 2D or 3D meshes for complex gas turbine domains, such as multi-stage, multi-passage turbomachinery geometries, exhausts, and cavities. More details about PADRAM can be found in [73, 74].

In this work, for regular airfoil blades, like the stator blade, and in some cases, the rotor blade, an O-H structured mesh topology was used. This approach utilises two different mesh blocks. As presented in the 2D example in Figure 2.3, starting from a blade (solid black line), an O-mesh block is created around the blade (green area). This gives good control over the mesh resolution and, therefore, a good boundary layer solution around the airfoil. Around the O-mesh, H-mesh blocks are used to fill in the more regular parts of the domain (orange areas). In this particular example, there are four H-mesh blocks, corresponding to the inlet and the exit of the domain, and the pressure and the suction sides of the blade.

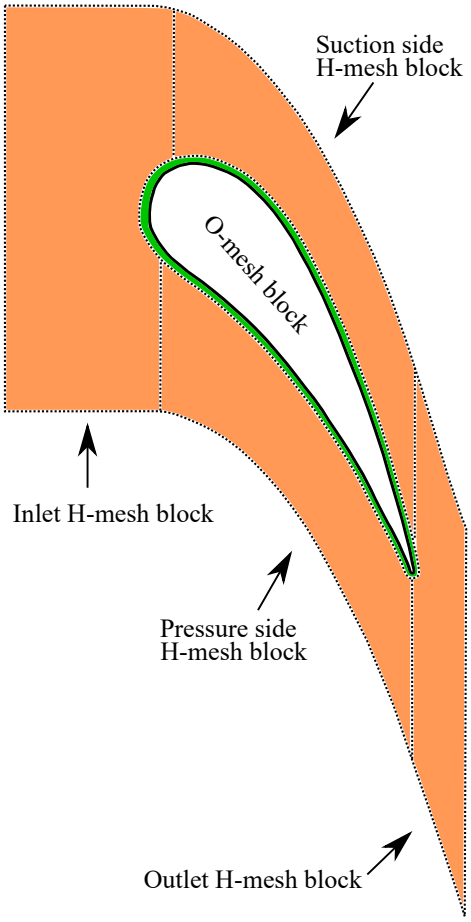

Figure 2.3: PADRAM O-H mesh topology

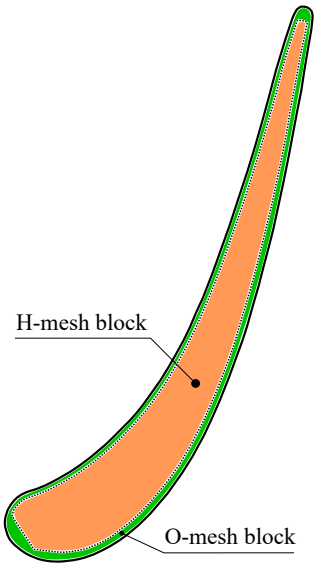

Figure 2.4: PADRAM butterfly tip mesh topology

In cases where the rotor domain needed to be meshed and the tip gap was present, the butterfly mesh topology was used to mesh the tip gap. This is presented in Figure 2.4. Starting from the tip outline, an O-mesh block is created inside the tip, following the tip outline (green area). The rest of the tip area is filled using a single H-mesh block (orange area) whose sides are morphed to correspond to the leading and trailing edge areas, as well as the pressure and suction sides.

2.2.2 BOXER unstructured meshing

Unstructured meshes were used in this work for the study of complex squealer topologies. More specifically, meshing tool caller BOXER was used, utilising the octree meshing approach. This approach is explained using Figure 2.5.

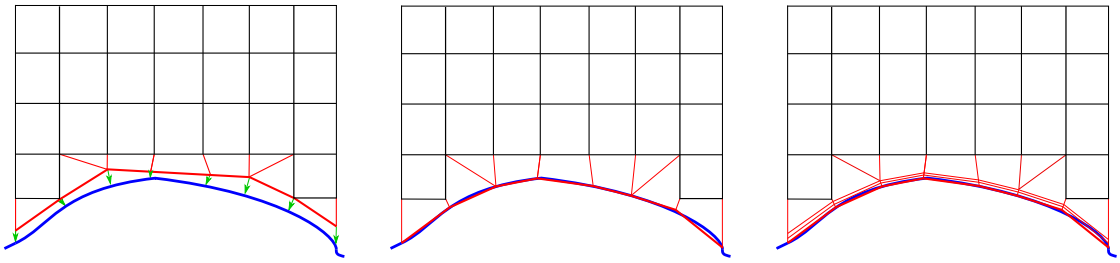

(a) Octree mesh (b) Body-fitted mesh (c) Layers extrusion

Figure 2.5: BOXER meshing process

Starting from the geometry outline (blue in Figure 2.5a), the numerical domain is filled with hexahedral cells of a specified size. This size is controlled by the level of octree mesh refinement. Octree mesh cells that are cut by the geometry outline are removed, and the octree mesh is generated. For the resulting octree mesh, the distance field is calculated, providing the information needed for adapting the octree mesh to the geometry surface. This results in new cells that fill the gap between the octree mesh (black in Figure 2.5a) and the geometry, which are shown in red in Figure 2.5a.

With the calculated distance field, the next step in mesh creation is to create a body-fitted mesh. For that, the octree mesh with the belonging distance field is approximated onto the geometry outline, resulting in a surface mesh. The surface mesh size can be independent of the octree mesh size, and if those two are different, the area that joins them is triangulated. This results in some tetrahedral cells to ensure there are no hanging nodes. With the surface mesh completed and joined

with an octree mesh through the distance field, the body-fitted mesh is completed, as shown in Figure 2.5b.

The body-fitted mesh is already suitable for setting up a CFD simulation, but in most cases, it requires a layer mesh for resolving the boundary layer gradients. To achieve that, after the body-fitted mesh is created, layer cells are extruded in the normal direction from the geometry outline, as shown in Figure 2.5c. This is done by growing the body-fitted mesh where the octree cells are being pushed away from the geometry outline, and mesh smoothing is applied in the octree mesh far-field. The boundary layer mesh is controlled by specifying the first layer height in the absolute value, the number of layers, and the expansion ratio of the boundary layer mesh. More details about this process and the BOXER can be found in [75].

Details of the Boxer meshes used in this work are given later in the corresponding sections.

2.3 Optimisation tools

This section describes the tools used for developing the optimisation process, including geometry parametrisation and optimisation strategies employed in this work.

2.3.1 Tip parametrisation

This work deals with the optimisation of both winglets and squealer tips. Two separate parametrisation approaches were used for these optimisations. The winglet parametrisation used a more traditional approach where each parameter was directly linked to morph a specific part of the tip. On the other hand, the squealer tip had a more flexible parametrisation to allow for topology changes. This included a step between the parameter definition and the actual geometry creation, allowing for a very flexible design space. Both of these parametrisations are presented in the following sections.

2.3.1.1 Winglet parametrisation

The winglet tip was parametrised and generated using PADRAM, as described in Section 2.2.1. PADRAM is capable of both parametrising the geometry and generating the mesh.

Starting with the tip outline of the datum blade as a basis, the winglet tip parametrisation is presented in Figure 2.6. The outline of the winglet tip is defined at five control points around the blade perimeter: one at the leading edge, one at the

suction side, one at the pressure side, and two at the trailing edge (Figure 2.6a). The locations of the leading edge and two trailing edge control points are fixed, while the locations of the pressure side and suction side control points are parameters, denoted as b_{PS} and b_{SS}. They can move along the respective edges between the leading and trailing edges (Figure 2.6b), specified as a portion of the datum blade's axial chord (between 0 and 1). With the overhang control point locations determined, the datum tip outline is parametrised for the overhang values as a portion of the axial chord o at each of the control points (Figure 2.6c). The overhang points are then moved from their positions on the datum tip outline in the normal direction for a given overhang value. After that, with the winglet overhang control points fully defined, the winglet tip outline is created using a B-spline interpolation between the overhang control points along the datum outline. The finished winglet outline is presented in Figure 2.6c.

With the winglet tip outline created, the tip is extruded for a straight length in the radial direction towards the hub, controlling the winglet tip thickness, denoted as d. The straight length is defined as a parameter at each of the 5 overhang control points separately and interpolated between them. It is also expressed as a portion of the axial chord.

After the extrusion of the tip, the last step is to join it with the datum blade. This is done by controlling the blending angle values at each overhang control point, denoted as β. The blending angle is also defined at each control point location separately. With the blending angle defined, a small fillet is applied between the created winglet tip and the datum blade. In total, this parametrisation has 17 design parameters.

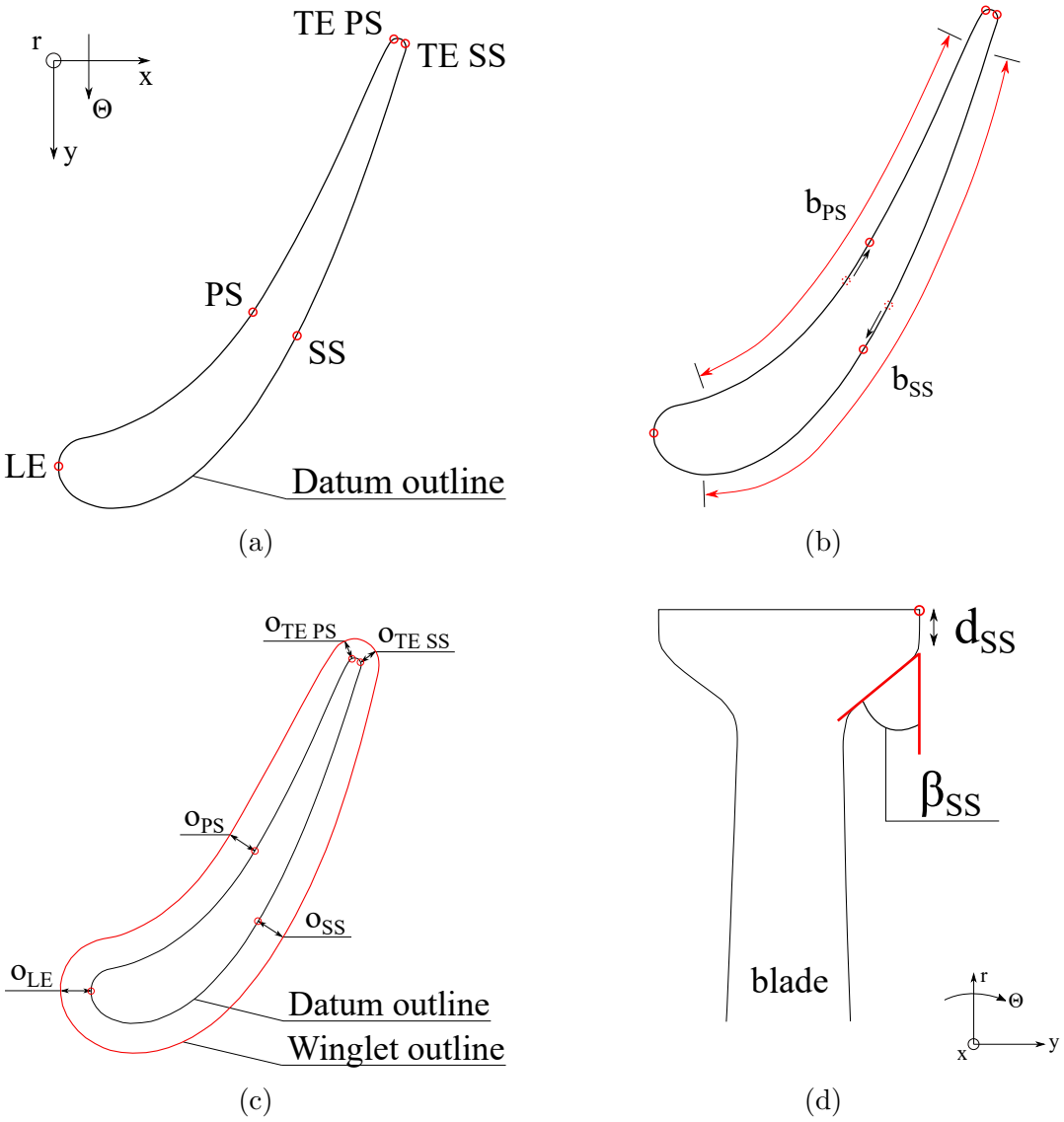

Figure 2.6: Winglet tip parametrisation

2.3.1.2 Squealer parametrisation

Squealer parametrisation traditionally included the parametrisation of squealer rim height and width [76, 77]. The full perimeter squealer (or simple squealer) created with PADRAM is presented in Figure 2.7. In this approach, the squealer tip is generated using the same butterfly tip mesh topology presented in Figure 2.4. The squealer rim is generated and meshed retaining the tip gap O-mesh and H-mesh blocks. Additionally, the squealer cavity is filled with an additional H-mesh block. Since the O-mesh block in the tip gap follows the shape of the squealer rim, two H-mesh blocks (cavity and tip gap) are rounded at the edges in the leading edge and trailing edge regions, resulting in highly skewed cells in their corners. This way, the

squealer height (or the depth of the squealer cavity) can easily be controlled by the cavity H-mesh block dimensions. Similarly, the squealer rim width is controlled by the thickness of the tip gap O-mesh block.

This parametrisation approach can be further extended to introduce squealer rim openings (or cuts) by simply removing part of the squealer rim and filling the gap by extending the tip gap O-mesh block into the cut. However, the squealer opening has to correspond to the tip gap O-mesh above the squealer rim. This can cause potential issues regarding the boundary layer mesh in the squealer opening since it has to follow the mesh resolution of the butterfly H-mesh block in the chordwise direction, meaning the two opposite ends of the squealer cut cannot have the boundary layer mesh. Also, with this approach, using the O-mesh as a basis, squealer rims can only be placed at or near the tip edge.

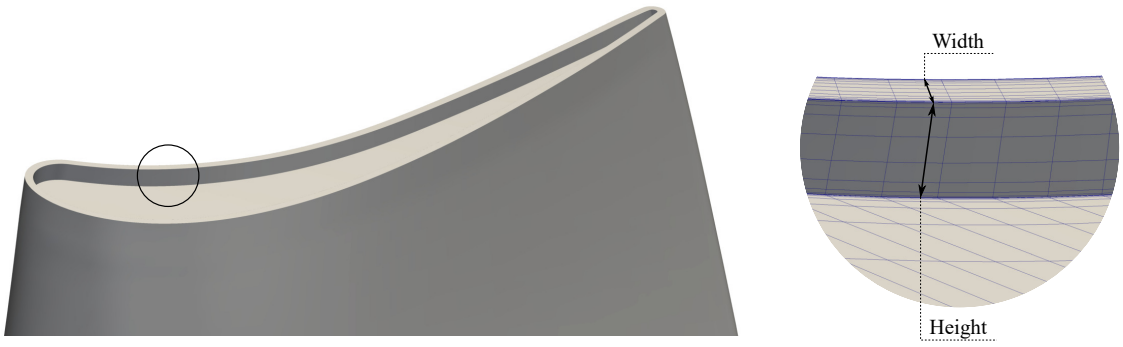

Figure 2.7: Simple squealer parametrisation

Since squealers operate by causing two or even more contractions of the flow over the squealer rims, which in turn leads to complex flow patterns in the squealer cavity, a different parametrisation approach is required to explore them in more depth. In this work, a squealer parametrisation was used that allowed for different squealer topologies, or in other words, different numbers of squealer rims placed at different parts of the tip. This was achieved using Mimic [78], a software for geometry parametrisation and creation from OPTIMAD Engineering Srl.

The inspiration for Mimic's parametrisation approach was taken from the work of Andreoli et al. [50] and Maesschalck et al. [51]. It starts with the idea that the tip surface can be represented by a non-dimensional square, as depicted in Figure 2.8. Using this approach, the tip surface outline can be divided into four parts (LE, TE, PS, and SS), each corresponding to one side of a square (Figure 2.8a). This square can then be populated with control points that serve as parameters. In this work,

different grids of control points were used, but the parametrisation is presented for a case of a 4x4 grid, as shown in Figure 2.8b.

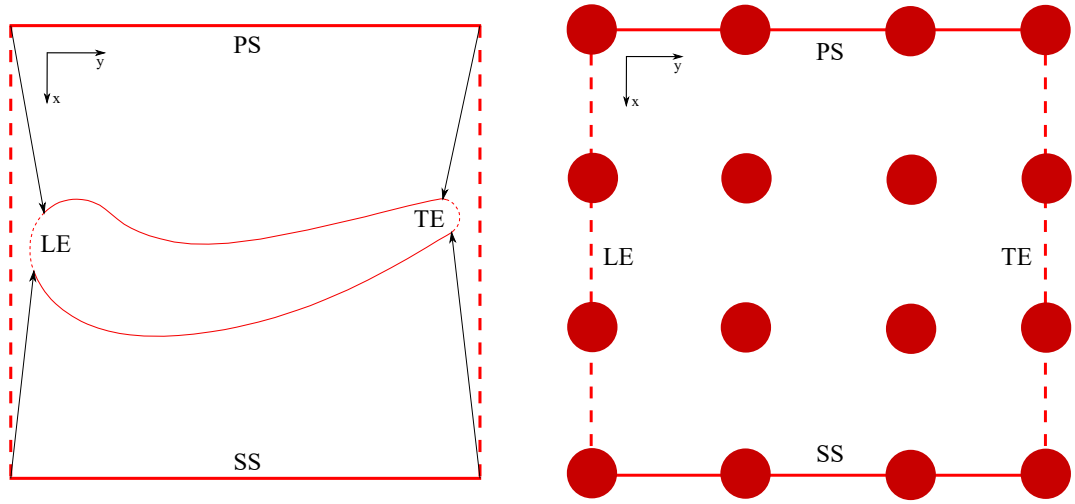

(a) (b)

Figure 2.8: Topology squealer tip parametrisation

Starting from a non-dimensional square and 4x4 grid presented in Figure 2.8b, the z-axis is added to create a non-dimensional cube with a unit height. The locations of the control points are fixed in the x and y directions, and they are only allowed to move in the z-direction.

Since there are 16 points and each is only allowed to move in the z-direction, this means that this parametrisation is done using 16 design parameters. For each of the control points, a z-value is determined, representing the height. The z-value can be either positive or negative, between 0 and 0.5. With the height determined, the points are moved into place, and a radial basis function (RBF) surface is created by interpolating through them (Figure 2.9a).

Next, at zero height (z=0), the RBF surface is cut with an x-y plane, as noted in Figure 2.9a. The resulting iso-cut (Figure 2.9b), on the x-y plane at z=0, produces a set of lines that are used to describe the squealer rims, as shown in Figure 2.9b. The colormap shows the z value of RBF surface.

Using the idea presented in Figure 2.8 that a non-dimensional square can be mapped onto a tip surface, the resulting iso-cut is mapped onto the provided tip outline. This way, a series of lines that are the product of cutting the RBF surface are used to describe the squealer lines, as shown in Figure 2.9c.

The latest step in the process is to convert this information into a 3D blade, which is accomplished by using an stl (stereolithography) CAD file format to describe the

surface through a number of points forming triangles. Specifically, stl points from the original recessed tip, which serve as the basis for morphing, are selected based on their proximity to the mapped squealer lines. These points are then extruded for a certain value, and the original triangles connecting them are morphed. This process results in the final watertight stl geometry. The chosen vicinity of points that will be extruded effectively controls the thickness of the squealer rim. If the rim is too close to the tip edge, it might become thinner due to insufficient area of the original tip available for extrusion. The extrusion value controls the rim height, and its direction is defined as the radial direction, resulting in squealer rims that are perpendicular to the original tip.

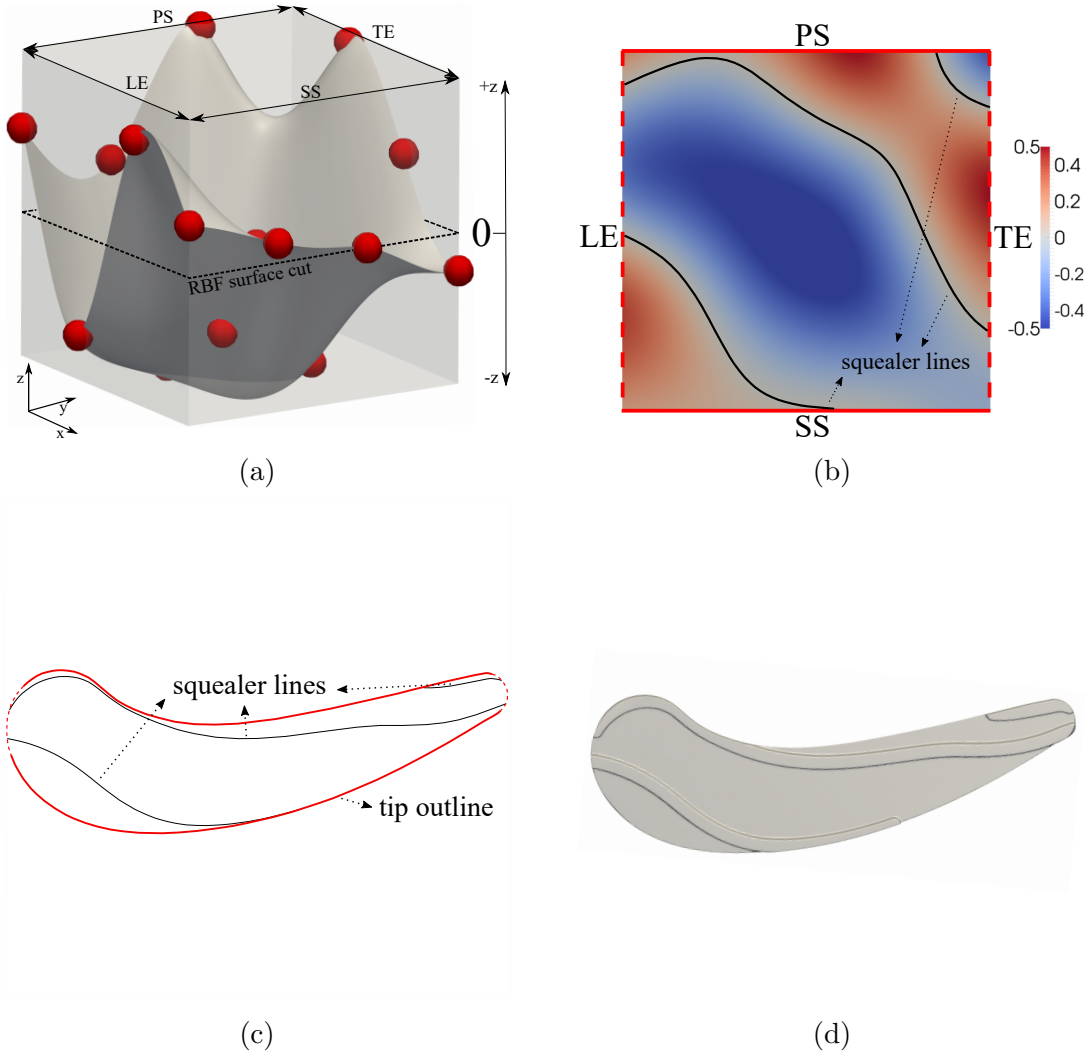

Figure 2.9: Squealer tip parametrisation

Final squealer tip is presented in Figure 2.10.

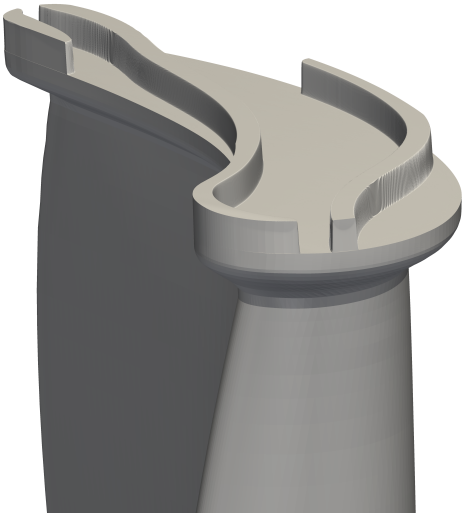

Figure 2.10: Final squealer tip

2.3.2 Blade skew parametrisation

To account for changes in the turbine inlet capacity and stage reaction, a blade skew parametrisation was included to control the velocity triangles. This was achieved by rotating the blade around its center, for rotor skew angle ψ_r. Blade skew was controlled at a single radial height, at midspan, without altering the datum radial shape. Figure 2.11 illustrates this parametrisation for the rotor blade. Starting from the datum blade shape presented at midspan, either a positive or negative skew was applied by rotating the blade around its center (blue dot). Negative skew assumed a clockwise direction, while positive skew assumed an anticlockwise direction.

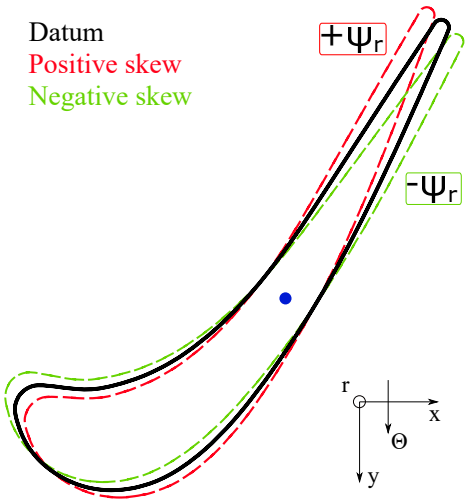

Figure 2.11: Rotor blade skew parametrisation

2.3.3 Gradient based methods

This section describes the gradient-based optimisation methods used in this work. First, the Multipoint Approximation Method (MAM), Rolls-Royce's in-house gradient-based optimiser, is explained. After that, surrogate models used for data regression are presented.

2.3.3.1 Multipoint Approximation Method

The Multipoint Approximation Method, or simply MAM, is an optimiser developed by Toporov et al. [79] that solves the optimisation problem through a series of optimisation sub-problems (iterations).

Starting from the initial point, MAM works by creating a design of experiments (DOE) for which it calculates an approximation function. Each approximation function is defined as a function of design variables as well as tuning parameters. Tuning parameters are determined by fitting the least square surface using the original function values (CFD runs) at design points.

A general optimisation problem is written as

$$\begin{aligned} min \quad & F_0(\boldsymbol{x}), F_j(\boldsymbol{x}) \leq 1 \ (j = 1, ..., M), \\ & A_i \leq x_i \leq B_i \ (i = 1, ..., N), \end{aligned} \tag{2.42}$$

where $\boldsymbol{x}$ refers to the vector of design variables. According to Polynkin and Toporov [80], MAM replaces the optimisation problem by a sequence of approximate optimisation problems as

$$\begin{aligned} min \quad & \tilde{F}_0^k(\boldsymbol{x}), \tilde{F}_j^k(\boldsymbol{x}) \leq 1 \ (j = 1, ..., M), \\ {A_i}^k \leq x_i \leq {B_i}^k, {A_i}^k \geq A_i, {B_i}^k \leq B_i \ & (i = 1, ..., N). \end{aligned} \tag{2.43}$$

where k is the iteration number.

The approximations $\tilde{F}_0^k(\boldsymbol{x})$ $(j = 0, ..., M)$ are determined using the method of weighted least squares as

$$min \quad \sum_{p=1}^{P} w_{pj} \left[F_j(\boldsymbol{x}_p) - \tilde{F}_j^k(\boldsymbol{x}_p, \boldsymbol{a}_j) \right]^2. \tag{2.44}$$

Minimisation is done with respect to the tuning parameters vector $\boldsymbol{a}_j$, w_{pj} are the weight coefficients and P is the number of points in DOE. The number of points P must not be lower then the number of design parameters in the vector $\boldsymbol{x}_p$.

In this work, to regress the design space, MAM's metamodel assembly developed by Polynkin and Toporov [80] was used. It relies on assembly of different approximation sub-models, which it combines through linear regression. Each of the approximation sub-models is created as explained in Equation 2.44, creating an approximation function.

Once the function is approximated and its optimum point is identified, this process is repeated by constructing a new DOE around the previous sub-point and performing another function approximation. The size of every subsequent sub-region is determined by the MAM based on the set of parameters that estimate the quality of the approximations and the location of the sub-optimum point in the current trust region. This way, the pace of narrowing down the sub-region affects the optimisation convergence speed. DOE used in every sub-region has the same number of points.

The convergence process of going through different sub-regions is simply illustrated for a two-objectives (x_1 and x_2) example in Figure 2.12. More information about MAM can be found in [81, 82].

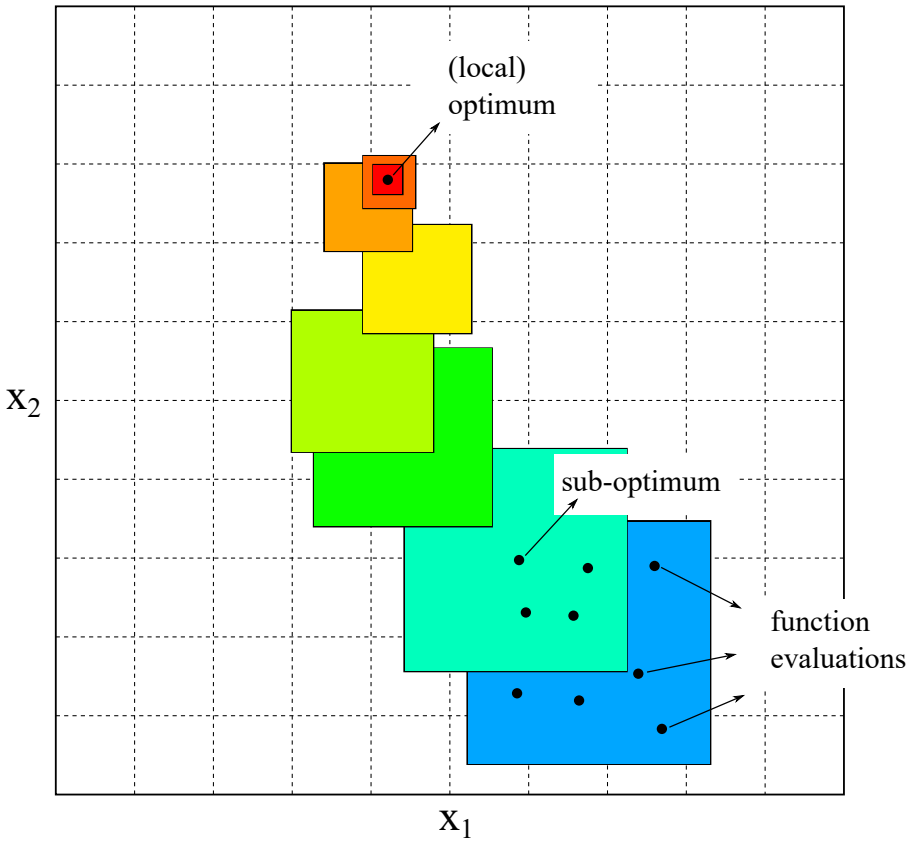

Figure 2.12: MAM

2.3.4 Response surface models

Response surface models, also known as surrogate or meta-models, are optimisation models that include the approximation of the objective function through a set of points. The idea of a response surface model is to save on optimisation computational costs by describing the objective function with sufficient accuracy through a "curve fit" [83].

Response surface models can be divided into one-stage and two-stage models. In a one-stage response surface model, a response surface is fitted to a dataset, and any required parameters are estimated from the response surface. In a two-stage model, these estimated parameters are treated as "true", and response surface prediction is used to compute the new points. This way, the initial sample can mislead the new search by potentially underestimating the error in the response surface. As a result, the response surface model can either stop too early or search too locally [84].

The creation and use of the response surface model are briefly explained in Figure 2.13. The first step in the creation of a response surface model is obtaining a sample or design of experiments (DOE). For that, a sampling method is needed. In

this work, sampling was done using Latin hypercube. Latin hypercube, first introduced by McKay et al. [85], is a sampling method that efficiently represents a design space by trying to represent every part of it while maximising the distance between the points to minimise the sample size. After obtaining the sample, a response surface model can be constructed. The response surface approximates the design space through provided sample points, effectively smoothing the objective function.

With the response surface model constructed, optimisation is performed either by using the gradient information or by approximating the objective directly from the response surface. With the objective function obtained, its value is compared to the response surface model prediction. If the two values correspond, or have an accepted deviation, optimisation is considered converged and finished. If the values from the objective evaluation do not match with the response surface prediction, the model needs to be improved by increasing its accuracy. Increasing the number of the response surface points and the process of providing the new data to improve the model prediction is known as infill. This is illustrated in Figure 2.13.

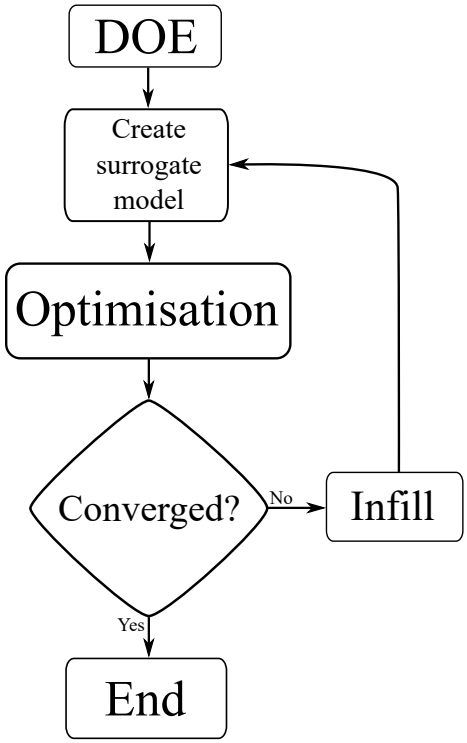

Figure 2.13: Response surface model optimisation

When creating a response surface, it is important to judge its accuracy before performing optimisation. In other words, the response surface needs to be validated. This

process is called cross-validation, which can be done through simple cross-validation or k-fold cross-validation [83].

For simple cross-validation, a dataset is divided into two parts. The first part is used to construct a response surface, while the second part, also known as the test dataset, is used for validation. This way, the response surface is created using a first, larger dataset, and its predictions for points in the test dataset are calculated. These predictions are compared with the actual values from the test dataset, and the accuracy of the response surface is obtained. The advantage of this approach is quick validation of the response surface, but the drawback is the non-use of all available points for constructing the response surface. Also, a misrepresentation of the whole design space when dividing the data is possible. This misrepresentation can be avoided by constructing two DOEs, one for creating a response surface and the other for validation.

K-fold cross validation of the response surface is done by dividing an initial dataset into a number of folds, m. Using the data from $m-1$ fold, a response surface is created and its prediction is compared with the values from the remaining fold. The measure of accuracy is recorded and the process is repeated, but this time changing the fold. This process is repeated m number of times until all the folds are used and the accuracy is expressed as the average of all sub-validations. The advantage of this approach is the use of all the data for the response surface creation and likewise, the validation against the all available data. The drawback of this method is the time needed to create the response surface m number of times which can be computationally expensive.

In this work, two different response surface approaches were used for the optimisation, Kriging response surface and the Artificial Neural Network (ANN) response surface. They are presented more in detail in next sections.

2.3.5 Kriging

Kriging, also called Gaussian process regression, is a response surface model that builds approximations for highly non-linear problems. Kriging works by describing how the function behaves by tuning the parameters of a statistical model. The Kriging statistical model that approximates function f can be written as

$$F(x) = \mu(x) + Z(x) \tag{2.45}$$

where $F(x)$ is a random variable resulting from the evaluation of x and has a normal distribution with mean μ and variance σ^2. $\mu(x)$ is an approximation function meant to capture some of the behaviour of f, and $Z(x)$ is a random variable. The Kriging model in which μ is considered constant or independent of x is called ordinary Kriging.

According to Martins and Ning [83], the power of Kriging lies in treating the correlation between the random variables. Although the random variable $Z(x)$ is unknown, some assumptions can be made about it. Consider two parameters in a sample, $x^{(i)}$ and $x^{(j)}$, and their corresponding random variables $Z(x^{(i)})$ and $Z(x^{(j)})$. Assuming a constant function, it is expected that $Z(x^{(i)})$ and $Z(x^{(j)})$ will be closer if $x^{(i)}$ and $x^{(j)}$ are closer. In other words, we expect correlation between the distance of $x^{(i)}$ and $x^{(j)}$ and the distance of $Z(x^{(i)})$ and $Z(x^{(j)})$. In Kriging, that correlation is expressed as

$$corr\Big(Z(x^{(i)}), Z(x^{(j)})\Big) = exp\bigg(-\sum_{l=1}^{n_d} \Theta_l \Big| x_l^{(i)} - x_l^{(j)} \Big|^{p_l} \bigg) \tag{2.46}$$

where n_d is a number of dimensions and Θ_l and p_l are the model parameters where $\Theta_l \geq 0$ and $0 \leq p_l \leq 2$.

The advantage of Kriging is its flexibility due to the wide range of correlation factors used when building the approximations. Because of this, Kriging response surface models are useful for modelling linear functions [83].

2.3.6 Artificial neural network

The Artificial Neural Network (ANN) response surface model used in this work was developed by Lopez et al. [86]. It relies on the use of artificial neural networks, in which information from a set of inputs is connected to the set of outputs through a structure of neurons whose behaviour can be trained to improve predictions. Artificial neural networks are characterised by their higher flexibility and better prediction compared to other response surface models due to their ability to interpolate unstructured data. However, because artificial neural networks are unstructured, ANN response surfaces usually require more data points for fitting to a high-dimensional system compared to other methods. In the approach by Lopez et al., this issue was resolved through the use of a dimension reduction (DR) algorithm, specifically Active Design Subspaces (ADS). Rather than determining a subset of the most important design parameters, active design subspaces work by identifying the most dominant

linear combinations between design parameters that provide the best description of the output variability.

Starting from an initial dataset, an ANN is constructed. Next, the network hyper-parameters, such as the number of hidden layers, the number of neurons in each hidden layer, the regularisation coefficient, and the dropout factor, are tuned using a grid search that evaluates several parameter combinations. During the parameter tuning grid search, the objective is to maximise the correlation coefficient R^2, which expresses the prediction from the network and the actual dataset.

After the network is fitted and tuned, active design subspaces are coupled. ADS identifies the linear combination of input parameters that describes the variability in an objective function the best. This is done through the eigenvalue decomposition of the function's gradient covariance matrix, C_{cov} as

$$C = \mathbb{E}[\nabla_x f \nabla_x f^T]. \tag{2.47}$$

In the iterative process, active design subspaces are employed to reduce the number of samples needed to fit a neural network to high-dimensional data, and the neural network is employed to learn the resulting ADS. As proposed by Lopez et al. [86], in this work, fitting the ADS included iterating on the number of samples employed to fit the ANN while monitoring the convergence of the first k eigenvectors of C_{cov}.

With the eigenvectors of the covariance matrix converged, ADS is identified, and the function is approximated using the most dominant directions. This information is then used to reduce the dimensionality of the original input data. As a result, identifying and exploiting the dominant directions in ADS usually accelerates the convergence of the optimisation since the ANN is fitted to the dataset of lower dimensionality.

Overall process of creating ANN response surface in a combination with ADS is shown in Figure 2.14.

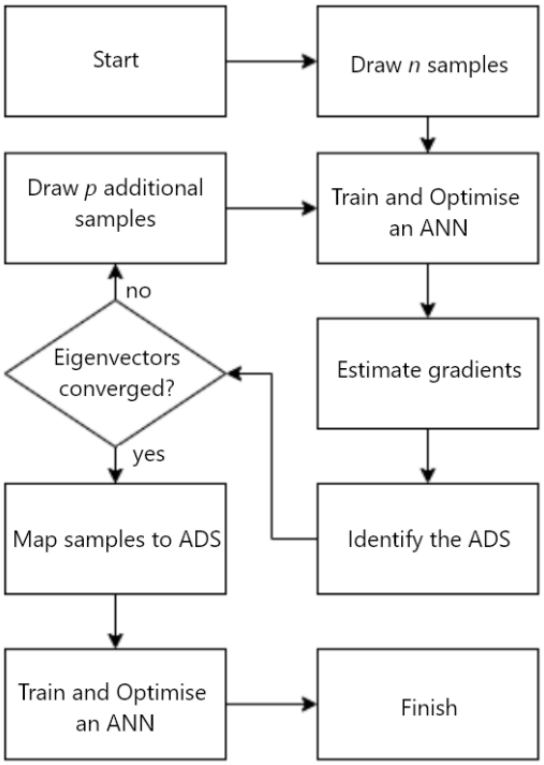

Figure 2.14: Iterative process of learning ADS and using it to fit the ANN to CFD samples [86]

2.3.7 Global search algorithms

Global search optimisation algorithms are optimisers that require zero-order information. This assumes that for a given design, only gradient-free information about the objective, and possibly the constraints, is fed into the optimiser, and derivative information is not used. This means that global search optimisation algorithms can work with discontinuous functions and, because of that, they are robust, tolerant to simulation failures, and can identify the global optimum. However, all of this leads to slower convergence.

There are many different global search algorithms and their divisions, which will not be explained here but can be found in [83] and [87]. More relevant to this work, global search algorithms can be divided by their use into direct algorithms and response surface (surrogate) based algorithms. In the latter, initial computations of the objective function are carried out to regress the design space, and after that, a global search is performed.

In this work, a particular type of genetic algorithm was used, both directly and

through the use of the response surface. It is described in more detail in the next section.

2.3.7.1 Genetic algorithm

A genetic algorithm is a stochastic global search method based on Darwin's theory of natural selection. Its basic approach starts with a selection of randomly generated designs called a generation. Each generation has a population with n_p points, or in this case, design parameters. Each member of the population is represented by a chromosome, and each design parameter is represented by a gene.

Genetic algorithms optimise the objective function by evolving populations inspired by biological reproduction. This includes three main steps: selection, crossover, and mutation. Selection assigns each population a fitness value based on the objective cost function (and a penalty function for constrained problems). Based on its fitness value, it is determined whether the population is more likely to survive and contribute to the gene pool. Crossover is inspired by chromosomal crossover, in which the genetic material of the fittest member is passed onto the new generation through reproduction. Finally, the mutation step mimics a genetic mutation in which random mutations are introduced to change the gene sequence.

The genetic algorithm used in this work is ARMOGA, or the Adaptive Range Multiobjective Genetic Algorithm, which is described in the next section.

ARMOGA

Adaptive range multiobjective genetic algorithm, or ARMOGA, is a type of genetic algorithm that was developed by extending the idea of adaptive range genetic algorithms (ARGAs) by Arakawa and Hagiwara [88]. The adaptive range genetic algorithm was created to search through a large design space more efficiently by applying range adaptation [89]. Range adaptation is performed in every n-th generation by calculating the mean and standard deviation for each design parameter. After that, a normal distribution around the most promising values of design parameters is applied. This is briefly illustrated in Figure 2.15, where x_i represents the design parameter.

The range adaptation approach was further extended by Sasaki et al. [90] to perform multi-objective optimisations. The basic idea of applying the normal distribution in the most promising regions was kept, but altered to include the parameter variations for different objectives. That was done by dividing the most promising region of design parameters into two parts and introducing a new zone in between,

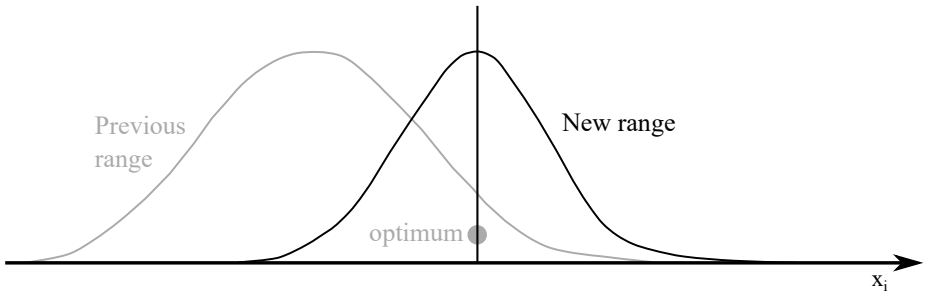

Figure 2.15: Design parameters range adaptation

effectively increasing the search area. According to the authors, the range adaptation approach was found to work more efficiently for multiple objectives too. ARMOGA was later used as the optimiser for different multi-objective applications and was found to generally perform better than other multi-objective genetic algorithms like non-sorting genetic algorithm (NSGA) [91, 92].

2.4 3-temperature model

Another important part of the computational methodology used in this work is the 3-temperature model. This model was used to express the blade heat load, which was one of the objectives in the aerothermal tip optimisations.

To explain how it works a Newton's law of cooling is given as

$$q = HTC(T_w - T_{aw}). \tag{2.48}$$

Here, q represents the wall heat flux, HTC represents the heat transfer coefficient, T_w is the wall temperature, and T_{aw} is the adiabatic wall temperature, also known as the fluid driving temperature. This law is commonly used to model the convective heat transfer in turbines and implies that the heat transfer coefficient is constant, does not depend on the wall temperature, and is determined only by the aerodynamics. This is shown in Figure 2.16a, where the wall heat flux depends only on the temperature difference, and the heat transfer coefficient, shown as the gradient of the wall heat flux, is constant. This results in a linear behaviour of the wall heat flux against the wall temperature.

The 3-temperature model, developed by Maffulli and He [25], relies on the finding that blade passage flows are affected by the blade wall temperature condition, which in turn affects the wall heat transfer. In other words, the heat transfer coefficient

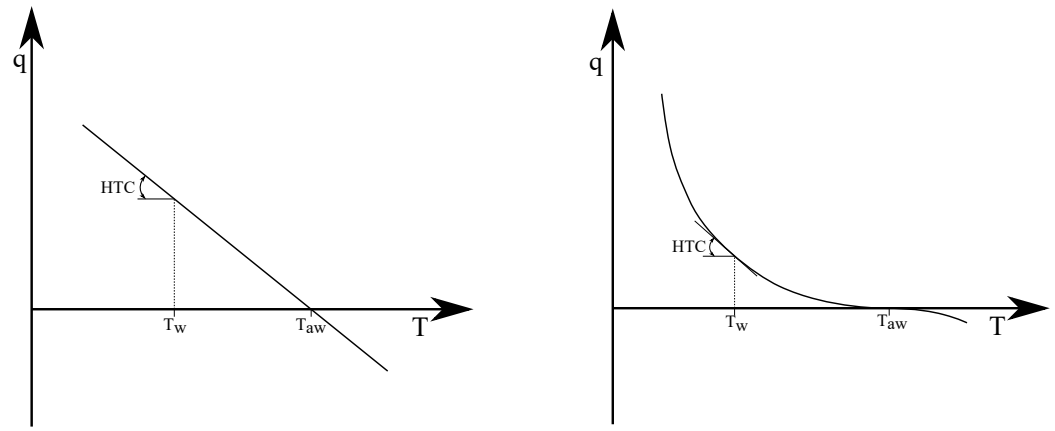

(a) (b)

Figure 2.16: Linear and non-linear heat transfer

is a function of the wall temperature, and therefore the linearity of Newton's law of cooling is not valid.

Since the heat transfer coefficient varies with temperature, it is not constant, and the heat flux against the wall temperature is non-linear, as shown in Figure 2.16b. Maffulli and He conducted extensive 2D and 3D studies [93, 94] on the effect of wall temperature on turbine flows and showed that the wall temperature condition can affect secondary flows, move shock position, and change the turbine inlet capacity.

Since real-life turbines operate with very complicated, unstable, and non-uniform blade surface temperatures, and since Maffulli and He [25] showed that an imposed blade wall temperature changes the turbine passage flow, it is clear that calculating the heat load using a single arbitrary uniform temperature condition introduces an error. This is particularly important when dealing with cold experiments, such as the MT1 turbine, where the heat load is conventionally obtained either by surface integrating the heat flux resulting from an imposed uniform blade wall temperature or by calculating the heat transfer coefficient at a near-adiabatic condition. Using this information for a real engine case can have a significant impact on the real flow behavior, as explained in Section 1.3.3 and Figure 1.14. In other words, the flow field and heat load obtained for a cold experiment can misrepresent the real engine case if the temperature scaling that both Maffulli and He [25] and Zhang and He [26] showed is not accounted for.

Therefore, in this work, the 3-temperature model suggested by Maffulli and He [25] was used. The heat transfer coefficient was calculated using the non-linear heat transfer equation given as

$$q = (h_0 + h_1 T_w)(T_w - T_{aw}) \tag{2.49}$$

where h_0 is a heat transfer coefficient constant and h_1 is a local heat transfer coefficient correction that depends on the wall temperature T_w. Equation 2.49, is a non-linear equation and three separate CFD simulations were required to find the unknowns h_0, h_1 and T_{aw}. Heat transfer coefficient is given as

$$HTC = h_0 + h_1 T_w \tag{2.50}$$

and it varies with a specific wall temperature T_w. In this work, the heat transfer coefficient was used as a measure of heat load and was calculated for a rotor blade wall temperature corresponding to the modern high-pressure turbine rotor blade temperature, as explained in Section 3.1.2.1.

Chapter 3

Computational model

In this chapter, a computational model is presented, which includes an explanation of the research case, its properties, and how they were evaluated. After that, the CFD model is presented and verified. Verification includes the mesh verification study, different approaches to modelling turbulence, and heat load modelling. After model verification, a validation of numerical tools and their application on the research geometry is given.

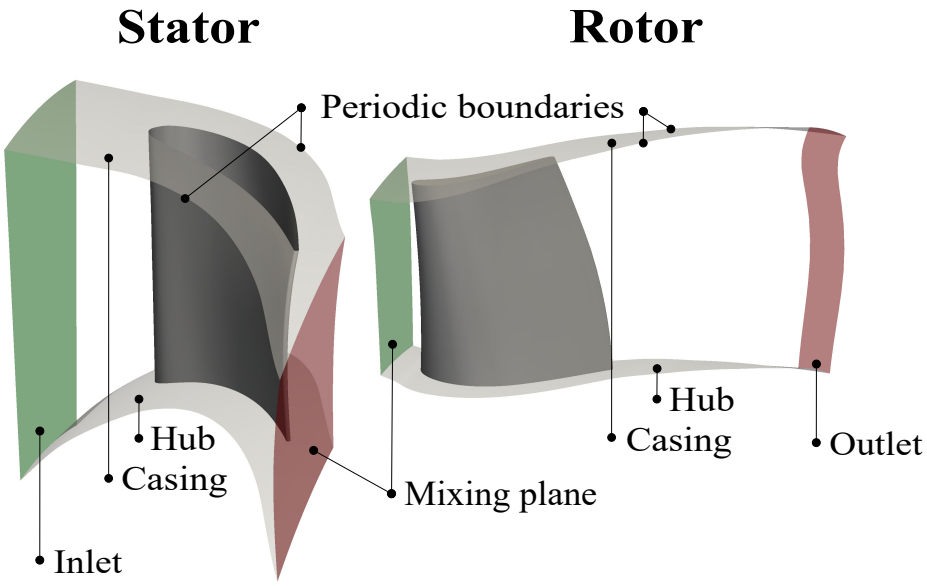

Figure 3.1: MT1 high pressure turbine geometry

This work has been carried out on the MT1 turbine presented in Figure 3.1. The MT1 turbine is a full annulus high pressure research turbine consisting of 60 stator and 32 rotor blades, using air as the working fluid. It has been tested in the Turbine Test Facility at QinetiQ (Farnborough, United Kingdom) and has a considerable amount of experimental data available [67]. Its operating point conditions, used in the

Parameter	Value
Stator Reynolds number based on NGV axial chord	1.61×10^6
Rotor Reynolds number based on rotor blade axial chord	5.24×10^5
Mach number at NGV exit	0.879
Inlet total temperature	444 K
Inlet total pressure	4.6 bar
Outlet static pressure	1.46 bar
Rotational speed	9500 rpm
Tip gap	1.5% span

Table 3.1: MT1 turbine operating conditions [67]

experiments, are presented in Table 3.1. It is a transonic, non-shrouded representation of the industry standard high pressure turbine with no real geometry features like cooling slots and fillets. Despite not having some real geometry features, it features no separation except for the usual vortical flow presented in Chapter 1. The boundary layer is attached in both stator and rotor domains. Throughout this thesis, the rotor tip gap was 1.5% of the rotor blade span.

The CFD model developed in this work included modelling of the turbine inlet as the pressure inlet boundary, specifying the uniform total temperature and total pressure as given in Table 3.1. The outlet of the turbine was specified as the pressure outlet with a radial distribution of static pressure, where the mean value corresponded to the value in Table 3.1. The interface between the two domains was modelled as a mixing plane in the steady and as a sliding plane in the unsteady simulations. Walls were set up as adiabatic or having a constant uniform temperature with a no-slip condition. The rotor domain had a rotation of 9500 rpm, apart from the rotor casing, which was kept fixed as in the experiment.

3.1 Model evaluation

In this section, the calculation of turbine properties is explained. These were used as the objectives and constraints in the optimisations.

3.1.1 Aerodynamic efficiency

The turbine efficiency was calculated as the stage isentropic efficiency presented in Section 1.1.2.1. Surface average values of the total enthalpy change were used as given in Equation 3.1. The accounting stations are shown in Figure 3.2.

$$\eta = \frac{h_{0,1} - h_{0,3}}{h_{0,1} - h_{0_{is},3}} \tag{3.1}$$

The isentropic state at the rotor outlet (3) was calculated from the expression for the isentropic expansion of an ideal gas.

Since $h = c_p \Delta T$, and since c_p is a constant, Equation 3.1 can then be rewritten as

$$\eta = \frac{T_{0,1} - T_{0,3}}{T_{0,1}[1 - \frac{p_{0,1}}{p_{0,3}}^{(\gamma-1)/\gamma}]} \tag{3.2}$$

where γ is the heat capacity ratio, which is 1.398 for air. The total temperatures in the above equations were taken as surface averages.

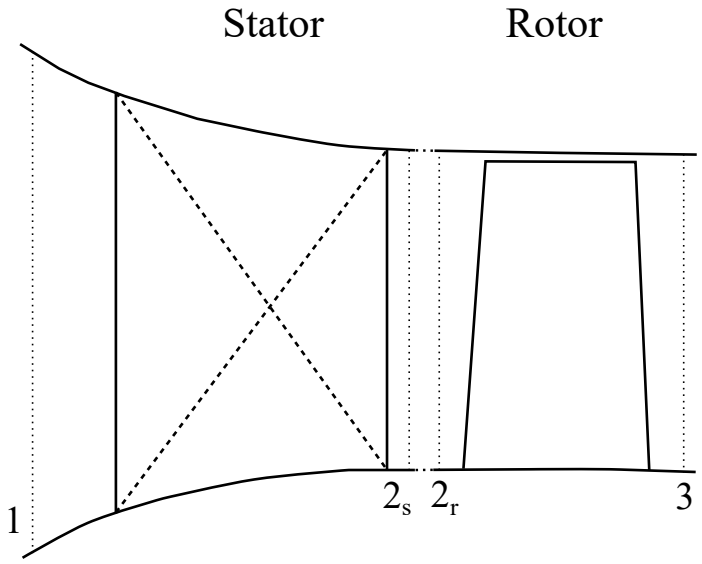

Figure 3.2: Meridional view of turbine stage

3.1.2 Heat load

In this work, the heat load was modeled using a 3-temperature method from Maffulli and He [25]. The model's methodology was previously introduced in Section 2.4, and here, its application on the tip optimisations is explained.

3.1.2.1 Temperature operating range of high pressure turbine rotor blades

Rotor blades in high pressure turbines operate in thermally very stressful environment. Flow arriving into the high pressure turbine comes from the combustor and is of the highest energy state during the whole expansion process. As presented in Figure 1.3, turbine blades have been continuously developed to endure in such a harsh environment and during the process of designing a turbine blade special attention has to be given to predicting the blade thermal load. This is particularly important as missing the rotor blade material temperature for only 10 K can half the blade's lifetime [95].

To define the blade operating temperature, temperature ratio (TR) is used. Temperature ratio is simply defined as the ratio of blade surface temperature $T_{rotor\ blade\ wall}$ over the total temperature at the turbine stage inlet $T_{0_{turbine\ inlet}}$. This way, rotor blade wall temperature is normalised against constant value of total temperature at the turbine stage inlet. It is given as

$$TR = \frac{T_{rotor\ blade\ wall}}{T_{0_{turbine\ inlet}}}. \tag{3.3}$$

Modern high pressure turbines in jet engines operate with temperature ratios of around 0.6. This means that the surface of the rotor blade has a far lower temperature value than the temperature of the surrounding fluid. This is made possible by the smart use of blade cooling and thermal barrier coating. Since these methods were not modelled in this work, the heat load was accounted for by modelling the temperature ratio of 0.6, corresponding to the rotor blade wall temperature of 266 K.

3.1.2.2 Heat load calculation

Starting from the non-linear heat transfer shown in Figure 2.16b, a 3-temperature model was built by calculating the flow field for three different blade surface temperature conditions. The process of determining these three temperatures is shown in Figure 3.3. In this figure, the x-axis is normalised and expressed in terms of the temperature ratio, TR.

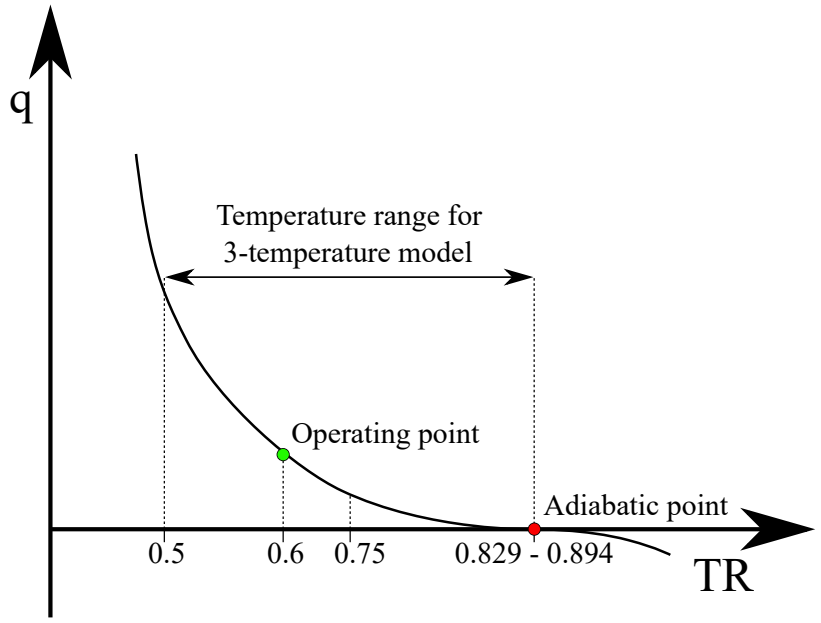

Figure 3.3: Temperature range of 3-temperature model

As explained in Section 2.4, a 3-temperature model was used to assess the rotor blade heat load by computing the locally corrected heat transfer coefficient for a specific rotor blade wall temperature. Since modern high pressure turbines operate with a temperature ratio of 0.6, the rotor blade wall temperature for which the heat transfer coefficient was computed was determined to be 266 K, as presented in Figure 3.3 as a green dot. To locally correct the heat transfer coefficient, it was necessary to build a 3-temperature model around this temperature.

Referring back to Equation 2.50, one of the three unknowns to resolve the non-linear heat transfer is the adiabatic wall temperature, T_{aw}. Since the adiabatic rotor blade wall temperature is non-uniform and varies between 368 and 397 K for the case of the MT1 turbine, the corresponding temperature ratio ranges from 0.829 to 0.894. The adiabatic wall temperature, which is the temperature for which there is no heat flux between the blade wall and adjacent fluid due to the absence of a temperature gradient, was obtained from the adiabatic CFD simulation of the whole turbine stage and was used as the upper limit for the 3-temperature model.

As the adiabatic wall temperature is necessary to resolve the 3-temperature model, not including it into the 3-temperature model would later require the interpolation. This could easily lead to errors. Therefore, adiabatic wall temperature was used as one of the three temperatures needed and was taken as the upper limit. It was obtained from the adiabatic CFD simulation of the whole turbine stage. For the lower limit, wall temperature below the operating point was needed. To ensure a good fit of the

non-linear function, rotor blade wall temperature corresponding to the temperature ratio of 0.5 was taken. And finally, the last temperature used for 3-temperature model was decided to be somewhere in between of the lower and upper limits. Rotor blade wall temperature corresponding to temperature ratio of 0.75 was used.

For these three rotor blade wall temperatures, CFD simulations were run and three unknowns(h_0, h_1 and T_{aw}) were obtained. Then, the heat transfer coefficient was calculated for the rotor blade wall temperature of 266 K using Equation 2.50 as explained in Section 2.4.

3.1.3 Turbine inlet capacity

Turbine inlet capacity was calculated using Equation 3.4, with the stage mass flow measured at the stator inlet and imposed values of total temperature and total pressure.

$$\Phi = \frac{\dot{m}_{0_{stage}} \sqrt{T_{0_{stator\ inlet}}}}{p_{0_{stator\ inlet}}} \tag{3.4}$$

3.1.4 Turbine stage reaction

The turbine stage reaction was calculated using the surface average values of static enthalpy, as given in Equation 3.5.

$$\Lambda = \frac{h_{rotor\ inlet} - h_{rotor\ outlet}}{h_{stator\ inlet} - h_{rotor\ outlet}} \tag{3.5}$$

3.2 Mesh verification study

To understand the effect of mesh resolution on the tip leakage flow, mesh verification studies were conducted for both the structured PADRAM and unstructured BOXER meshes. These studies were conducted in two stages: aerodynamic and heat transfer verification.

The aerodynamic mesh verification study was conducted first for the datum tip case, and the results are presented in the next two sections. Once the aerodynamic meshes were verified, they were used as the initial points for the heat transfer mesh verification studies.

Since the optimisations performed later included the modelling of the heat load on different tip shapes, separate heat transfer mesh verification studies were conducted

for each of them. These are presented in the corresponding optimisation sections, along with the rest of the optimisation setups.

3.2.1 Aerodynamic mesh verification study

3.2.1.1 Structured mesh

Structured meshes were created using PADRAM, following the O-H mesh topology presented in Section 2.2.1, for both stator and rotor blades, and using the butterfly mesh topology for the rotor tip gap. The verification study was done by varying the overall mesh size, where all mesh blocks were gradually refined in all directions, increasing the overall mesh size. Special attention was given to the values of the first cell height and resulting y+. All meshes that had more than 1 million cells for the whole turbine stage had maximum y+ values in the order of unity, ensuring good boundary layer resolution and therefore a fair comparison.

The results of the aerodynamic structured mesh verification study are presented in Figures 3.4 and 3.5. The aerodynamic turbine properties measured in the verification study were the adiabatic efficiency, leakage mass flow normalised against the single rotor passage mass flow, turbine inlet capacity, and stage reaction.

The PADRAM mesh verification study for the adiabatic efficiency and normalised leakage mass flow is presented in Figure 3.4, where the mesh size accounts for both stator and rotor meshes. As shown, after a few coarse meshes with a mesh size below 2 million cells, both efficiency and leakage mass flow became mesh size independent. Little change was visible for both properties for meshes with more than 2 million cells.

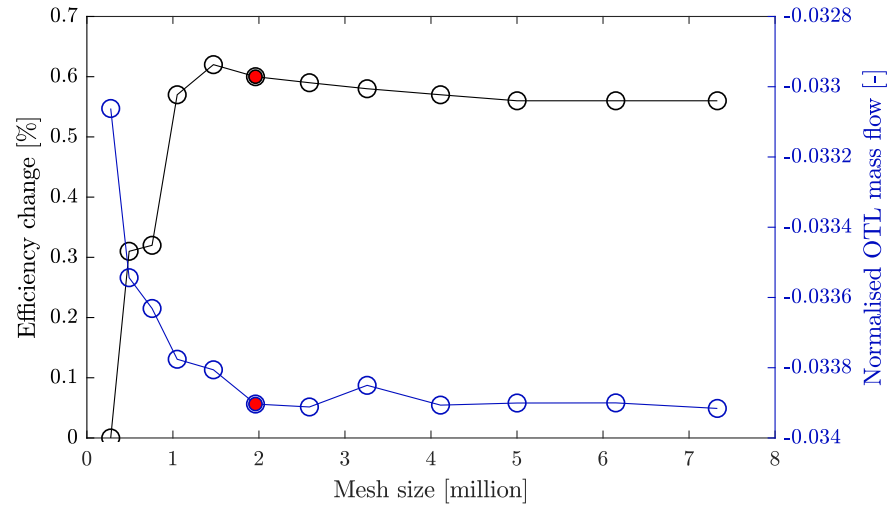

Figure 3.4: Structured PADRAM mesh verification study - efficiency and OTL mass flow

Results of the verification study for turbine inlet capacity and stage reaction are presented in Figure 3.5. It can be observed that the inlet capacity and stage reaction began to converge even before the efficiency and tip leakage mass flow. After 1 million cells in the turbine stage, little variation in these properties was observed.

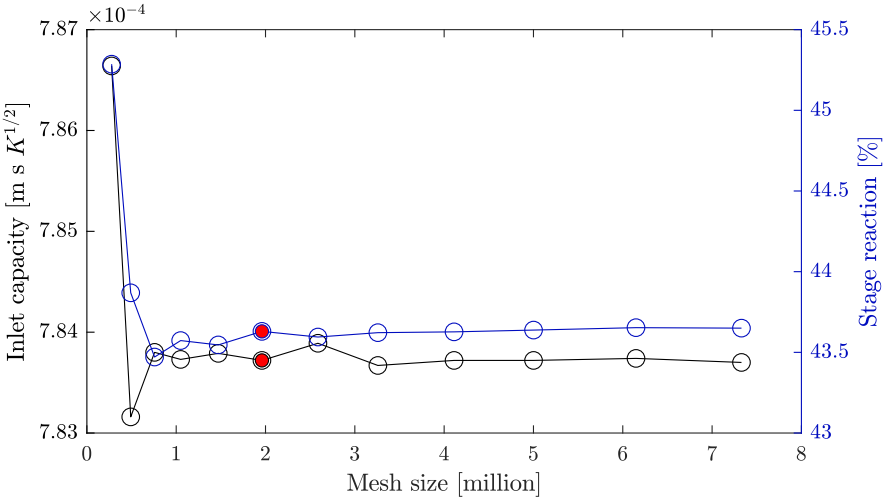

Figure 3.5: Structured PADRAM mesh verification study - inlet capacity and stage reaction

As shown in Figures 3.4 and 3.5, only negligible variations in stage efficiency, tip leakage mass flow, and the turbine inlet capacity and stage reaction were observed after the stage mesh count reached almost 2 million cells. Therefore, the stage mesh

corresponding to almost 2 million cells was taken as mesh size independent and used in further studies (noted as a red dot in Figures 3.4 and 3.5). For this mesh, the stator mesh count was around 0.7 million, and the rotor mesh count was around 1.3 million. Details of this mesh are presented in Section 3.2.1.2.

3.2.1.2 Details of the verified structured mesh

The mesh size independent structured PADRAM mesh (red dot in Figures 3.4 and 3.5) is shown in Figure 3.6. Figure 3.6a shows the joint of the stator blade and hub, and Figure 3.6b shows the rotor blade tip.

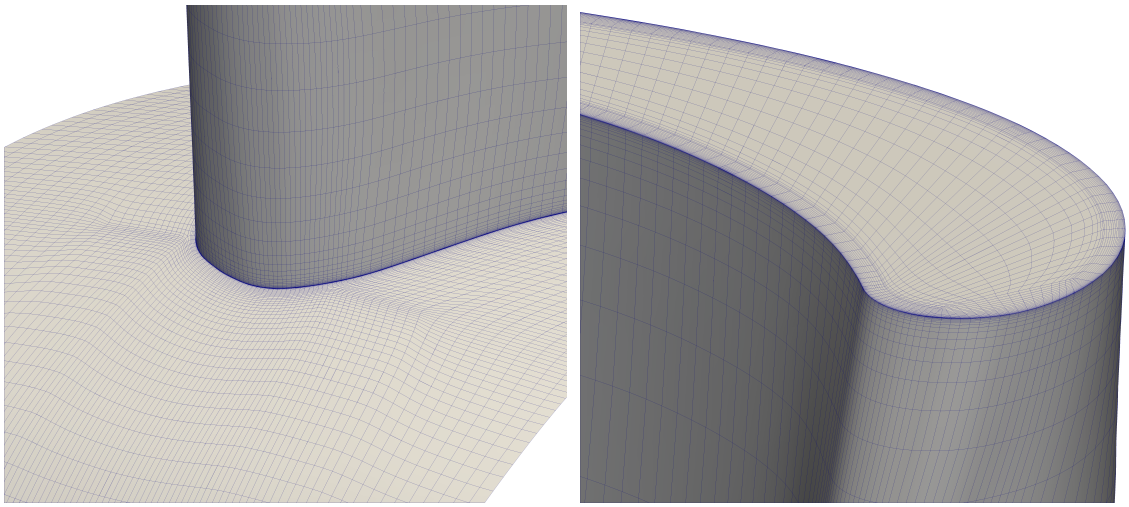

(a) Stator blade and hub (b) Rotor blade tip

Figure 3.6: Verified structured stage mesh

For the mesh shown above, y+ contour plots are given for the pressure and suction sides of the rotor blade in Figure 3.7. The maximum y+ value in the whole domain was the most difficult to control in the tip area and especially around the tip edge. In all other parts of the domain, y+ values did not exceed 1. As shown, the maximum y+ values on the rotor blade were around 5, visible in a very narrow region around the tip edge. In this region, the flow contracts and accelerates flowing into the tip gap. The first cell height in this region was controlled through the O-mesh around the blade and the first cell height in the radial direction in the tip gap. In this case, 25 radial mesh points were used in the tip gap to ensure good flow resolution, as well as a suitable y+ value while keeping the cell expansion ratio of 1.5.

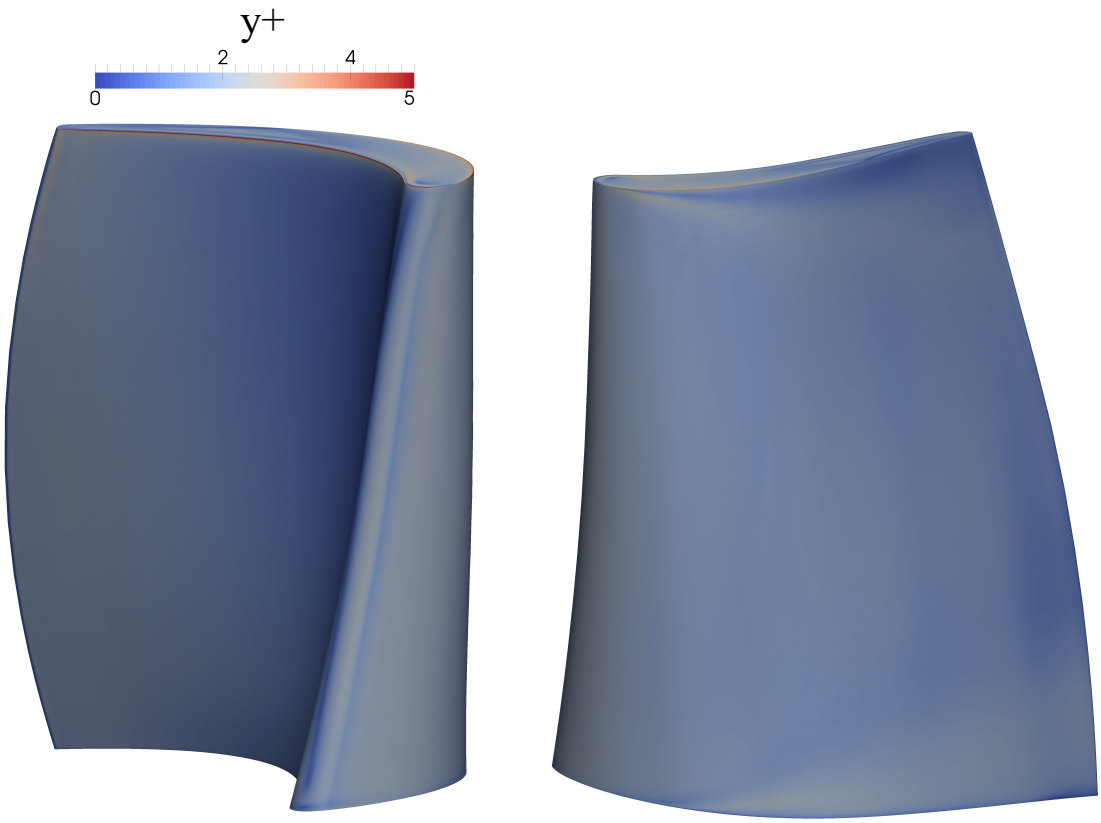

(a) Pressure side

(b) Suction side

Figure 3.7: y+ values on the rotor blade for verified structured mesh

3.2.1.3 Unstructured mesh

Unstructured meshes were created with BOXER, as presented in Section 2.2.2, but only for the rotor domain. Since the stator domain was not modified in the optimisations, a structured mesh was used for it since it has better quality and a far lower cell count. An unstructured mesh verification study was done using the mesh verified PADRAM stator mesh, and only the rotor mesh was altered. The results of the unstructured mesh verification study are presented in Figures 3.8 and 3.9, where mesh size stands for the stage mesh size, including both the stator and the rotor domains. Five different rotor meshes were tested. Mesh refinement included octree mesh refinement, and all other mesh properties were scaled based on it. In all meshes, the rotor tip gap and wake regions were additionally refined to resolve all the flow gradients.

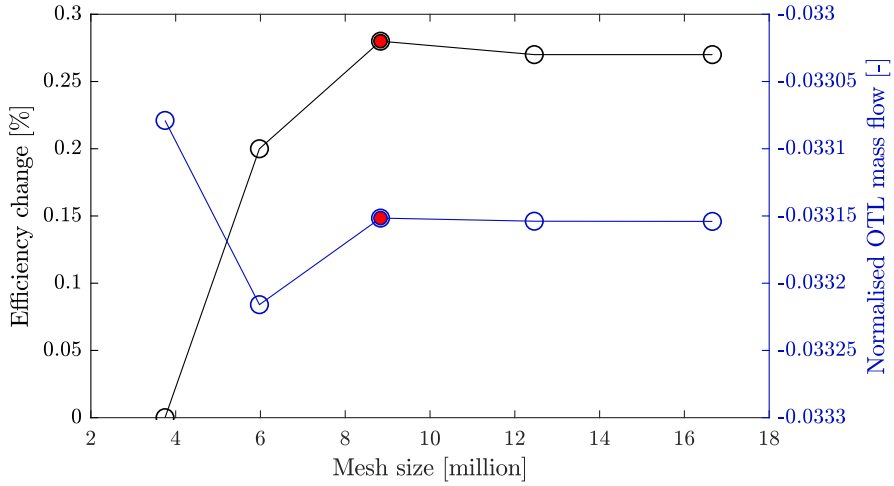

Figure 3.8: Unstructured BOXER mesh verification study - efficiency and OTL mass flow

As presented in Figure 3.8, both adiabatic efficiency and normalised tip leakage mass flow quickly converged after the total stage cell count surpassed 8 million cells. After that, only small variations in efficiency and leakage mass flow were seen.

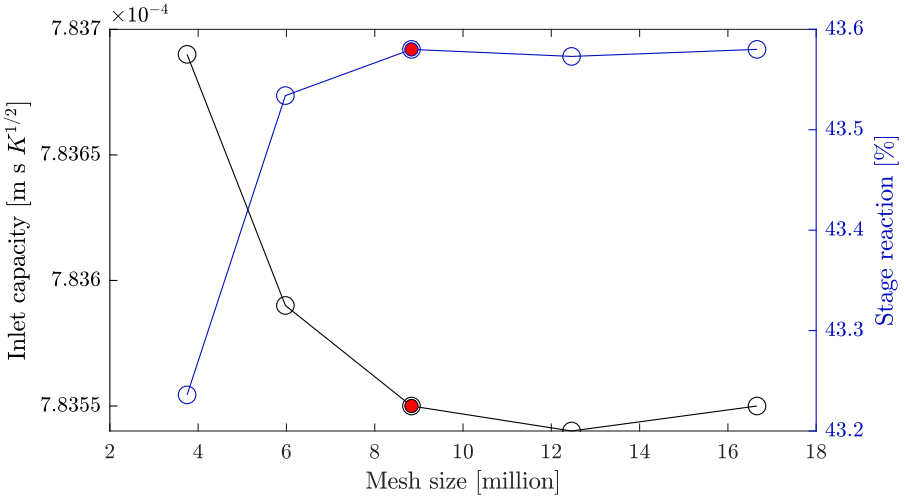

Figure 3.9: Unstructured BOXER mesh verification study - inlet capacity and stage reaction

Similar to the case of stage efficiency and leakage mass flow, inlet capacity and stage reaction became mesh size independent after the stage mesh count surpassed 8 million cells. All four measured properties converged around the same mesh size, in contrast to the structured mesh verification study where turbine inlet capacity and stage reaction became mesh independent at a mesh size of almost half of the

final mesh. Finally, the stage mesh with 9 million cells was taken as the verified unstructured mesh (noted with a red dot in Figures 3.8 and 3.9). The rotor domain accounted for around 8 million cells from almost 9 million cells for the whole stage. Details of the rotor domain are given in Section 3.2.1.4.

3.2.1.4 Details of the verified unstructured mesh

Figure 3.10 presents the details of the rotor domain's unstructured BOXER mesh for the tip surface and the tip gap radial distribution. In the case of an unstructured mesh, it was essential to have a very fine tip surface mesh to correctly predict complicated tip gap flow behaviour. Since the flow around the rotor blade below the tip region was much more uniform, mesh requirements in that region were far lower. Therefore, the tip gap region was additionally refined, which is visible in Figure 3.10. Above approximately 0.8 span, the blade has a much finer surface mesh (span is expressed between 0 and 1 where 0 denotes turbine hub, and 1 denotes turbine casing). This has also resulted in a finer volume mesh, visible in Figure 3.10b.

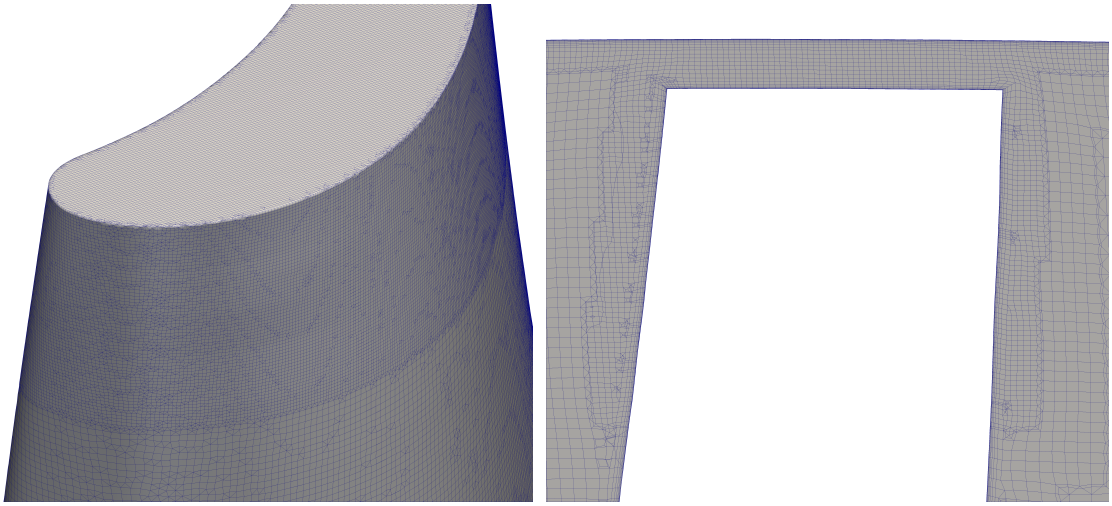

(a) Tip surface mesh (b) Tip gap radial mesh

Figure 3.10: Verified unstructured rotor mesh

In the BOXER software, the first cell height of the boundary layer mesh was easily controlled for each surface, which ensured low values of y+. The contour of y+ is shown in Figure 3.11.

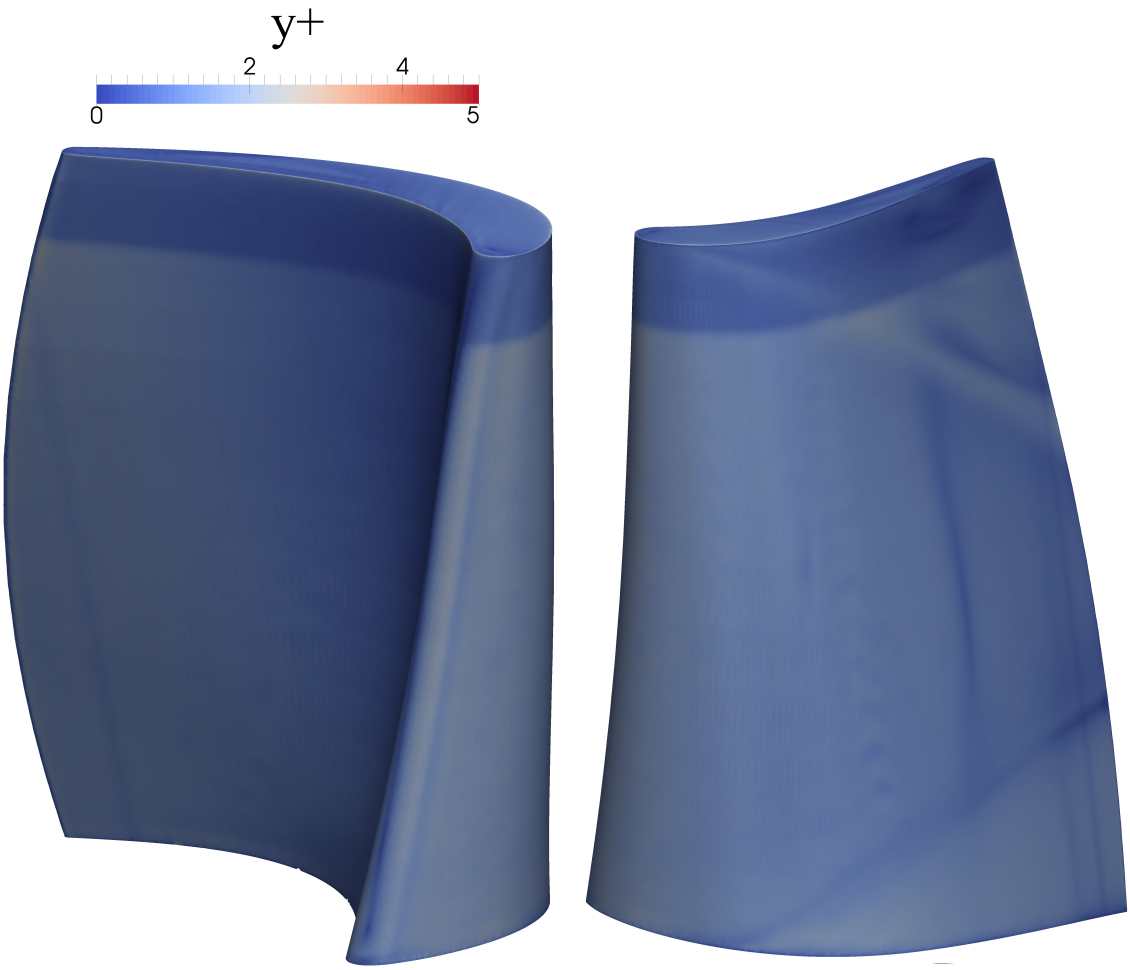

(a) Pressure side (b) Suction side

Figure 3.11: y+ values on the rotor blade for verified unstructured mesh

As shown in Figure 3.11, for the majority of the rotor blade surface, y+ values did not exceed 3. Even with the same boundary layer mesh setting, including the cells expansion of 1.5, y+ values in the blade tip region were around 1 due to the finer surface mesh. These values of y+ for both structured and unstructured meshes were assumed to be sufficient for the aerodynamic simulations.

3.3 Validation

3.3.1 Flat plate heat transfer

Heat transfer validation of a numerical code was done on a simple 2D case of flow over a flat plate, which was also used by Maffulli [96]. Turbulent flow regime with a Reynolds number of 1×10^6 was calculated using two numerical solvers, Hydra

Parameter	Value
Inlet total temperature	300 K
Inlet total pressure	101906.2 Pa
Outlet static pressure	101325 Pa
Wall temperature	310 K
Turbulence intensity	1 %
Turbulence length scale	1×10^{-3} m

Table 3.2: Flat plate heat transfer boundary conditions

and ANSYS Fluent. The numerical results were compared against the analytical solution given by Reynolds et al. [97] in Equation 3.6, using a Prandtl number of 0.7. The maximum free-stream Mach number was around 0.1, meaning that the flow was effectively incompressible. Although this is not ideal, since this study is about compressible flow of similar Reynolds number but in transonic regime, a wide range of established analytical solutions was beneficial in validating the heat transfer.

$$Nu_x = 0.0296 Pr^{0.6} {Re_x}^{0.8} \left(\frac{T_w}{T_\infty} \right) \tag{3.6}$$

The simulated 2D domain is presented in Figure 3.12, and the boundary conditions used are given in Table 3.2. The same mesh was used for all the cases presented, and it was verified beforehand as mesh size independent with a y+ value below 1.

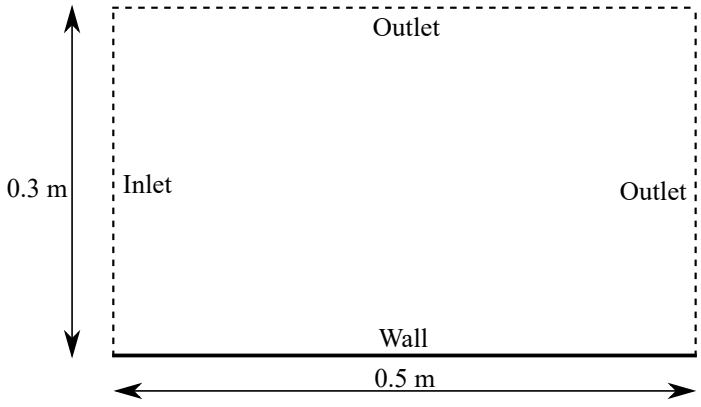

Figure 3.12: Flat plate validation geometry

The flat plate heat transfer results are presented in Figure 3.13 for two turbulence models, Spalart-Allmaras and k-ω SST. Results show very good agreement with the

analytical expression for both turbulence models and both codes. A small deviation can be seen close to the inlet in the case of Hydra with k-ω SST turbulence model. After half the distance, an overprediction of Nusselt number is visible for the simulation in Fluent with Spalart-Allmaras turbulence model. However, its magnitude is small. Overall, all results were found to give good agreement with the analytical expression.

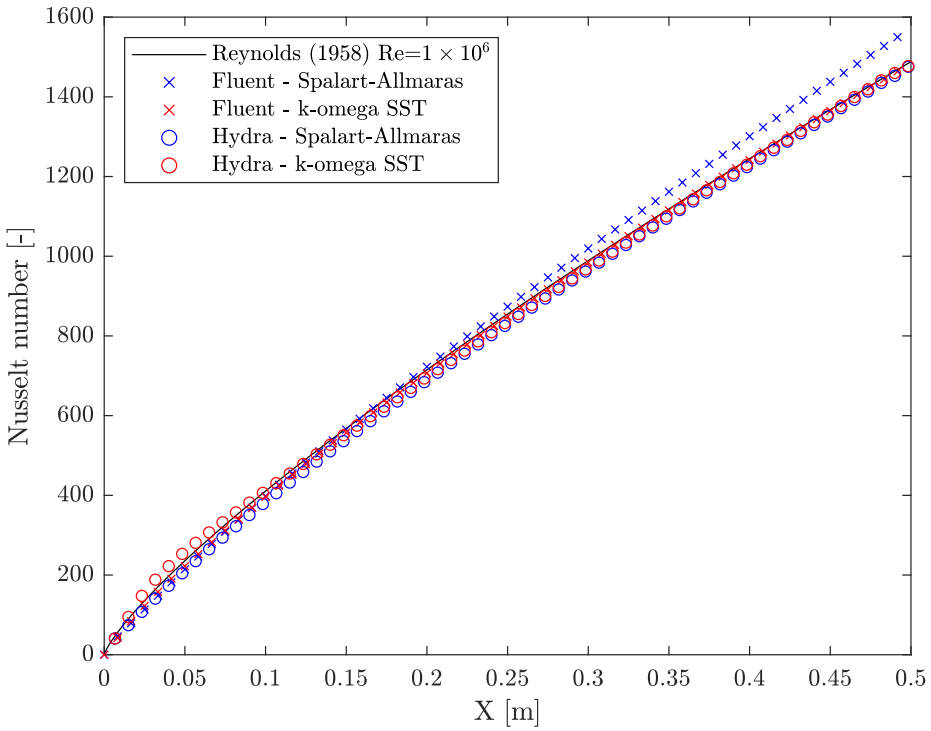

Figure 3.13: Results of flat plate heat transfer validation

3.3.2 High pressure turbine stage

3.3.2.1 Steady case

The CFD model presented in Figure 3.1 was validated against the experimental data given by Simone et al. [98]. For that, a verified structured mesh shown in Section 3.2.1.2 with Spalart-Allmaras turbulence model was used.

Results are given in the form of the isentropic Mach number calculated using Equation 3.7 at three blade spans for the stator blade. To clarify, span is expressed between 0 and 1 where 0 denotes turbine hub, and 1 denotes turbine casing. Also, static pressure was non-dimensionalised against the inlet total pressure at the rotor blade midspan. In Equation 3.7, γ stands for the specific heat capacity ratio and

throughout this work has a value of 1.4 as the working fluid is air. Numerical results are presented against the experimental data in Figure 3.14.

$$M_{is} = \sqrt{\left(\left(\frac{p_{0,inlet}}{p}\right)^{\frac{\gamma-1}{\gamma}} - 1\right)\frac{2}{\gamma-1}} \tag{3.7}$$

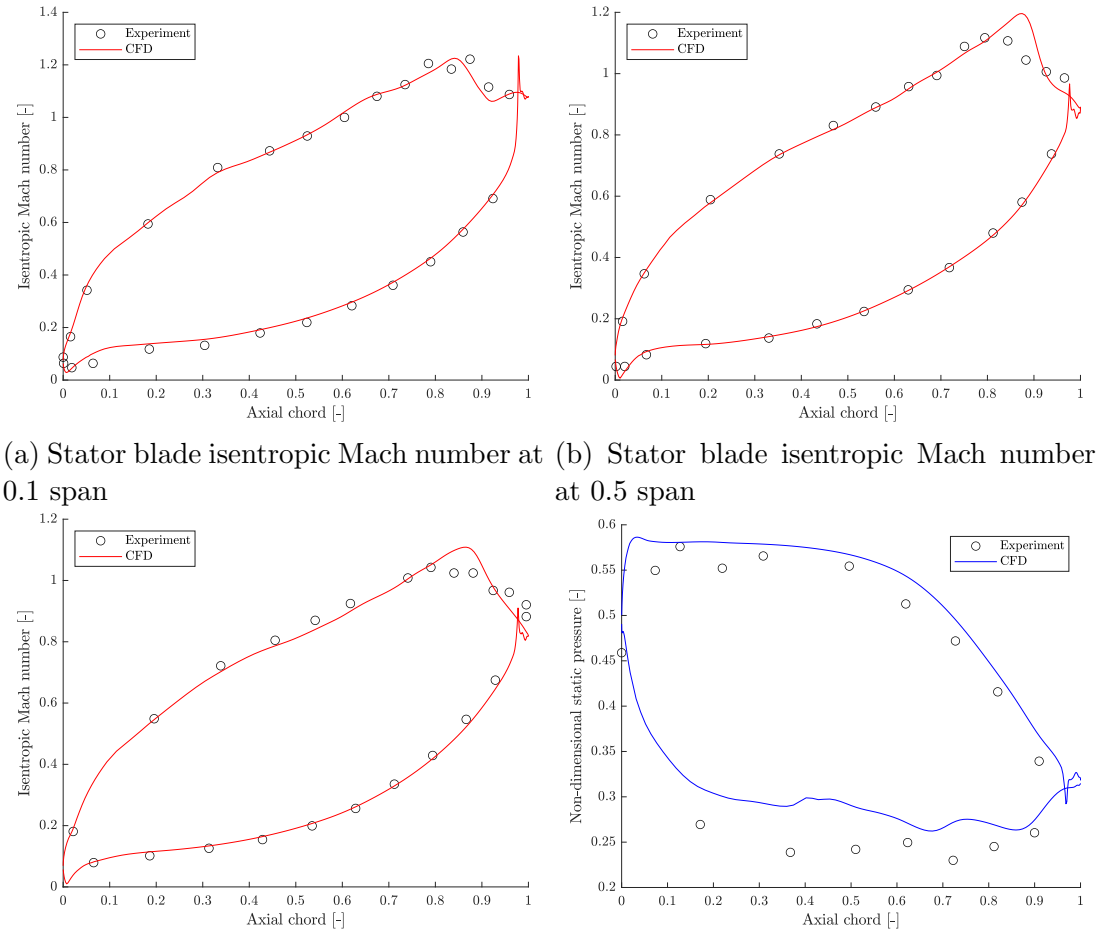

(a) Stator blade isentropic Mach number at 0.1 span

(b) Stator blade isentropic Mach number at 0.5 span

(c) Stator blade isentropic Mach number at 0.9 span

(d) Rotor blade non-dimensional static pressure at 0.5 span

Figure 3.14: Results of MT1 passage flow validation

Numerical results show good agreement with the experimental data for all three spans of the stator blade. The only region where numerical results deviate from the experimental data is the aft portion of the suction side, where the stator domain is characterized by a strong shock. Similar deviations have been reported by other authors [99, 100].

In the rotor domain, the non-dimensional static pressure was found to be slightly overpredicted at all regions of the blade, with higher deviations seen at the suction side of the rotor blade (Figure 3.14d). These results were also reported by other authors who used the MT1 turbine for their work [98, 99, 100].

3.3.2.2 Unsteady case

Since the steady simulation showed some deviation from the experimental data, an unsteady simulation was carried out to see the effect of unsteady flow features on the validation. The unsteady simulation was carried out using a Spalart-Allmaras turbulence model, and the mesh and boundary conditions were the same as those in the steady approach presented in Section 3.3.2.1.

Unsteady stator-rotor interaction was modelled using a sliding plane as the interface between the stator and the rotor. In contrast to the mixing plane used in the steady simulations, the sliding plane does not radially average out the flow properties at the stator-rotor interface. Instead, it passes them through the interface from the stator to the rotor, retaining the flow features such as wakes and vortices.

MT1 turbine, as previously mentioned, consists of 32 stator and 60 rotor blades, resulting in a pitch of 11.25° and 6° respectively for one passage. This pitch has no effect on the steady case with a mixing plane, as the flow properties are radially averaged at the stator-rotor interface. However, in the unsteady case where flow phenomena pass through the interface, the pitches of the stator and rotor domains must correspond. In the case of the MT1 turbine, the smallest pitch at which the stator and rotor domains would have a conformal interface was a quarter of the annulus (8 stator and 15 rotor blades). Since this was expected to be computationally expensive, the approach of altering the rotor domain geometry was taken.

The approach from Salvadori et al. [99] was followed, which included scaling the rotor domain using the *reduced count ratio* technique. This involved increasing the number of rotor blades from 60 to 64, which allowed the same stator-rotor pitch for 1 stator blade and 2 rotor blades. However, because the rotor blade number was increased, the rotor blade had to be scaled and skewed to maintain the constant pitch-to-axial-chord ratio. In other words, since the rotor pitch was changed from 6° to 5.625°, the axial chord was changed proportionally. Finally, the rotor blade was skewed to retain the datum inlet capacity. The final rotor geometry is presented in Figure 3.15.

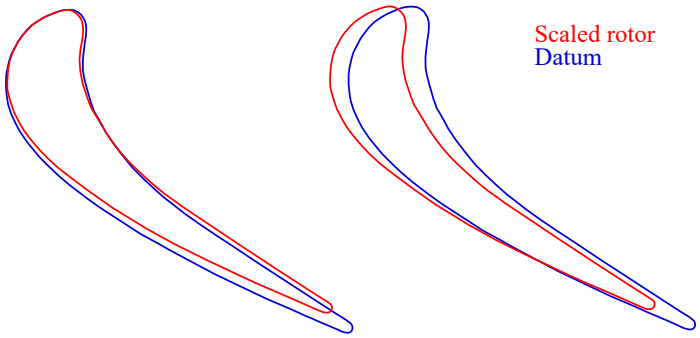

Figure 3.15: Rotor blade scaling

Before moving on to the unsteady simulation, the scaled rotor geometry was simulated in a steady simulation using a mixing plane approach, and it was compared to the results with the datum geometry. This is presented in Figure 3.16. It can be seen that scaling the rotor blade had almost a negligible effect on the stator domain, where minor differences in the shock strength can be seen. Differences in flow between the two geometries are more obvious in the rotor domain, where the static pressure decreases at the second half of the blade pressure side and increases on the suction side. Nevertheless, the flow differences resulting from altering the rotor domain seemed to be minor, and this geometry was simulated using the unsteady approach.

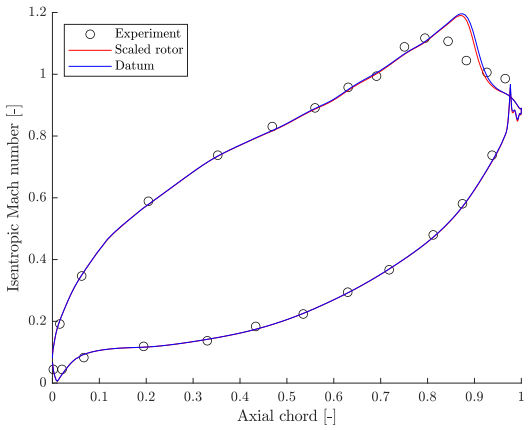

(a) Stator blade isentropic Mach number at 0.5 span

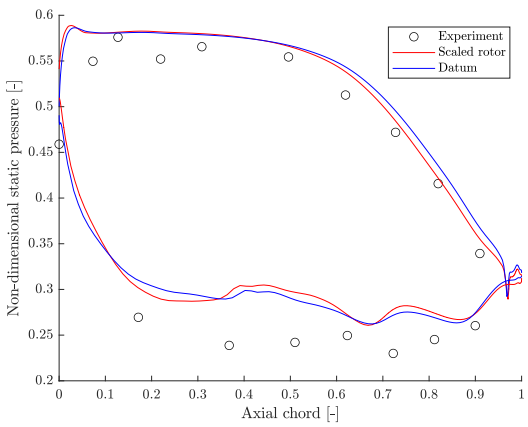

(b) Rotor blade non-dimensional static pressure at 0.5 span

Figure 3.16: Comparison of result for datum and rotor scaled geometry

The unsteady simulation was initialised using the converged steady simulation with a sliding plane interface and was run until convergence in the form of periodic behaviour was achieved. In this case, the period is the time for a rotor blade to pass one stator passage pitch. Since one stator passage has a pitch of 11.25° and

Turbulence model	Spalart-Allmaras
No. of periods	6
Timesteps per period	200
Iterations per timestep	20

Table 3.3: MT1 turbine operating point

the turbine angular speed is 995 rad/s, the time for one period was calculated to be $1.973\,725 \times 10^{-4}$ s. The setup of the unsteady simulation is presented in Table 3.3. The unsteady simulation was run for 6 periods, which were divided into 200 timesteps each. In each timestep, 20 iterations were performed. These values resulted from preliminary simulations done beforehand and internal studies conducted at Rolls-Royce. Similar unsteady simulation setups were also used by other researchers [100].

Different properties were monitored to judge the convergence of the unsteady simulation like the isentropic efficiency and mass flows, temperatures and pressures at the inlet at the outlet boundaries. The simulation converged and entered the quasi-steady state after 6 periods and its history is presented in Figure 3.17.

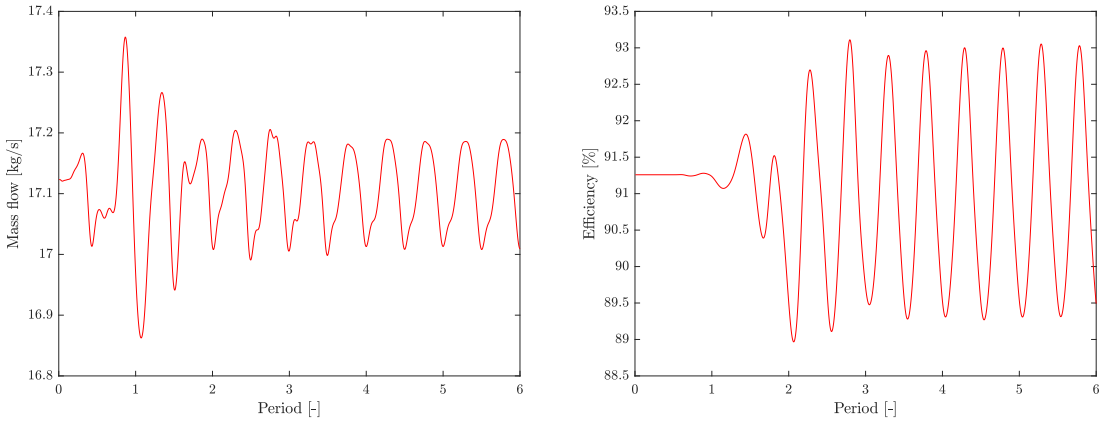

(a) Turbine mass flow at the stator outlet (b) Turbine stage efficiency

Figure 3.17: Unsteady simulation convergence history

Data from unsteady simulation was time averaged for the whole 6th period and compared with the experimental values. This is presented in Figure 3.18. For brevity, stator data is show only at the midspan.

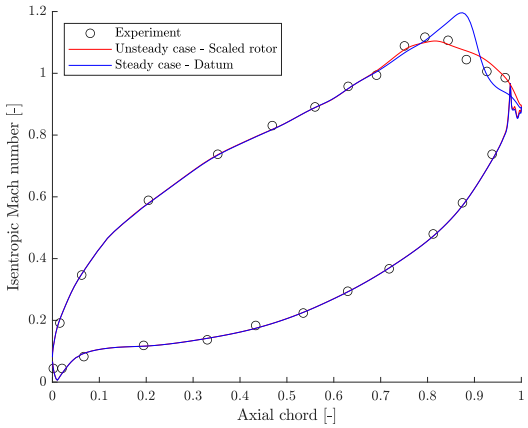

(a) Stator blade isentropic Mach number at 0.5 span

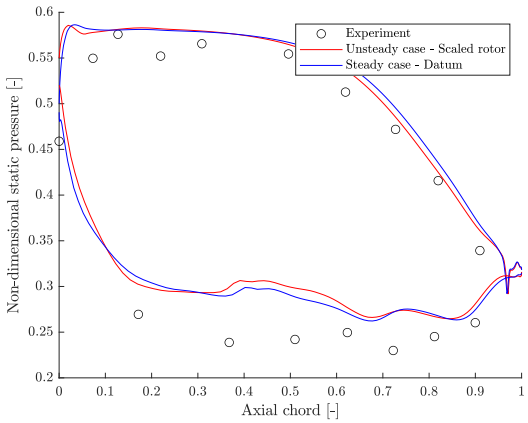

(b) Rotor blade non-dimensional static pressure at 0.5 span

Figure 3.18: Comparison of steady and unsteady simulation results

Considering the changes resulting from scaling the rotor domain shown in Figure 3.16, Figure 3.18 shows that the unsteady simulation had no effect on the rotor domain compared to the steady approach. The most visible difference is the averaging of the aft stator blade suction side shock, and in this region, the unsteady simulation was found to be much closer to the experimental data. This finding is in agreement with the findings from Beard et al. [100].

Since the unsteady approach showed no significant change, especially in the rotor domain that was in the scope of this work, the modelling approach using steady simulation with a mixing plane was used for the upcoming optimisations.

3.3.3 Tip gap

To ensure the CFD model's accuracy in the tip region, which was of particular interest in this work, the modelling approach had to be validated in this region too. Since MT1 turbine has no experimental data for this region that could be of use, another research case had to be found. For that, Oxford's High Speed Linear Cascade (HSLC) was used, shown in Figure 3.19.

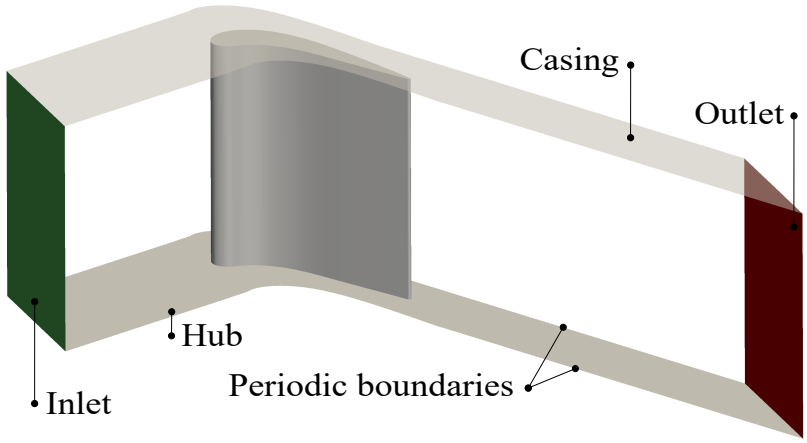

Figure 3.19: HSLC geometry

The modelling approach in the tip gap was validated against the experimental data provided by Zhang et al. [101]. The experimental data are available in the form of isentropic Mach numbers at 0.5 and 0.95 of the span, as well as the tip Nusselt number contours for three tip gaps of 0.5 %, 1 %, and 1.5 % of the blade span. The Nusselt number resulting from the CFD simulation was calculated using the following equation as

$$Nu = \frac{C_{ax} HTC}{k_T} \tag{3.8}$$

where C_{ax} represents the characteristic length, which in this case is the blade axial chord, HTC stands for the heat transfer coefficient, and k_T is the thermal conductivity. For this validation, a structured PADRAM mesh was used with the k-ω SST turbulence model.

The experimental data showing isentropic Mach numbers are presented in Figure 3.20. Figure 3.20a shows very good agreement between the experimental and numerical results at 0.5 of the blade span. Some deviation from the experimental results is visible on the blade suction side at around 0.3 of the axial chord, where the isentropic Mach number is slightly underpredicted by the CFD. More noticeably, the isentropic Mach number is overpredicted in the aft suction side region. The overprediction of the isentropic Mach number at the blade suction side close to the trailing edge was found to be caused by a strong shock wave that impinged on the blade surface, overpredicting the isentropic Mach number at the suction side by almost 0.2.

The agreement between the experimental and CFD results was also found to be very good for 0.95 of the span, where again, the most noticeable difference was only

at the second half of the blade suction side. This region was largely affected not only by the strong shock, as in the case of 0.5 of the span, but also by the strong over tip leakage vortex. In this case, the leakage flow would start exiting the tip gap around 0.5 of the axial chord and rub on the blade. This phenomenon seems to be hard to capture with steady CFD simulations. Nevertheless, since the CFD overpredicted the isentropic Mach number in this region by around 0.1, the overall agreement of experimental and numerical data is considered to be sufficient.

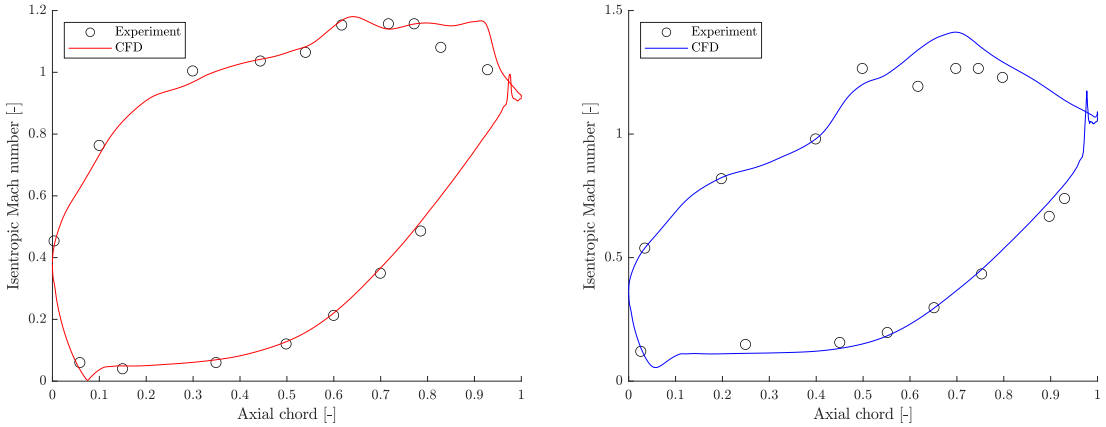

(a) Isentropic Mach number at 50 % span (b) Isentropic Mach number at 95 % span

Figure 3.20: Results of HSLC passage flow validation

Tip gap validation is presented in Figure 3.21, where CFD results for structured PADRAM and unstructured BOXER meshes are given alongside the experimental data. As shown, at the front part of the tip, experiments show an increased level of Nusselt number. In this region, the flow was found to be subsonic, leading to a higher level of heat transfer and therefore Nusselt number. As the gap opens up from 0.5 % towards 1.5 %, more leakage flow enters the tip gap, leading to an increase in the U-shaped high heat transfer area and the level of heat transfer. This trend was well predicted by the CFD. However, in the case of the PADRAM mesh, overprediction of heat transfer in this region is visible for all the tip gaps. The magnitude of heat transfer in the case of the BOXER mesh is lower and agrees well with the experimental result.

The second half of the HSLC's tip is characterised by the supersonic flow condition, which decreases the heat transfer level and therefore the Nusselt number. Experimental data shows lines of increased Nusselt number alongside the pressure side edge due to the tip leakage flow separation over the tip edge, more visible as

the tip gap increases. This was again overpredicted by the CFD with the PADRAM mesh and agreed well with the experiment in the case of the BOXER mesh.

Experiments showed that the middle part of the blade for 0.5 % and 1 % of the tip gap is characterised by the low Nusselt number, where this region was found to be much smaller in the case of the 1.5 % tip gap. This behaviour was well predicted by the CFD with the BOXER mesh, apart from the fact that these regions stretched all the way across the tip in the case of the experiments. CFD with the PADRAM mesh showed an overprediction of heat transfer in this region for the 0.5 % tip gap and agreed quite well for the other two.

In the case of the 1.5 % tip gap, experiments showed stripes of high and low heat transfer, parallel to the pressure side separation stripe, which were a result of the oblique shock waves reflecting between the blade tip and the casing. This was captured by the CFD with the structured PADRAM mesh but was only slightly visible in the case of the BOXER mesh.

The general flow disagreement between the experiment and CFD with the PADRAM mesh can be explained by the perfectly sharp tip edge in the CFD model, which affected the flow pressure side separation and, therefore, the heat transfer significantly. In contrast, the experimental blade had a tip edge of a finite radius, which caused the separation to behave differently.

Apart from the shock reflections for the largest tip gap case, the BOXER mesh was found to have better agreement with the experimental data. One reason for this was that the octree meshing approach slightly changed the tip edge, causing a rounded tip outline to some extent. This had an impact on the flow results.

Despite the differences in heat transfer level prediction, the overall agreement in the comparison of flow patterns, subsonic and supersonic flow conditions, and changes in heat transfer with the size of the tip gap was found to be good for both CFD approaches. Therefore, these models were found to be good representations of the experimental approach.

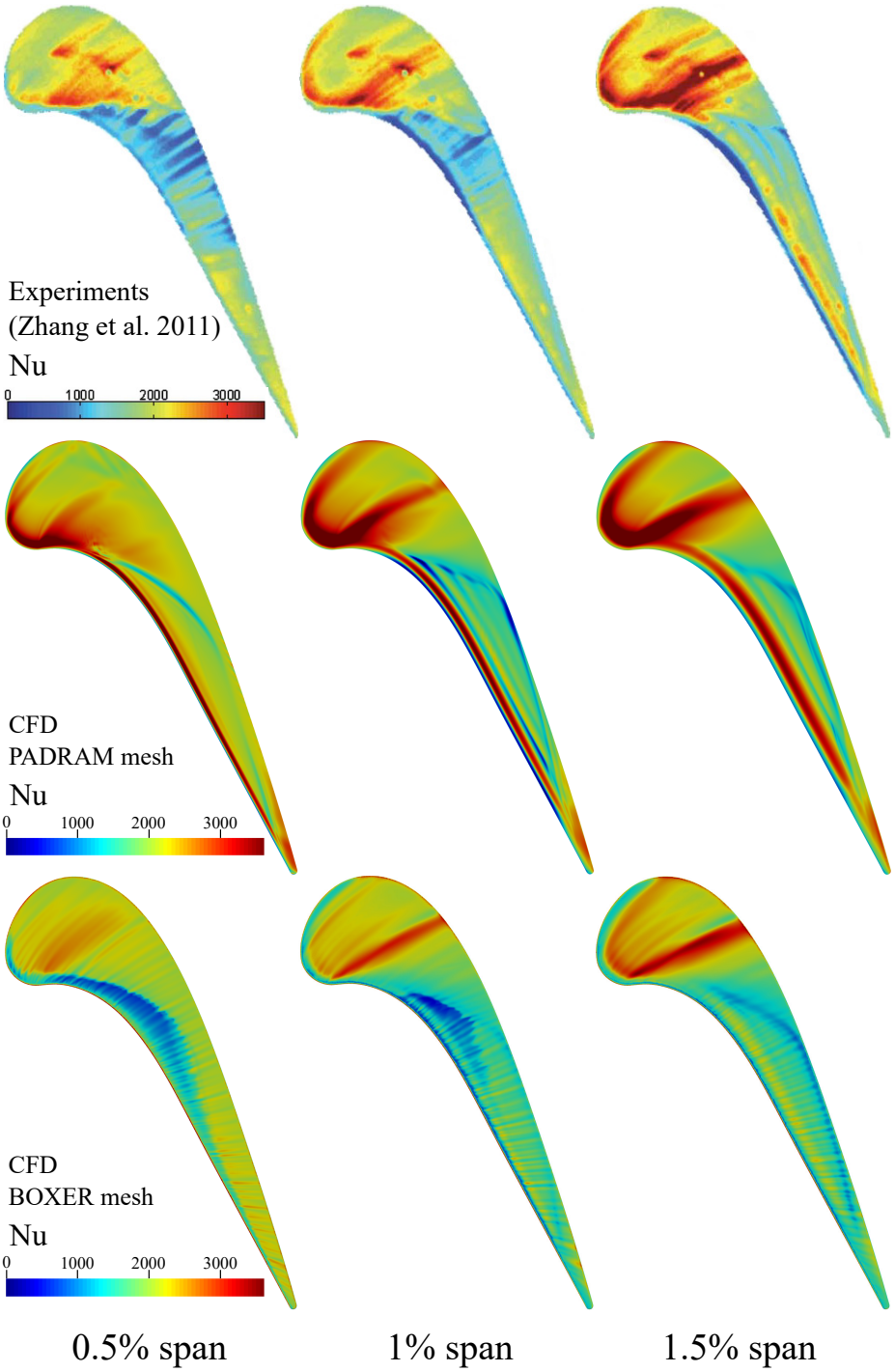

Figure 3.21: Results of HSLC tip gap validation

3.4 Turbulence model effect

The effect of turbulence models on the flow was examined using the converged structured PADRAM mesh. Two turbulence models were compared, Spalart-Allmaras and

k-ω SST.

The effect of the turbulence models on the pressure distribution around the blade is presented in Figure 3.22. As shown, the effect of the two compared turbulence models was found to be negligible. Switching from the already presented Spalart-Allmaras to the k-ω SST turbulence model did not change the flow pressure distribution around either of the blades. The shock wave position was found to be slightly moved towards the trailing edge in the case of the k-ω SST turbulence model. Additionally, both turbulence models showed the same deviation from the experimental data in the rotor domain.

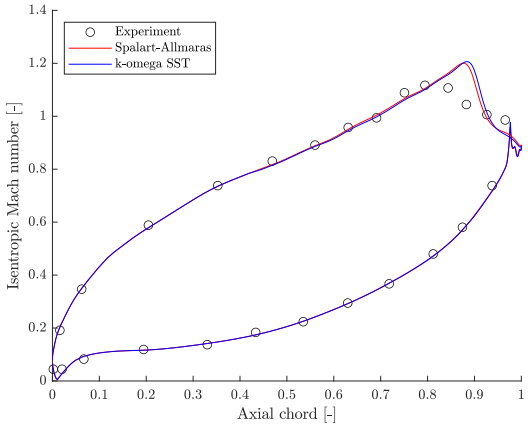

(a) Stator blade isentropic Mach number at 0.5 span

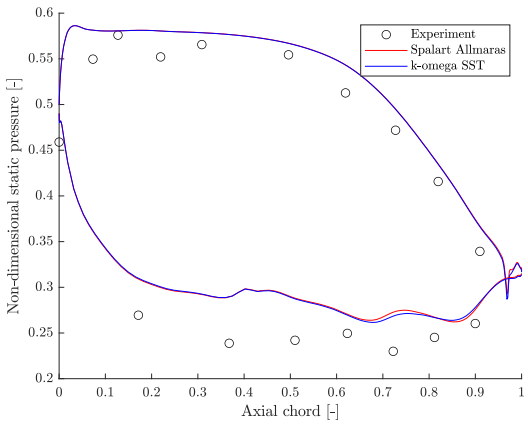

(b) Rotor blade non-dimensional static pressure at 0.5 span

Figure 3.22: Comparison of turbulence models

More differences between the two turbulence models were found in regions away from the wall. The k-ω SST turbulence model accounts for turbulence dissipation, where the Spalart-Allmaras does not, resulting in differences in vortices and wakes. This led to different flow dissipation predictions and, as a result, different efficiency predictions.

To observe the difference in the two turbulence models away from the walls in the flow region containing wakes and vortices, static pressure was radially averaged at 0.5 axial chord downstream of the rotor blade trailing edge. The plane at 0.5 axial chord downstream of the rotor blade trailing edge where the static pressure was averaged is shown in Figure 3.23.

Radially averaged static pressure for the two turbulence models is shown in Figure 3.24. As shown, the two turbulence models show little difference in the bottom half of the blade passage where flow is not largely separated. The only difference in this region is between 0.2 and 0.4 of the blade span due to the growing corner vortex.

The upper region of the blade passage is characterised by the tip leakage flow and its vortex, and the passage vortex. Static pressure was found to decrease in areas of vortex-dominated flow, resulting in flow friction and energy dissipation. Therefore, differences between the two turbulence models are more visible in this region when observing the static pressure. Considering the almost identical static pressure prediction between the two turbulence models at 0-0.2 and 0.4-0.6 of the span, it is safe to say that these turbulence models predict the wake dissipation almost equally, and the only difference is due to the vortical flow.

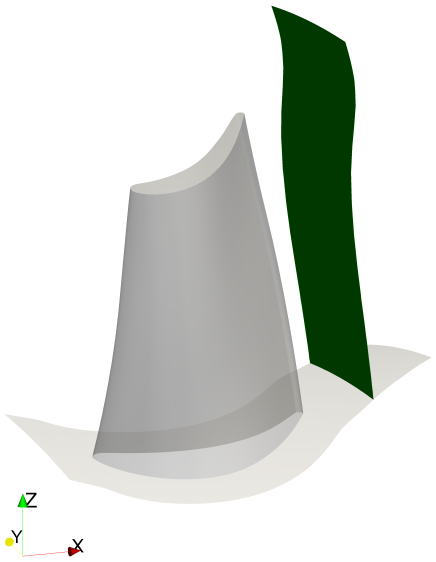

Figure 3.23: Plane at 0.5 C_{ax} downstream of trailing edge

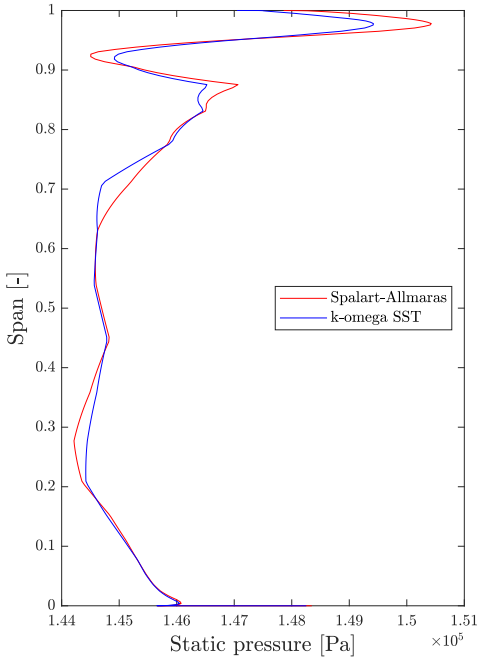

Figure 3.24: Radially averaged static pressure at 0.5 C_{ax} downstream of trailing edge

Chapter 4

Winglet tip optimisation

As explained in Section 1.3.4, Schabowski and Hodson [35] found in their study on winglets that the main operating principle of winglet tips is the reduction of driving pressure caused by overtip leakage flow. Winglet overhangs protruding from the tip edge away from the blade reach the area of increased static pressure, effectively reducing the overtip side pressure difference. This results in a lesser driving force for the tip leakage flow, which in turn decreases the aerodynamic losses and ultimately increases the turbine stage's performance.

Since the aim of this study was to go beyond the state of the art and develop a novel and superior aerothermal performance tip and optimisation methodology, the optimisation of the winglet tip was performed first.

This chapter presents the setups and results of various winglet tip optimisations. To understand the benefits of the winglet tip, aerodynamic winglet tip optimisation was performed first, followed by aerodynamic optimisation with constraints. Turbine inlet capacity and stage reaction were constrained and kept at near datum values. Finally, multidisciplinary winglet optimisation with constraints was carried out by optimising the winglet tip for aerodynamic performance and heat load.

4.1 Aerothermal structured mesh verification study

Aerothermal structured mesh verification study was carried out on a typical winglet tip, created by hand. Its design parameters are given in Table 4.1.

Starting from the aerodynamically verified structured mesh presented in Figure 3.6, an aerothermal mesh verification study was conducted by creating three additional rotor meshes. This was done by gradually refining all mesh blocks and resulted in three different rotor meshes with sizes of 3, 6, and 12 million cells. For

Parameter	Applied value
PS location, b_{PS} [% of edge length]	50
SS location, b_{SS} [% of edge length]	50
Overhangs: $o_{LE}, o_{PS}, o_{SS}, o_{TE\ PS}, o_{TE\ SS}$ [C_{ax}]	0.05, 0.05, 0.05, 0.05, 0.05
Straight lengths: $d_{LE}, d_{PS}, d_{SS}, d_{TE\ PS}, d_{TE\ SS}$ [C_{ax}]	0.005, 0.005, 0.005, 0.005, 0.005
Blending angles: $\beta_{LE}, \beta_{PS}, \beta_{SS}, \beta_{TE\ PS}, \beta_{TE\ SS}$ [°]	60, 60, 60, 60, 60

Table 4.1: Design parameters of a winglet tip used in aerothermal structured mesh verification study

these meshes, flow properties related to aerodynamic performance at adiabatic conditions and heat flux at a temperature ratio of 0.6 were monitored. As mentioned in Section 3.1.2.1, this assumes that the aerothermal simulation was run by imposing a constant rotor blade wall temperature of 266 K. The rest of the boundary conditions were standard, given in Table 4.5.

During the aerothermal mesh verification study, integrated heat flux levels on the blade and separately on the winglet tip were monitored. Since winglet tips are characterised not only by the complex flow over the tip but also on the undersides of the overhangs, the undersides of the tip overhangs need to be included as part of the tip. Therefore, the tip was defined as the blade area above 0.9 of the blade span.

The aerothermal mesh verification study results are summarised in Table 4.2. Mesh size represents the rotor mesh size only, as the stator mesh used for all cases was the same. It can be seen that the difference in adiabatic efficiency is very small for all three meshes. Over tip leakage mass flow, normalised against the single rotor passage mass flow, was found to stay the same when the mesh was refined from 6 to 12 million cells. Integrated heat flux on the whole blade was found to be very similar for all three cases due to consistent results in large areas of blade pressure and suction side. However, some differences were observed in the tip region. Overall, meshes of 6 and 12 million cells gave very similar results, and after closer examination, it was decided to use the 6 million mesh in the optimisation.

The heat flux for these three meshes with a wall temperature of 266 K is presented in Figure 4.1. As shown, the heat flux for all three cases is very similar, both around the blade and at the tip. Refining the mesh from 3 million cells did not reveal any

Rotor mesh size [million]	Efficiency difference [%]	OTL mass flow [%]	Tip to blade heat flux ratio [%]
3	0	3.87	21.13
6	0.02	4.14	20.73
12	0.04	4.14	20.88

Table 4.2: Aerothermal structured rotor mesh verification study

new flow phenomena, and the differences in surface integrated values were found to be caused by smoother resolution of the increased heat flux patches.

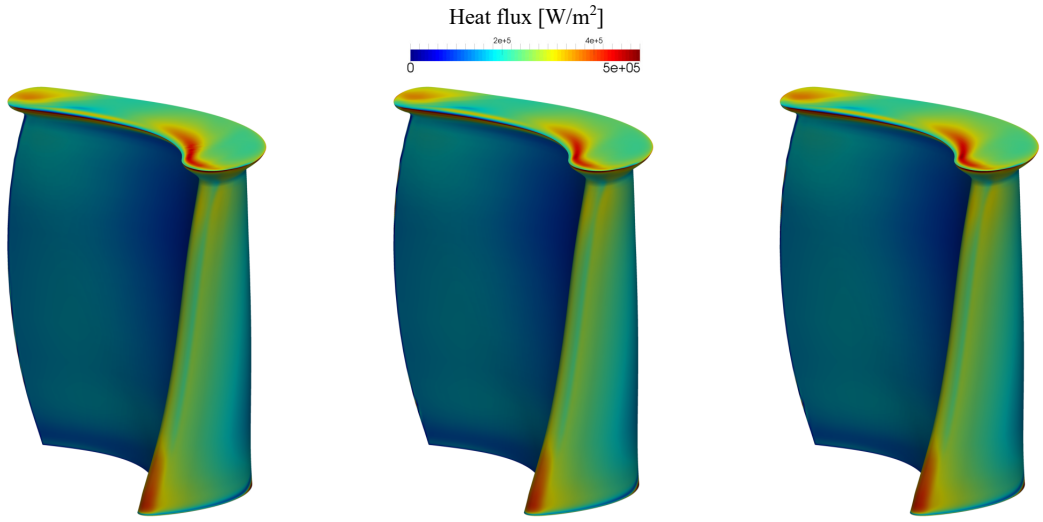

(a) 3 million (b) 6 million (c) 12 million

Figure 4.1: Heat flux for three different winglet tip meshes

Based on all the presented results, a rotor mesh of 6 million cells was considered to be mesh size independent and was used in the optimisation. This is explained in more detail in Section 4.4.2.1, where the CFD model is described.

4.2 Accuracy of the 3-temperature model

In this section, the accuracy of the 3-temperature model is presented for the case of an arbitrary winglet tip. Using the aerothermally verified mesh presented in Section 4.1, the heat transfer coefficient was computed using the 3-temperature model for the rotor blade wall temperature corresponding to TR of 0.6 (266 K), as explained in Section 3.1.2.2. It is presented in Figure 4.2.

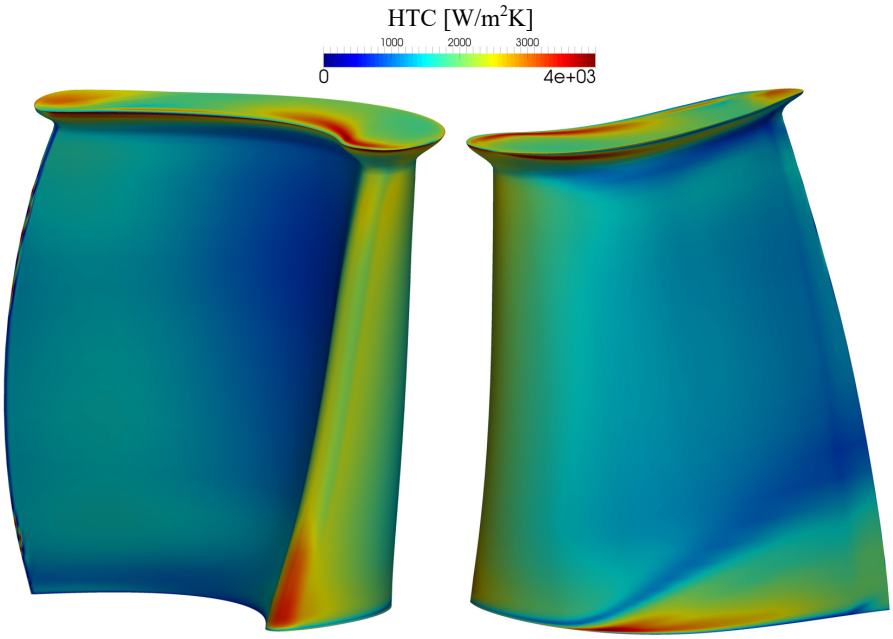

Figure 4.2: Heat transfer coefficient on rotor blade with winglet tip for a wall temperature corresponding to TR of 0.6

As shown in Figure 4.2, the heat transfer coefficient on the blade wall was found to be characterised by the local flow conditions like flow impingements and separations. It is positive as it represents a heat flux gradient which is always positive.

To assess the accuracy of the 3-temperature model, the heat flux was reconstructed using Equation 2.49 for the rotor blade wall temperature corresponding to a TR of 0.6. This was done by multiplying the heat transfer coefficient shown in Figure 4.2 with the temperature differential between the adiabatic wall temperature and the rotor blade wall temperature corresponding to a TR of 0.6. The reconstructed heat flux was then compared with the heat flux from a direct CFD simulation obtained by imposing a constant wall temperature at the rotor blade corresponding to a TR of 0.6. These two heat fluxes are compared in Figures 4.3 and 4.4.

Figure 4.3 shows the pressure side heat flux from two sources: a direct CFD run and a reconstructed heat flux from the 3-temperature model. As shown, the two sources of heat flux compared very closely, and the actual differences were hard to observe. This can be explained by the fact that the pressure side is characterised by the attached flow, with no large pressure gradients and without flow features that are affected by the wall temperature condition. However, looking at the tip area, where this was not the case, the heat fluxes were also found to match well.

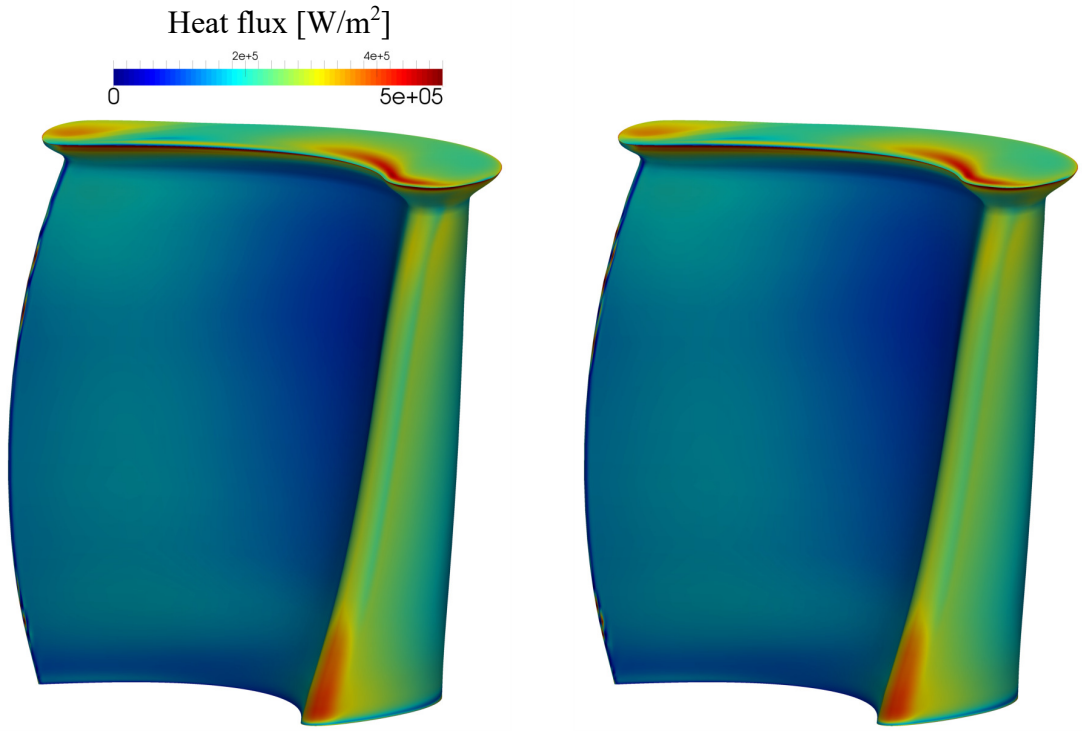

(a) CFD (b) 3-temperature model

Figure 4.3: Comparison of heat flux on rotor blade pressure side for wall temperature corresponding to TR of 0.6

Heat fluxes from two different sources are shown for the blade suction side in Figure 4.4. Unlike the heat flux on the pressure side presented in Figure 4.3, there are noticeable differences in the two heat flux values. This is particularly noticeable in the second portion of the blade, towards the trailing edge. To show these differences in more detail, the measure of heat flux error is introduced.

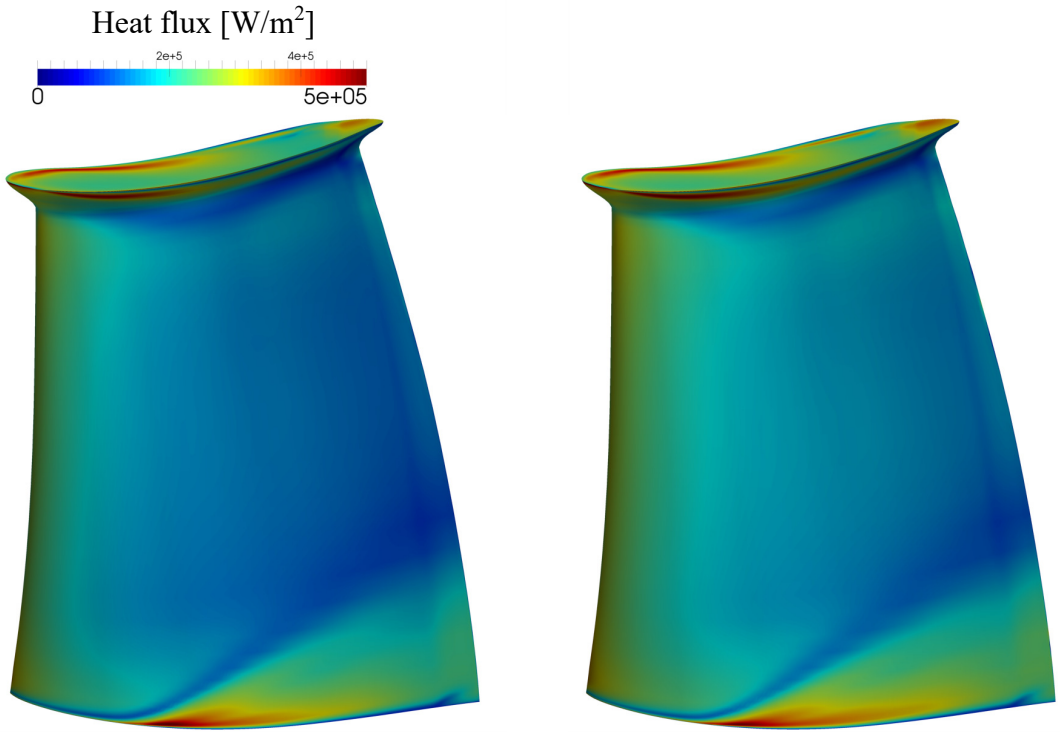

(a) CFD (b) 3-temperature model

Figure 4.4: Comparison of heat flux on rotor blade suction side for wall temperature corresponding to TR of 0.6

Heat flux error was calculated as

$$q_{error} = \left(\frac{q_{3-temp} - q_{CFD}}{q_{CFD}} \right) \cdot 100 \tag{4.1}$$

where q_{3-temp} represents the heat flux obtained with the 3-temperature model, and q_{CFD} represents the heat flux resulting from a direct CFD simulation. It essentially represents a difference in the heat flux obtained from the 3-temperature model relative to the heat flux from direct CFD, thus showing the accuracy of the 3-temperature model.

The heat flux error on the blade pressure and suction sides is shown in Figure 4.5. The figure shows that in the leading edge area, the 3-temperature model slightly underpredicted and overpredicted the heat flux in two streaks, varying up to $\pm 10\,\%$. In this region, a small amount of flow separation was found, and large pressure gradients due to the stagnation region were observed. At the rest of the pressure side, the heat flux error was found to be almost negligible, being less than $1\,\%$. On the other hand, the blade suction side, shown in Figure 4.5b, was characterised by a larger

heat flux error due to the large pressure gradients and detached flow. The heat flux obtained by the 3-temperature model was mostly overpredicted in the second half of the suction side, with the exception of the winglet tip underside, where two streaks of underpredicted and overpredicted heat flux can be seen. Small portions of this region had an error of up to $\pm 10\,\%$. This was due to the strong vortical flow present in this region, as a result of the passage and the over tip leakage vortices. At the aft portion of the blade suction side, a more noticeable region of overpredicted heat flux was visible, stretching through the whole blade span. In this region, the flow was characterised by the large pressure gradients due to the strong shock, where the 3-temperature model overpredicted the heat flux by up to $5\,\%$. Overall, with some differences in unstable flow areas, the two sources of heat flux were found to match quite well.

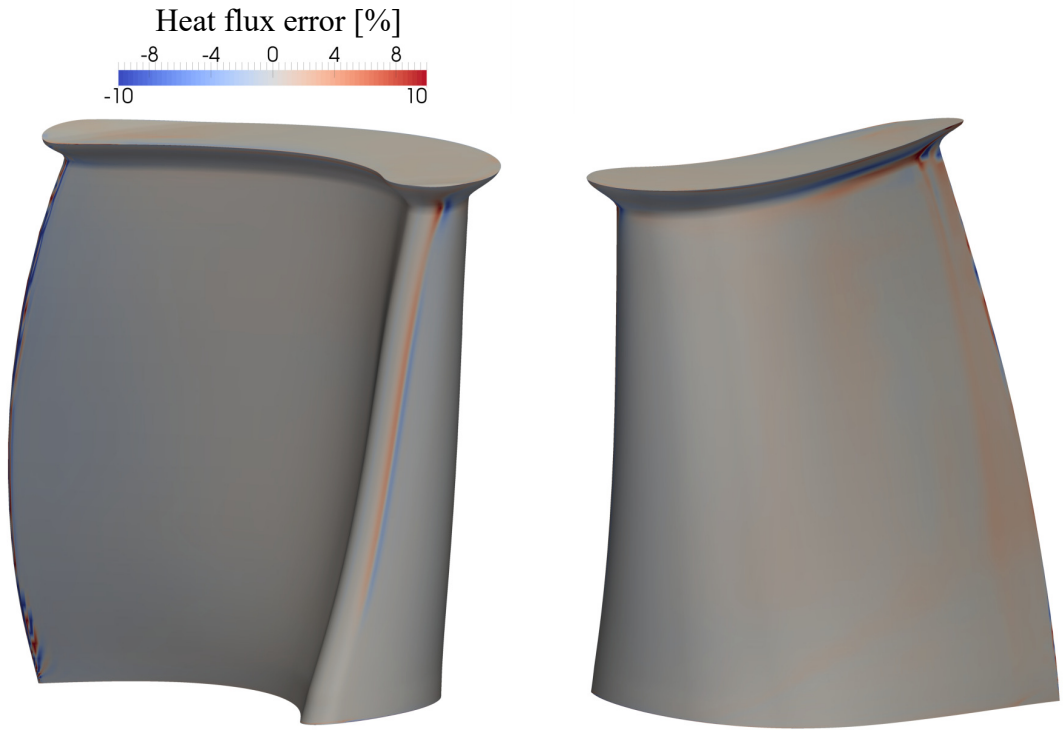

(a) (b)

Figure 4.5: Heat flux error

Integrated heat flux values for the whole blade area and the tip are presented in Table 4.3. The integrated values of both heat flux sources were found to be very similar for both the whole blade and the tip. The accuracy of the integrated value was important from the optimisation point of view, where the integrated, and not the local value of heat flux, was fed into the optimiser. The good agreement of these

	Integrated heat flux - blade [W]	Integrated heat flux - tip [W]
Direct CFD	610.66	126.60
3-temperature model	611.17	126.56
Error [%]	0.08	-0.03

Table 4.3: 3-temperature model error in the case of a winglet tip

values shows that using this process, the heat load was accurately represented as the optimisation objective.

Additionally, considering that using this approach, heat load was represented without introducing the local flow error that only single CFD run with imposed wall temperature would bring (discussed before, study by Zhang and He [26]), it can be concluded that this approach is worth using in the optimisation.

4.3 Investigations on turbine inlet capacity and stage reaction

As explained in Sections 1.1.2.2 and 1.1.2.3, special attention must be paid to the turbine inlet capacity and stage reaction during the design of a turbine rotor blade. If the turbine datum design is altered, as in optimisation, these turbine properties should be kept close to datum values.

In this work, for the performed winglet optimisations, turbine inlet capacity and stage reaction were treated as constraints. Following the approach of Shahpar and Caloni [102], they were allowed to change up to $\pm$ 0.5 % from the datum values.

To understand the changes in inlet capacity and stage reaction, initial studies were carried out on their variations. These included skewing only the stator and only the rotor blade at a time. Blade skew was applied as explained in Section 2.11 and Figure 2.11, in the range of -1° to 1° using 1 design parameter for each blade, controlled at the blade midspan.

4.3.1 Turbine inlet capacity and stage reaction for a datum case

In addition to the datum value, changes in turbine inlet capacity and stage reaction were monitored at 6 additional blade angles for the stator and the rotor blades, respectively. These were positive and negative values of 0.1°, 0.5°, and 1°.

The results of this study are presented in Figure 4.6. The blue line shows the inlet capacity and stage reaction changes when only stator blade skew was applied, and the red line shows the same for only the rotor blade skew. The dotted lines in both figures denote the upper and lower constraint limit, a change of ± 0.5 % from the datum value.

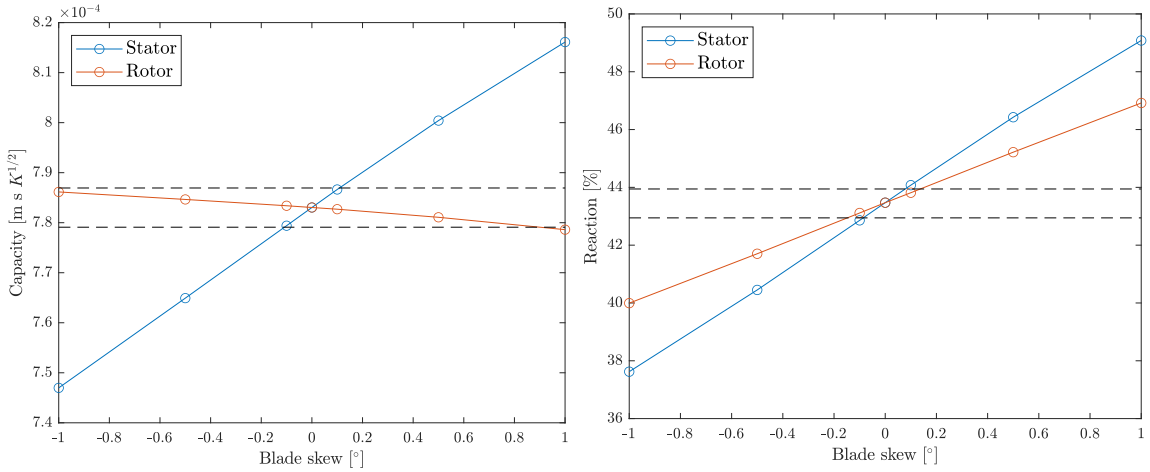

(a) Turbine inlet capacity

(b) Turbine stage reaction

Figure 4.6: Change in the turbine inlet capacity and stage reaction with blade skew

As shown in Figure 4.6a, the turbine inlet capacity significantly changed with the stator blade skew, whereas the rotor blade skew was found to have only a minor effect on it. The reason for this was found to be the fact that the turbine stage in question was choked in the stator domain, and even a small change in stator skew meant a big change in the passage throat area, which affected the turbine mass flow. Applying a stator blade skew larger than around ± 0.1 ° resulted in the turbine inlet capacity violating the constraint limit.

In the case of the rotor blade, the inlet capacity was found to stay within the allowed change limit for almost the whole range of skew angles tested. Only after the rotor skew angle was greater than around 0.8 °, was the inlet capacity found to be too low. Although the rotor blade skew did not change the turbine stage throat area, it did change the velocity distribution in the rotor domain. This led to static pressure changes at the outlet of a stage, which as a result changed the mass flow and, therefore, the turbine inlet capacity.

The turbine stage reaction, shown in Figure 4.6b, was found to change significantly for both stator and rotor blade skew. It was found that the blade skew of around 0.1 ° in either direction changed the stage reaction by more than the allowed value. The

stator blade skew was found to have almost 50 % larger effect on the stage reaction than the rotor blade skew.

4.3.2 Turbine inlet capacity and stage reaction for a blade with winglet tip

A similar study of the blade skew effect on the turbine inlet capacity and stage reaction was done for the case of a full overhang winglet tip shown in Figure 4.7.

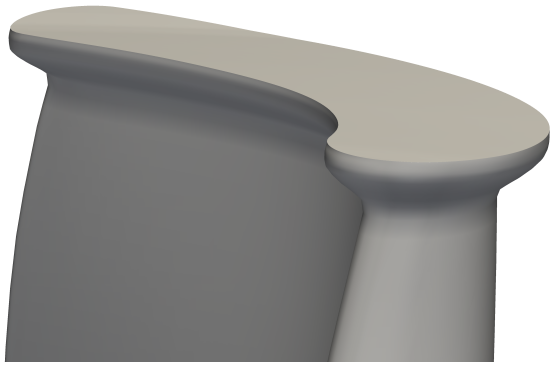

Figure 4.7: Winglet tip for the study of blade skew effect on the turbine inlet capacity and stage reaction

Turbine inlet capacity and stage reaction changes for stator and rotor blade skew are given in Figure 4.8, where dotted lines present the allowed change from the datum values. As shown, the addition of winglet tip changed both the datum inlet capacity and stage reaction, which is visible at the value of 0 ° skew. However, the inlet capacity change was found to be minor and lower, at only 0.16 % from the datum, whereas the stage reaction change was significant and increased by 1.53 %.

Turbine capacity was found to be mostly affected by the stator blade skew, similar to the case of the datum tip. For the rotor blade skew, it was found to be within the allowed change window for all the negative skew angles tested, and for positive skew angles of up to 0.5 °.

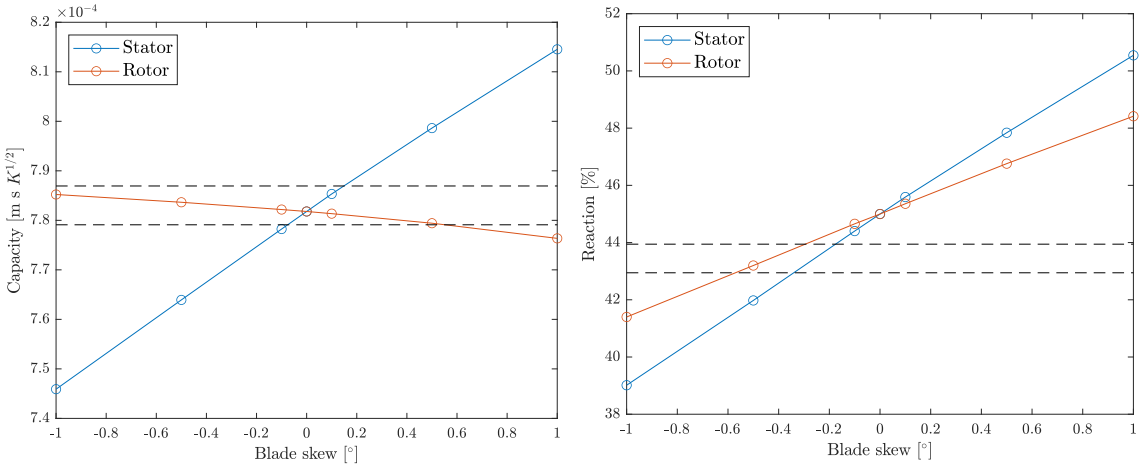

(a) Turbine inlet capacity

(b) Turbine stage reaction

Figure 4.8: Change in turbine inlet capacity and stage reaction with blades skew

Since the turbine stage reaction needed to be decreased to meet the datum value, negative skew angles of the stator and rotor blades were considered. It can be seen that either the stator blade skew of $-0.35\,°$, or the rotor blade skew of $-0.6\,°$, would bring the stage reaction into the allowed change limit. However, if applied, these skew angles would violate the inlet capacity limit for the stator blade case. In the case of the rotor blade, the inlet capacity change requirements would still be met.

Therefore, in this optimisation, to keep the inlet capacity and stage reaction within the allowed change limit, it was decided to use only the rotor blade skew, as it had the ability to correct the stage reaction without violating the inlet capacity constraint.

4.4 Optimisation setup

In this section, the winglet optimisation setup is presented. This includes presenting the values of design parameters and the CFD model used. Since winglet tip optimisation included several separate optimisations performed differently, their optimiser strategies with flowcharts are given in the respective sections.

4.4.1 Design parameters

The winglet tip was parametrised as explained in Section 2.3.1.1 and Figure 2.6 using 17 design parameters. The allowed range for each parameter is given in Table 4.4. These parameter values were the same for all winglet optimisations performed in this work. To account for the changes in inlet capacity and stage reaction, the constrained winglet optimisations also had a single rotor blade skew parameter. Following the

Parameter	Minimum value	Maximum value
PS location, b_{PS} [% of edge length]	20	80
SS location, b_{SS} [% of edge length]	20	80
Overhangs: $o_{LE}, o_{PS}, o_{SS}, o_{TE\ PS}, o_{TE\ SS}$ [C_{ax}]	0	0.1
Straight lengths: $d_{LE}, d_{PS}, d_{SS}, d_{TE\ PS}, d_{TE\ SS}$ [C_{ax}]	0	0.05
Blending angles: $\beta_{LE}, \beta_{PS}, \beta_{SS}, \beta_{TE\ PS}, \beta_{TE\ SS}$ [°]	10	80
Rotor blade skew, ψ_r [°]	-1	1

Table 4.4: Winglet tip optimisation design parameters

findings given in Section 4.3.2, the allowed change was between -1° and 1° of the blade skew. Therefore, the constrained (inlet capacity and stage reaction) winglet optimisation had 18 design parameters, 17 for winglet tip and 1 for rotor blade skew.

4.4.2 CFD model

4.4.2.1 Mesh

Since winglet optimisation was later extended to aerothermal optimisation, and since the aerodynamically optimised winglet tip was later compared with aerothermally optimised tips, the same mesh was used for all winglet optimisations. The mesh used was aerothermally verified in Section 4.1. For both the stator and rotor domains, a structured O-H mesh was generated using PADRAM and is presented in Figure 4.9.

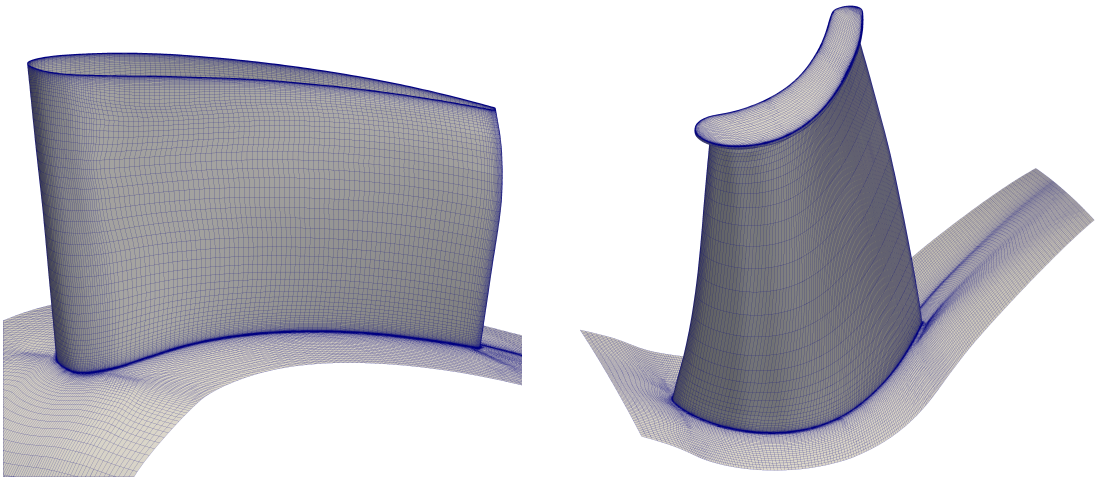

(a) Leading edge (b) Trailing edge

Figure 4.9: Turbine stage mesh for winglet optimisations

The overall size of the rotor mesh was around 6.2 million cells, and the stator mesh size was about 2 million cells. The tip gap mesh used in this optimisation had 60 radial mesh points, and its leading and trailing edge details are presented in Figure 4.10. The tip gap O-mesh block had 30 points across the blade tip, and the tip H-mesh block had 40 points across the blade tip.

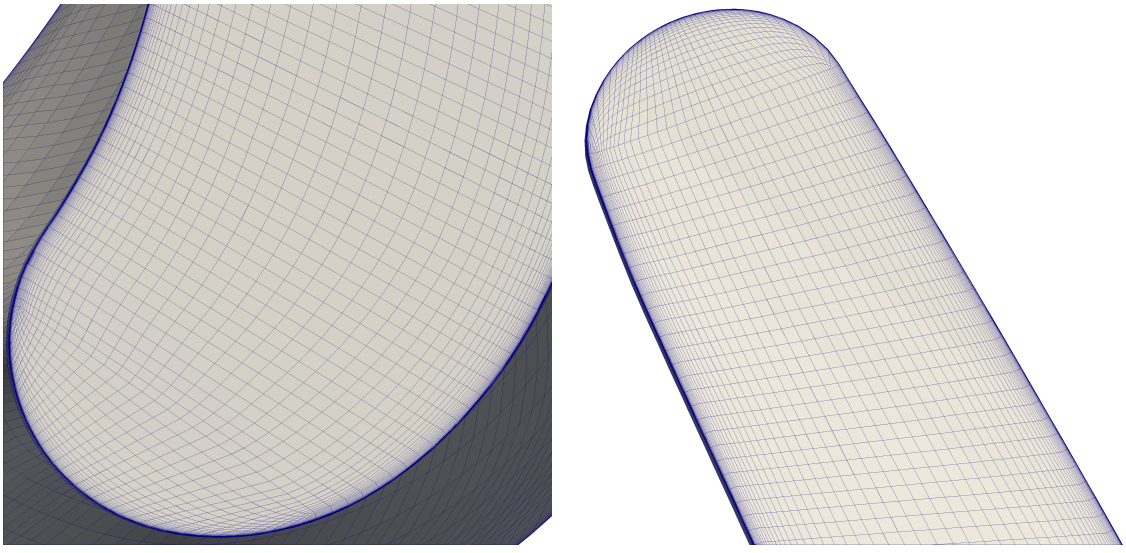

(a) Leading edge (b) Trailing edge

Figure 4.10: Tip gap mesh detail

To ensure good resolution of the boundary layer, especially in the aerothermal simulations, special attention was paid to the y+ value. The mesh used in these

optimisations had a boundary layer mesh expansion ratio of 1.2, and for most of the blade surface, the y+ value was below 1. This is shown in Figure 4.11.

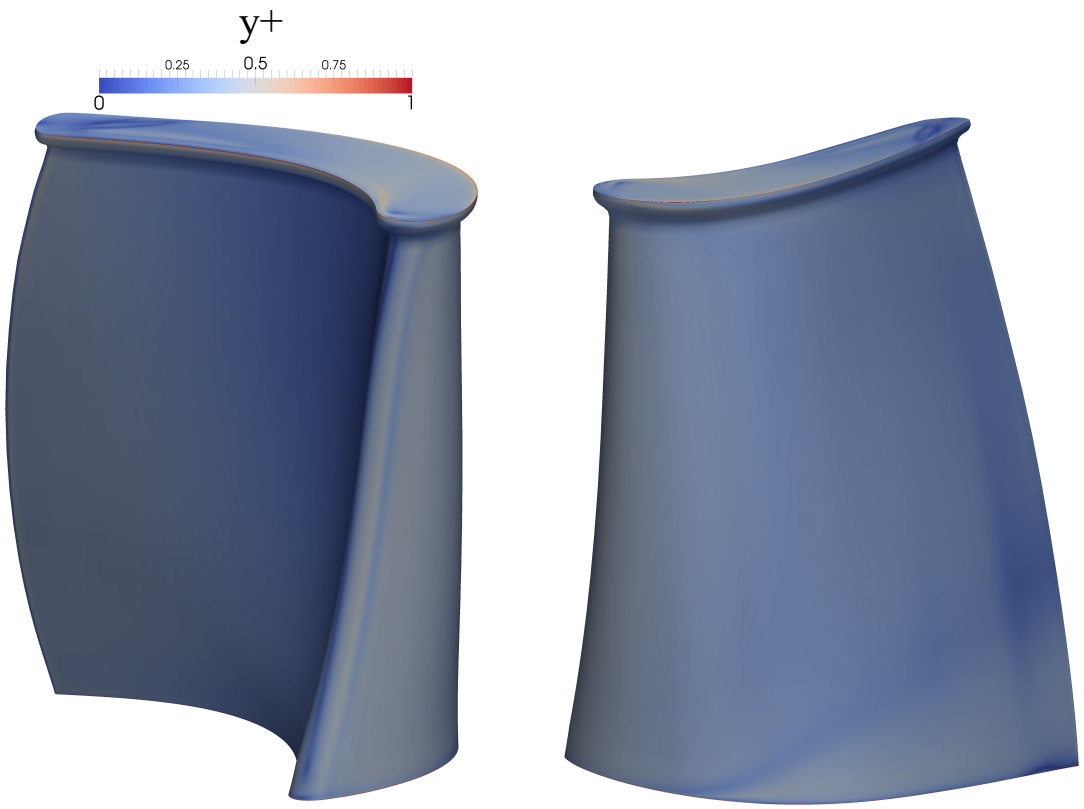

(a) Pressure side

(b) Suction side

Figure 4.11: y+ values on rotor blade with winglet tip for PADRAM aerothermal mesh

4.4.2.2 Boundary conditions and turbulence model

Boundary conditions used in this optimisation are presented in Table 4.5. Values of temperatures and pressures imposed at inlet and outlet boundaries correspond to MT1 turbine experimental values given in Table 3.1. Mixing plane was used at the stator-rotor interface. For turbulence modelling, k-ω SST turbulence model was used.

4.5 Aerodynamic optimisation

Aerodynamic optimisation was performed first, without any constraints. In the following sections, the optimisation strategy is given, and the results of the optimisation are presented, along with the method for the additional correction of inlet capacity and stage reaction. Finally, the optimum design is presented.

Boundary	Condition
Stator inlet	$p_0,\ T_0$
Stator outlet	mixing plane
Rotor inlet	mixing plane
Rotor outlet	p_{st}
Hubs, casings, blades	No-slip adiabatic walls

Table 4.5: MT1 turbine operating point

4.5.1 Optimiser

For this optimisation, the multipoint approximation method (MAM) was used as the optimiser. The optimisation problem was defined as explained in Section 2.3.3.1, and the isentropic turbine stage efficiency was used as the objective function $f_i(x)$. It was calculated as described in Section 3.1.1. The flowchart of this optimisation is given in Figure 4.12.

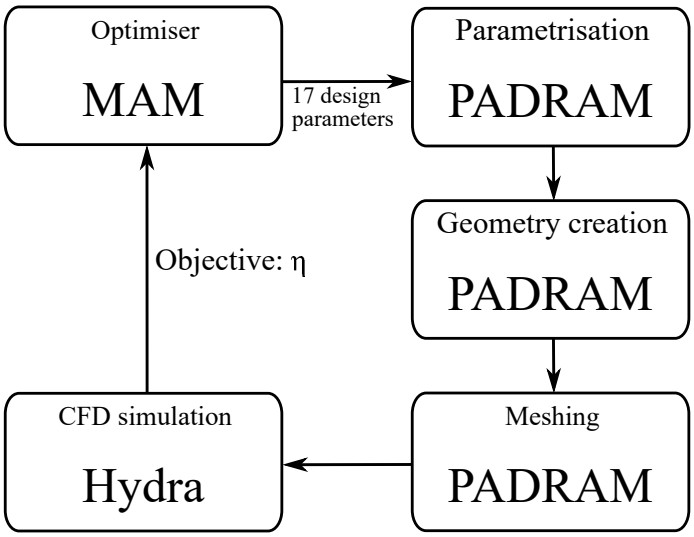

Figure 4.12: Aerodynamic winglet tip optimisation flowchart

The design parameters used for the optimisation are given in Table 4.4 with their minimum and maximum allowed values. As this optimisation is unconstrained, rotor blade skew was not used, resulting in 17 design parameters in total. The optimisation was run with MAM having 40 design points in each of the sub-regions.

4.5.2 Results

The aerodynamic winglet tip optimisation was initialised with a design having all design parameters halfway in the allowed change range, presented in Table 4.4. It was run for five MAM sub-regions in total (initial+4), until the aerodynamic efficiency converged. This resulted in 197 designs with efficiency not changing through the last 40 designs (last MAM sub-region) for not more than 0.1 %. This is shown in Figure 4.13. The reason why some designs are missing is due to the failure in the automatic design process and were excluded from the MAM sampling.

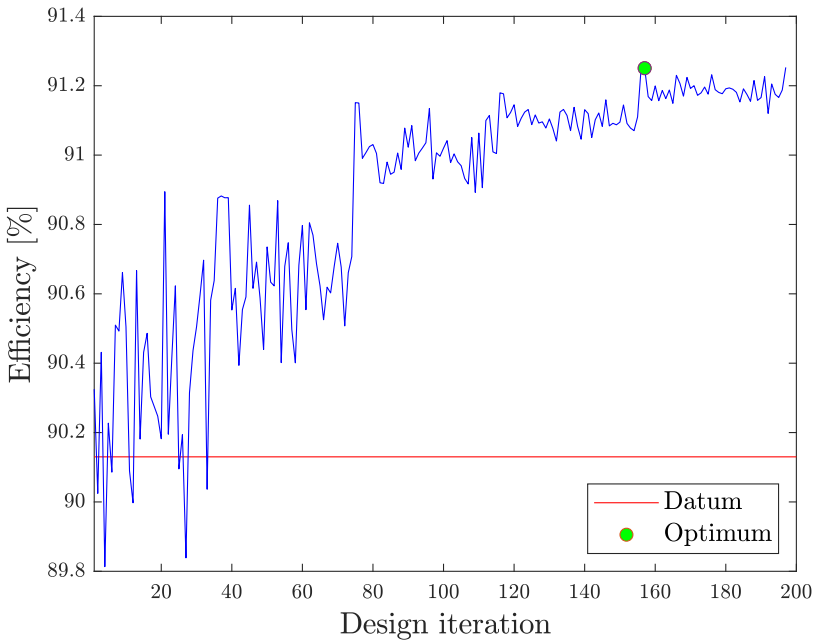

Figure 4.13: Aerodynamic winglet optimisation convergence

Figure 4.13 shows that almost all tested winglet designs had a higher efficiency than the datum tip. Some designs with lower efficiency than the datum were tested in the early stage of the optimisation and were quickly discarded by the optimiser. These designs were found to be winglet tips with very small blending angle values that created a very thick and inefficient winglet tip. The properties of a design with the optimum winglet tip are presented in Table 4.6.

Since inlet capacity and the stage reaction were not constrained in this optimisation, the stage reaction of the optimum design was found to violate the allowed change design condition, as it was found to be 1.72 % higher than the datum tip. It had to be brought down. For that, a study of the change in inlet capacity and stage reaction for the stator and rotor blade skew was carried out. This is presented in the following section.

Property	Change from the datum [%]
Efficiency	1.13
Inlet capacity	-0.13
Stage reaction	1.72

Table 4.6: Turbine properties of the aerodynamic optimum winglet tip

4.5.3 Correction of inlet capacity and stage reaction for optimum design

The first step in the correction of inlet capacity and the stage reaction was to analyse their changes with the stator and rotor blade skew. This has been done as presented in Figure 4.14.

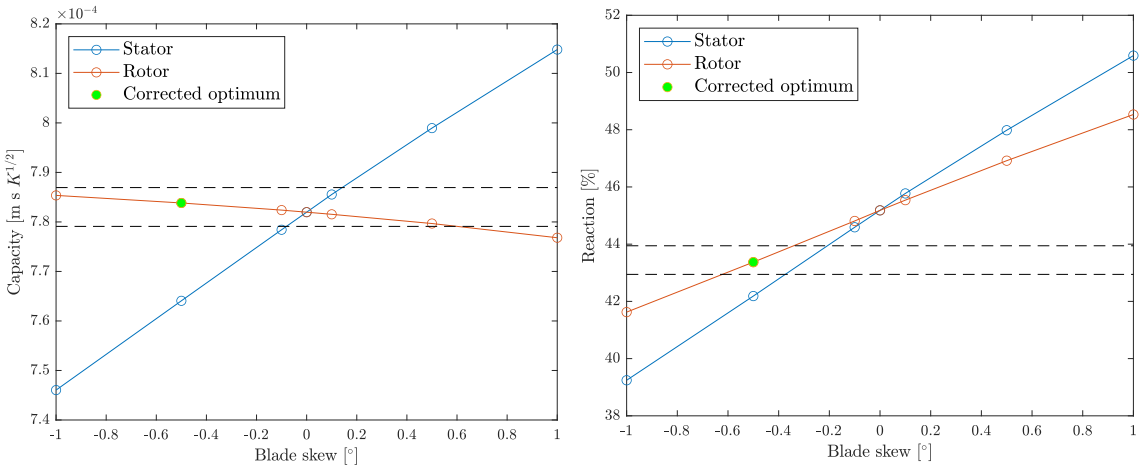

(a) Turbine inlet capacity

(b) Turbine stage reaction

Figure 4.14: Change in turbine inlet capacity and stage reaction with blades skew

As shown in Figure 4.14, the turbine inlet capacity of the optimum design was only slightly changed from the datum value and did not need correcting. However, the turbine stage reaction needed to be considerably lowered, and negative stator and rotor blade skew values were needed for that purpose, as illustrated in Figure 4.14b. Since negative stator blade skew would considerably decrease the inlet capacity, negative rotor blade skew was chosen instead. As seen from Figure 4.14b, a negative rotor blade skew of $-0.5\,^\circ$ would bring the stage reaction within the allowed change window without altering the inlet capacity too much, as presented in Figure 4.14a. This design change is represented by the green dot in Figure 4.14.

Property	Change from the datum [%]
Efficiency	1.04
Inlet capacity	0.10
Stage reaction	-0.09

Table 4.7: Turbine properties of the unconstrained - additionally corrected aerodynamic optimum winglet tip

Parameter	Applied value
PS location, b_{PS} [% of edge length]	59
SS location, b_{SS} [% of edge length]	72
Overhangs: $o_{LE}, o_{PS}, o_{SS}, o_{TE\ PS}, o_{TE\ SS}$ [C_{ax}]	0.1, 0.017, 0.1, 0.1, 0.001
Straight lengths: $d_{LE}, d_{PS}, d_{SS}, d_{TE\ PS}, d_{TE\ SS}$ [C_{ax}]	0.001, 0, 0, 0, 0.0014
Blending angles: $\beta_{LE}, \beta_{PS}, \beta_{SS}, \beta_{TE\ PS}, \beta_{TE\ SS}$ [°]	78, 34, 62, 74, 58

Table 4.8: Aerodynamically optimised winglet tip design parameters

The properties of the additionally corrected winglet tip are provided in Table 4.7. It can be observed that after the correction, both the inlet capacity and the stage reaction were only slightly different from the datum and well within the allowed change window, varying by no more than 0.1 %. However, lowering the stage reaction from the change from the datum of 1.72 % to −0.09 % caused a minor decrease in efficiency of 0.09 %.

4.5.4 Analysis of the optimum design

The optimum winglet tip is presented in Figure 4.15, and its parameter values are summarised in Table 4.8. To illustrate the values of winglet overhangs, the winglet tip outline is shown in black alongside the datum tip outline in red. Three tip cross sections are presented to show the straight lengths and blending angles applied, labelled A-A at the leading edge region, B-B around the tip center, and C-C at the trailing edge region.

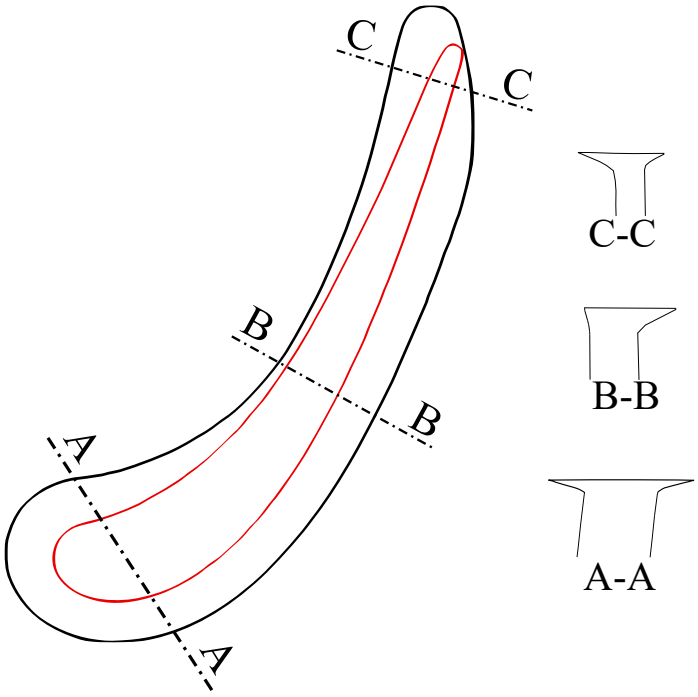

Figure 4.15: Aerodynamically optimised winglet tip

As shown in Figure 4.15 and Table 4.8, large overhangs have been applied at the leading edge region, blade suction side, and at the pressure side of the trailing edge. At these locations, the maximum allowed values of overhangs were applied. At the blade pressure side, a small overhang was applied, with a value of just 17 % of the maximum allowed. No overhang was applied at the suction side of the trailing edge. As shown in the three tip cross sections, straight lengths applied to all overhangs were negligible, resulting in sharp winglet tips. Blending angles applied were small, on the lower side of the allowed range. However, in the leading edge region (cross section A-A), blending angles were smaller than in the downstream tip sections B-B and C-C.

This result is somewhat contrary to the findings of Coull et al. [38], who performed a parametric study on winglet tips and found that winglets with maximum leading edge, pressure, and suction side overhangs had the highest efficiency. However, they did not perform an optimisation, and overhangs at the trailing edge were not part of the parametric study. Nevertheless, the benefits of large leading edge and suction side overhangs were confirmed by other researchers [35, 103].

4.6 Aerodynamic optimisation with constraints

This optimisation had the same setup as the optimisation in Section 4.5, except that turbine inlet capacity and stage reaction constraints were included, along with one extra design parameter. Each constraint was allowed to change up to $\pm$ 0.5 % from the datum value. The extra parameter was the rotor blade skew, which was allowed to change between $-1\,^\circ$ and $1\,^\circ$.

4.6.1 Optimiser

For this optimisation, as in the case of an unconstrained optimisation, the multipoint approximation method was used. The constraints function $g_i(x)$ included turbine inlet capacity (Φ) and stage reaction (Λ), which were calculated as given in Sections 3.1.3 and 3.1.3. The number of design parameters was increased by one compared to the unconstrained optimisation, including the rotor blade skew for controlling the inlet capacity and stage reaction. Overall, the optimisation had 18 design parameters, presented in Table 4.4. The optimisation flowchart is presented in Figure 4.16. The optimisation was run with the MAM, using 42 design points in each of the sub-regions.

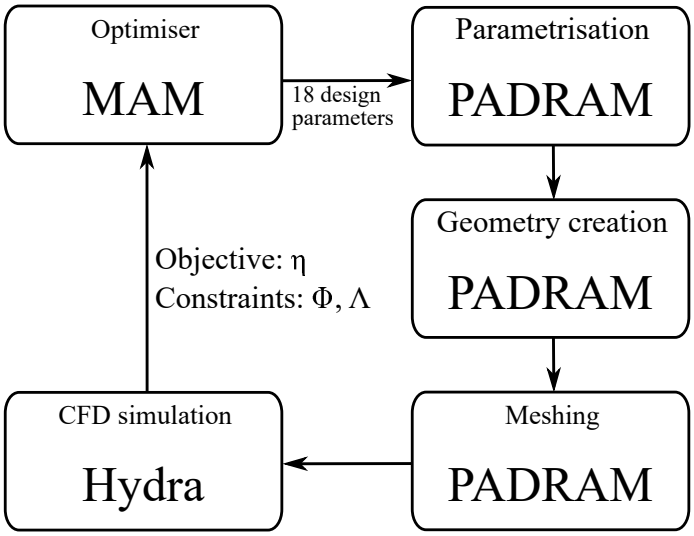

Figure 4.16: Aerodynamic winglet tip optimisation with constraints flowchart

4.6.2 Results

This optimisation took 5 MAM sub-regions to converge. Its results are presented in Figure 4.17. The inlet capacity and stage reaction constraints are presented alongside

the efficiency change for all designs, and the efficiency is also presented separately for successfully constrained designs only.

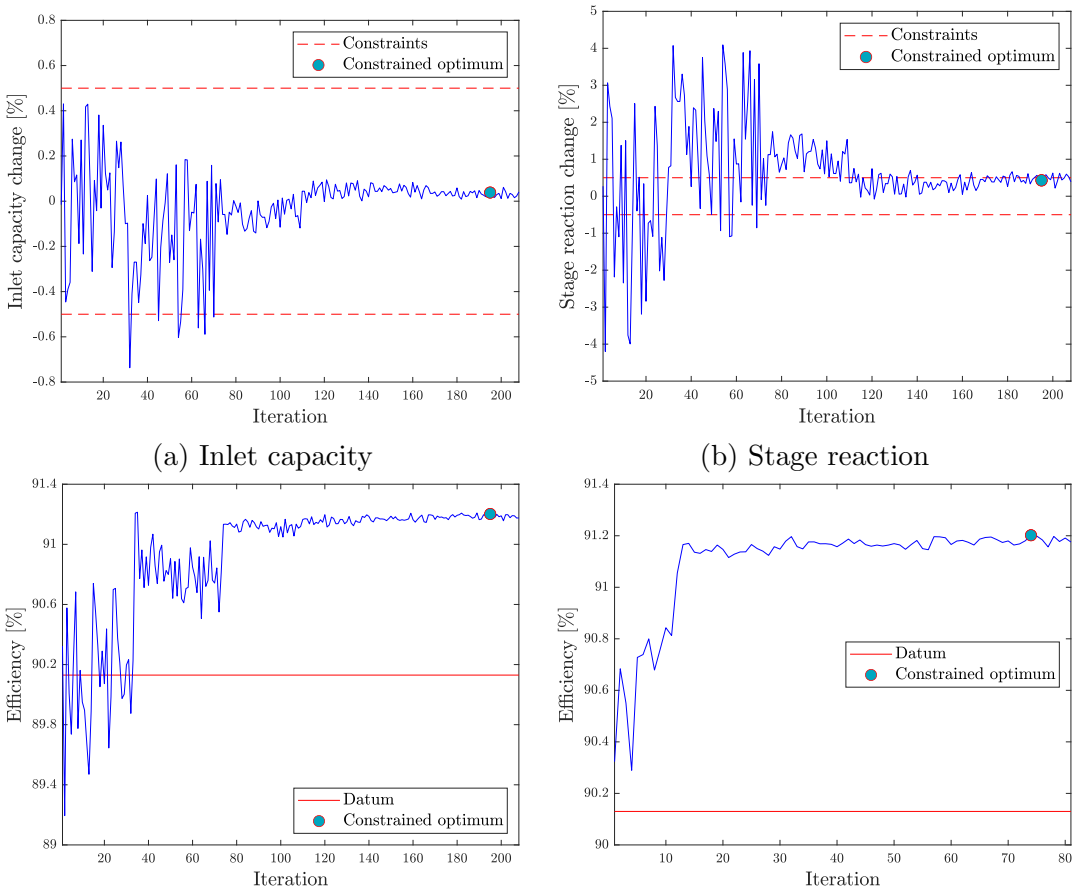

(a) Inlet capacity

(b) Stage reaction

(c) Efficiency

(d) Successfully constrained efficiency

Figure 4.17: Constrained aerodynamic optimisation turbine properties change

Figure 4.17a shows the inlet capacity change during the optimisation. It can be seen that very few designs violated the inlet capacity constraint during the optimisation. Those designs were found to be characterised by very thick tips caused by small blending angles and large straight lengths. Because of their thick tips, they lowered the rotor throat area below the stator value, which, as a result, decreased the inlet capacity below the allowed value. After approximately 70 design iterations, the inlet capacity was constrained to only near-datum values and did not change too much in the second half of the optimisation.

Stage reaction change during the optimisation is presented in Figure 4.17b. It took around 110 design iterations to converge towards the allowed change value. It is interesting to note that the stage reaction was always kept near the upper constraint

Property	Change from the datum [%]
Efficiency	1.07
Inlet capacity	0.04
Stage reaction	0.43

Table 4.9: Turbine properties of the constrained aerodynamic optimum winglet tip

Parameter	Applied value
PS location, b_{PS} [% of edge length]	66
SS location, b_{SS} [% of edge length]	47
Overhangs: $o_{LE}, o_{PS}, o_{SS}, o_{TE\ PS}, o_{TE\ SS}$ [C_{ax}]	0.1, 0.037, 0.1, 0.1, 0.001
Straight lengths: $d_{LE}, d_{PS}, d_{SS}, d_{TE\ PS}, d_{TE\ SS}$ [C_{ax}]	0, 0, 0, 0.0025, 0
Blending angles: $\beta_{LE}, \beta_{PS}, \beta_{SS}, \beta_{TE\ PS}, \beta_{TE\ SS}$ [°]	80, 71, 65, 53, 28

Table 4.10: Successfully converged and aerodynamically optimised winglet tip design parameters

limit. The reason for that was found to be that higher stage reaction led to higher efficiency, as explained in Equations 3.1 and 3.5.

Efficiency for all design iterations is presented in Figure 4.17c. It can be seen that, similar to the case of unconstrained optimisation, most designs had higher efficiency than the datum. After approximately 70 designs, efficiency reached convergence, and most of the changes were a result of different rotor blade skew values to constrain the stage reaction.

Efficiency of all the designs that met the constraint requirements is presented in Figure 4.17d. From 208 design iterations, 82 were successfully constrained, mostly in the second part of the optimisation.

Turbine properties of the most efficient optimum design that met the constraint requirements are presented in Table 4.9. The successfully constrained optimum design had an efficiency increase of 1.07 % over the datum with the inlet capacity and stage reaction change of 0.04 % and 0.43 %, respectively.

Successfully converged optimum winglet tip is presented in Figure 4.18. Its design parameters are listed in Table 4.10. It features a similar winglet tip outline as

the unconstrained optimum presented in Figure 4.15, with some differences. It has maximum overhangs at the leading edge, suction side, and pressure side of the trailing edge, same as the unconstrained optimum. Some differences can be seen on the pressure side overhang, which was, in the case of a constrained optimum, 37 % of the maximum allowed value. Another difference between the two winglets can be seen on the suction side where the suction side control point location is in this case around halfway between the leading and trailing edge, resulting in a smoother aft suction side overhang as it disappears at the trailing edge. In the case of an unconstrained optimum, the control point was moved more downstream, creating a high turning effect of the tip's trailing edge. Blending angles applied were similar for both cases, where the highest angles were found in the leading edge region and were slightly decreased further down. The rotor blade skew angle applied in the case of a constrained optimum was $-0.67\,°$.

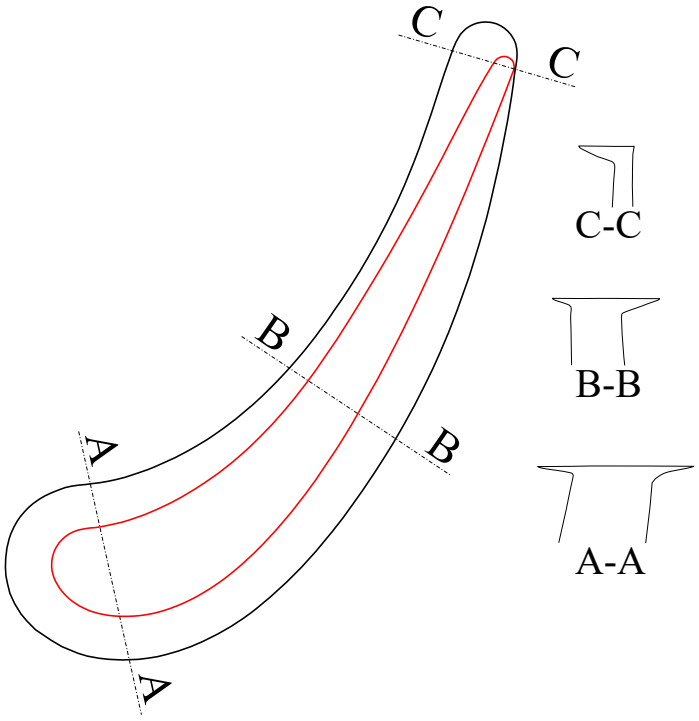

Figure 4.18: Successfully converged and aerodynamically optimised winglet tip

Two winglets are shown with their overhangs overlapping for easier comparison in Figure 4.19. As presented, both winglets had very similar leading edge region overhangs. Regarding the pressure side, the constrained optimum winglet, shown in red, had a bigger overhang at the second half of the pressure side. Although in the case of an unconstrained optimum, the pressure side overhang value was lower, because

of different placement of the pressure side control point, early pressure side had a greater overhang created at the first half of the blade. At the blade suction side, the unconstrained winglet featured a slightly larger winglet overhang, especially before the trailing edge region where overhangs in both cases were not applied. Overall, in the suction side region, both winglets had similar tip widths, achieved through slightly different parameters values.

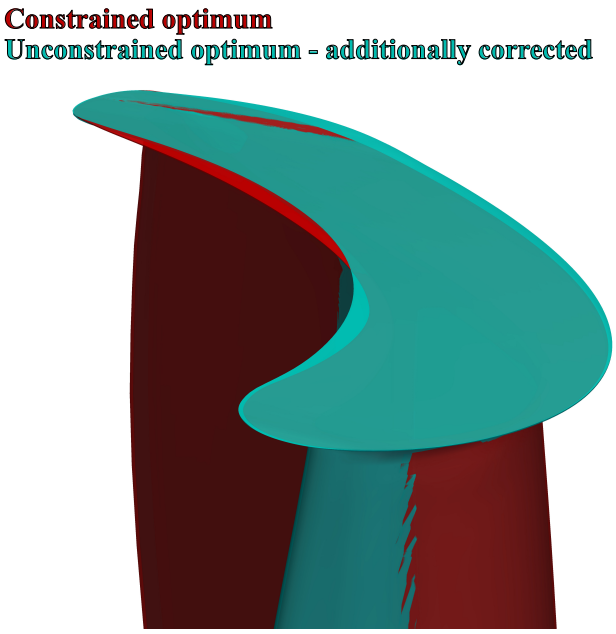

Figure 4.19: Comparison of the constrained and unconstrained - additionally corrected optimum winglet tips

To quantify the effect of different winglets on the flow, static pressure around the winglet tip edges for both winglets is shown in Figure 4.20. In the leading edge region, as both winglets had very similar designs, static pressure differences were negligible up to 0.3 of the axial chord. After this point, in the first half of the pressure side, the constrained optimum featured a smaller overhang resulting in lower static pressure compared to the unconstrained optimum. In the second half of the pressure side, the constrained optimum featured a larger overhang, resulting in increased pressure over the unconstrained optimum. Regarding the suction side, the unconstrained optimum had a slightly larger overhang, resulting in higher static pressure up until 0.8 of the axial chord, where both pressures stayed almost constant until the trailing edge, with the constrained optimum's static pressure being slightly higher.

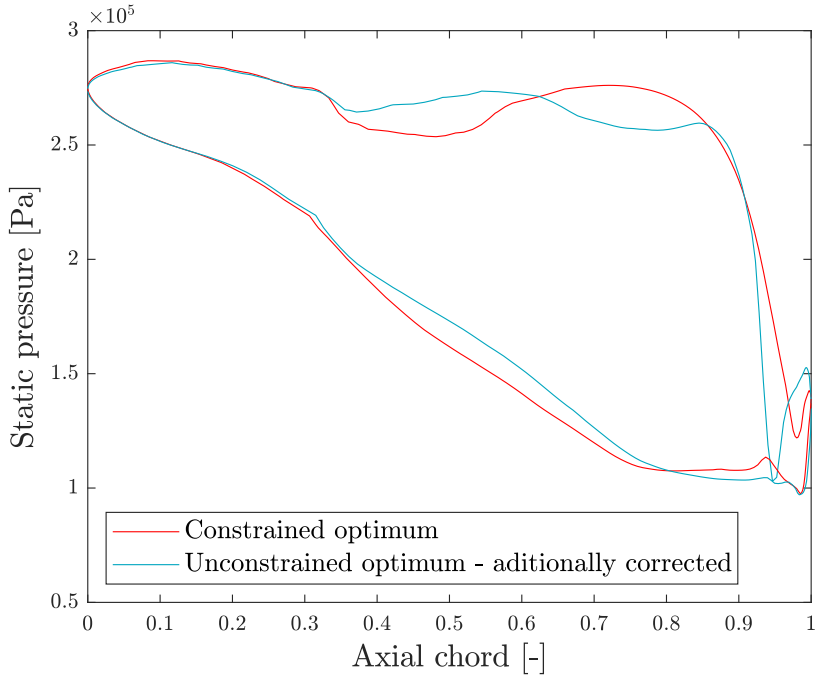

Figure 4.20: Pressure distribution around the constrained and unconstrained - additionally corrected optimum winglet tips

4.6.3 Analysis of the optimum design

In this section, the constrained optimum winglet tip and its flow properties are analysed and compared with the datum tip to quantify the efficiency benefit.

Figure 4.21 presents the static pressure distribution around the constrained optimum winglet and the datum tips. It can be seen that, when compared with the datum, almost the whole winglet tip is in the region of higher pressure. Starting from the leading edge, because of large overhangs, the whole winglet leading edge area had considerably higher pressure than the datum. This is particularly noticeable for the winglet suction side, which was higher than the datum for almost 1×10^5 Pa, resulting in a far lower pressure difference across the tip. Pressure on the winglet tip pressure side was higher than the datum for the whole length of the pressure side, except at the mid-axial chord. At mid-axial chord, winglet overhang was the smallest and almost negligible, causing the pressure side pressure to drop to a datum value. Further down, because of the large overhang at the pressure side of the trailing edge, pressure around the winglet tip was again considerably higher than the datum. Pressure at the suction side was also higher for the winglet tip case, with some exceptions close to the trailing edge. Because of the big suction side overhang, the pressure difference

between the winglet and the datum tips was greater at the suction side rather than at the pressure side, especially at the front part of the tip.

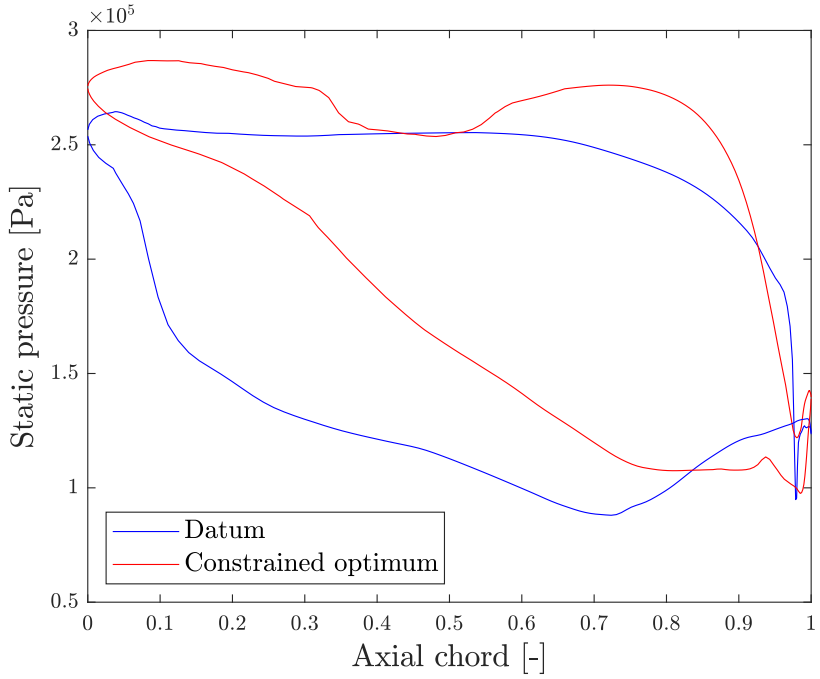

Figure 4.21: Pressure distribution around datum and constrained optimum winglet tip

As shown in Figure 4.21, in the region around 0.7 of the axial chord, static pressure at the datum tip suction side had a noticeable dip, which was not the case for the winglet tip. The reason for this was found in the over tip leakage vortex that rubbed the datum blade suction side, causing a region of very low static pressure. This is shown in Figure 4.22, where the suction side static pressure is given for the datum and optimised winglet blades. It can be seen that around the middle of the datum blade suction side, which corresponded to the region between 0.5 and 0.8 of the axial chord, there was a region of low static pressure. This region did not stretch all the way to the datum because as the blade turns, the tip leakage vortex detached from the blade surface, which caused the static pressure to rise towards the trailing edge.

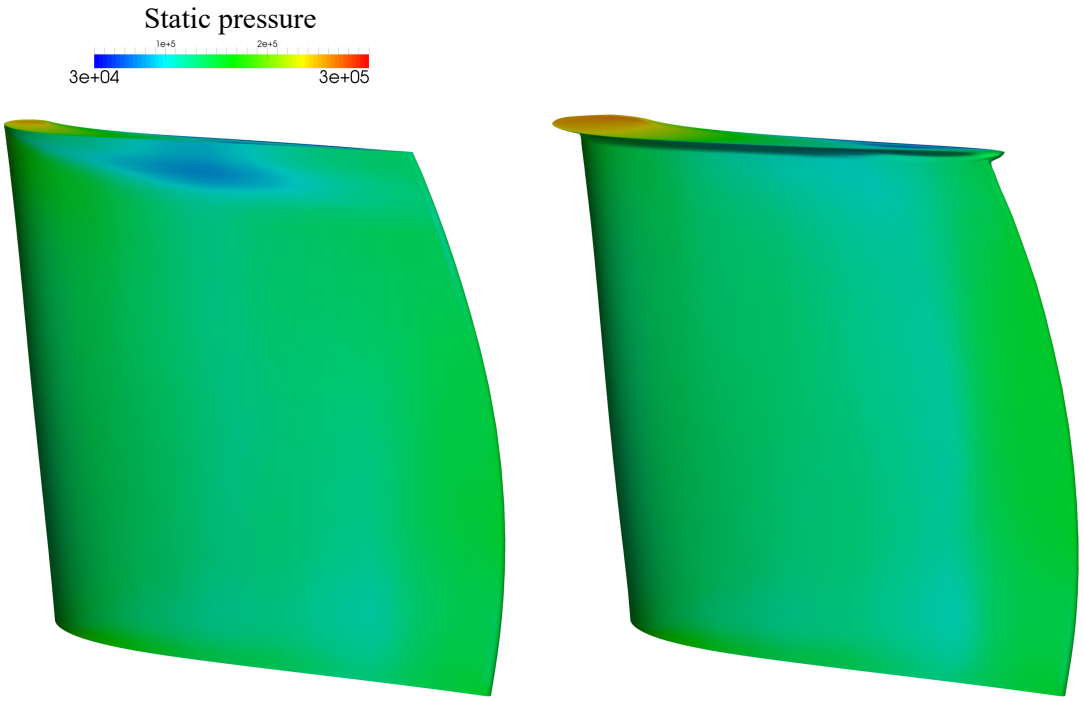

(a) Datum (b) Constrained optimum

Figure 4.22: Static pressure at blade suction side

The over tip leakage vortex is shown for both the datum and optimised winglet tips in Figure 4.23. Due to the large overhang on the winglet suction side, the over tip leakage vortex was pushed away from the blade and into the region of higher pressure. This had several benefits. Firstly, the over tip leakage vortex did not decrease the static pressure at the blade suction side as it had in the case of the datum, resulting in a lower pressure difference across the tip and ultimately less leakage flow. Secondly, since the vortical flow was characterised by large shearing losses, injecting it into the region of higher pressure decreased the mixing-driving pressure gradients and ultimately resulted in fewer shearing losses.

Another feature of winglet tips observed in Figure 4.23 was the absence of the passage vortex. The passage vortex formed in the case of the datum as the fluid passed around the blade and was pushed under the over tip leakage vortex by the leakage flow. These two vortices counter-rotated, causing a detrimental shearing effect. In the case of a winglet tip, the over tip leakage vortex and passage vortex merged together, leading to a more favourable mixing process.

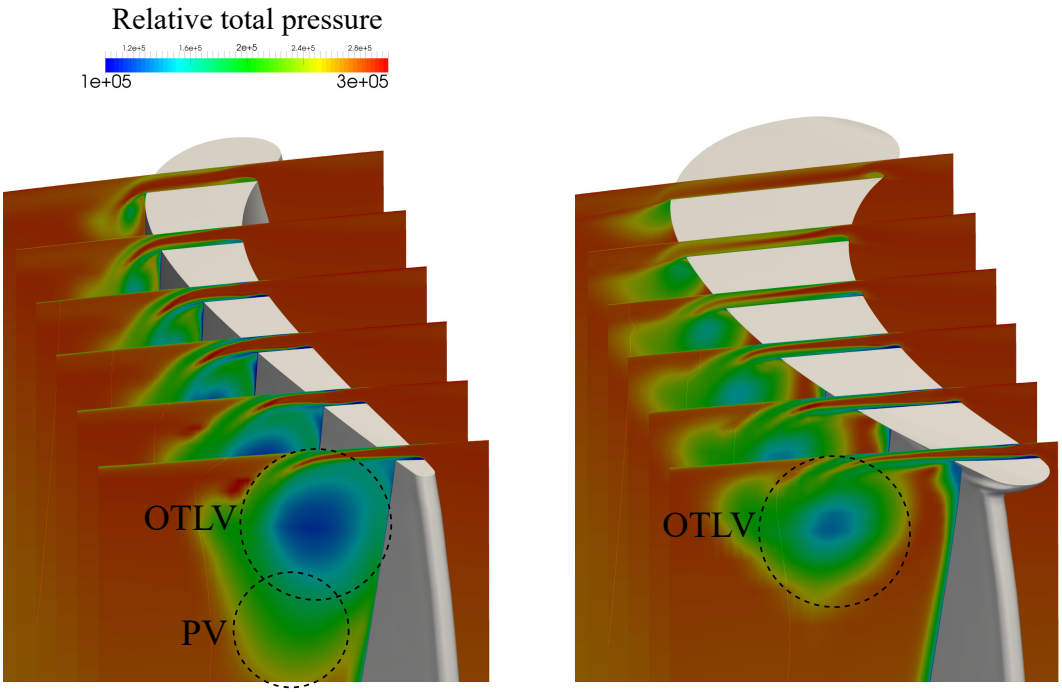

(a) Datum (b) Constrained optimum

Figure 4.23: Over tip leakage vortex

To quantify the effect of the over tip leakage flow on flow shearing losses, the circumferentially averaged entropy at 0.5 of the axial chord downstream of the trailing edge is shown in Figure 4.24.

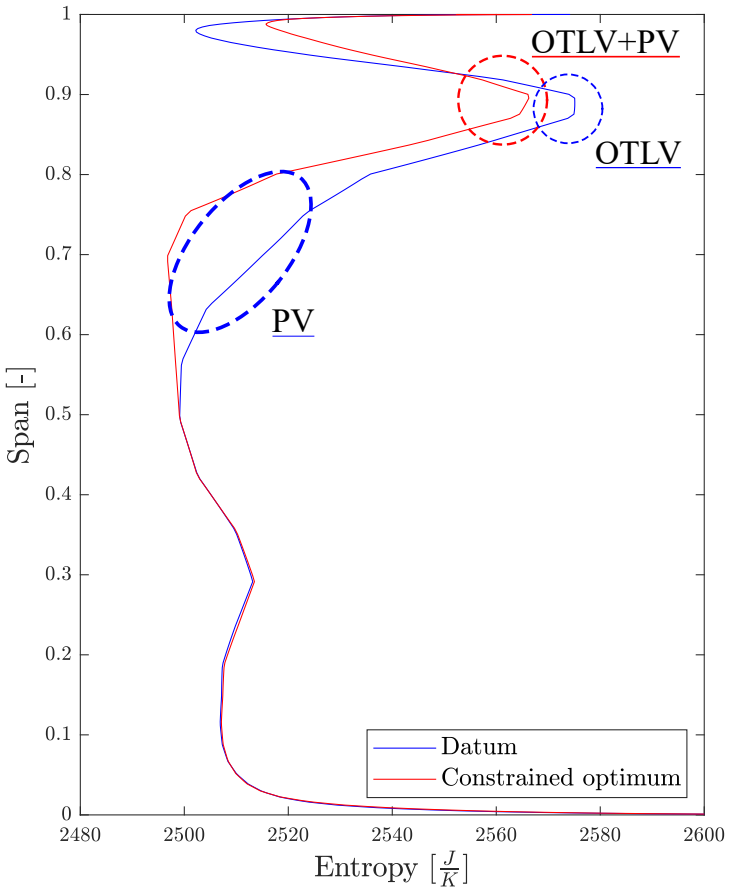

Figure 4.24: Circumferentially averaged entropy field at 0.5 C_{ax} downstream of the trailing edge

Starting from the casing (span=1), it can be seen that the constrained optimum winglet had a higher entropy production than the datum blade in the region above 0.95 of the span. This was due to the flow crossing the wider winglet tip, resulting in larger boundary layer losses. Below 0.95 of the span, the entropy began to decrease for the winglet tip, and two regions were identified. The region between 0.8 and 0.9 of the span was affected by the over tip leakage vortex, which was, as explained in Figure 4.23, lower for the winglet tip. This is also visible here as lower entropy production in the case of the winglet tip. Additionally, below 0.8 of the span, the absence of passage vortex in the case of the winglet tip is clearly visible, which again favourably resulted in the winglet tip's entropy production. Below midspan, the flow was unaffected by the addition of the winglet tip, and the entropy was the same for both cases.

To analyse how the increased static pressure around the winglet tip affected the leakage mass flow, the tip leakage mass flow was measured at the tip suction side and compared against the datum. For that, a tip suction side surface was created as shown in Figure 4.25. The surface covered the suction side distance from the leading to the trailing edge, and the mass flow was interpolated along the tip edge. The surface length was normalised against the x-axis. Similar surfaces were created for other analysed tips, always stretching between the leading and trailing edges and normalised against the x-axis.

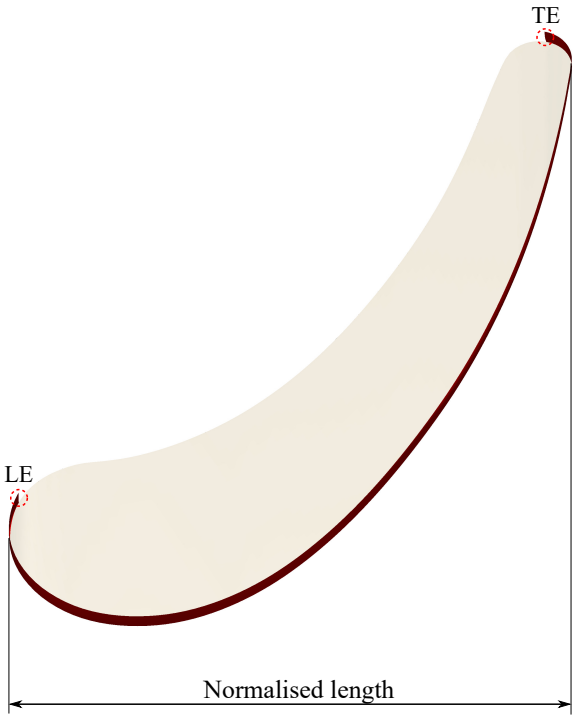

Figure 4.25: Suction side surface for measuring the tip leakage mass flow

Tip leakage mass flow distribution measured at the blade suction side is shown in Figure 4.26 for the datum and optimum constrained winglet tips. Positive mass flow indicates flow entering the tip gap area, and negative mass flow indicates flow leaving the tip gap area.

As shown, in the whole leading edge region, up to around 0.15 of the suction side surface length, mass flow was entering the tip gap area for the case of the winglet, whereas for the case of the datum tip, that was only the case until 0.05 of the suction side surface length. Ingestion of the flow in the whole leading edge region was found to be a common feature of winglets with large leading edge overhangs, matching the findings from Coull et al. [38]. After the mass flow became negative, which meant

leaving the tip gap, the amount of mass flow leaving the tip gap for the datum tip increased at a much higher rate than for the case of the winglet. That pointed to a good sealing effect of the winglet tip in the first half of the tip, caused by the small static pressure difference, previously shown in Figure 4.21.

The mass flow of the datum tip was found to drop at a high rate until around 0.3 of the suction side surface, after which it stayed roughly constant. In the case of the winglet tip, it fell almost linearly until 0.75 of the surface length. As the winglet tip had the highest pressure difference across the tip after 0.75 of surface length, tip leakage mass flow in that region was the highest, and most of the flow that left the tip gap did so at the late suction side. This was not the case for the datum tip, where the maximum amount of leakage flow was reached around 0.7 of the suction side surface length. At that point, the static pressure was found to be the lowest, affected by the strong over tip leakage vortex. Overall, the amount of leakage flow for the winglet tip was found to be almost half of that for the datum, lower by 51.6 %.

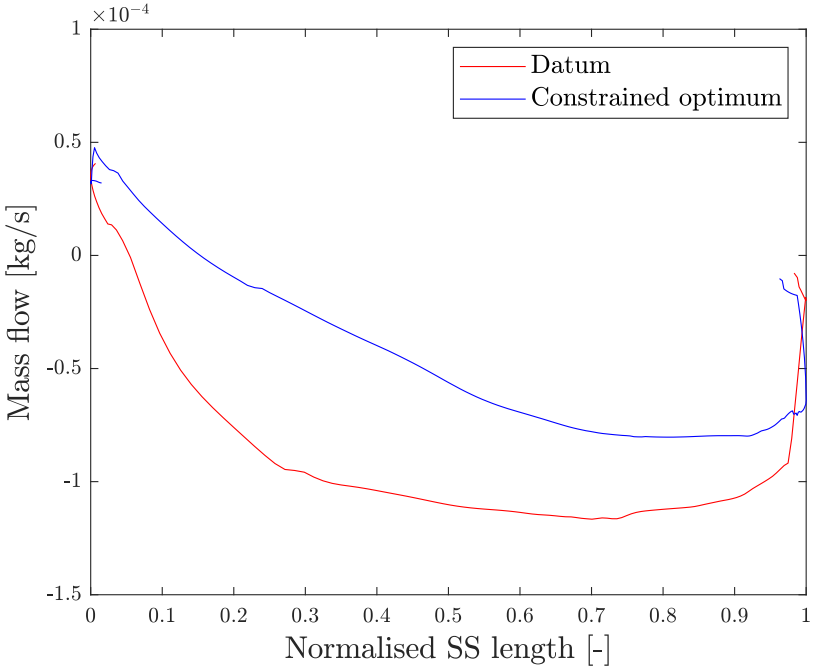

Figure 4.26: Suction side tip leakage mass flow comparison

Since the optimum design did not result in the winglet tip with overhangs of the maximum allowed value, to understand the effect of decreasing the overhang on the pressure side and the suction side of the trailing edge, these designs were created by hand and examined in more detail. These designs are shown in Figure 4.27.

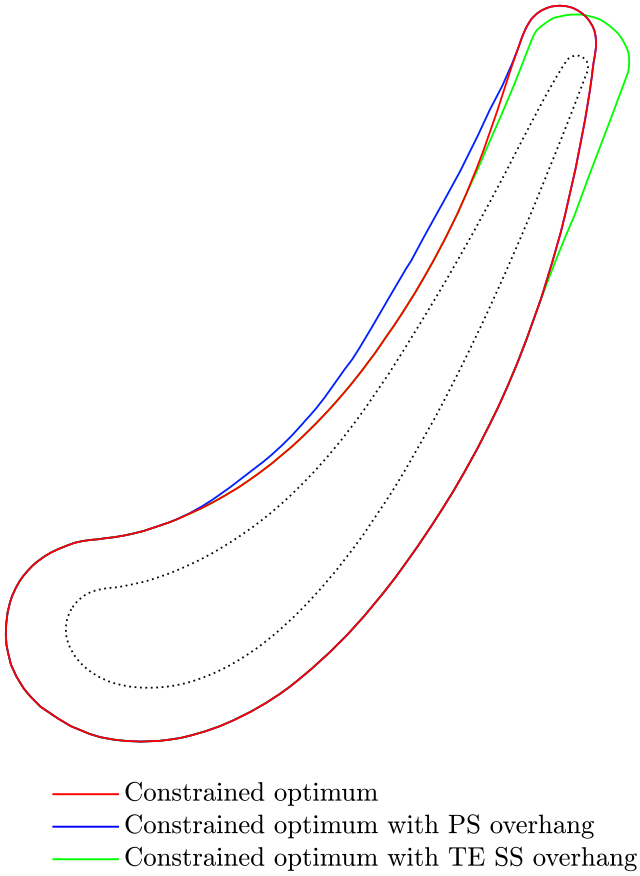

Figure 4.27: Two additionally examined designs (with PS and TE SS overhangs) alongside optimum tip and the datum (dashed)

Two designs were created starting from the optimum tip. In the first design, the pressure side overhang was increased to the maximum value (0.1 of axial chord), keeping all other design features unchanged. The same process was repeated for the second design in which the same amount of overhang was applied to the suction side of the trailing edge. For the optimum winglet and the two additional designs, the static pressure around the tip is shown in Figure 4.28.

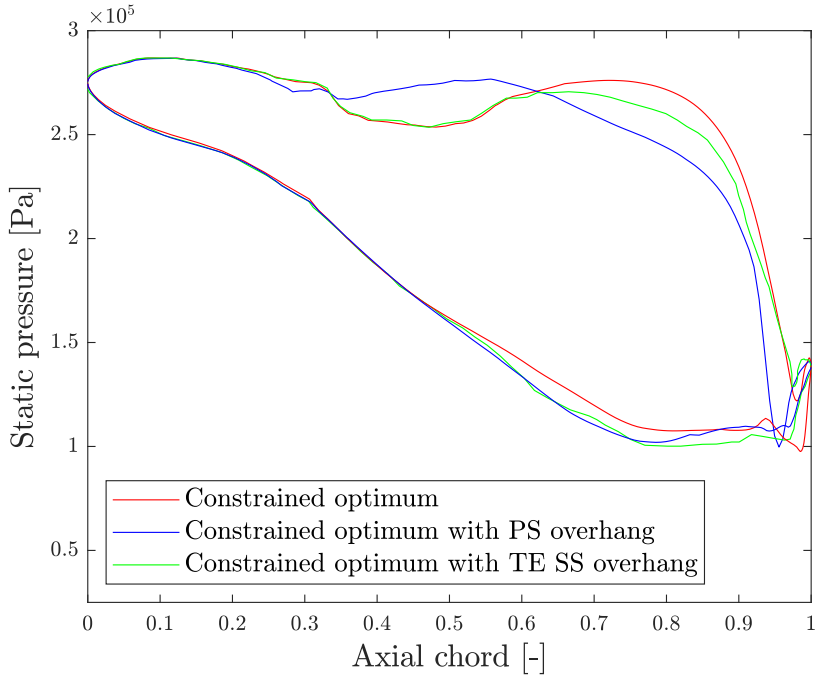

Figure 4.28: Pressure distribution around optimum winglet and designs with PS and TE SS overhangs

As shown, all three winglet tips had similar pressure distributions where the more noticeable differences were on the pressure side. Increasing the pressure side overhang resulted in an increase in the static pressure around the mid-chord, which resulted in a higher pressure difference across the tip. Also, full pressure side overhangs lowered the static pressure at the second half of the tip. In the case of the suction side, the pressure side overhang slightly lowered the suction side static pressure after the 0.5 of the axial chord.

Adding the overhang at the suction side of the trailing edge did not cause a significant pressure difference at the pressure side, and only a small decrease was observed close to the trailing edge. However, it did lower the static pressure in the whole second half of the suction side. Overall, the pressure difference across the tip remained the same. Both tips had a minor decrease in efficiency compared to the optimum, with a decrease of 0.1 % for the full pressure side overhang and 0.08 % for the overhang at the suction side of the trailing edge.

To analyse how the changes in static pressure affected the amount of leakage mass flow, the mass flow distribution was calculated at the suction side of the tip gap for these two tips and compared with the optimum. This is shown in Figure 4.29. As shown, a very similar distribution of mass flow was noticed for all tips, with only minor differences. The mass flow distribution was almost identical for all three tips

in the first half of the tip gap, with most differences being in the region after 0.6 of the suction side surface length. Overall, the differences in the two additional cases did not increase the overall leakage mass flow by more than 2 % from the optimum value.

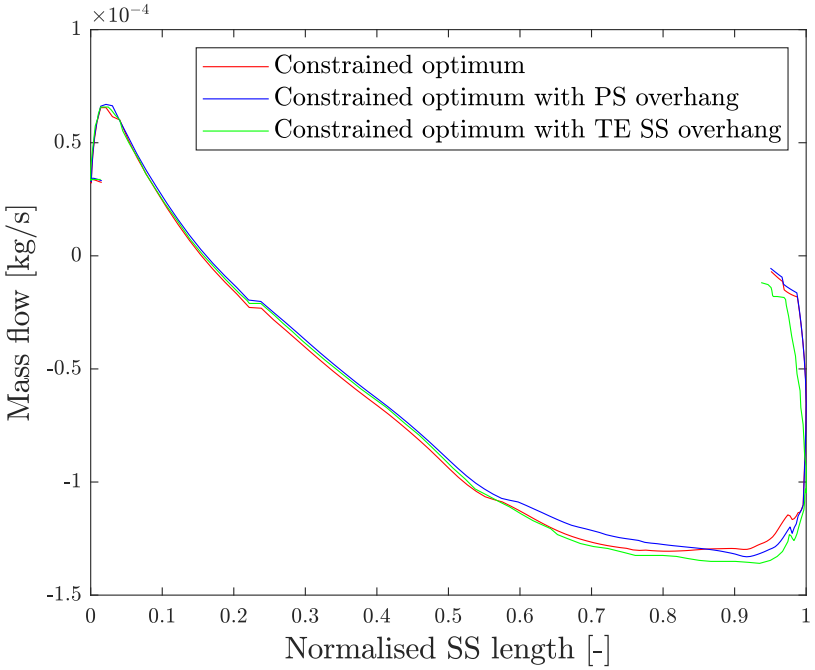

Figure 4.29: Over tip leakage mass flow around optimum winglet and designs with PS and TE SS overhangs

4.7 Aerothermal optimisation

With the constrained aerodynamic optimisation successfully performed, which had converged to the best performing tip design, aerothermal optimisation was carried out next. Its setup and results are presented in the upcoming sections.

4.7.1 Optimiser

In aerothermal optimisation, the objective function $f(x)$ was defined as a combination of two separate objectives: stage efficiency and the integrated heat transfer coefficient as

$$f(x) = \alpha f_1(x) + (1 - \alpha) f_2(x) \tag{4.2}$$

where α was the weighing factor. Separate objectives were calculated as

$$f_1(x) = \frac{1 - \eta(x)}{1 - \eta(x_{ref})} \tag{4.3}$$

$$f_2(x) = \frac{HTC_{blade}(x)}{HTC_{blade}(x_{ref})} \tag{4.4}$$

where datum rotor blade tip is represented by x_{ref}. Since the optimisation setup included the minimisation of the optimisation objectives, the inverse of efficiency was used. Also, since the addition of the winglet tip was expected to affect not only the heat load on the tip but also the region below the blade tip, it was necessary to include the whole blade when calculating the heat load objective. Thus, the heat load objective was calculated as the surface integrated heat transfer coefficient over the entire blade area.

Optimisation was performed by combining the two objectives into a single one, as the optimiser could not handle separate objectives. However, since the scope of this optimisation was to assess two objectives, this was not the ideal solution. To overcome this, three separate aerothermal optimisations were done by varying the weighing factor α. These will be explained later in the results section. By creating the Pareto front that way, this optimisation approach still provided a useful relationship between efficiency and heat load concerning the winglet tips. To the author's knowledge, this contributes to the state of the art since published data on winglet tips Pareto front are very limited.

All three separate optimisations used the same design parameters given in Table 4.4. The optimisation had a total of 18 design parameters. Using MAM, each of the three optimisations was run for six sub-regions, with 40 designs in each sub-region. The flowchart of a single aerothermal optimisation with a constant weighing factor is given in Figure 4.30.

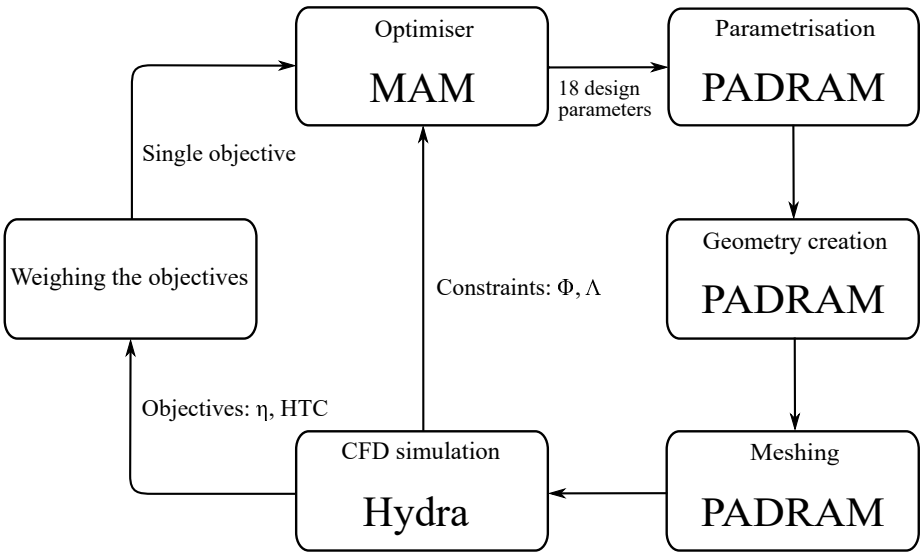

Figure 4.30: Aerothermal winglet tip optimisation with constraints flowchart

4.7.2 Results

Aerothermal optimisation using equal objective weights, $\alpha = 0.5$ in Equation 4.2, was performed first. To evaluate its convergence, a Pareto front showing the trade-off between the surface integrated heat transfer coefficient and the efficiency change is shown in Figure 4.31.

As presented in Figure 4.31, all designs had an increased value of the integrated heat transfer coefficient compared to the datum. The reason for this was that the addition of the winglet increased the blade area, which consequently increased the heat load since it was area integrated. However, some winglets behaved better than others heat load-wise, where for similar efficiency increases, the heat load increase was much smaller. These are the designs that were of the most interest.

When optimising the turbine tips, it is important to take care of the heat load, especially when the blade area is altered, as increased heat load requires more cooling, which lowers the efficiency of the whole engine. Therefore, the heat load needs to be minimised for a certain efficiency increase.

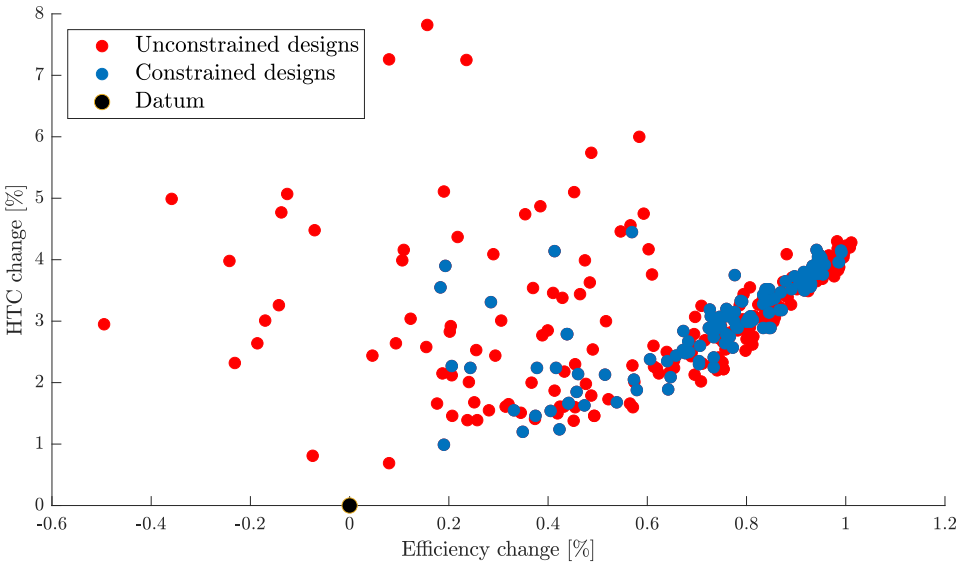

Figure 4.31: Pareto front for aerothermal optimisation with equal objectives weights

Figure 4.31 shows all the designs in the optimisation, where designs that violated at least one constraint are shown in red, and successfully constrained designs are shown in blue. To judge the optimisation convergence, it is worth noting that the Pareto front is populated with both unconstrained and constrained designs. This shows that the Pareto front is properly resolved, and the optimisation is converged.

Since Equation 4.2 focuses on a small region of designs, to populate other parts of the Pareto front shown in Figure 4.31, two other optimisations were carried out. Efficiency dominated optimisation was done by using the weight value of $\alpha = 0.75$ in Equation 4.2. That put more focus on the efficiency increase rather than the heat load. Similarly, heat transfer coefficient dominated optimisation was done using the weight value of $\alpha = 0.25$, where more emphasis was put on the integrated heat transfer coefficient change. The Pareto front showing the results of all three optimisations is presented in Figure 4.32.

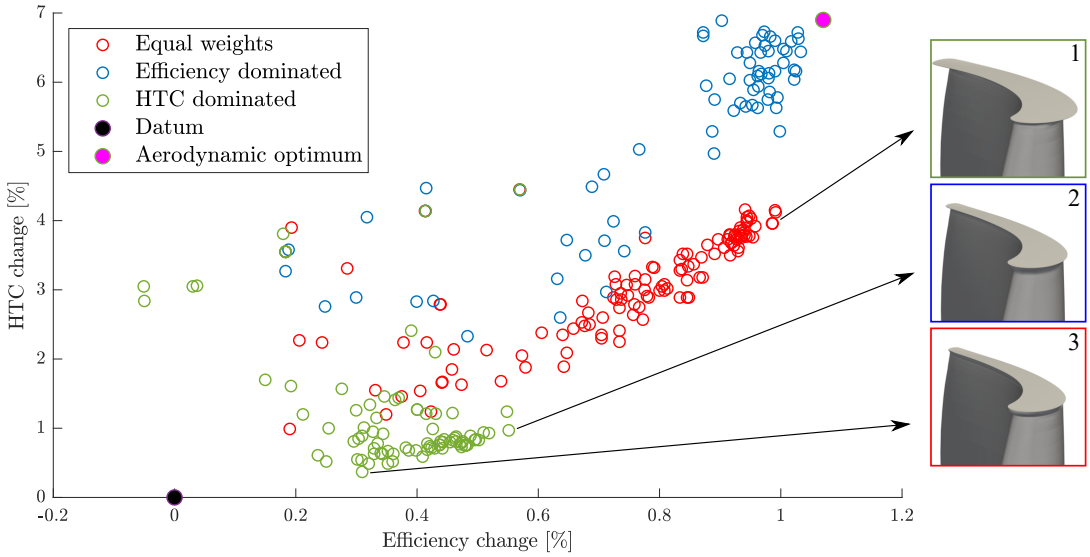

Figure 4.32: Pareto front for aerothermal optimisations with different objective weights

Figure 4.32 presents the Pareto front as a combination of three separate optimisations performed, including only the successfully constrained designs. The constrained aerodynamic optimum winglet tip, presented in Figure 4.18, is shown in purple as a reference to Pareto front designs. The efficiency dominated optimisation, whose results are shown in blue, explored the area around the aerodynamic optimum, identifying some designs that brought almost the same efficiency benefit as the aerodynamic optimum, with considerably lower heat load. On the other hand, the heat transfer coefficient dominated optimisation explored designs that had up to 0.6 % of efficiency increase over the datum, for a heat load increase of up to 1 %.

Since the objective definition had a single minimum objective solution, the optimiser had clustered points around that point in a search for a global minimum, leaving other regions of the Pareto slightly unpopulated. To resolve that, other weights could have been used. However, the trend of the Pareto front as HTC augmentation with efficiency increase in Figure 4.32 was visible, and the Pareto front designs were further analysed.

4.7.3 Analysis of the Pareto front designs

To describe the differences between designs on the Pareto front, three winglet tips were selected, as shown in Figure 4.32.

Design 1 was chosen as the design with the lowest heat load increase for an efficiency improvement of 1 %. Design 2 was chosen as the most efficient design with a heat load increase of up to 1 %. Design 3 was chosen as the most efficient design with the lowest recorded heat load.

For the selected designs, winglet tip outlines showing the applied overhangs are shown in Figure 4.33 alongside the datum outline in red. It can be seen that design 1 featured large overhangs at the front part of the suction side, at the late pressure side, and the pressure side of the trailing edge. A small overhang was applied at the leading edge and the front portion of the pressure side. As already seen for the case of an aerodynamic optimum, no overhangs were present at the suction side of the trailing edge.

Design 2 had the largest overhang at the leading edge and the early suction side. On the pressure side, a small overhang of constant value was applied, stretching until the trailing edge.

Design 3 featured the smallest amount of overhangs amongst the three winglets. Overhangs were applied at the leading edge and at the early pressure and suction sides, where after around 0.3 of axial chord, no overhang was present at either pressure or the suction side. A very small overhang was applied at the trailing edge, on both pressure and suction sides.

All three winglets featured sharp winglet tip edges with very little straight length applied. Interestingly, in the case of low heat load winglets 2 and 3, at the leading edge region, some amount of tip winglet tip extrusion through straight length parameter was applied. That resulted in slightly blunt leading edge winglets.

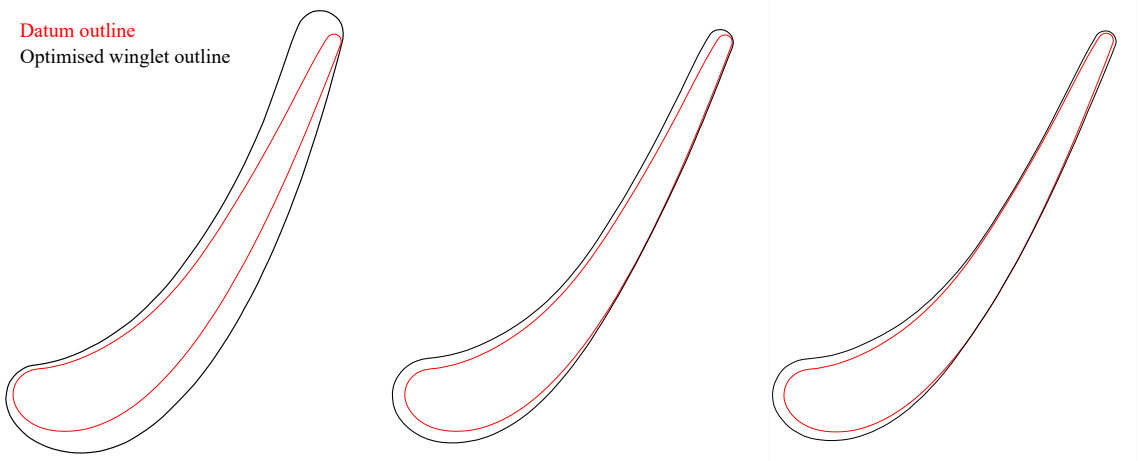

(a) Design 1 (b) Design 2 (c) Design 3

Figure 4.33: Over tip leakage vortex

4.7.3.1 Aerodynamic properties

To analyse the flow differences between the three winglet tips, the static pressure around the tips was plotted as shown in Figure 4.34 and compared against the datum. Starting from the leading edge, similar leading edge static pressure was visible for all the winglets and the datum, in contrast to the aerodynamic optimum shown in Figure 4.21. The three analysed winglets had very similar leading edge pressure distribution with very small pressure difference between the pressure and suction sides. Also, after around 0.1 of axial chord in the case of design 1 and around 0.15 for designs 2 and 3, pressures on the pressure and suction sides were almost equal. This feature has not been observed for the aerodynamic optimum winglet. It was found to be connected with the blunt leading edge overhangs. After the leading edge regions, all three winglets had higher static pressure on both pressure and suction sides than the datum, with some exception in the early pressure side of design 3. The highest pressure side static pressure was seen for design 1 and was slightly lower for design 2. Design 3, having no overhang in the second part of the pressure side, had very similar pressure to the datum. It can be concluded that the static pressure value on the pressure side is directly connected to the size of the pressure side overhang. On the suction side, all designs had higher static pressure than the datum where, interestingly, in the first half of the tip, designs 2 and 3 had higher suction side static pressures than design 1, despite having smaller overhangs.

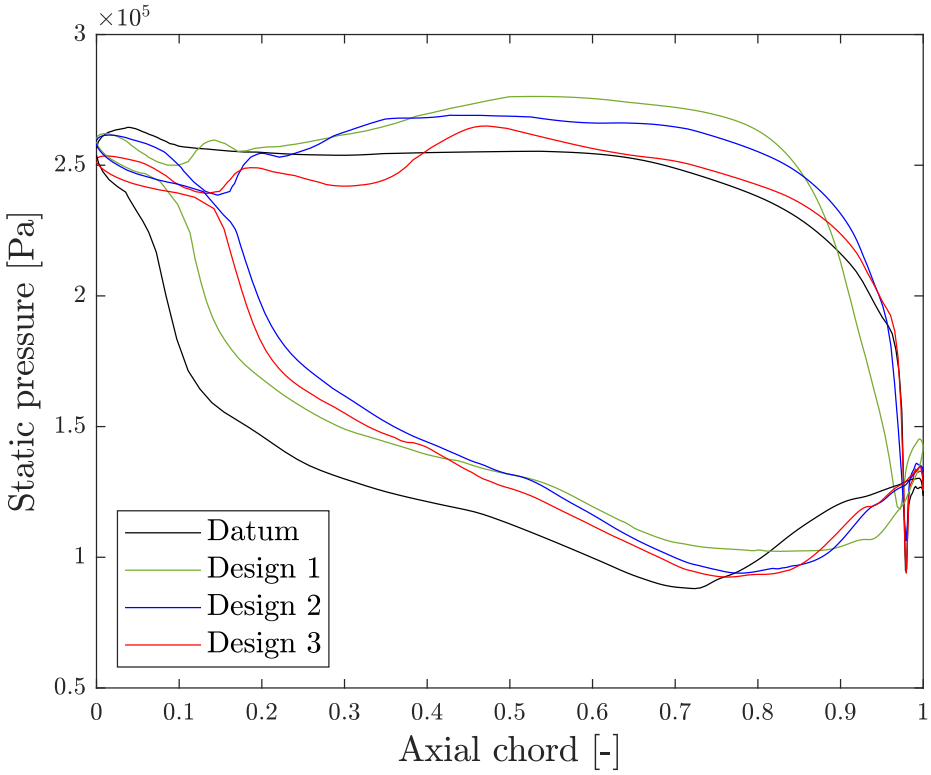

Figure 4.34: Pressure distribution around the designs at the Pareto front

The overtip leakage mass flow measured at the suction sides of the tip gap for the three winglets and the datum is shown in Figure 4.35. Despite having a far lower pressure difference around the leading edge over the datum, the three winglets had a similar mass flow distribution at the early suction side, as did the datum. A more noticeable difference in the amount of leakage flow was seen after around 0.1 of the suction side length where the amount of mass flow increased at a much slower rate for the winglets compared to the datum. Between 0.1 and 0.6 of the suction side length, design 1 had a much lower amount of leakage mass flow, despite not being as dominant as the other two winglets when looking at the static pressure around the tip. It is worth noting that design 1 in this region featured a large suction side overhang where designs 2 and 3 did not. After around 0.6 of the suction side length, all three winglets had a very similar distribution of leakage mass flow until the end, which was overall much lower than the datum. Compared to the datum, design 1 had 47.7 %, design 2 had 41.3 %, and design 3 had 37.4 % lower mass flow than the datum tip.

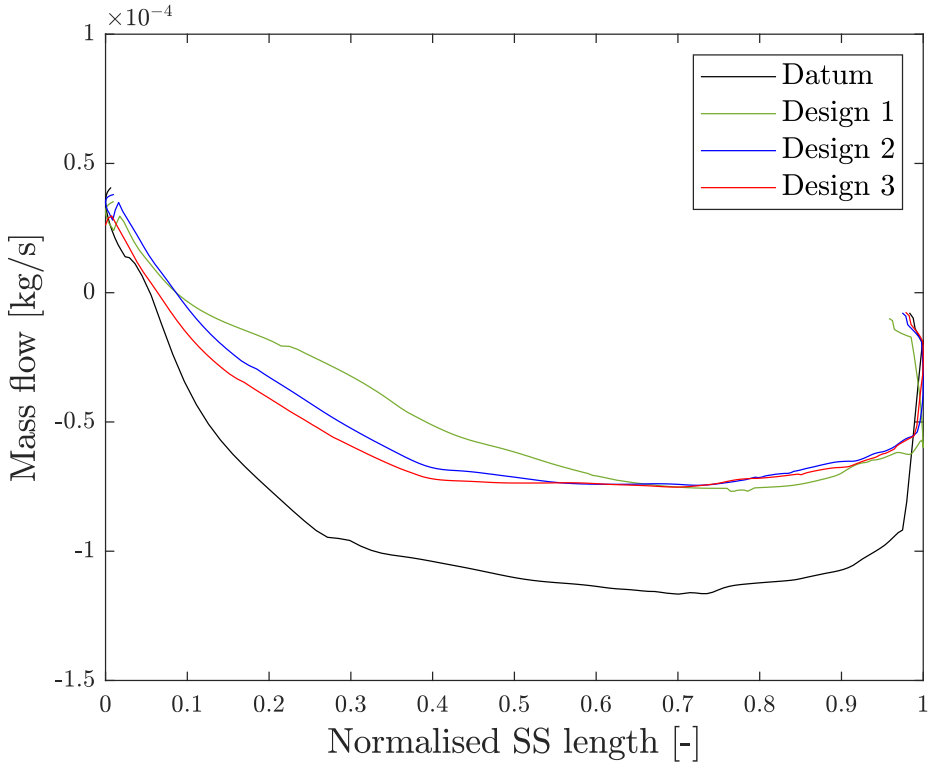

Figure 4.35: Tip leakage mass flows for the designs at the Pareto front

Over tip leakage flow for three winglet designs, along with the datum, is visualised in Figure 4.36. Starting from design 1, which had a similar overhang distribution as the constrained aerodynamic optimum winglet tip (shown in Figure 4.23b), it can be seen that its over tip leakage vortex was the smallest in size among the three winglet tips. The reason for this was the smallest amount of leakage mass flow. Also, because of its largest suction side overhang, design 1 had an over tip leakage vortex detached from the suction side of the blade (shown in detail in Figure 4.36b). Designs 2 and 3 featured similar behaviour of the over tip leakage vortices in the way that, as the over tip leakage vortices originated, they were partly detached from the blade suction sides, but eventually, as they grew, started to fully rub the blade. This can be seen in Figures 4.36c and 4.36d, where, as the respective over tip leakage vortices reached the trailing edges, they fully rubbed the blades. Another feature of designs 2 and 3, which was not the case for design 1, was the existence of the passage vortex, visible below the over tip leakage vortex (noted in Figures 4.36c and 4.36d). Regardless of decreasing the amount of over tip leakage flow by around 40 %, and not being very far from the over tip leakage mass flow of design 1, in the case of designs 2 and 3, merging of the over tip leakage and passage vortices was not completely successful. This is seen as a larger area of decreased relative total pressure below the over tip leakage

vortices of designs 2 and 3, also clearly observable for the datum. This phenomenon can be further seen when looking at circumferentially averaged entropy behind the blades. Between designs 2 and 3, a slightly larger vortex core and passage vortex were observed for design 3.

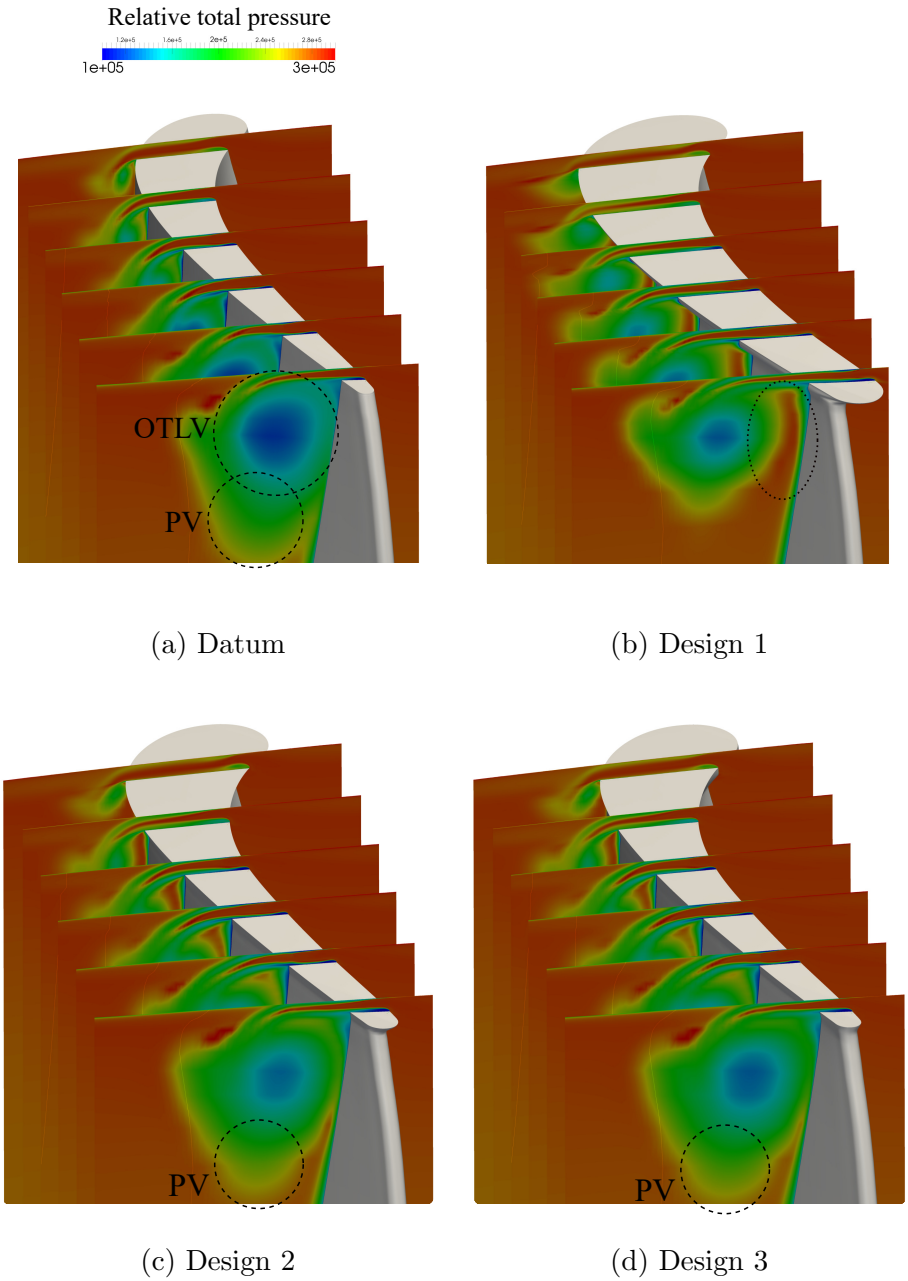

(a) Datum

(b) Design 1

(c) Design 2

(d) Design 3

Figure 4.36: Over tip leakage vortex for 3 winglet tips

To analyse how different over tip leakage vortex behaviours affected the resulting entropy production, circumferentially averaged entropy was plotted at 0.5 axial chord

downstream of the trailing edge, as shown in Figure 4.37. Three designs were compared with the datum, and immediately, it was seen that designs 2 and 3 had very similar entropy production and were different from design 1. Starting from the casing, designs 2 and 3 were found to have slightly lower entropy production compared to the datum, which was assumed to be a favourable shape in this region due to its smaller tip width and lower boundary layer losses. Winglet 1 was found to behave in this region as the previously shown aerodynamic constrained optimum, having larger entropy production than the datum. Around 0.85 to 0.9 of the span, in the region that corresponds to the over tip leakage vortex core, datum tip had the highest entropy due to the largest vortex size and the highest adverse pressure gradients. However, below this region, around 0.8 of the span, datum tip was again found to have lower losses than winglets 2 and 3, despite having a much higher amount of tip leakage flow with a strong vortex core rubbing on the blade. Only below around 0.7 of the span winglets 2 and 3 had smaller entropy than the datum due to the smaller passage vortex. Also, regardless of around 0.25 % of the efficiency difference between designs 2 and 3, entropy was found to be very similar between these two winglet tips. Design 1 was found to be inferior to designs 2 and 3 above 0.85 of the span but had much lower entropy in the region between 0.6 and 0.85 of the span. In this region, design 1 produced far smaller entropy due to the absence of the passage vortex. Below 0.5 of the span, flow was found to be unaffected by any tip change and all tips had very similar entropy production.

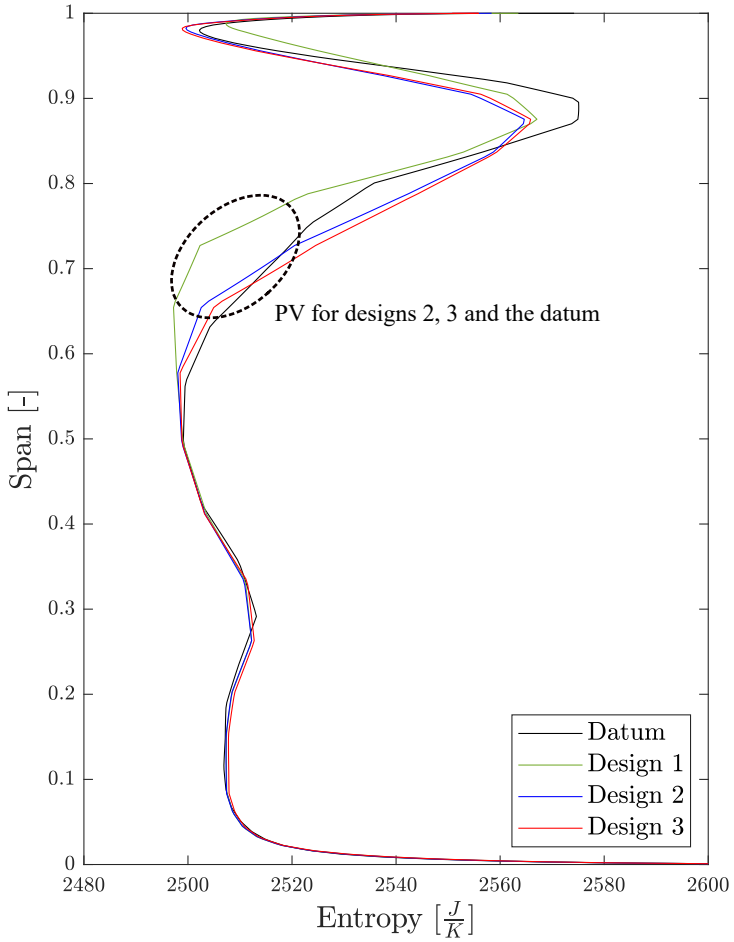

Figure 4.37: Circumferentially averaged entropy field at 0.5 C_{ax} downstream of the trailing edge

4.7.3.2 Heat load properties

With the flow properties of selected winglet tips explained, the heat transfer coefficient was shown using contours to analyse the effect of the flow on the heat load. The area of interest included the tip and the upper half of the blades, where the flow was altered from the datum, as suggested by the radial entropy plots.

The heat transfer coefficient on the winglet tips was looked into first and is shown in Figure 4.38 for all three winglet designs. As presented, the heat transfer coefficient was found to be the highest on the winglet tip at the leading edge region as a result of flow separation over the tip edge. Other regions of increased heat transfer were the areas alongside the pressure side tip edge and the suction side portion of the trailing edge. Streaks of increased heat transfer along the leading edge and the pressure side

were found to be caused by the flow impinging on the tip as a result of contraction over the separation bubble that formed next to the tip edge. As the front portion of the tip experienced subsonic flow conditions, the heat transfer coefficient was higher in that area after the separation, with the area of increased heat transfer coefficient stretching until the suction side in the front portion of the tip. As the flow reached supersonic condition in the second half of the tip, the tip heat transfer coefficient dropped, and heat transfer coefficient stripes became visible. Those were a result of the tip gap shock reflections. After the shock reflections, as the flow reached the area close to the trailing edge, it became subsonic again. This caused the increased heating of the aft portion of the tip, which was most visible in the case of design 1. Overall, the tip heat load was found to be very similar for designs 2 and 3, with design 1 having most of its differences in the second half of the tip as a result of supersonic flow.

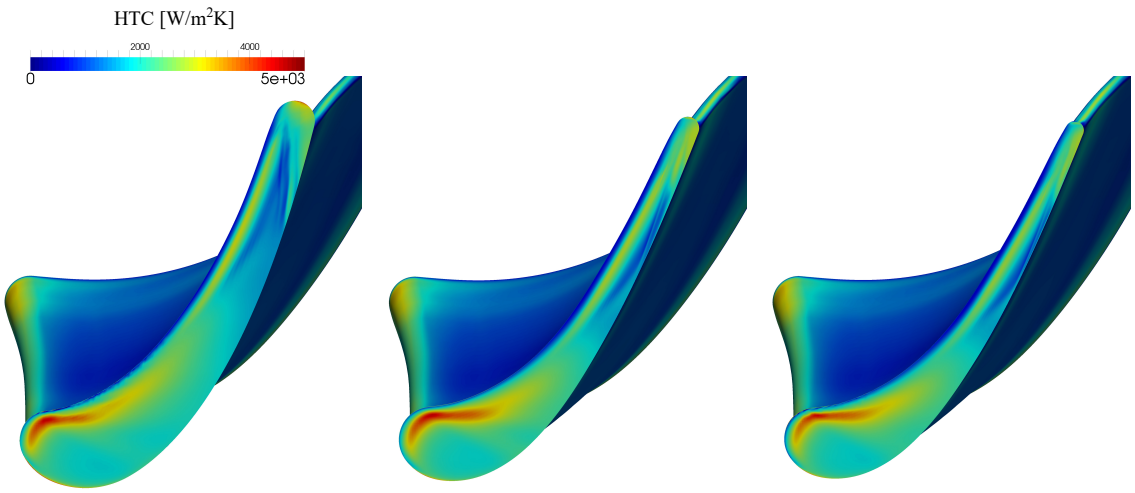

(a) Design 1 (b) Design 2 (c) Design 3

Figure 4.38: Contours of heat transfer coefficient at winglet tips

Heat transfer coefficients for the selected winglet tips are shown on the leading edge and the pressure side in Figure 4.39. It can be seen that differences in heat load were visible only for the region close to the tip. At the leading edge, differences in heat load were small between the three winglets, even though winglets 2 and 3 had more blunt leading edge overhangs compared to design 1. A small region of increased heat transfer coefficient can be observed at the tip edge of the leading edge, which is a common feature for all sharp corners. Most differences in heat load can be seen in the second portion of the tip as a result of different pressure side overhangs applied. Design 1 had a large overhang at the late pressure side and the pressure side

of the trailing edge, which prevented the flow in this region from escaping over the blade. This resulted in a very high heat load area at the underside of the pressure side overhang but also in a low heat load at the pressure side of the blade. The underside of the pressure side was found to be the region with the highest heat transfer coefficient of the whole winglet tip. Designs 2 and 3 had smaller pressure side overhangs, which meant more flow escaped over the tip. It can be seen that the heat load was higher at the aft part of the blade close to the tip in those cases compared to design 1. Design 2 pressure side overhang also experienced high heat load but resulting in less heat load at the blade region below it, compared to design 3.

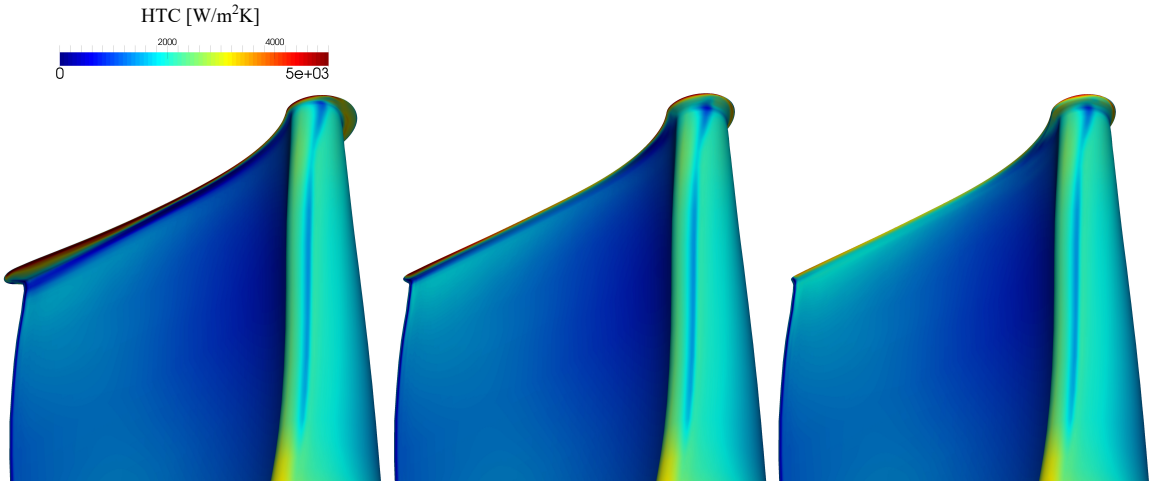

(a) Design 1 (b) Design 2 (c) Design 3

Figure 4.39: Contours of heat transfer coefficient at winglets pressure side

As the over tip leakage vortex forms alongside the suction side, heat load differences between different tips are of special interest in this region. These are shown in Figure 4.40. Starting from the leading edge, it can be seen that the underside of the suction side experienced high heat load, especially in the front part as the flow started to separate. This was found to be highest in the case of design 1, which had the largest suction side overhang. However, the level of heat load on the underside of the suction side overhang was still considerably lower than that of the underside of the pressure side overhang. In the second part of the blade, heat load was only governed by the over tip leakage vortex, more specifically, by its size and proximity to the wall. Design 1 had the lowest heat load in this area since it had the smallest over tip leakage vortex that was fully detached from the wall. In the case of designs 2 and 3, the over tip leakage vortex was rubbing against the blade, as shown in Figure 4.36, resulting in an area of increased heat load. This area stretched from the early suction

side where the over tip leakage flow originated, all the way to the trailing edge, growing as the over tip leakage vortex augmented. Design 3, having the largest amount of tip leakage flow between the three winglet tips, which in turn resulted in the largest over tip leakage vortex, had the largest area of increased heat load in this region.

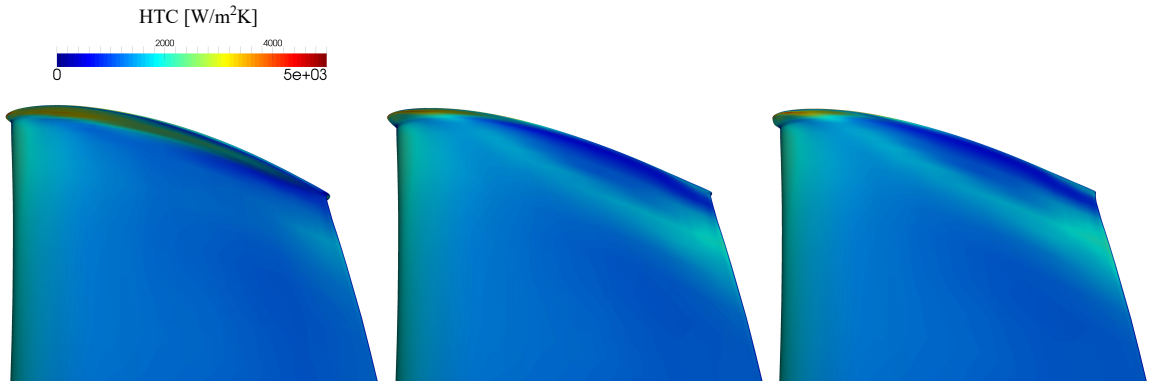

(a) Design 1 (b) Design 2 (c) Design 3

Figure 4.40: Contours of heat transfer coefficient at winglets suction side

4.7.3.3 Variation of efficiency and heat load with tip gap size

As the jet engine goes through different operating modes, based on different power requirements, such as those during take-off and cruise, its components perform differently. The tip gap in unshrouded turbine rotors is affected and controlled by different factors, such as thermal expansion or active tip gap control systems. In other words, it is expected that the engine will never run with always the same tip gap. Therefore, when designing a turbine tip, it is important to take into account the variability of blade performance for changes in the tip gap size. In order to do that, in this work, the performance of the most interesting designs was investigated for different tip gaps apart from the nominal.

Figures 4.41 and 4.42 present the variation of efficiency and the integrated heat transfer coefficient with the tip gap size. Apart from the nominal tip gap of 1.5 % of the span used in the optimisations, smaller tip gaps of 0.5 % and a larger tip gap of 2.5 % of the span were tested.

Figure 4.41 shows that the efficiency decreased almost linearly for all the winglets presented as the tip gap increased. However, higher efficiency tips (winglet 1 and 2) experienced a more linear change in efficiency with the change of the tip gap, compared to the lower efficiency tips, winglet 3 and the datum. This was particularly obvious for the change of the tip gap from nominal to the smaller tip gap of 0.5 % of the span. At that tip gap, designs 2 and 3 were found to have an efficiency very

similar to the datum blade, where design 2 lost more efficiency than design 3 over the datum. Design 1, which had 1 % higher efficiency at the nominal tip gap, was found to be only 0.3 % more efficient than the datum at the lowest tip gap tested.

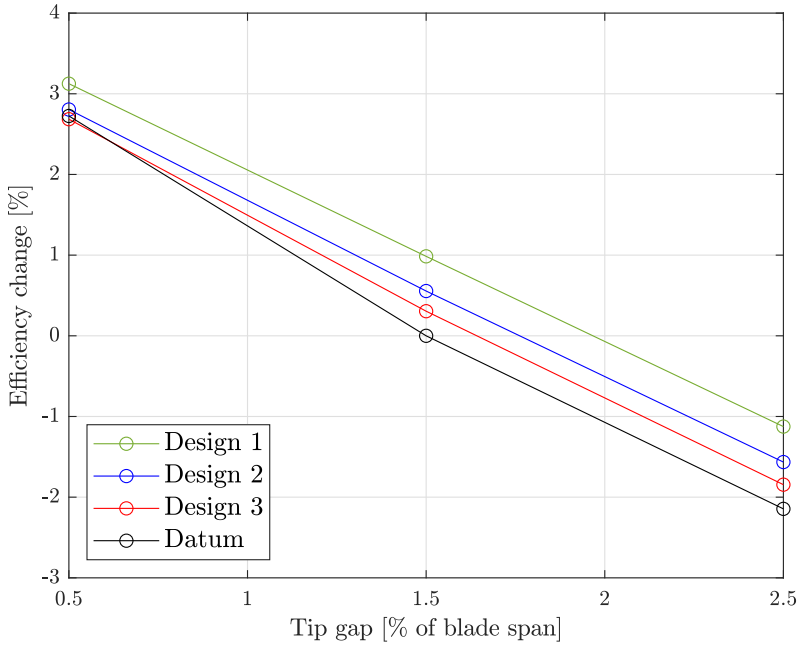

Figure 4.41: Efficiency variation

The variation of tip heat load, expressed as the surface integrated heat transfer coefficient with the tip gap size, is presented in Figure 4.42. As expected, it was found that closing the tip gap caused less heat load on the tip due to the lower amount of leakage flow. This is in agreement with previous results from Zhang et al. [101], where similar behaviour was observed. However, some exceptions were noticed for the low heat load winglets 2 and 3 and the datum. As the tip gap opened up from 1.5 % to 2.5 % of the span, the heat load for these designs stayed nearly constant and even reduced for the datum. Similar behaviour of low heat load winglets was reported by Coull et al. [38].

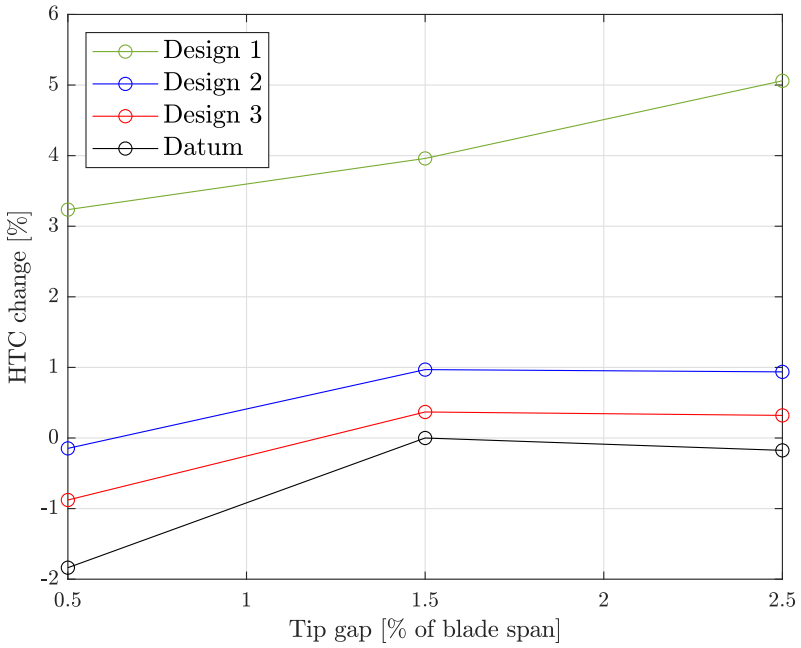

Figure 4.42: Heat transfer coefficient variation

Chapter 5

Squealer tip topology optimisation

With winglet optimisations performed, another tip design approach was investigated. These were the squealer tips, which were topologically optimised. The most recent studies in squealer optimisation showed a new and interesting approach to squealer topology optimisation. As explained by Anderoli et al. [50] and De Maesschalck et al. [104], a novel way of defining the squealer design space can lead to new turbine tip operating principles, resulting in superior performance and heat load properties.

This chapter presents the setups and results of different squealer topology optimisation approaches. To understand the tools and test the methods, a simple aerodynamic single rim squealer optimisation was performed first. With successful optimisation carried out, this approach was then extended into a larger design space capable of parametrising more complex squealers. The focus was on understanding the methods for successful topology optimisation, and a few different approaches were taken, as explained in the text sections. Finally, with the most promising method identified, aerothermal squealer topology optimisation was performed.

5.1 Aerodynamic single rim squealer topology optimisation

5.1.1 Optimisation setup

Simple optimisation of the squealer tip featuring only one squealer rim was performed first, and its setup is given in Figure 5.1. The squealer tip was parametrised using mimic, as explained in Section 2.3.1.2. However, to create a single rim squealer, an RBF surface of low complexity with only four control points was used. As before, the geometry was created using both PADRAM and mimic, where PADRAM was used to create the baseline blade on which the squealer rim was morphed using mimic. The

CFD mesh was created using both PADRAM and BOXER, where the PADRAM mesh was used for the stator domain. As the stator domain was not altered, a structured PADRAM mesh was used for it because of its favourable size and mesh quality. Finally, MAM was used as the optimiser.

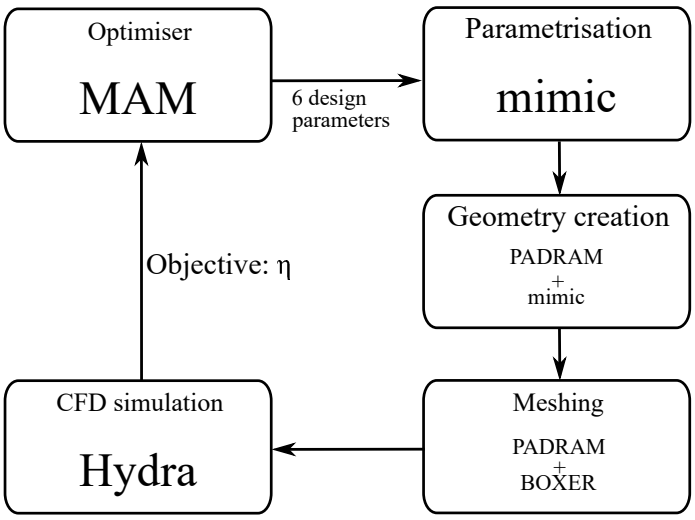

Figure 5.1: Single rim squealer optimisation flowchart

Parametrisation of the squealer tip is shown in Figure 5.2. The single rim squealer tip was parametrised and created using mimic. As only one squealer rim was investigated in this optimisation, a simple RBF surface controlled only by four points was defined (red dots in Figure 5.2a). Out of these four points, two points were assigned to the pressure side, and two points to the suction side of the datum tip. Pressure side points were allowed to move only in the positive z-direction between 0 and 0.5, while suction side points were also allowed to move only in the negative z-direction between -0.5 and 0. Since the RBF surface cut was always done at a zero-height, this approach allowed the definition of a single squealer line free to move between the pressure and suction side of the tip. This process had four design parameters.

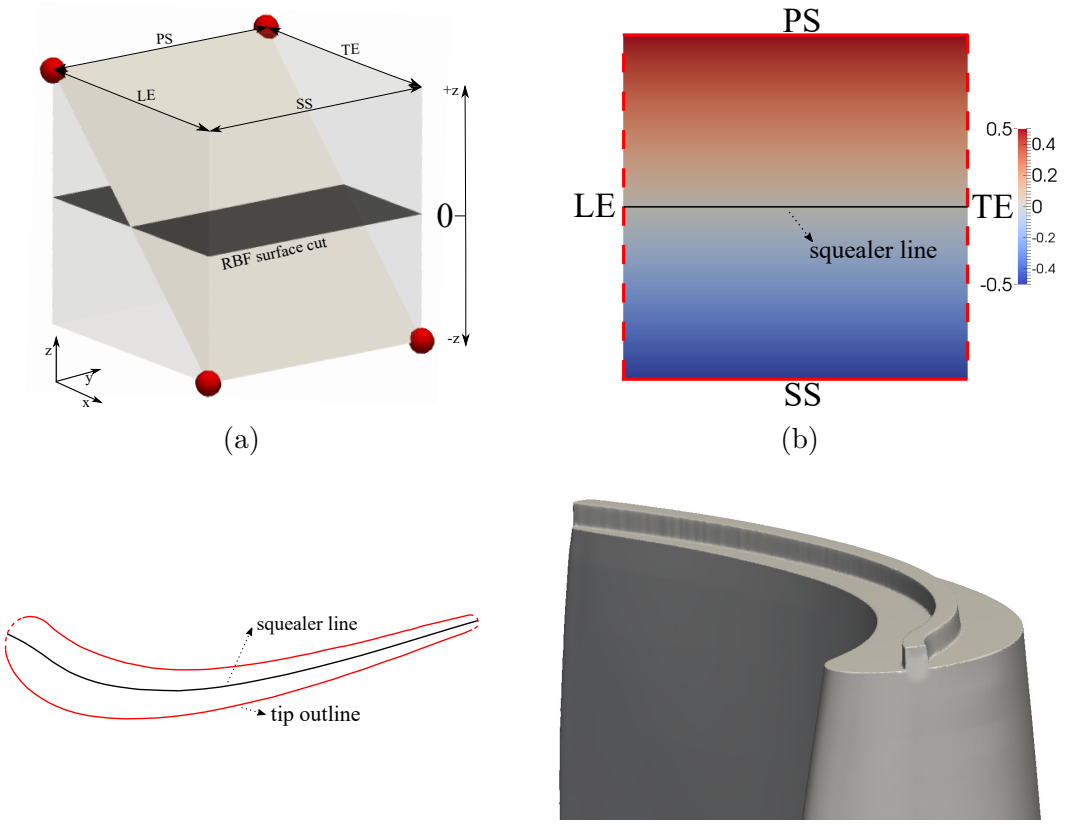

Figure 5.2: Single squealer tip parametrisation

Apart from the location of the squealer rim, its height and width were also parametrised. The squealer rim height was allowed to vary between 0.0085 and 0.05 of the datum blade axial chord or between 33 % and 200 % of the tip gap, which was always constant at 1.5 % of the blade span. The squealer rim width was parametrised to observe the effect of flow reattachment on the squealer tip and was allowed to vary between 0.01 and 0.03 of the datum blade axial chord.

As explained in Section 2.3.1.2, once the squealer line was defined, it was mapped onto the datum tip and extruded to a certain height. To ensure a constant tip gap, the baseline blade height would vary as determined by the optimiser, and the rest of the tip gap would be filled with the squealer rim.

Overall, this optimisation had six design parameters and was performed using MAM with 11 design iterations in each of the sub-regions.

5.1.2 CFD model

CFD simulations were performed using the Spalart-Allmaras turbulence model, and the boundary conditions were the same as those used in the winglet optimisations presented earlier in Table 4.5.

BOXER was used to mesh the rotor domain, and the mesh used was the verified mesh presented in Section 3.2.1.3. To demonstrate its use on the mimic-created squealer tips, it is shown on the optimised tip introduced later in Figure 5.3.

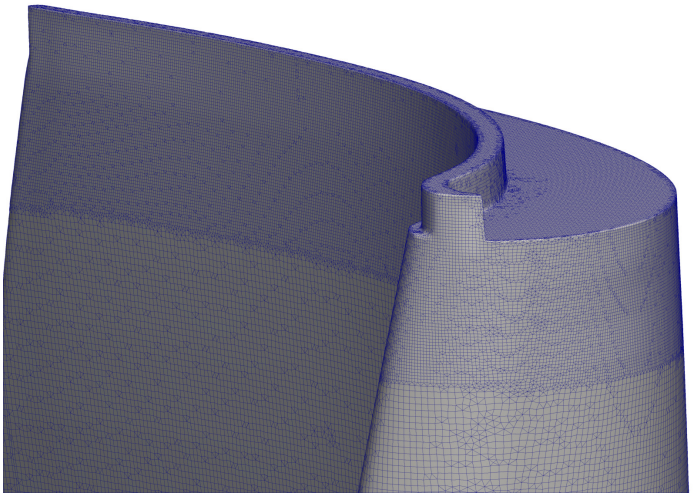

Figure 5.3: Single rim squealer BOXER mesh

As mentioned in the verification study, the upper portion of the blade, including the tip and its underside, was further refined to provide good resolution of even the thinnest squealer rims. This is further supported by the y+ contour plot for the same mesh, shown in Figure 5.4.

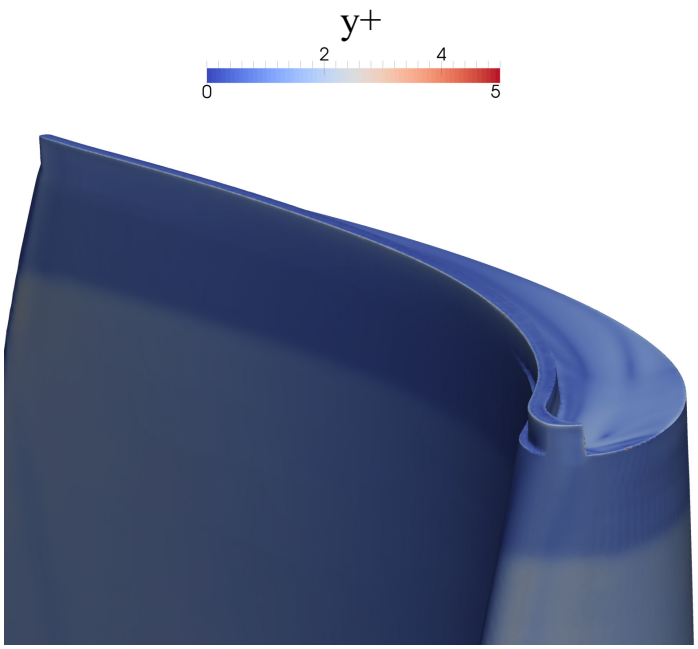

Figure 5.4: y+ contour for the single rim squealer BOXER mesh

As shown in the figure, y+ throughout the blade was at the order of unity, including the tip region and squealer rims, which is very important for this case.

5.1.3 Optimisation results

The optimisation was run for 6 MAM sub-regions, and its convergence history is presented in Figure 5.5. As shown, most of the tested designs had efficiency higher than the datum. The least efficient designs were found to have the squealer rim on, or very close to, the suction side of the tip.

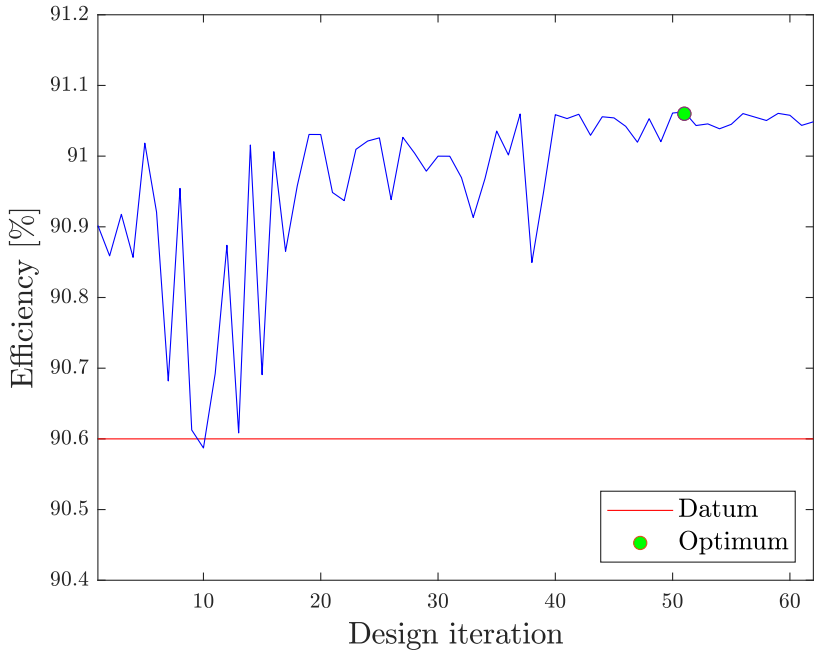

Figure 5.5: Single rim squealer optimisation history

Optimum design is presented in Figure 5.6. As can be seen, the optimum design featured a squealer rim moved completely to the pressure side edge of the tip, except for a small region at the early pressure side where the line was placed slightly away from the tip edge. The reason for this was found to be the need to close the leading edge region as much as possible. With the parametrisation used, only a single squealer rim was allowed, so it was not possible to completely close the leading edge region while having the rim on the pressure side, and a trade-off had to be found.

The height of the optimum squealer rim was found to be 0.037 of the datum blade axial chord, which was around 50 % larger than the tip gap. Regarding the squealer width, the optimum design featured a squealer rim width of 0.011 of the axial chord, which was around 50 % of the tip gap. These results were found to be in agreement with the study by Schabowski and Hodson [35], who found that squealers with a width smaller than the tip gap were a favourable option over wider squealer rims, as they prevented flow reattachment on top of them.

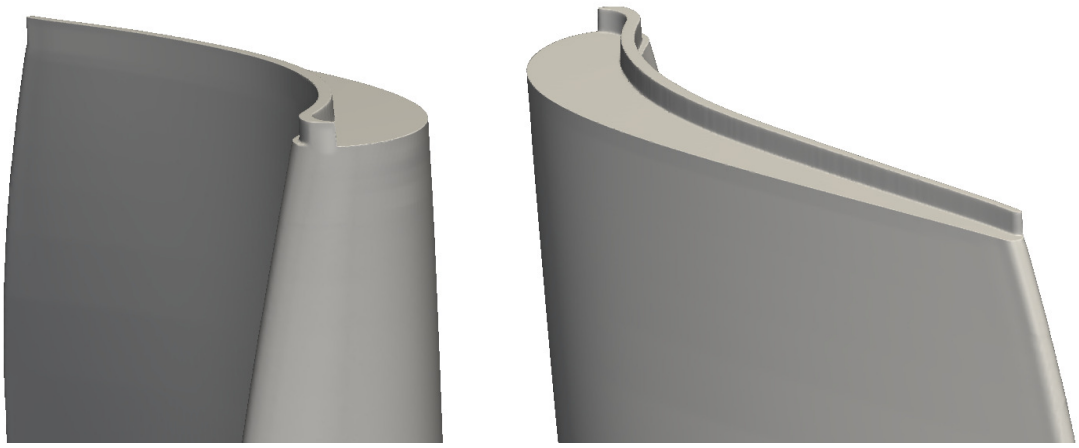

(a) Leading edge and pressure side (b) Trailing edge and suction side

Figure 5.6: Optimum single rim squealer tip

5.1.4 Analysis of the optimum single rim squealer tip

To examine the flow differences caused by the addition of a squealer rim, the static pressure was plotted around the datum and optimum squealer tips at 0.95 of the span. Even though the tip gap used was 1.5 % of the span, the static pressure was plotted at the same span for both tips to have a fair comparison between the designs. The pressure comparison is shown in Figure 5.7.

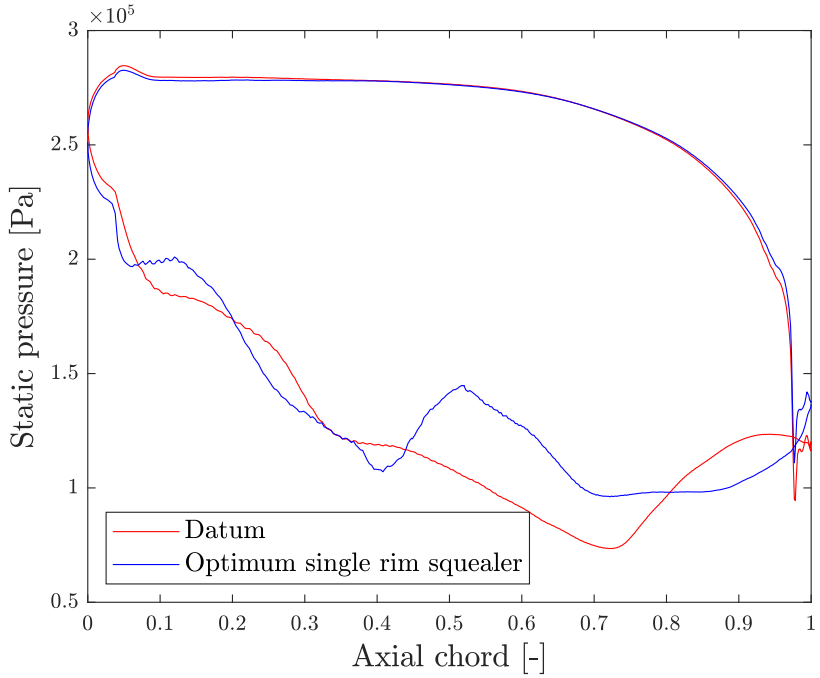

Figure 5.7: Pressure distribution at 0.95 of the span around the datum and optimum single rim squealer tips

As shown in Figure 5.7, the two tips had a very similar static pressure distribution at the pressure side. Since the squealer rim was located on the pressure side in the case of squealer, and since pressure was plotted for both blades at 0.95 of the span, which was 0.035 of the span away from the datum tip and the top of the squealer rim edges, flow differences were found to be negligible in this region. However, the two designs were found to have quite different flows at the suction side, affected by the tip leakage flow. Starting at the leading edge, the static pressures of the two designs started to differ after about 0.05 of the axial chord. Until 0.4 of the axial chord, the static pressures of both blades were similar and gradually dropping, where the optimum squealer had slightly higher pressure in the region between 0.1 and 0.2 of the axial chord. That changed between 0.2 and 0.3 of the axial chord where the suction side static pressures reversed. In the region between 0.5 and 0.8 of the axial chord, the static pressure of the optimum squealer was considerably higher than the datum, lowering the over tip pressure difference, especially in the region after 0.5 of the axial chord. Close to the trailing edge, the pressure difference was again in favour of the datum tip until the trailing edge.

To see how the static pressure around the tip influenced the amount of leakage mass flow, the tip leakage mass flows measured at the suction side of both datum and optimised squealer tips are presented in Figure 5.8.

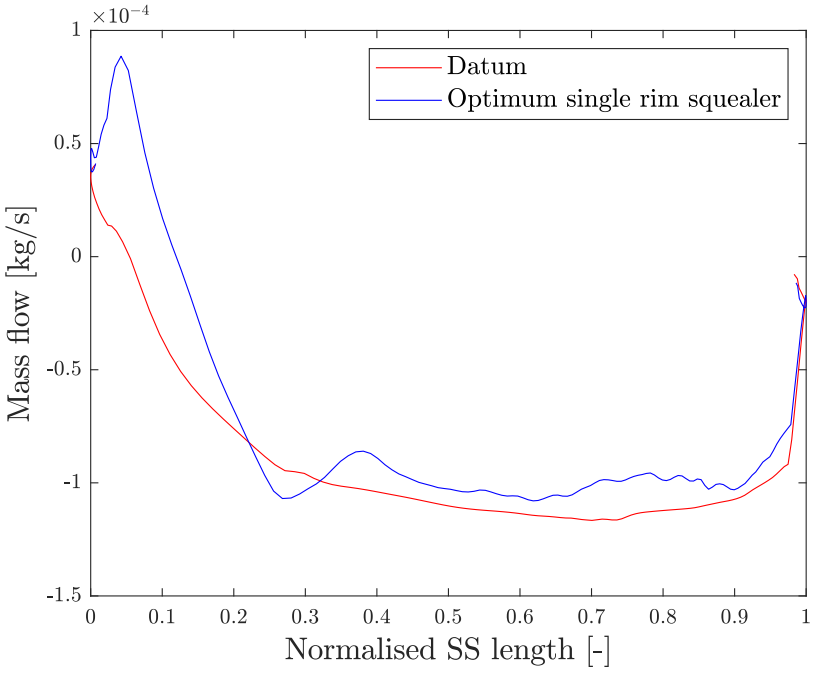

Figure 5.8: Suction side tip leakage mass flow comparison

Leading edge region of the squealer tip was only partially closed by the squealer rim. That means the squealer rim only covered the pressure side portion of the leading edge. The suction side portion had an effectively large tip gap. Therefore, since the flow entering the tip gap over the early part of the squealer rim resulted in a low-pressure circulation vortex, and since the leading edge area was partially closed, the leakage flow was found to keep entering the squealer cavity until around 0.15 of the axial chord. In the case of the datum, that was only until around 0.05 of the axial chord. Thus, in the leading edge region, it can be seen that the effect of a partially closed leading edge moved downstream of the point at which over tip leakage flow started to leave the tip gap.

For both tips, the amount of leakage flow was found to rapidly increase in the front part of the tip until around 0.3 of the axial chord from where, for both tips, it stayed roughly constant. In this region, the optimum squealer was found to have slightly lower leakage mass flow than the datum, until the trailing edge. Nevertheless, both tips had a roughly constant rate of tip leakage mass flow. Overall, by integrating the two curves, the single squealer was found to have $-17.4\,\%$ lower amount of leakage mass flow than the datum, mostly due to the benefits in the leading edge region.

To visualise the tip gap flow and the resulting amount of leakage mass flow that formed the over tip leakage vortex, slices of relative total pressure were used, as presented in Figure 5.9.

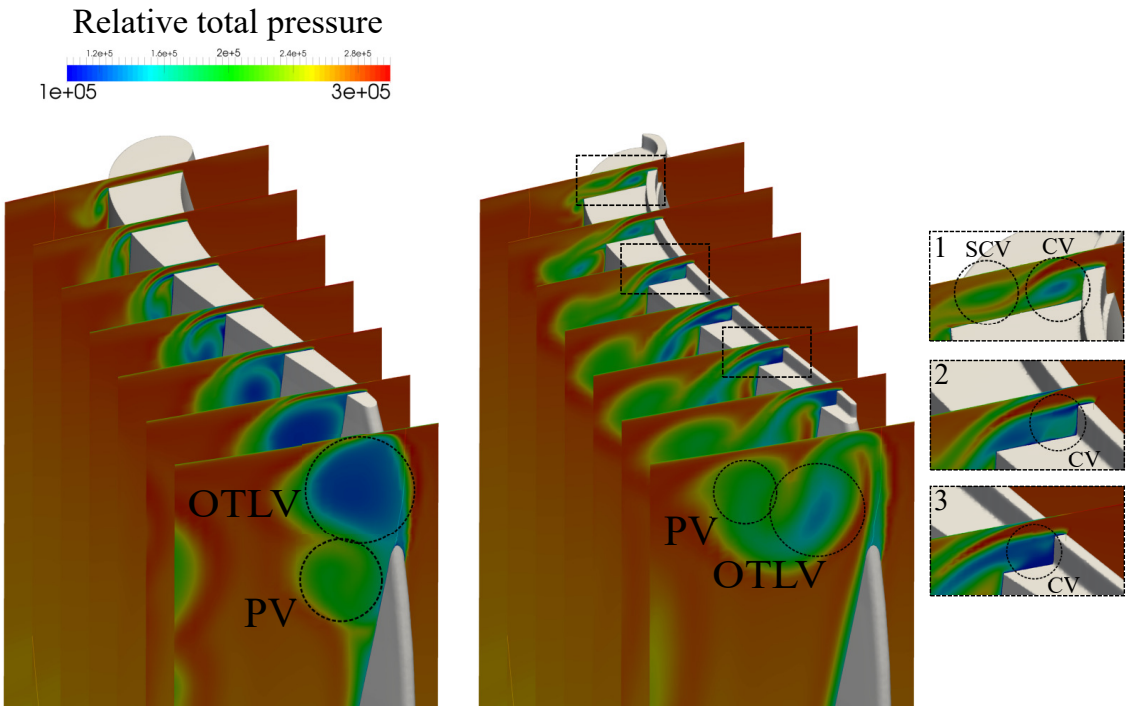

(a) Datum (b) Optimum single rim squealer

Figure 5.9: Over tip leakage vortex

As seen in Figure 5.9b, the flow that entered the tip gap contracted over the squealer rim, causing a separation bubble on top of it. The leakage flow that entered the tip gap and its behaviour changed with the axial chord as the tip region narrowed down towards the trailing edge. At the widest part of the tip, around the leading edge, a corner vortex (CV) formed next to the squealer rim (detail 1).

Due to the relative movement of the casing, from the suction side to the pressure side, part of the leakage flow got entrained and rolled into the scrapping vortex (SCV). This is visible in detail 1 of Figure 5.9b. As the tip narrowed towards the trailing edge, there was no space for corner and scrapping vortices to coexist, and the scrapping vortex disappeared. After about 0.3 of the axial chord, the tip gap area was only filled with the corner vortex, as shown in detail 2. However, as the squealer cavity width further narrowed down, the corner vortex started to decrease in size, and most of its flow left the tip gap until around 0.7 of the axial chord. This is visualised in Figure 5.10, showing a contour of the Q criterion with a value of 6^{10}.

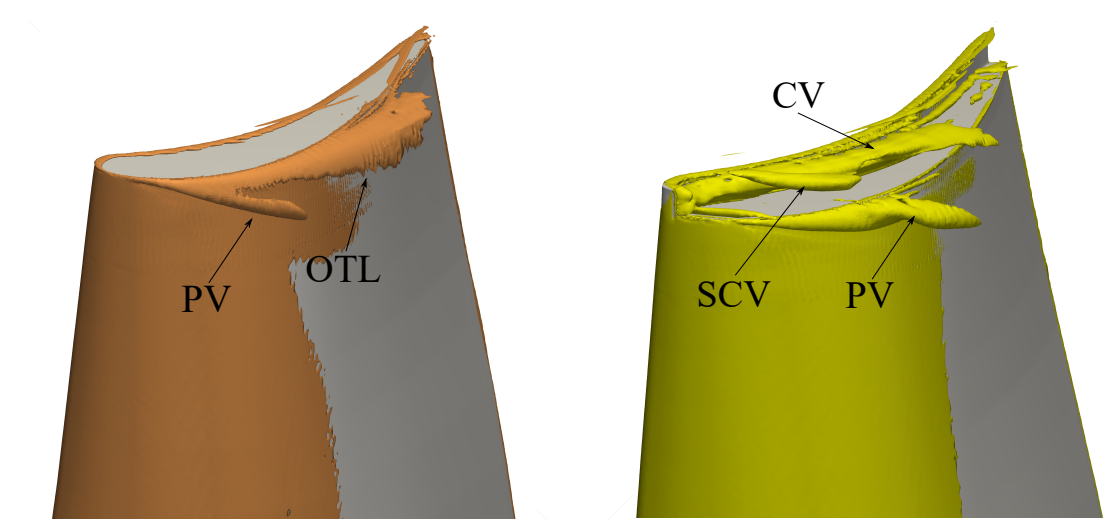

(a) Datum (b) Optimum single rim squealer

Figure 5.10: Tip leakage flow visualised using Q criterion (6^{10})

After around 0.7 of the axial chord, when most of the corner vortex flow had exited the squealer cavity, only a small amount of vortical flow was present, and the sealing effect was mitigated. This caused the single rim squealer to behave like a datum tip with leakage flow passing over it.

However, because there was no barrier on the suction side, the leakage flow that exited the tip gap had more momentum pointing downwards, and an over tip leakage vortex formed at a lower spanwise region than in the case of the datum tip. This is visible in both Figures 5.9 and 5.10. Flow with momentum pointing downwards meant that over tip leakage flow exiting the tip gap was not parallel with the turbine casing, following the blade profile as in the case of the datum. Instead, it had a trajectory towards the hub not following the blade curvature profile. Interestingly, in the case of the optimum squealer, the passage vortex was pushed aside of the tip leakage vortex and these two vortices merged. Similar to what was seen in the cases of winglet tips, because of its downwards momentum, the over tip leakage flow formed a vortex further away from the blade, which had a beneficial effect on shearing losses. In the case of the datum tip, the passage and over tip leakage vortices can be clearly distinguished.

To see how the different tip leakage flow behaviour between the optimum single rim squealer and the datum tips affected downstream flow, circumferentially averaged entropy was plotted at 0.5 of the axial chord downstream of the trailing edge. This is presented in Figure 5.11.

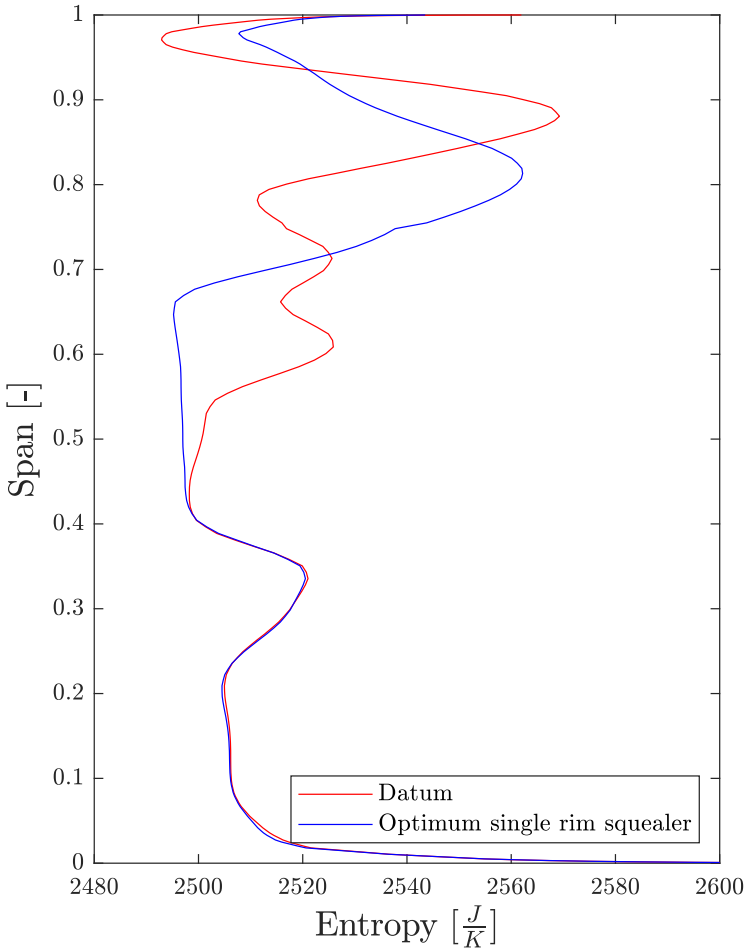

Figure 5.11: Circumferentially averaged entropy field at 0.5 C_{ax} downstream of the trailing edge

Starting from the casing, in the case of a single squealer, tip gap flow was characterised by strong vortical flow, resulting in considerably higher entropy production in the region around 0.95 of the span compared to that of a datum tip. Further downstream, around 0.9 of the span, in the region affected by an over tip leakage vortex, the datum tip had higher entropy production than the squealer tip. In the case of a squealer, the region affected by the over tip leakage vortex was at a lower span (around 0.8) as the squealer over tip leakage vortex developed lower than in the case of a datum (as visible in Figure 5.9). However, because it merged with the passage vortex, this area had higher entropy production than the over tip leakage vortex area of the datum. The passage vortex of the datum was visible in the region between 0.55 and 0.75 of the span. In the same region, below 0.7 of the span, the squealer tip

had much lower entropy production as there was no vortical flow present.

5.2 Aerodynamic squealer tip topology optimisation

After successfully performing simple aerodynamic squealer topology optimisation, the approach was further extended to analyse the realistic state of the art engine-like tips.

First, the geometry parametrisation will be presented, starting from the baseline blade and then moving to the parametrisation approach. After that, initial results will be given. Then, different optimisation approaches were taken, including the regression of the design space through a response surface and constraining an initial design space to the most promising subspace for more detailed investigation. Finally, results from each approach are presented.

5.2.1 Optimisation setup

Based on previous findings from single squealer rim optimisation, the width of the tip is an important parameter in squealer tip optimisation, as it plays a crucial role in the size and strength of the squealer cavity vortices. To ensure the sealing effect in the squealer cavity, vortices need enough space to form. From a literature survey, it was found that the state of the art engine shroudless tips are a combination of a winglet base with a squealer on top of it [105, 106]. Therefore, in squealer tip topology optimisation, a winglet tip was used as a baseline blade to resemble the actual engine blade's tip. However, as the focus of this optimisation was on the squealer optimisation, winglet tip was kept constant for all designs and was not part of the optimisation parameters.

The baseline winglet tip used for creating a squealer tip on top of it was based on previous winglet optimisation findings and is shown in Figure 5.12. It had full overhangs around the tip, except on the suction side of the trailing edge. The winglet tip thickness was constant around the perimeter and was set to the value of the squealer rim width. The design parameters of the baseline winglet tip are given in Table 5.1.

Parameter	Applied value
PS location, b_{PS} [% of edge length]	50
SS location, b_{SS} [% of edge length]	70
Overhangs: $o_{LE}, o_{PS}, o_{SS}, o_{TE\ PS}, o_{TE\ SS}$ [C_{ax}]	0.1, 0.1, 0.1, 0.1, 0.001
Straight lengths: $d_{LE}, d_{PS}, d_{SS}, d_{TE\ PS}, d_{TE\ SS}$ [C_{ax}]	0.02, 0.02, 0.02, 0.02, 0.02
Blending angles: $\beta_{LE}, \beta_{PS}, \beta_{SS}, \beta_{TE\ PS}, \beta_{TE\ SS}$ [°]	60, 60, 60, 60, 60

Table 5.1: Design parameters of baseline winglet tip used in squealer tip topology optimisation

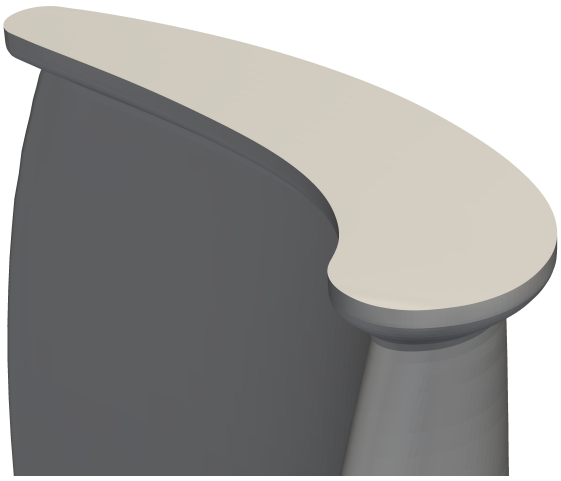

Figure 5.12: Baseline blade for squealer topology optimisation

The squealer tip was parameterised using mimic, as explained in Section 2.3.1.2 and Figure 2.9. To enable the creation of up to three parallel squealer rims, a 4x4 grid of control points was used to create a radial basis function surface. This means that four rows of RBF surface control points were used across the tip. And to enable a high degree of curvature of squealer rims, four RBF surface control points were used along the tip. This has resulted in a total of 16 RBF surface control points, whose z-axis values served as design parameters. Each control point could vary its z-axis height between -0.5 and 0.5, as described in Figure 2.9. This resulted in a total of 16 design parameters. Squealer rim width and height in this case were kept constant and were larger than the tip gap for 43 % and 86 %, respectively. The tip gap was

constant for all cases and was 1.5 % of the blade span, measured from the squealer rim top surface.

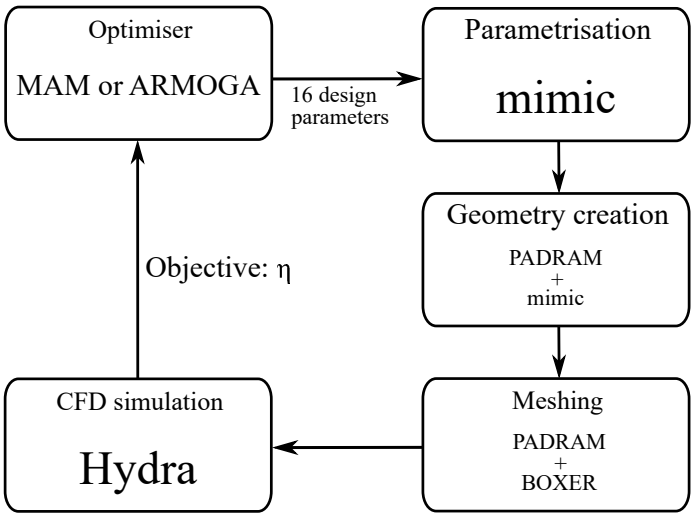

Figure 5.13: Aerodynamic squealer topology optimisation flowchart

The optimisation workflow is presented in Figure 5.13. Same as in the case of single rim squealer optimisation, the stator domain was meshed using a structured PADRAM mesh, and the rotor domain was meshed using BOXER. Finally, two different optimisers were used: MAM and ARMOGA.

5.2.2 CFD model

The CFD model used a mesh based on the mesh verification study presented in Section 3.2.1.3. The boundary conditions used were the same as in the winglet and single rim squealer optimisations presented earlier, given in Table 4.5. This included adiabatic simulations using a Spalart-Allmaras turbulence model. The BOXER mesh used in this optimisation for the case of the mimic-created tip is shown in Figure 5.14.

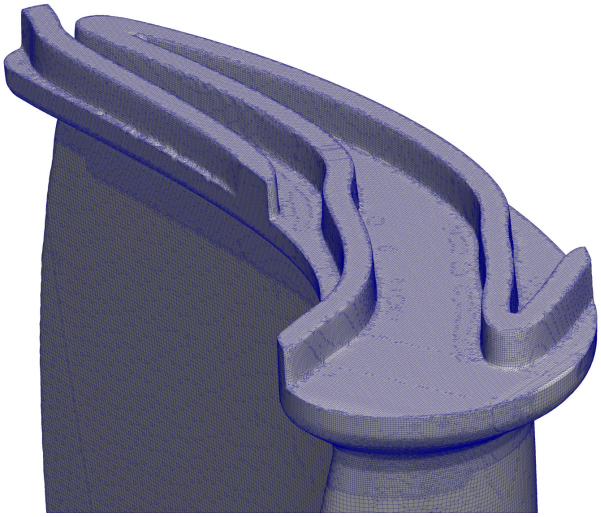

Figure 5.14: Topology squealer BOXER mesh

For the same mesh, y+ contour is given in Figure 5.14. It shows that for the whole blade area, y+ was at the order of unity, ensuring good boundary layer resolution.

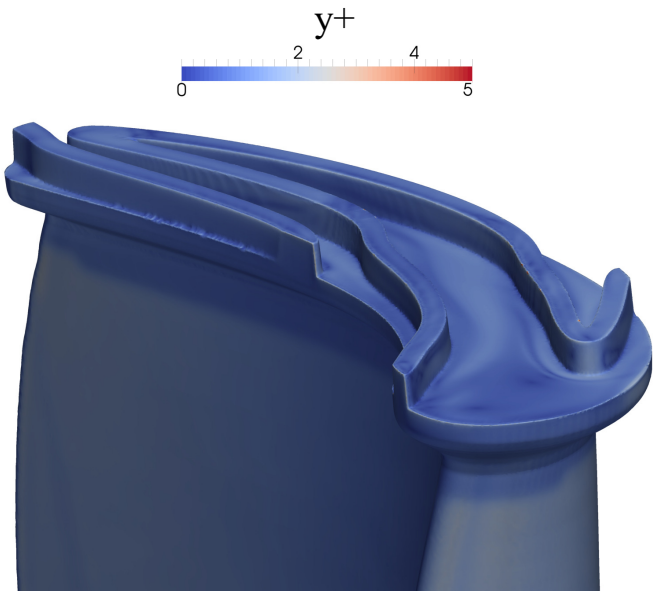

Figure 5.15: y+ contour for the topology squealer BOXER mesh

5.2.3 MAM optimisation

Aerodynamic optimisation was first carried out using MAM as the optimiser. The optimisation was run using 40 design points in MAM's sub-region, which was 2.5 times the number of design parameters and was assumed to be sufficient based on previous findings.

However, the MAM optimisation did not converge. Although MAM had been shown to quickly converge with a low-complexity design space in the winglet optimisation and with a simple radial basis function surface in the single rim squealer optimisation, it experienced regression issues when applied to a high-complexity design space such as the 4x4 control points grid that created the RBF surface.

Due to the complex squealer tip parametrisation used in this optimisation, resulting in a highly non-linear design space, MAM was unable to approximate the objective function using its linear regression. As it moved through sub-regions, after three sub-regions and 120 designs, it was unable to find a correct direction to shrink the trust region further and find an optimised design. In other words, of the 120 designs generated, the last 40 designs all had very similar design parameters that resulted in noticeably worse efficiency than some of the best performing designs from the first and second sub-regions. This was clear evidence that MAM had become stuck in a local minimum. The optimisation's results are shown in Figure 5.16.

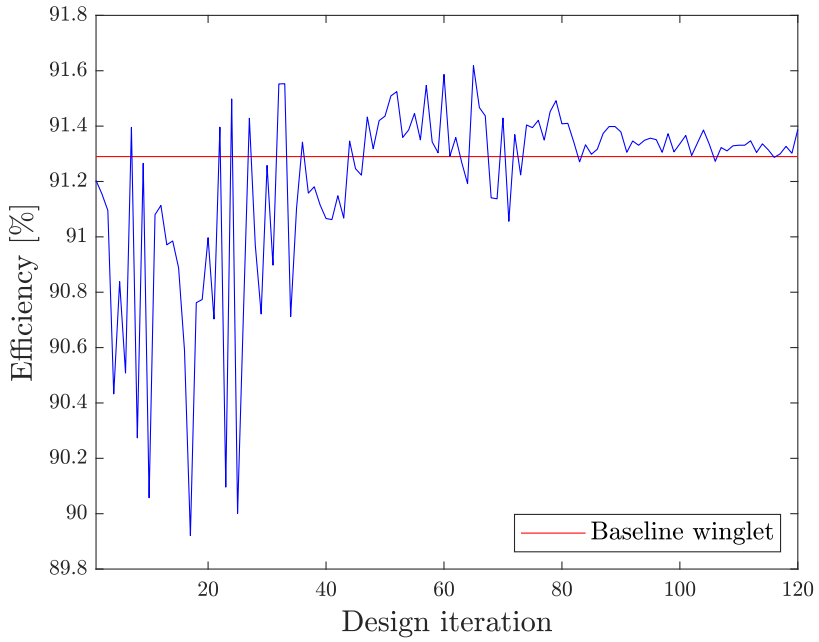

Figure 5.16: Results of initial MAM optimisation

5.2.4 ARMOGA optimisation on a response surface

Because of MAM's inability to deal with this design space and perform a successful optimisation, another approach was needed. To get around this problem and to investigate the design space more in detail, ARMOGA was used as the optimiser, with a surrogate model. In ARMOGA optimisation, the parametrisation approach was

kept the same as in the previous optimisation with MAM, using 16 design parameters explained in Section 5.2.1.

To create a surrogate model, the design of experiments (DOE) was generated using a Latin hypercube sampling approach. Two hundred designs were created for which CFD computations were performed. After that, the objective functions of these designs were interpolated using a Kriging response surface. The Kriging response surface used in this work was *Ordinary Kriging* from PyKriging. Its code and details are open-source and available on the PyKrige website [107].

Since this response surface was meant to be used as a two-stage model, its accuracy needed to be determined. That was done by performing a simple cross validation. To perform simple cross validation, a separate dataset that would be used as a reference was needed. It had a size of 20 designs and was generated using a Latin hypercube for which objective function values were acquired through CFD computations. Cross validation was then carried out by calculating the objective function for all 20 designs from the reference dataset using Kriging response surface prediction and comparing it to the actual value from the CFD. To assess the accuracy of the Kriging response surface, the coefficient of correlation, R^2, and the root mean square error, $RMSE$, were calculated. The results of cross validation show that after creation, the Kriging response surface with 200 designs had a very poor prediction of the design space, having a coefficient of correlation value of only 0.0065 and a root mean square error of 3.266.

To improve the response surface accuracy, the infill method explained in Figure 2.13, in which more points were fed into the response surface model, was used. The infill method was carried out by running ARMOGA optimisation on the existing response surface and updating it with 5 optimum designs per update.

Optimum designs that were to be used as updates to the existing response surface were selected as the ones for which ARMOGA optimisation predicted the best efficiency after being run for 20 generations with 30 designs in each generation. After ARMOGA's prediction, CFD computations were run for these 5 designs, and their design vectors and objective functions were fed into the response surface as real data. ARMOGA's setup used in this optimisation is given in Table 5.2.

The response surface update was repeated in batches of 5 designs per update, a total of 40 times, resulting in a total of 400 designs (200 initial and 200 updated designs) in the response surface. Throughout the infill process, measures of response surface accuracy (coefficient of correlation and root mean square error) were calculated

Number of generations	20
Size of generations	30
Starting generation of range adaptation	5
Interval generation of range adaptation	5
Relaxation coefficient of range adaptation	0.7
Crossover rate	1
Crossover parameter	2
Mutation rate	0.1
Mutation parameter	5

Table 5.2: ARMOGA optimiser setup

after every 10 updates (50 new designs). The change in overall response surface accuracy with its size is presented in Figure 5.17.

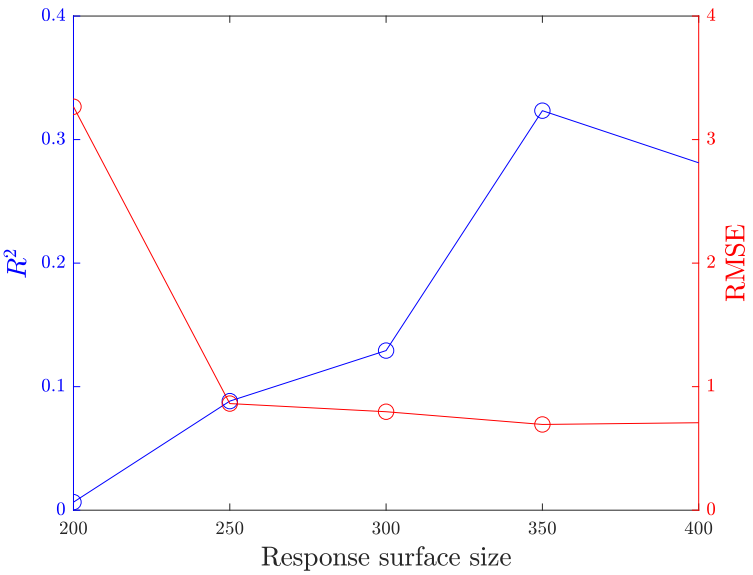

Figure 5.17: Kriging response surface accuracy

As shown in Figure 5.17, significant accuracy improvement of the Kriging response surface was recorded with the infill method. The coefficient of correlation was increased to around 0.4, and the root mean square error was decreased below 1. It is interesting to note that a significant change in the root mean square error was seen already after 50 updated designs, after which the value of around 0.9 was reached and did not change significantly with further updated designs. In the case of the coefficient of correlation, it improved at a roughly linear pace. In this process, the root mean square error was found to be a better parameter to assess the response

surface's accuracy, as it gave an idea of the size of the efficiency's prediction error. When dealing with turbomachinery efficiency improvements, an improvement at the order of magnitude of a few tenths of a percent can be very significant. Thus, if the response surface error is larger than the achievable optimisation gain, optimisation can be misleading.

To visualise the inadequate accuracy of the Kriging response surface, its efficiency prediction for the test dataset of 20 designs is plotted in Figure 5.18 against the CFD-computed efficiency for two cases. Figure 5.18a shows the accuracy of Kriging's efficiency prediction for the initial 200 designs with which it was initially created. Figure 5.18b shows the Kriging efficiency prediction after performing 40 updates, resulting in an overall Kriging size of 400 designs. As shown, after creation, the Kriging response surface had much larger efficiency variation for the 20 test dataset designs, predicting efficiency differences from worst to best of nearly 12 %. In reality, as shown by CFD computations for these 20 designs on the x-axis, that difference was around 4 %, where all designs but one were in the 2 % efficiency difference region.

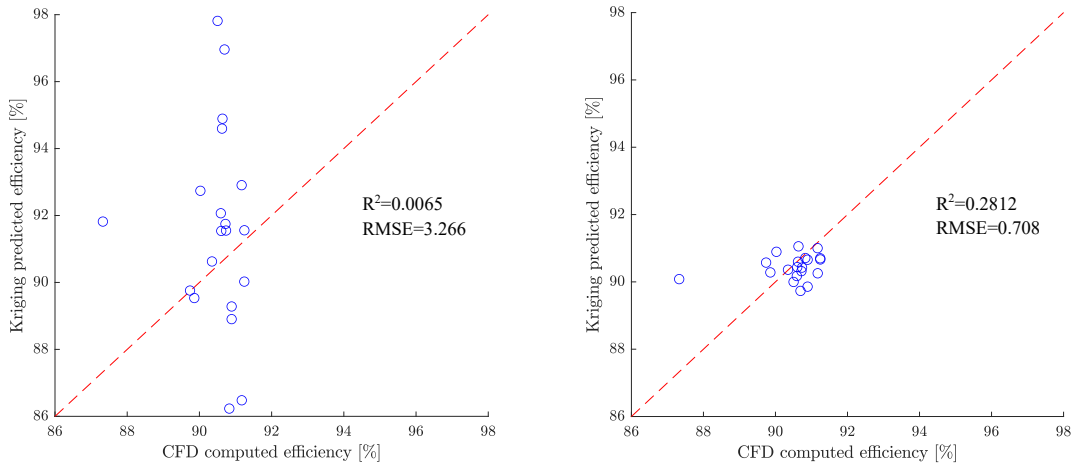

(a) 200 designs (b) 400 designs

Figure 5.18: Kriging response surface accuracy before and after the updates

After 40 infill updates of the Kriging response surface, which resulted in a total of 400 designs, the Kriging efficiency variation between the 20 test designs was significantly reduced, as shown in Figure 5.18b. About half of the test designs were accurately predicted, with an efficiency error of less than 0.1 %. For the other half of the test dataset, the error was larger, and one design had a considerably poor prediction. This design was in the low efficiency region, and the poor prediction of that region was found to be caused by the strategy of performing the infill updates.

Since the update strategy was to refine the response surface prediction around the optimum point predicted by ARMOGA, the low-efficiency region of the overall design space was continuously neglected and left less populated. This caused low prediction in that region and overall bad accuracy results of the response surface.

The alternative to this approach would be a general re-population of the design space, increasing the number of points by doing a new design of experiments. However, that was assumed to be computationally very expensive, and another approach was taken, which is presented next.

5.2.5 Constrained design space optimisation

After the inability of the Kriging response surface to accurately regress the design space of topology squealer optimisation, it was decided to focus on the most promising region of the initial design space. This was done by constraining some of the initial design parameters to a specific design subspace. In order to do that, all 400 designs from the response surface approach were analysed, and different topologies were examined. These are shown in Figure 5.19. The efficiency changes of designs in Figure 5.19 from the baseline winglet blade of the same tip gap are given in Table 5.3.

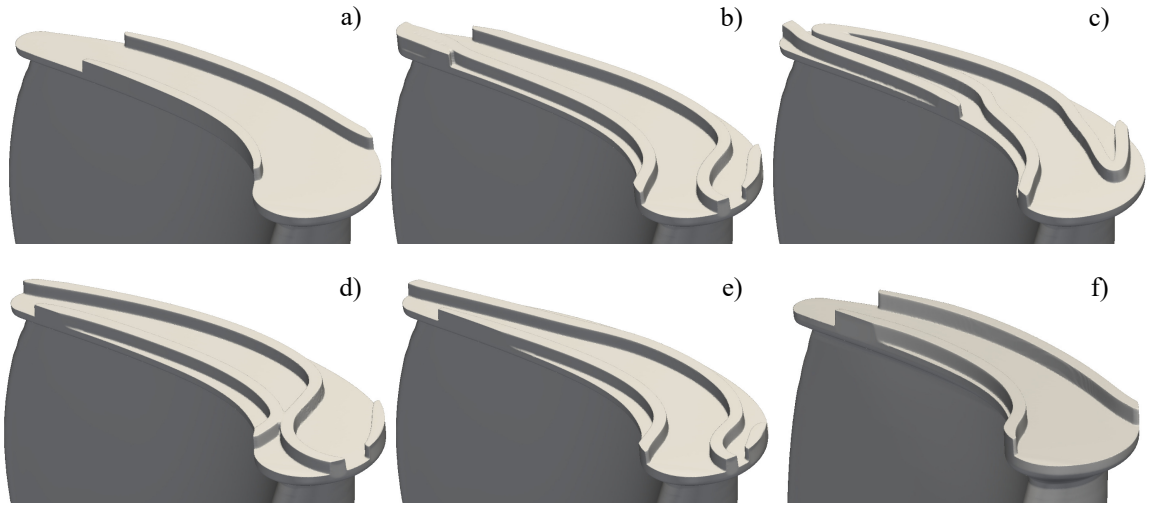

Figure 5.19: Best performing squealer topologies from response surface approach

As presented in Figure 5.19, the initial parametrisation approach explained in Figure 2.9 allowed for up to three parallel squealer rims to be created on the tip, alongside squealer rim openings. This parametrisation had the ability for squealer rims to remain continuous and to either open or close the leading and trailing edge regions. All of this has allowed for different topologies to be created and optimised.

Design	Efficiency change [%]
a)	+0.04
b)	+0.12
c)	+0.13
d)	+0.13
e)	+0.18
f)	+0.32

Table 5.3: Best performing designs efficiency increase

Looking at the best performing designs in Figure 5.19, it can be seen that all designs featured two parallel squealer rims, except for design c) which had three. Also, all designs had both leading and trailing edge openings, features that are known to be state of the art. Furthermore, upon observing the flow differences of different topologies, it was noticed that the different placement of the squealer rims across the tip also had a big effect. Placing the squealer rims away from the tip edge formed the squealer shelves, which were found to have a significant impact on the overtip leakage flow.

Based on all of these findings, as well as the findings from Schabowski and Hodson [35], Caloni et al. [48], and most recently, from De Maesschalck et al. [104], it was decided to constrain the initial design space into the most promising design subspace as presented in Figure 5.20. This included a parametrisation that allowed for the creation of up to two parallel squealer rims with possible openings (or cuts), each alongside pressure and suction side, and also ensured the squealer leading and trailing edge openings.

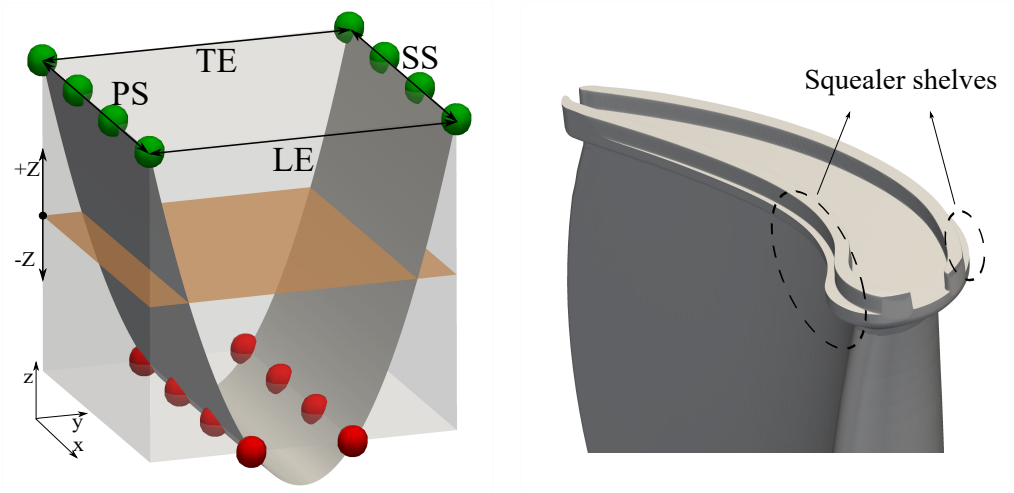

(a) Design parameters (b) Resulting blade

Figure 5.20: Constrained squealer topology design space

To ensure the creation of up to two squealer rims, the initial design space presented in Figure 2.9 was simplified by constraining the allowed movement of half of the points that created the radial basis function surface. The number of points and therefore the design parameters were kept at 16. The points corresponding to the pressure and suction side surfaces, shown in green in Figure 5.20, were allowed to move as before in the whole range of the z-direction, both positive and negative. However, the other half of the points (shown in red) were allowed to move just in the negative z-direction. By keeping the red points negative, it was ensured that up to two parallel squealer rims would be created. The squealer tip created with the parametrisation shown in Figure 5.20a is shown in Figure 5.20b.

Allowing the whole range of the z-direction for the green points meant that openings on the squealer pressure and suction side rims were possible. This is shown in Figure 5.21.

In Figure 5.21, both the effect of allowing half of the control points to move in the whole z-direction, alongside constraining the other half to the negative z-direction, is explained. Starting from the control points that were assigned to the pressure side, two of them that controlled the squealer at the front portion of the blade (shown in the black dotted detail of Figure 5.21a) were brought into negative z-values to eliminate the pressure side squealer rim in the front portion of the tip. This way, cuts in squealer rims were made possible for both pressure and suction side squealers, simply by bringing down the control points in green into negative values.

To change the position of the squealer rims across the tip and create and change the size of squealer shelves, the effect of changing the values of control points that were always kept negative is shown in the red dotted detail of Figure 5.21a. Starting from the control points shown in Figure 5.20a, two control points in the front portion of the tip's suction side were brought from the value of -0.5 to -0.05. This changed the position of the suction side squealer rim, bringing it much closer to the middle of the tip. This is shown in Figure 5.21b. This created a much larger squealer shelve than in the case of a blade shown in Figure 5.20b.

With the used parametrisation, a range of topologies was allowed to be created, trying different combinations of squealer rim openings and the position of the squealer rim across the tip.

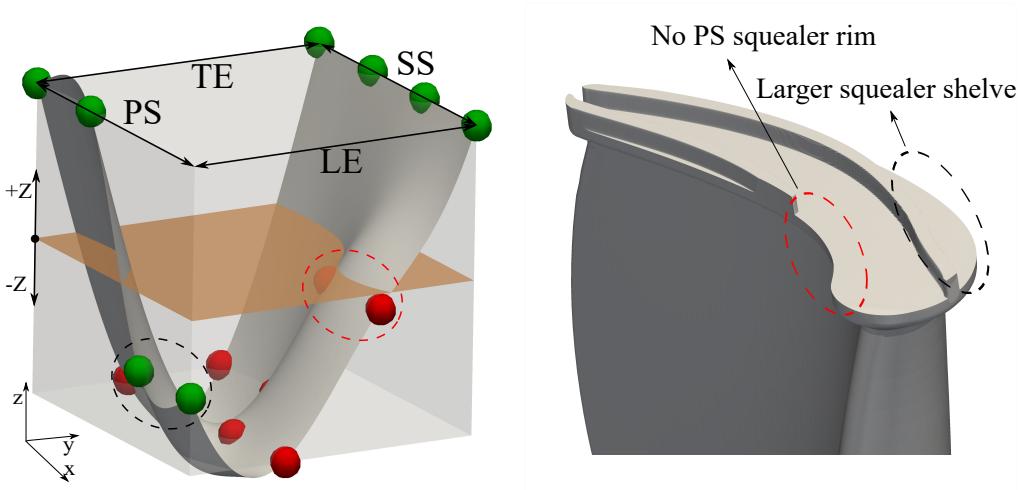

(a) Design parameters

(b) Resulting blade

Figure 5.21: Effect of changing design parameters in constrained squealer topology design space

The optimisation was run using the MAM optimiser for eight sub-regions, each of which had 40 design iterations. Its convergence history is given in Figure 5.22. The efficiency of the tested designs is plotted against the baseline winglet with the same tip gap. It can be seen that the optimisation took around 200 designs to converge, after which no large jump in efficiency was observed. In the first part of the optimisation, which corresponded to two MAM's narrowing of the trust regions, large efficiency changes are visible. In that stage, up to around the 80th iteration, the optimiser was performing a wide direction search, which resulted in some bad designs that had no or very small squealer rims. Those designs resulted in having bad efficiency values, lower by 1.5 % compared to the baseline winglet. However, despite the creation of some bad

designs, the initial phase had some designs that performed significantly better than the baseline winglet. With that information at hand, despite dealing with a design space that allowed different topologies, the optimiser successfully narrowed down the search region, and after around the 80th design iteration, almost all designs were better performing than the baseline.

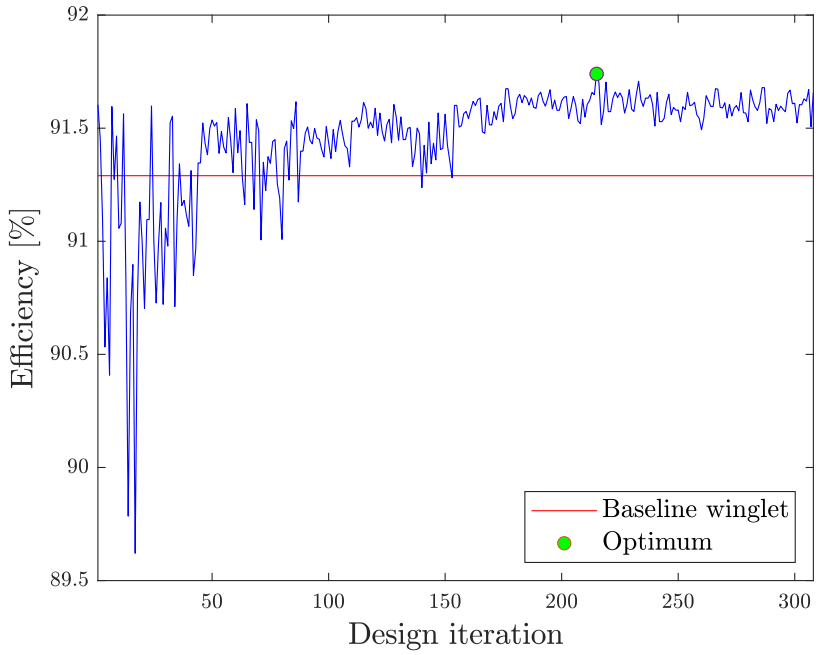

Figure 5.22: Constrained squealer topology optimisation convergence

After around the 200th design iteration, all designs had similar topologies, with small variations in squealer rim positions and their lengths. This caused the optimisation convergence to be slightly noisy as it had some impact on the performance. However, in that region, all tested tips had efficiency variations of not more than 0.15 %, and the optimisation was assumed to have converged and was stopped. The optimum design, having an efficiency increase of 0.46 % over the baseline winglet, is presented in Figure 5.23.

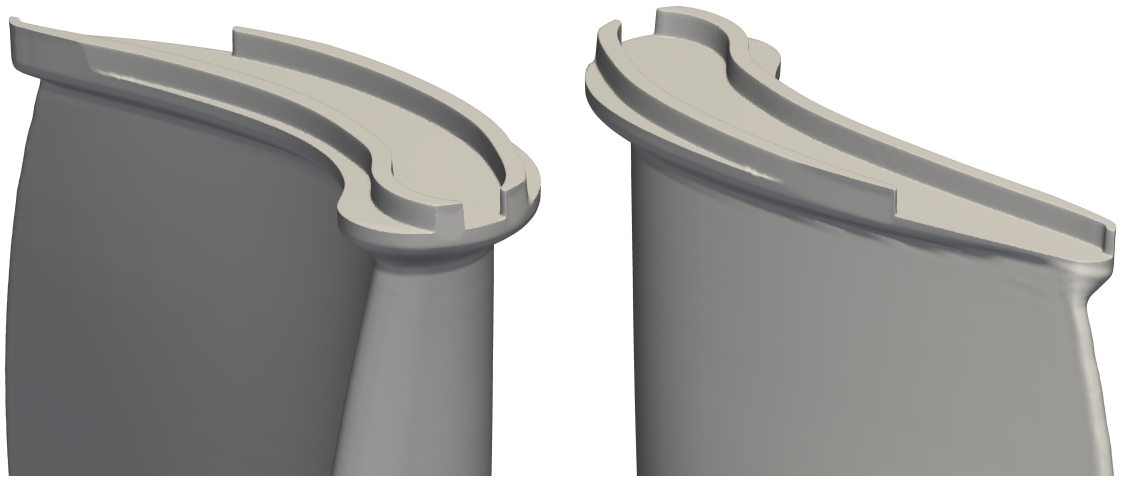

(a) Leading edge and pressure side (b) Trailing edge and suction side

Figure 5.23: Optimum topology squealer

As presented in Figure 5.23, the optimum squealer tip featured both pressure and suction side squealer rims, which were ensured by the parametrisation and had openings at the leading and trailing edges. Additionally, it had an opening at the suction side of the trailing edge, which is a common feature of high-efficiency squealers, as seen in studies by Anderoli et al. [50] and De Maesschalck et al. [104]. Another interesting feature of this squealer tip was that, in the first half of the tip around the leading edge region, squealer rims were moved away from the tip edge, narrowing down the squealer cavity width. Conversely, opposite behaviour was seen in the trailing edge region, where squealer rims were kept at the tip edge, resulting in the widest possible squealer cavity.

To explain the sources of efficiency increase, the flow features of the optimised design were examined more in detail and compared against the baseline winglet tip. The pressure distribution around the tip was plotted first, as shown in Figure 5.24.

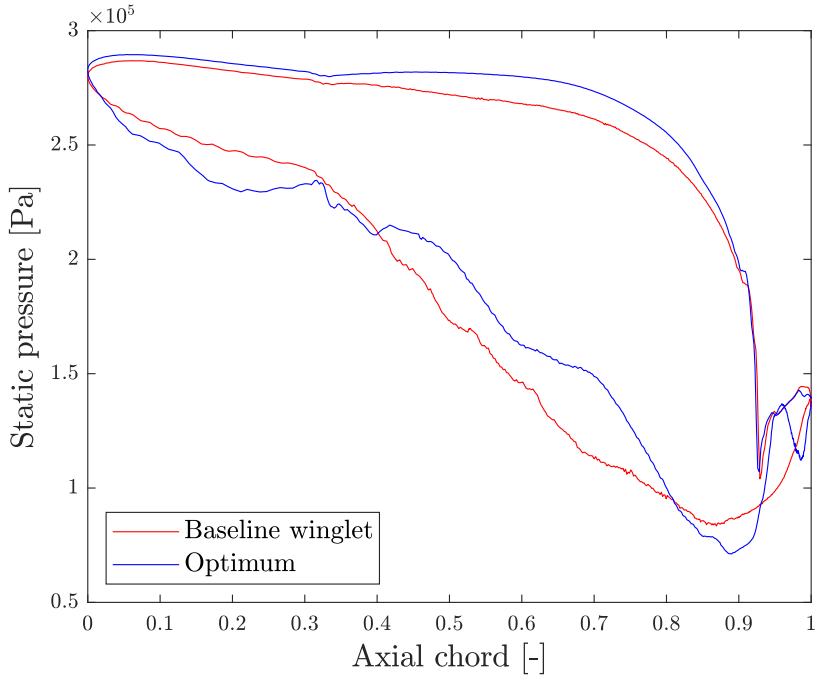

Figure 5.24: Pressure distribution around the baseline winglet and optimum squealer tips

As shown, the pressures around the two tips were quite different. The baseline winglet had features already seen in the winglet tips, with a very small pressure difference in the whole leading edge region, up to 0.3 of the axial chord. After that, the suction side pressure started sharply decreasing, caused by the over tip leakage vortex formation. In the case of the optimum squealer, the pressure difference was similar, with mostly both pressure and suction side pressures higher than in the case of the baseline winglet. This was found to be caused by the squealer shelves, which caused a stagnation region on the pressure side and pushed the leakage flow away from the tip on the suction side.

It is important to note that, since this comparison involves comparing essentially two different tips, a winglet and a squealer with gaps, it was not possible to plot the pressure at the same span. The pressure was then plotted around the winglet outlines, as that was the fairest comparison. But because the flow, and therefore the static pressure, was changed by the squealer rims, which were away from the winglet outlines, it was difficult to judge the performance of the squealer tip based on the static pressure. Thus, flow differences were further examined by looking at the tip leakage mass flow.

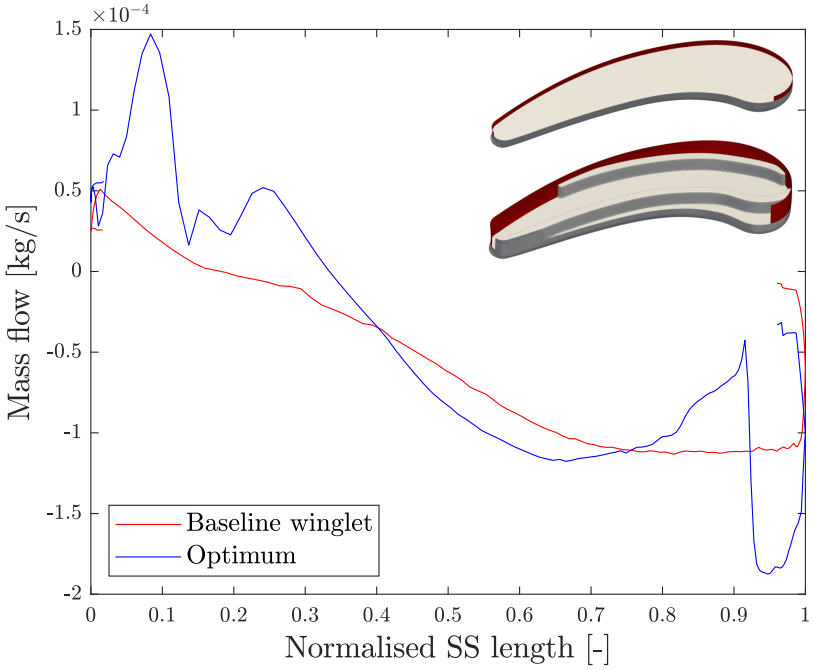

Figure 5.25: Suction side tip leakage mass flow comparison

Mass flow around the baseline winglet and optimum squealer tips is shown in Figure 5.25. Two tips with suction side surfaces, on which tip leakage mass flow was measured (in red), are shown alongside the mass flow distributions. Positive mass flow denotes flow entering the tip gap and negative leaving the tip gap. It can be seen that both tips had mass flow entering the tip gap in the early portion of the suction side. This ended around 0.15 of the suction side length in the case of the baseline winglet. In the case of the optimum squealer, a big jump in mass flow entering the tip gap was seen around 0.1 of the suction side length. That region corresponded to the leading edge opening. Around 0.15 of the suction side, mass flow sharply decreased but still stayed positive, indicating that the flow was still entering the tip gap. The location of a sharp drop around 0.15 of the suction side corresponded to the area where the suction side rim was originating, right on the tip edge. Tip mass flow was still positive from that point until approximately 0.35 of the suction side. This was caused by the suction side squealer shelf that entrained the flow into the corner between the tip and the suction side rim. After around 0.35 of the squealer tip's suction side length, flow started to leave the tip gap and quickly rose over the winglet's value as the suction side squealer shelf narrowed. Around 0.7 of the suction side length, the squealer's suction side shelf ended and the leakage flow started to decrease as the suction side rim reached the tip edge. In this region, just before the

suction side squealer opening, little leakage flow was seen to leave the tip gap. After around 0.9 of the suction side, the suction side rim opened up, and the leakage flow increased considerably, reaching the maximum suction side value.

Overall, after integrating the two curves, it was found that the optimum squealer tip had 20.05 % lower leakage mass flow than the baseline winglet tip.

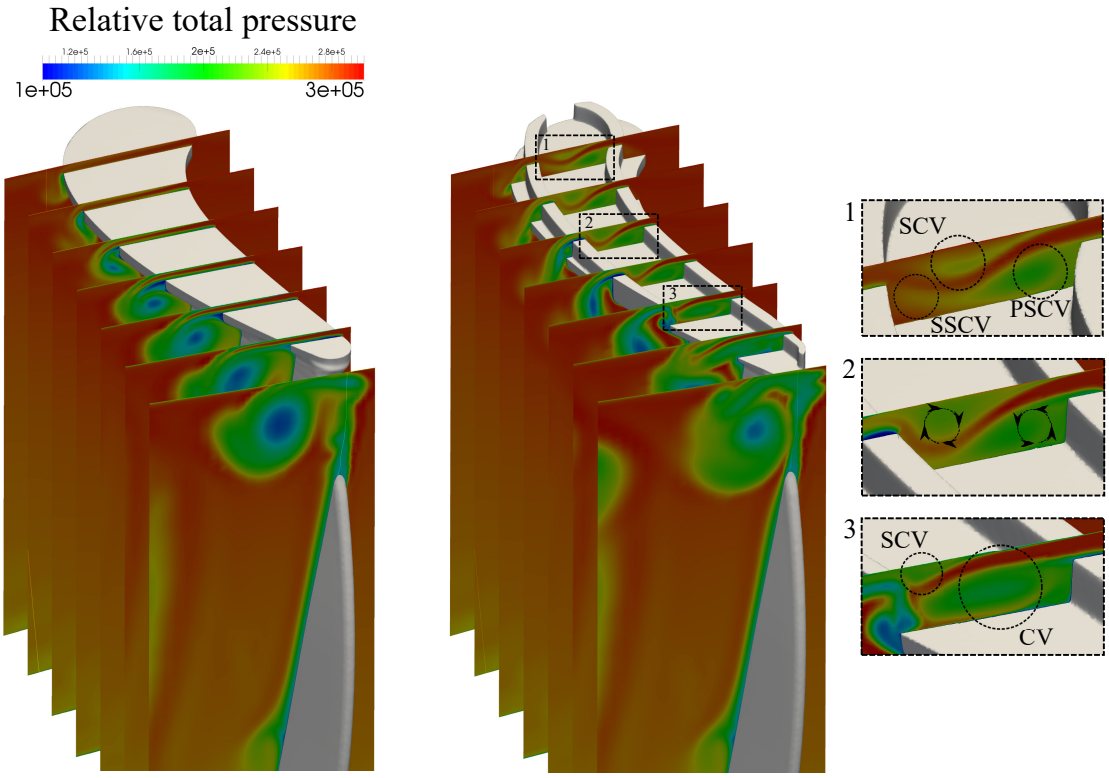

(a) Baseline winglet (b) Optimum

Figure 5.26: Over tip leakge vortex

Tip leakage of the two tips is visualised in Figure 5.26, showing slices of relative total pressure. In the leading edge region of the squealer cavity, flow entering the squealer cavity over the pressure side rim rolled up into a pressure side corner vortex (PSCV) that developed alongside the pressure side rim. Flow that entered the squealer cavity through the opening at the leading edge split into two parts. One part rolled into the scrapping vortex, which stretched alongside the suction side rim, and the other part rolled into the suction side corner vortex (SSCV) alongside the suction side rim. These three vortices are shown in detail 1 in Figure 5.26b. As the scrapping vortex enlarged, the suction side corner vortex was pushed out of the tip gap and initiated the over tip leakage vortex. After around 0.4 of the axial chord, only two vortices remained in the tip gap, the counter rotating pressure side corner vortex and

the scrapping vortex, shown in detail 2. Further down the squealer cavity, once the suction side rim ended, leakage flow that formed the scrapping vortex left the tip gap through the opening at the late suction side. After that, the corner vortex filled the whole squealer cavity and exited the tip gap at the trailing edge area. These squealer tip leakage flow features are also shown in Figure 5.27, using the contours of the Q criterion.

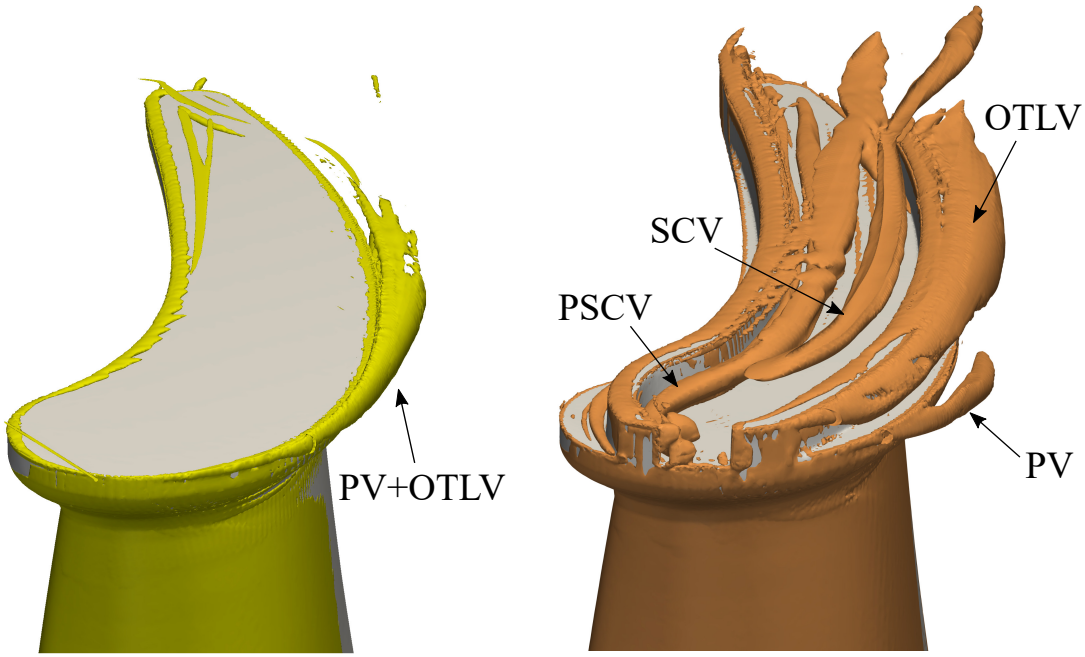

(a) Baseline winglet tip

(b) Optimum tip

Figure 5.27: Tip leakage flow visualised using Q criterion (6^{10})

The contours of the Q criterion present a good image of the different vortices found inside the squealer cavity. It can be seen that constant placement of the squealer rims away from the tip edge in the front portion of the blade ensured a constant squealer cavity, which in turn made possible the formation of squealer cavity vortices resulting in a good sealing effect. Also, it is worth noting the different behaviour of the tip leakage and passage vortices. In the case of the baseline winglet, these two vortices were found to merge, as noted in Figure 5.27a. In the case of the optimum squealer, the over tip leakage vortex formation was delayed and the passage vortex was separated. This resulted in slightly different shearing losses in the blade's wake. To see how the leakage flow affected shearing losses, the radially averaged entropy is shown for both tips in Figure 5.28.

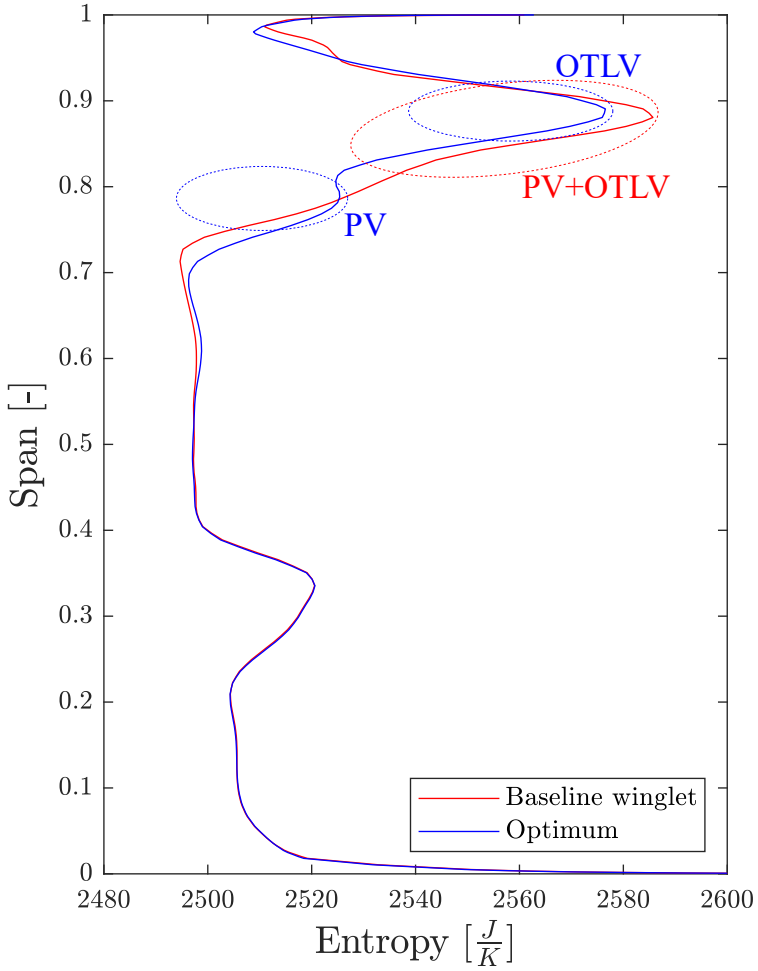

Figure 5.28: Circumferentially averaged entropy field at 0.5 axial chord downstream of the trailing edge

Interestingly, starting from the casing, despite the more complicated tip leakage flow, the optimum squealer was found to have slightly smaller entropy creation than the baseline winglet tip. This is seen in the region above 0.95 of the span. Between 0.8 and 0.9 of the span, the baseline winglet had larger entropy creation because of its increased amount of leakage flow, and therefore, the shearing losses. The squealer tip had a weaker tip leakage vortex in strength, but larger in size, stretching further down compared to the baseline winglet. In the region around 0.75 of the span, additional loss for the squealer was caused by the passage vortex, as noted in Figure 5.28. Below 0.7 of the span, no difference was seen between the two tips.

5.3 Aerothermal squealer tip topology optimisation

With the successful performance of aerodynamic topology optimisation using a topology-based parametrisation approach, the next step was to conduct aerothermal optimisation.

For this optimisation, the constrained squealer topology design space presented in Figure 5.20 was used. The aerothermal model was built using the 3-temperature model, as explained in Section 4.2, and previously used in the aerothermal winglet tip optimisation in Section 4.7.

Before applying the same modelling approach to the aerothermal squealer tip topology optimisation, the unstructured Boxer mesh had to be verified for the heat transfer results. This is presented first, followed by the accuracy of the 3-temperature method, after which a final model is given.

After that, different optimisation strategies are explained, response surface-based genetic algorithm optimisation, and separately, direct genetic algorithm optimisation. For each approach, the optimisation strategy is presented alongside the results and analysis of the specific tip shapes.

5.3.1 Aerothermal unstructured mesh verification study

Similar to the case of an aerothermal structured mesh study for winglet optimisation explained in Section 4.1, an unstructured Boxer mesh was firstly verified for the aerothermal results. This was done by starting from the aerodynamically verified mesh presented in Section 3.2.1.3, which was used in the aerodynamic topology optimisations presented in Sections 5.1 and 5.2. From the rotor mesh used in the aerodynamic squealer topology optimisation, two additional rotor meshes of 22 and 31 million cells were created. This study was done on the blade with a winglet squealer tip that was created by hand, using the same parametrisation presented in Figure 2.9. Using the same baseline winglet as presented in Figure 5.12 and Table 5.1 to create a winglet squealer tip, the squealer rim width and height were also in this case kept constant. The squealer rim width and height were larger than the tip gap for 43 % and 86 %, respectively. The tip gap was constant with a value of 1.5 % of the blade span, measured from the squealer rim top surface.

All three meshes had the same first cell height in the boundary layer mesh with an expansion ratio of 1.2. The mesh with 11 million cells had 20, the 22 million mesh had 30, and the mesh with 31 million cells had 40 cells in the boundary layer mesh. This

resulted in similar y+ values which were at the order of 1, as shown in Figure 5.29. Other refinements included refining the tip region and blade surface mesh as this was very important to capture the surface heat transfer correctly. All three meshes had the same refinement strategy, but their level varied.

For these meshes, both aerodynamic and aerothermal properties were observed. For that, two CFD simulations were run for each mesh, one adiabatic and one aerothermal. Adiabatic simulations were done using standard MT1 turbine boundary conditions given in Table 4.5. Aerothermal simulations were done using the same boundary condition but also imposing a constant rotor blade wall temperature of 266 K.

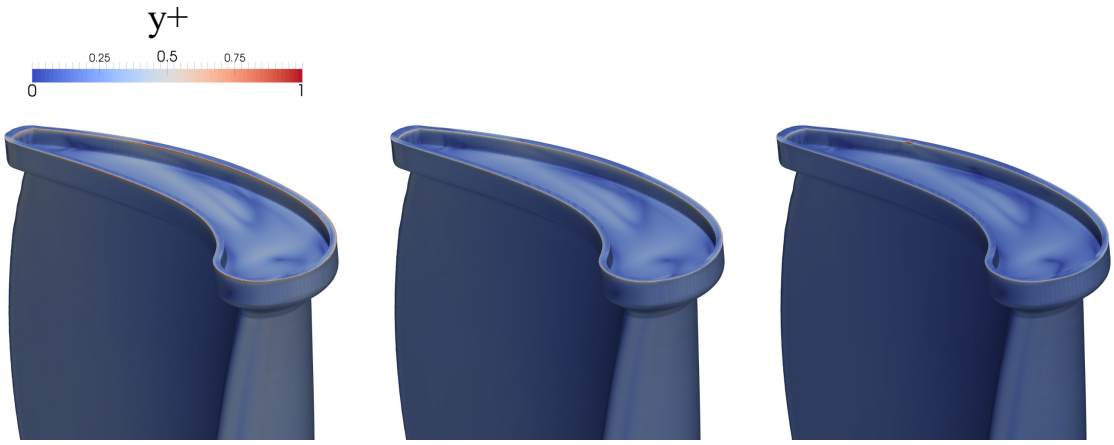

(a) 11 million (b) 22 million (c) 31 million

Figure 5.29: y+ contours for three different winglet squealer tip meshes

The heat flux from the aerothermal simulations on the blades with winglet squealer tip for the three tested meshes is shown in Figure 5.30. It can be seen that all three meshes produced similar tip gap flow features and, therefore, similar heat transfer results. Focusing on the tip, hotspots were found to be at the same location and of similar size for all three meshes. Leakage flow separation in the tip leading edge region was also predicted similarly for all three meshes, but the two finer meshes had slightly higher heat transfer there. Another hotspot on the cavity floor, which stretched through the middle of the tip, was also predicted similarly for all three meshes and was a result of a trapped vortex. By observing its magnitude, it was found that it was slightly underpredicted by the coarsest mesh. At the late suction side part of the squealer rim, over which a significant part of the leakage flow was found to leave the tip gap area, another hotspot was seen. All three meshes had a very similar prediction of that phenomenon.

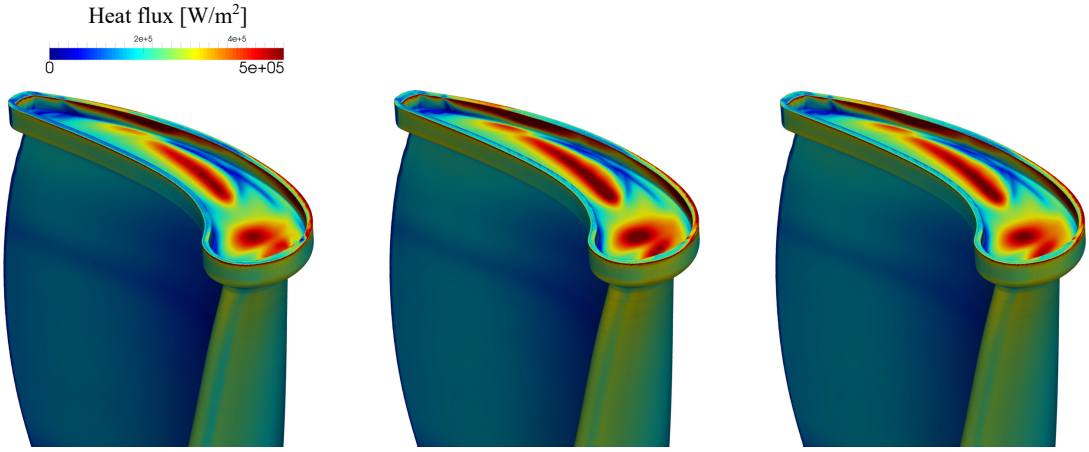

(a) 11 million (b) 22 million (c) 31 million

Figure 5.30: Heat flux for three different winglet squealer tip meshes

Apart from heat transfer, efficiency, and tip leakage mass flow, adiabatic simulations were also conducted to monitor them. The efficiency difference between all the meshes was very small, only 0.08 % from the coarsest to the finest mesh. The tip leakage flow was integrated over the blade suction side and normalised against the single passage flow, and only negligible differences were observed. Finally, the tip heat transfer was normalised against the heat transfer over the whole blade. Refining the mesh from 11 to 22 million changed the tip to blade heat transfer ratio by almost 1 %, but this value did not change significantly with further refinement to the finest mesh. These results are summarised in Table 5.4. The mesh with 22 million cells was assumed to be mesh size independent and was used in the following optimisations. It is illustrated in Figure 5.31.

Rotor mesh size [million]	Efficiency difference [%]	OTL mass flow [%]	Tip to blade heat flux ratio [%]
11	0	3.74	25.20
22	-0.06	3.72	26.26
31	-0.08	3.81	26.42

Table 5.4: Unstructured rotor mesh verification study

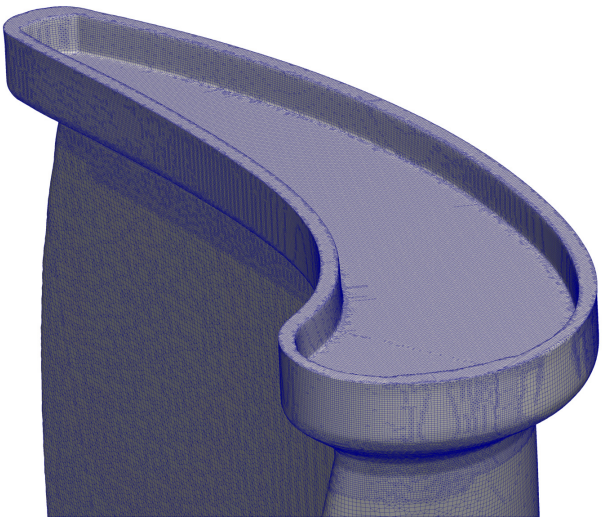

Figure 5.31: Aerothermally verified unstructured mesh used in the optimisations

5.3.2 Accuracy of the 3-temperature model

In this section, the accuracy of the 3-temperature model is presented for a winglet squealer tip that was created with mimic, using the same baseline blade shown in Figure 5.12. Same as in the case of winglet optimisation, the heat transfer coefficient was computed for a wall temperature corresponding to a TR of 0.6 (266 K) using Equation 2.50 with the 3-temperature model. The heat transfer coefficient on the winglet squealer blade is shown in Figure 5.32.

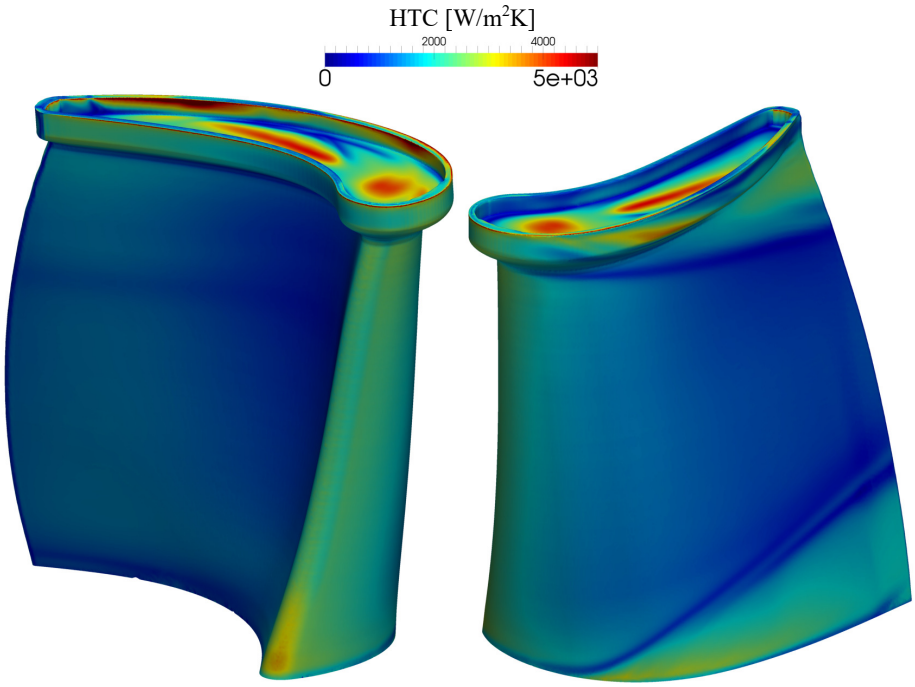

Figure 5.32: Heat transfer coefficient on the blade with a winglet squealer tip for a wall temperature corresponding to TR of 0.6

The Figure 5.32 shows that the heat transfer coefficient on a winglet squealer tip results in a much more complicated tip heat load compared to the winglet tip. This is caused by the more complex tip geometry that produces more complex flow, characterised by different tip cavity separations and vortices. These result in complicated heat transfer hotspots, especially on the squealer cavity floor and the suction side squealer rim. To evaluate how well the 3-temperature model predicts this behaviour, heat flux was computed for the case of the wall temperature corresponding to a TR of 0.6 using both direct CFD and the 3-temperature model. The comparison of these results is shown in Figure 5.32.

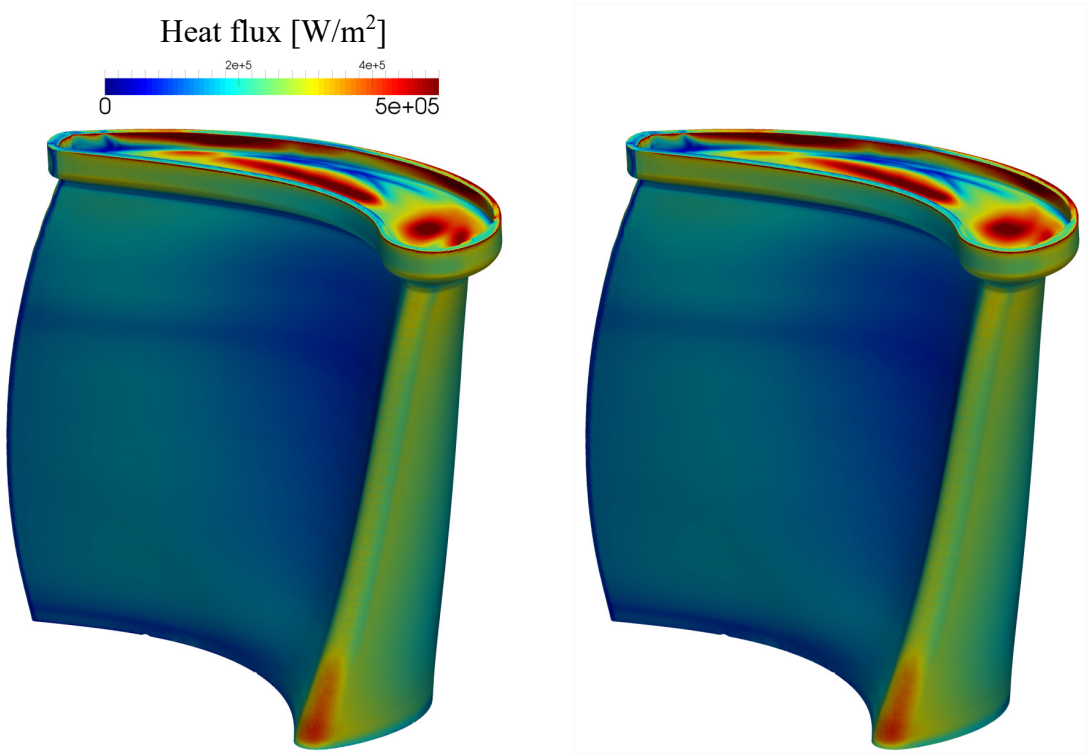

(a) CFD (b) 3-temperature model

Figure 5.33: Comparison of heat flux on blade pressure side for wall temperature corresponding to TR of 0.6

The wall heat flux on the blade pressure side was found to be similar for both sources, and upon comparing two contours, no difference was immediately observed. However, some differences can be noticed at the squealer cavity floor in the leading edge region, where the two models had slightly different predictions of the leakage flow separation. A similar situation was found on the blade suction side, as shown in Figure 5.34. There, both models had almost identical predictions of the flow separation, including the rubbing of the over tip leakage vortex at the late suction side.

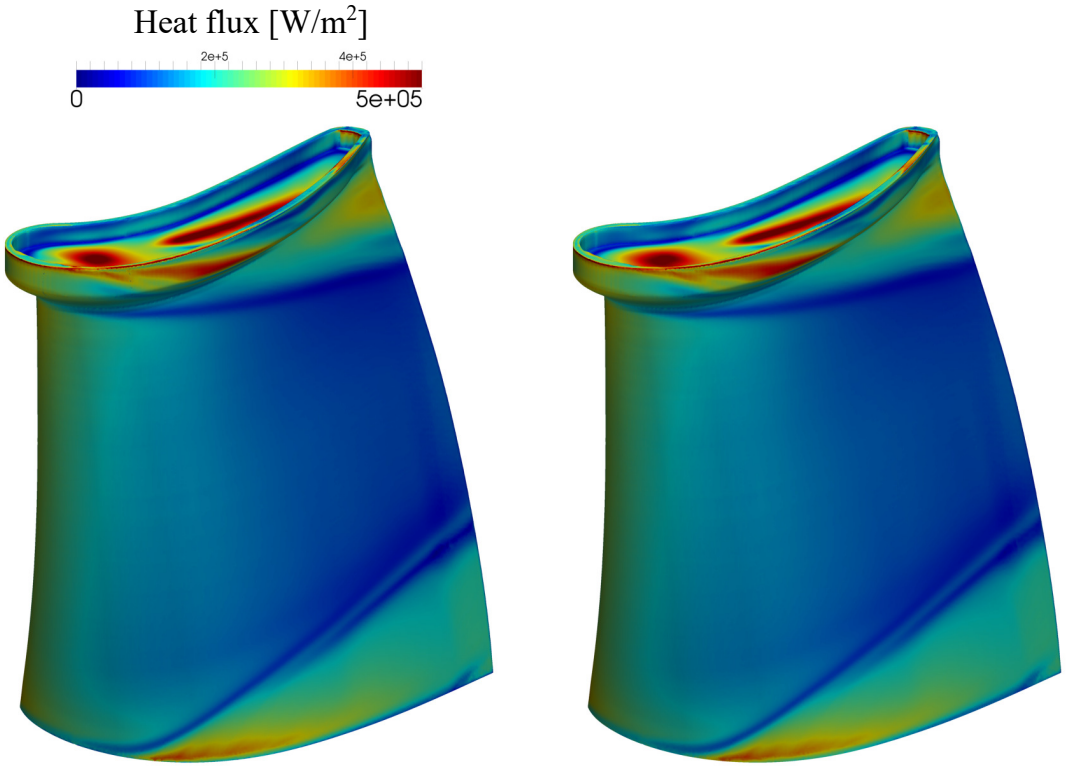

(a) CFD (b) 3-temperature model

Figure 5.34: Comparison of heat flux on blade suction side for wall temperature corresponding to TR of 0.6

To quantify the differences between the two sources in more detail, the heat flux error was calculated using Equation 4.1, and the results are shown in Figure 5.35.

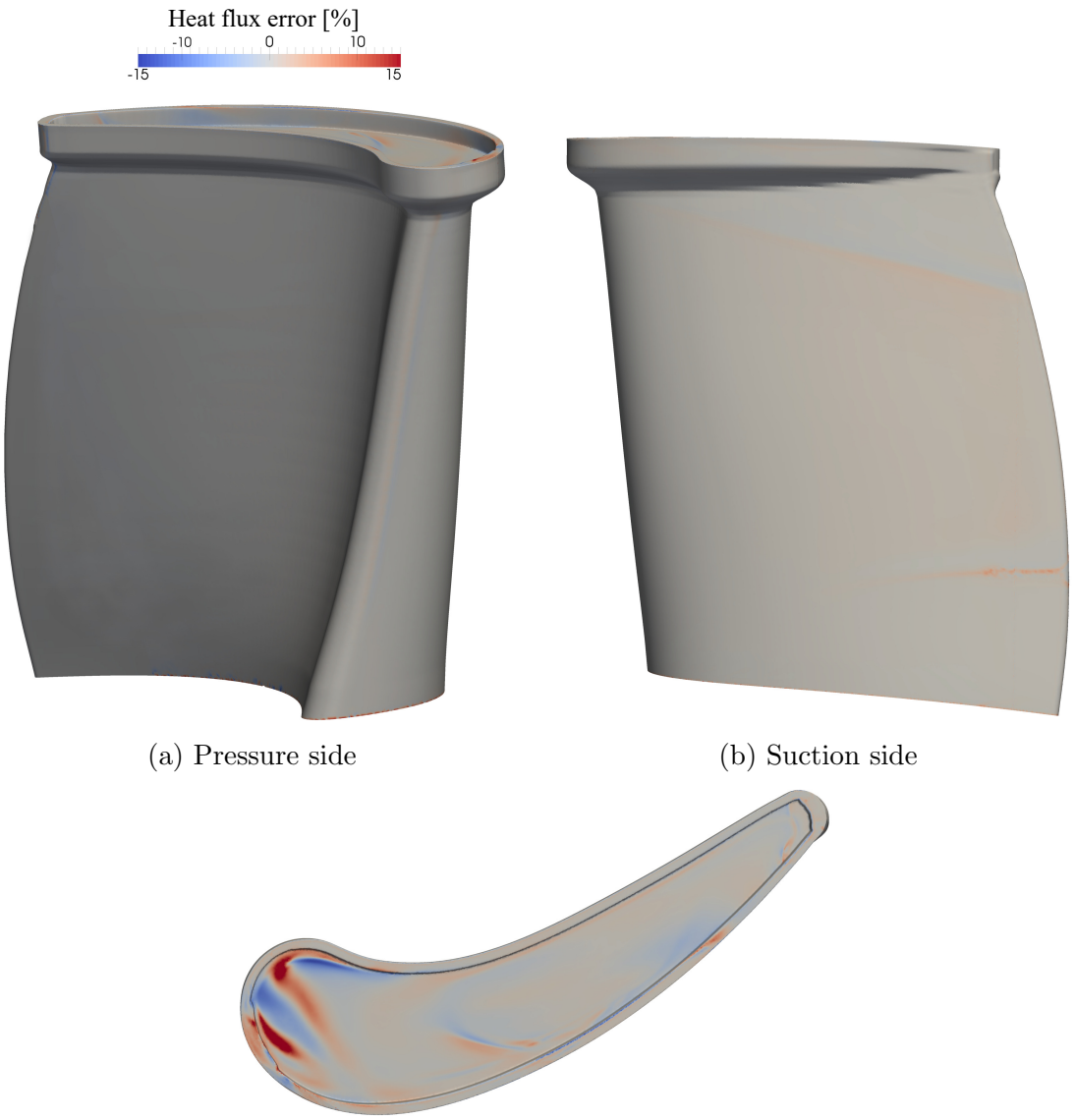

(a) Pressure side

(b) Suction side

(c) Tip

Figure 5.35: Heat flux error on a blade with the winglet squealer tip

The Figure 5.35 shows that the 3-temperature model gave a very good prediction of the heat flux on the pressure side of the blade. The region with the highest error in Figure 5.35a was found to be the leading edge stripe, stretching through the whole blade span. But even in this region, the error was very small.

More noticeable error is present on the blade suction side, shown in Figure 5.35b. Similar to what was seen in the case of the winglet tip (Figure 4.5), the 3-temperature model had a poorer prediction on the suction side and in the regions where the flow had lower pressure and was separated. An overprediction of heat flux of up to 5 % was found at the second half of the blade suction side, under high flow turning and low

	Integrated heat flux - blade [W]	Integrated heat flux - tip [W]
Direct CFD	638.33	162.37
3-temperature model	639.71	162.58
Error [%]	0.22	0.13

Table 5.5: 3-temperature model error in the case of a squealer tip

pressure. A slight underprediction was seen in the region where the over tip leakage flow rubbed the blade and joined with the rest of the passage flow.

The highest heat flux error was found in the squealer cavity, where large regions of overpredicted and underpredicted heat flux were seen, reaching up to $\pm$ 15 %. This is shown in Figure 5.35c.

Large differences in heat flux were noticed, especially in the front portion of the tip, in the leading edge region. These were found to be caused by different predictions of flow impingement and separation locations. Interestingly, the heat flux error contour patterns were found not to follow the flow patterns seen in Figure 5.33. A similar level of heat flux error at the tip for the case of a winglet squealer was also found by Zhang and He [26].

In the end, the heat fluxes obtained from the two sources were integrated over the whole blade surface and the tip, separately. These are shown in Table 5.5. Despite some errors by the 3-temperature model on the blade suction side and on the tip, when the heat flux was integrated over the whole blade surface, an overprediction of only 0.22 % was found. By integrating only over the blade tip, an overprediction of 0.13 % was found.

Looking at the contour plots and the overall integrated values, it can be concluded that if hot regions are of special interest in the design process, the 3-temperature method is not particularly accurate in the flow-sensitive regions. However, since in these optimisations, the integrated value of the heat transfer coefficient was used as the heat load objective, the 3-temperature model was found to give an accurate representation of the heat load objective as the optimisation objective.

5.3.3 Surrogate model optimisation

The surrogate model optimisation was carried out by running ARMOGA on the artificial neural network (ANN) response surface. To create the artificial network response surface, a dataset of 300 design points was used, which came from two sources. Before carrying out the surrogate model optimisation, initial direct ARMOGA optimisation

study was done, resulting in 150 design points. With the data obtained, it was decided that it would be used to create a response surface. However, since this data came from direct ARMOGA optimisation and was assumed not to have a good overall representation of the design space, this needed to be addressed. Therefore, 150 designs were additionally created using a DOE with a Latin hypercube. For a total of 300 designs gathered, CFD simulations were run, and the objectives were extracted. For these two objectives, separate artificial neural network response surfaces were created. Finally, with the two ANN response surfaces obtained, two optimisations were run, both using ARMOGA as the optimiser. To judge the accuracy and capability of this optimisation approach versus the optimisation presented in Section 5.2, aerodynamic optimisation was run using only the efficiency response surface. Separately, both the efficiency and the heat transfer coefficient response surfaces were used in the aerothermal optimisation.

In this aerothermal squealer topology optimisation, parametrisation of the squealer was done using mimic. To be more specific, mimic's constrained design space was used, explained in Section 5.2.5 and Figure 5.20, having the same design parameters and their limits.

CFD simulations were run using boundary conditions given in Table 4.5 and k-ω SST turbulence model. The 3-temperature method was used to obtain the heat transfer coefficient at a rotor blade for a temperature of 266 K. The overall optimisation approach is illustrated in Figure 5.36.

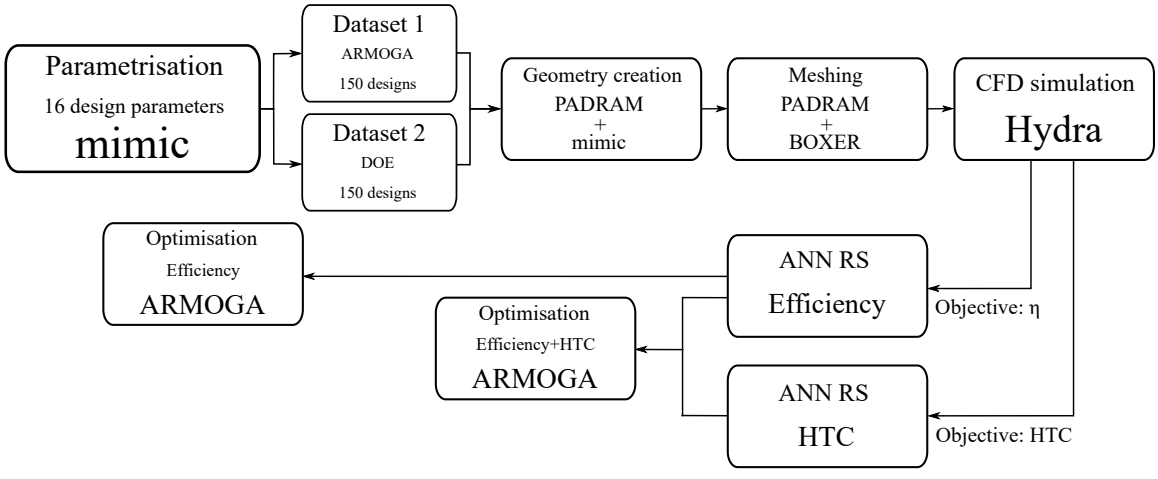

Figure 5.36: Aerothermal surrogate model squealer topology optimisation flowchart

5.3.3.1 Creating ANN response surfaces

300 design points that were used to create the ANN response surfaces are summarised in Figure 5.37. The optimisation objectives, efficiency, and the integrated heat transfer coefficient, were scaled against the winglet squealer design taken as a reference.

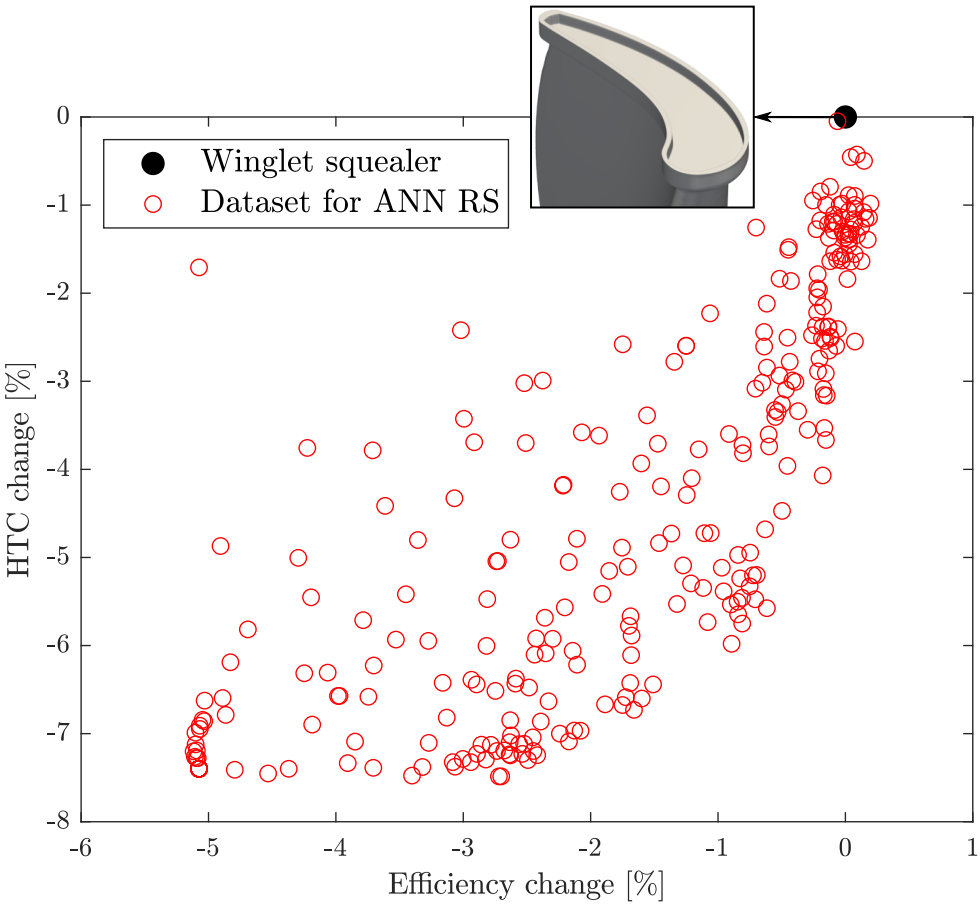

Figure 5.37: Dataset for ANN response surfaces creation

It can be seen that the used dataset covers a wide range of potential designs, with efficiency values ranging from more than 5 %, and heat transfer coefficient for almost 8 %. Also, there is a clear formation of the Pareto front visible, with regions of high efficiency and low heat transfer coefficient being more refined. These regions were further refined because half of the dataset came from ARMOGA-based optimisation that was slowly converging towards the Pareto front regions by the time it was terminated.

Using the dataset presented in Figure 5.37, two separate ANN response surfaces were created, one for efficiency and the other for the heat transfer coefficient. During the response surface creation process, the hyper-parameters of the neural networks

Parameter	Lower limit	Upper limit
Number of HL	1	4
Number of neurons in each HL	16	256
Regularisation coefficient	0	0.02
Dropout factor	0	0.4

Table 5.6: Hyper-parameters tuned in grid search

Response surface	R^2	MAE	MSE
Efficiency	0.983	0.231	0.124
HTC	0.948	0.031	0.004

Table 5.7: Accuracies of artificial neural network response surfaces for efficiency and the heat load

were tuned through a grid search, maximising the coefficient of correlation. The hyper-parameters for the grid search are given in Table 5.6. To check the accuracies of the created response surfaces, the coefficient of correlation was calculated through k-fold cross-validation, as explained in Section 2.3.4. During this process, the whole dataset was divided into 20 folds.

Accuracies of the ANN response surfaces with the highest R^2 values after hyper-parameters tuning are presented in Table 5.7. It can be seen that both response surfaces predicted the design space very well, with the efficiency response surface having an R^2 value of 0.983 and the heat load response surface having an R^2 value of 0.948. However, despite the high R^2 value of the efficiency response surface, the mean average error (MAE) was still quite high with a value of 0.231.

The next step in this process was to explore the possibility of using active design subspaces (ADS). To do this, an iterative process was carried out as explained in Section 2.3.6. The goal was to identify the linear combination of design parameters that best described the objective function. The convergence of eigenvalue decay for both objectives was monitored. However, the eigenvalue convergence was not as rapid as desired, indicating that the majority of the system's variability could not be captured with only a few dominant directions. To illustrate this, the cumulative energy against the most dominant directions is plotted in Figure 5.38 for both response surfaces.

Response surface	R^2	MAE	MSE
Efficiency	0.982	0.252	0.135
HTC	0.943	0.032	0.004

Table 5.8: Accuracies of ADS coupled ANN response surfaces for efficiency and the heat transfer coefficient

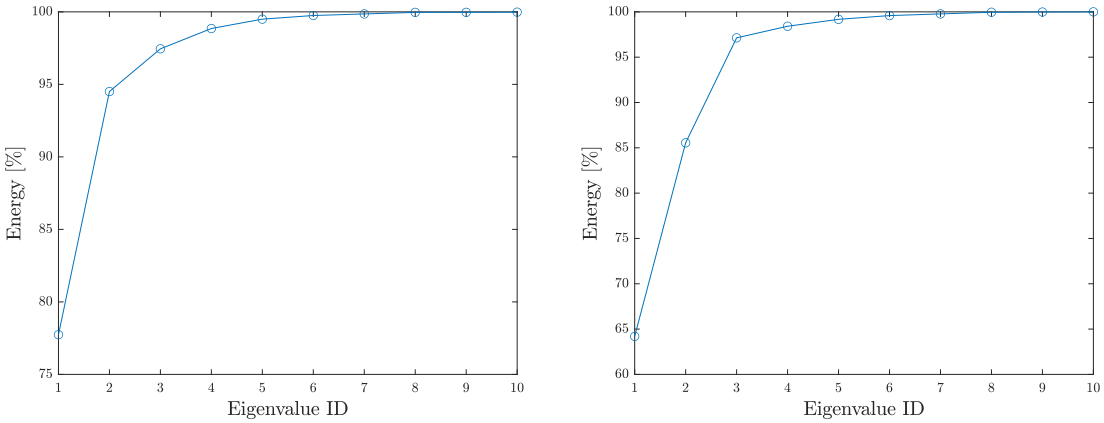

(a) Efficiency (b) Heat transfer coefficient

Figure 5.38: Cumulative energy for ANN response surfaces

It can be seen that 10 dominant directions were needed to describe the system's variability for both objectives. While most of the system's variability is described using the first 6 dominant directions, it was decided to use the first 10 directions to explore whether ADS can improve on the original design space. Using the 10 most dominant directions, an ADS was constructed and ANN response surfaces were recreated for both objectives. The accuracies of the ADS ANN response surfaces were calculated again through k-fold validation, and their results are presented in Table 5.8.

5.3.3.2 Optimisation using ANN response surfaces

When comparing the accuracies of the ANN response surfaces with (Table 5.8) and without (Table 5.7) the ADS, very small differences can be observed. In fact, employing the ADS slightly decreased the accuracy of both response surfaces, where the most noticeable change is in the MAE value of the efficiency. This is contrary to the findings of Lopez et al. [86], who managed to slightly improve the ANN response surface using the ADS, for a similar initial accuracy as in this case.

Despite the fact that employing the ADS slightly lowered the accuracy of the ANN response surface, the ADS-coupled ANN response surfaces were used with ARMOGA to see if a better design could be found. The ADS was used with 10 dominant directions, and the optimisations were performed in two ways. In the first approach, both response surfaces were used to run a two objective ARMOGA optimisation, treating both efficiency and heat load equally. In the second approach, focusing only on the efficiency, only the efficiency ANN response surface was used in a single objective ARMOGA optimisation. The setup of the ARMOGA optimisations was the same as in the optimisations done with the Kriging response surface, and its details are given in Table 5.2.

Both optimisations were run for 20 design generations, where each generation had 30 design points. After that, 5 designs for which the optimiser predicted the best performance were selected from each of the optimisations. In the efficiency only optimisation, these were 5 designs with the highest predicted efficiency. In the two objective aerothermal optimisation, these were the designs for which the sum of the two objectives was the lowest. These designs are shown alongside the initial dataset in Figure 5.39.

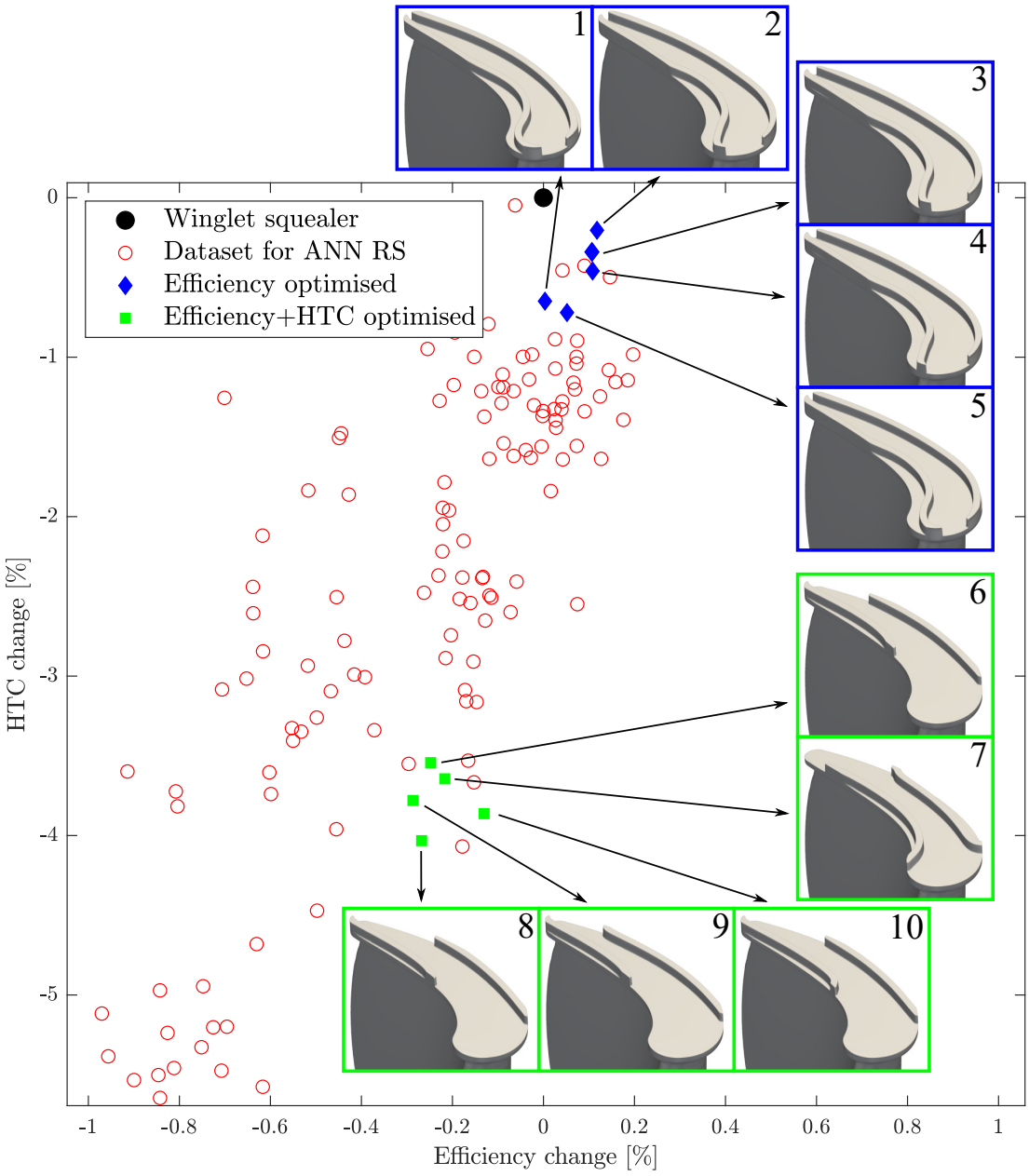

Figure 5.39: Optimisation results on ANN response surfaces

Figure 5.39 presents the optimised designs from two separate ARMOGA runs on the ANN response surfaces alongside the initial dataset points. An incomplete dataset from Figure 5.37 is shown to have a closer look at the optimised designs in question. For the 5 optimum points from each of the two optimisations, predicted by ARMOGA, actual CFD simulations were run to get the real objective values. In this Figure, these designs are shown with real CFD values. Optimum designs from the single objective optimisation are shown in blue, and optimum designs from the two

objective optimisation are shown in green.

It can be seen that efficiency-only optimised designs were all of a very similar topology, having the full length of both squealer pressure side and suction side rims. Also, all designs featured pressure side squealer shelves as a result of placing the front portion of pressure side rims away from the tip edge. All this resulted in a similar performance, where efficiency variation for all efficiency-optimised designs was inside 0.12 %. Design 1, the worst performing from the 5, was found to have the same efficiency as the winglet squealer taken as a reference. Despite the fact that all designs but one improved the efficiency over the winglet squealer, none of the designs reached the area of improvement of around 0.2 %, where the best performing designs in the initial dataset were. However, designs 2, 3, and 4 were found to be on the Pareto front.

Optimum designs from the two objective optimisation, shown in green in Figure 5.37, were, similarly as in the case of efficiency-only optimised designs, all but one found to have the same topology. In that group, only design 7 was found to have a slightly different topology. In that design, the pressure side rim was placed around the middle of the tip, contrary to all other designs in green where the pressure side rim was at the second half of the tip, towards the trailing edge. Since these designs were treating both objectives equally, they were all found to have lower efficiency than the winglet squealer. However, heat load was considerably reduced, lower by approximately 4 % than in the case of a winglet squealer. Interestingly, despite the very similar designs of tips 9 and 10, which resulted in very similar heat load levels, the efficiency difference between the two was found to be 0.16 %, which was quite significant. This shows the difficulty of exploring these topologies and optimising inside them. Between all 5 designs from the two objective optimisation, only design 10 was found to be on the Pareto front.

Despite both optimisations placing at least one design on the Pareto front once CFD simulation was run, it can be concluded that in both optimisations, the optimization objectives were mispredicted. This was found to be related to mean average errors of the both response surfaces that were, regardless of having good coefficients of correlations, still too large. Possible ways of dealing with this would be increasing the response surface datasets or updating the datasets through an infill method. Both methods, based on previous findings, were assumed to be quite expensive since only the ANN response surface generation took around 50 hours using 6 nodes with 24 cores each.

Number of generations	7
Size of generations	30
Starting generation of range adaptation	2
Interval generation of range adaptation	1
Relaxation coefficient of range adaptation	0.7
Crossover rate	1
Crossover parameter	2
Mutation rate	0.1
Mutation parameter	5

Table 5.9: ARMOGA optimiser setup

Although the ANN response surface approach did not produce many results that would properly populate the Pareto front, it was considered a success, showing that the surrogate model approach can be successful in approximating the complexity of the design space. Therefore, instead of updating the response surfaces, a different approach was taken, where a direct genetic algorithm optimisation was run without the surrogate model. The details of this approach will be explained in the following Section.

5.3.4 Genetic algorithm optimisation

Direct genetic algorithm optimisation (without response surface) was performed using the constrained squealer topology design space presented in Figures 5.20 and 5.21. CFD simulations were run using the boundary conditions given in Table 4.5 and the k-ω SST turbulence model. The 3-temperature method was used to obtain the heat transfer coefficient at a rotor blade for a wall temperature of 266 K. ARMOGA was used as the optimiser, optimising both efficiency and the blade area integrated heat transfer coefficient. Its setup is given in Table 5.9.

The optimisation was run for 7 generations with 30 designs in each generation. In generation 1, it was initialised using a design of experiments. Also, no constraints were part of this optimisation. The optimisation convergence was judged by populating the Pareto front. Once most designs in the latest generation populated the Pareto front, optimisation was considered converged and stopped. The optimisation flowchart is given in Figure 5.40.

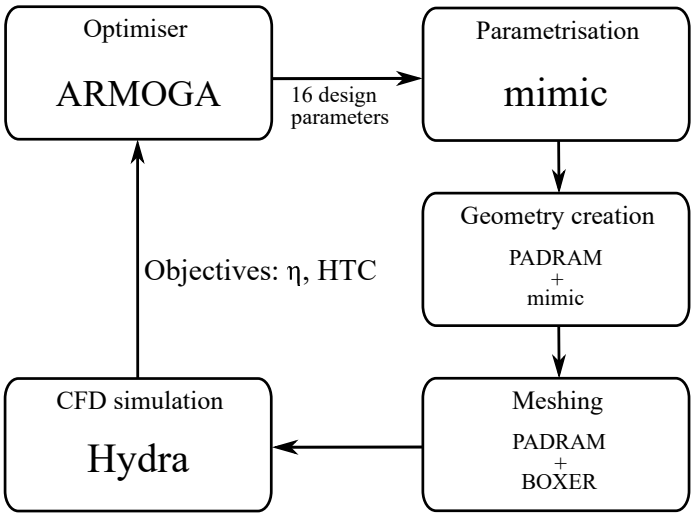

Figure 5.40: Aerothermal ARMOGA squealer topology optimisation flowchart

Figure 5.41 presents the optimisation results. All design points are normalised against the winglet squealer tip (Figure 5.29), which was taken as a reference. The generations shown in Figure 5.41 are coloured differently to show the optimisation evolution and convergence.

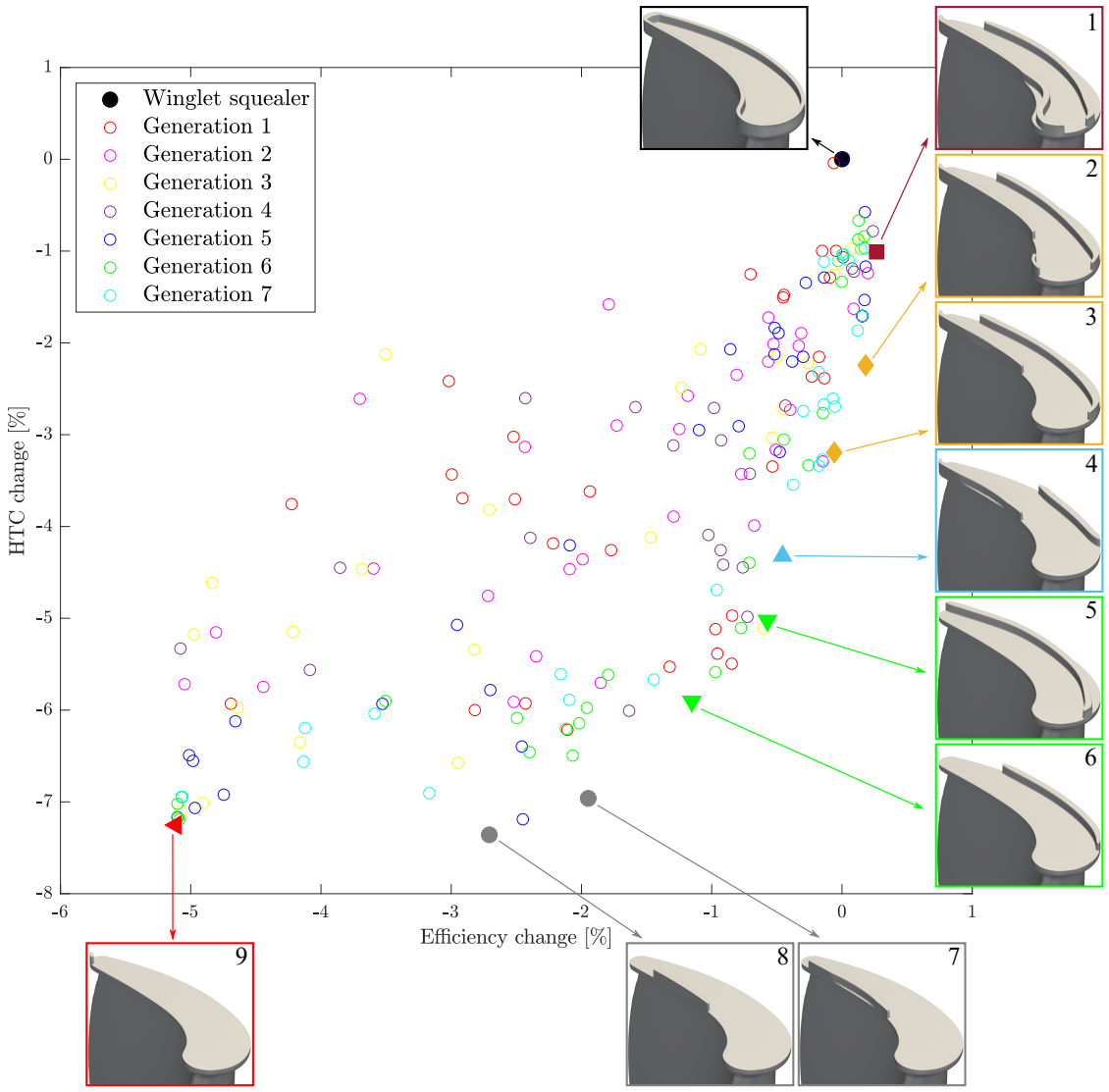

Figure 5.41: Aerothermal ARMOGA optimisation Pareto front

As seen in the figure, not many designs had better efficiency than the reference winglet squealer. However, all designs had a lower heat load. This is because many different topologies were created in this optimisation. To get a good overview of the effect of different topologies on optimisation objectives, all designs on the Pareto front were analysed, and the most interesting ones were grouped based on their topology. These designs were then grouped by different topologies and shown in detail alongside the Pareto front. They are explained more thoroughly next.

Starting from the winglet squealer, it can be immediately seen that no tips had a higher heat load than the winglet squealer. This is explained later in this section. Furthermore, it can be seen that most of the designs also had lower efficiency than

the winglet squealer. However, the optimisation ended up with many designs that had both increased efficiency and lower heat load, and designs that had significantly lower heat load while retaining almost all of the winglet squealer's efficiency.

The most efficient designs featured almost a full length of both pressure and suction sides squealer rims, with small openings at the late suction side. This was the case for design 1, which was the most efficient. In the case of designs with a partial pressure side and a full suction side rim, for a small price in efficiency, heat load was decreased up to around 3 %, as in the case of designs 2 and 3. Further down the Pareto front, all designs had considerably lower efficiency than the winglet squealer tip, but with much lower heat load. Design 4 represented the topology of designs with both partial squealer rims. Designs 5 and 6, and all the designs that had lower efficiency than those, had only one squealer rim. It was found that the tip with a single squealer rim placed on the suction side had a much higher heat load than the tip with a squealer rim on the pressure side. Designs 7 and 8 had only a partial pressure side squealer rim and much lower efficiency than the winglet squealer. Finally, design 9 featured only a very small squealer rim at the very end of the pressure side. Since that design effectively acted as a winglet with an increased tip gap (no squealer rims), it had the lowest efficiency of all the designs in the optimisation. And since it had no squealer rims accounting for less heat load surface, its heat load was amongst the lowest.

Between all the designs described, two designs of different promising topologies were chosen and further analysed.

Design 1, shown in burgundy, was chosen as it had the highest efficiency of all the designs created. It featured two full length squealer rims with an opening at the late suction side. Its efficiency improvement over the winglet squealer tip was found to be 0.27 %. It also had -1.01 % lower heat load.

Design 3, shown in orange, was chosen as it had only slightly lower efficiency than the winglet squealer but considerably lower heat load. Its efficiency was lower by -0.06 % and its heat load was -3.19 % lower than the winglet squealer tip.

Static pressure for all three tips was analysed first. It was plotted around the winglet outline, which was the same for all three tips. This is shown in Figure 5.42.

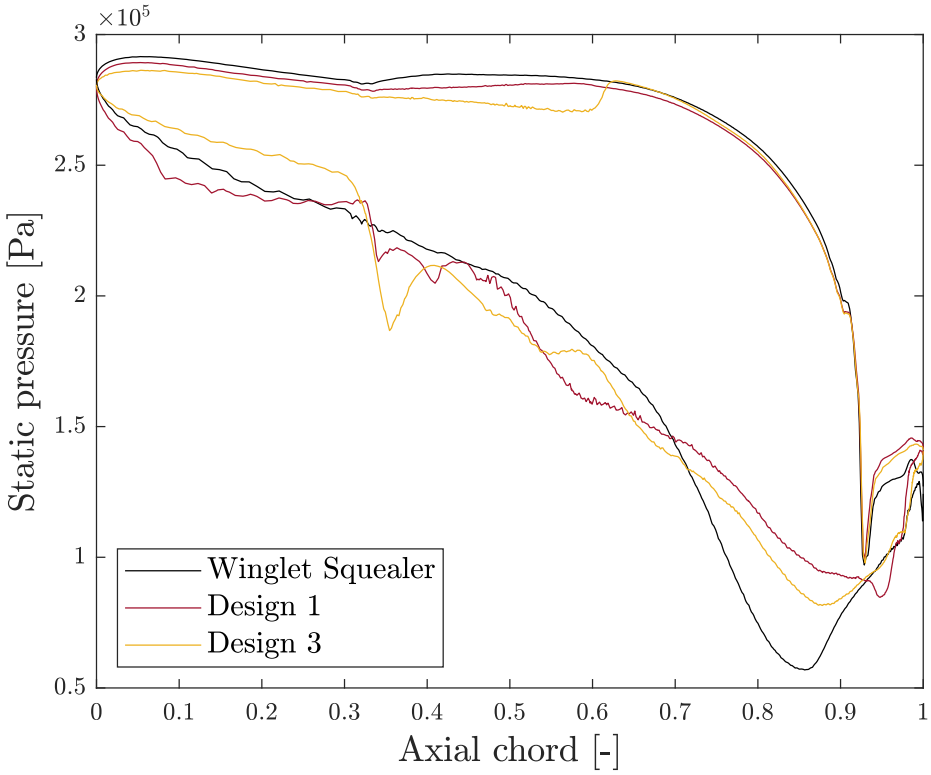

Figure 5.42: Pressure distribution at 0.94 % of the span around squealer tips

Static pressure on the pressure sides of all three tips was found to be similar, with some larger differences observed for design 3. In the case of design 3, the static pressure on the pressure side was slightly dropping until 0.6 of the axial chord, whereas in the case of the winglet squealer and design 1, it remained roughly constant. Until 0.6 of the axial chord, design 3 had no pressure side squealer rim, and there was a big tip gap present. At 0.6 of the axial chord, the pressure side rim of design 3 began, stretching all the way until the trailing edge. Since it was located right at the tip edge, for the rest of the pressure side, all tips had almost identical pressure side static pressure, as they all featured a squealer rim at the tip edge in this region.

Static pressure on the suction sides was very different between the three tips. In the leading edge region, up to 0.3 of the axial chord, design 3 had considerably higher pressure than the winglet squealer and design 1. The largest pressure difference over the tip in this region was seen for design 1. At 0.3 of the axial chord, both designs 1 and 3 began to form suction side squealer shelves, as the suction side squealer rim was placed away from the tip edge. This caused a recirculating flow in the suction side squealer shelve regions for both designs. As these suction side shelve recirculation vortices had low pressure cores, this effect resulted in a considerable decrease in suction side static pressures. The suction side squealer shelve ended around 0.7 of

the axial chord for design 1 and at around 0.8 for design 3. In the case of the winglet squealer, after around 0.7 of the axial chord, suction side static pressure started to drop rapidly and was lower than the static pressure of designs 1 and 3 until the end of the tip. This was caused by the large over tip leakage vortex rubbing on its suction side. As designs 1 and 3 had no rubbing of the tip leakage vortex against the blade, their late suction side static pressures were significantly higher, resulting in much smaller over tip pressure differences.

To observe how the static pressure influenced the tip leakage mass flow, the mass flow was integrated around the suction sides for the three tips, as shown in Figure 5.43.

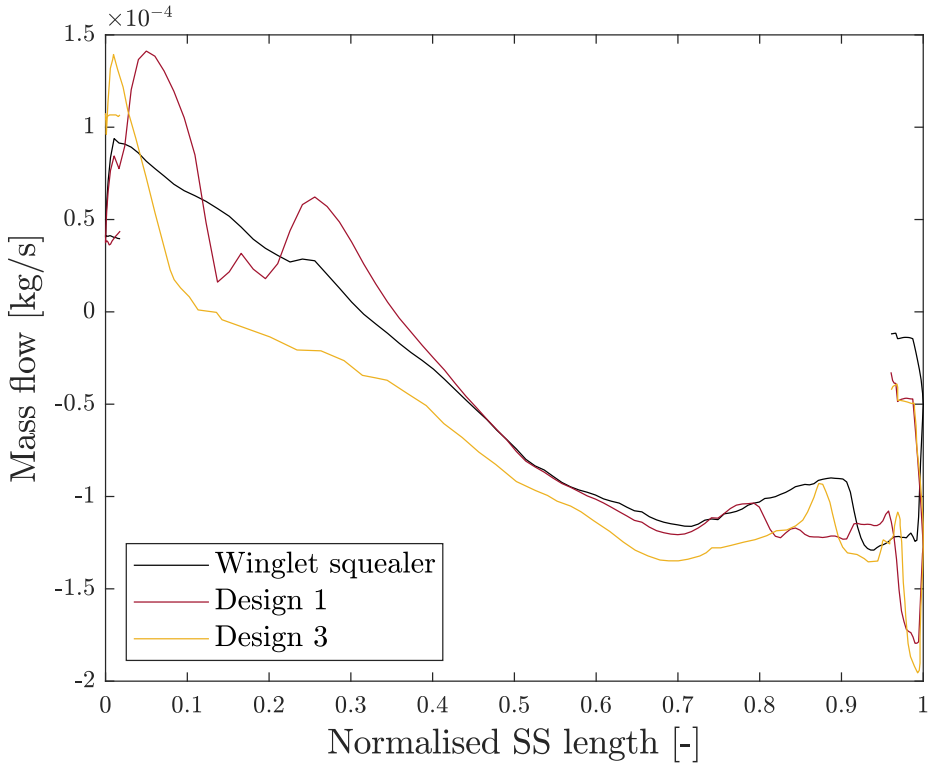

Figure 5.43: Suction side tip leakage mass flow comparison

Starting from the leading edge region, mass flow entered the tip gap for all three tips. Both designs 1 and 3 had similar maximum mass flow values, but in the case of design 3, mass flow entering the tip gap quickly reversed, starting to leave after 0.15 of the suction side length. In the case of design 1, mass flow was found to enter the tip gap until approximately 0.35 of the suction side length. In the case of the winglet squealer, mass flow entered the tip gap until 0.3 of the suction side length, which resembled design 1. However, this was found to be caused by different effects. After 0.3 of the suction side length, leakage mass flow in the case of the winglet squealer

started to leave the tip gap and linearly increased until approximately 0.7 of the suction side length, after which it remained roughly constant until the trailing edge. In the case of design 1, the amount of leakage flow entering the tip gap was very high around 0.1 of the suction side, at the location of a leading edge opening. The small decrease visible between 0.1 and 0.2 of the suction side length was caused by the suction side squealer rim, placed at the tip edge. After 0.2 of the suction side length, the suction side squealer rim was placed away from the tip edge, forming a suction side squealer shelve that entrained the leakage flow. This is visible as an increase in leakage flow entering the tip region around 0.3 of the suction side length in the case of design 1. After that, similarly to the winglet squealer, design 1's tip leakage flow leaving the tip gap sharply increased until approximately 0.7 of the suction side length, after which it remained roughly constant until the trailing edge opening. Both designs 1 and 3 had trailing edge openings placed almost identically, and this is visible as an area of increased leakage flow after 0.95 of the suction side length. In those regions, leakage mass flows for both designs 1 and 3 were very similar.

Overall, it was found that design 1 had a $-7.76\,\%$ lower tip leakage mass flow than the winglet squealer tip. In the case of design 3, tip leakage mass flow was found to increase by $41.36\,\%$ over the winglet squealer, despite having a favourable over tip pressure difference. Such a big difference was found to be caused by the design 3's inability to entrain the early suction side leakage flow into the tip region. As design 3 had no pressure side squealer, there was no enclosed squealer cavity to cause flow ingestion around the leading edge.

To visualise the leakage flow over the three tips, contours of relative total pressure are shown in Figure 5.44.

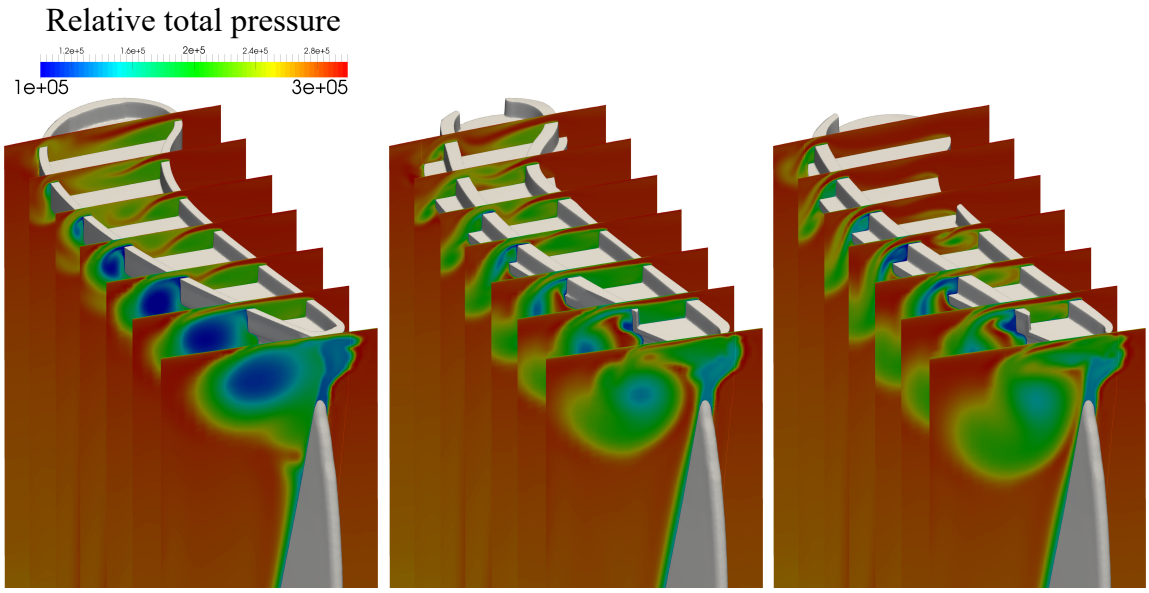

(a) Winglet squealer (b) Design 1 (c) Design 3

Figure 5.44: Over tip leakage vortex

Interestingly, relative total pressure contours show that despite design 3 having a larger tip leakage mass flow, the strongest over tip leakage vortex was present for the winglet squealer tip. This is seen as the over tip leakage vortex with the lowest pressure core. Also, the over tip leakage vortex in the case of a winglet squealer blade was found to rub the late suction side of the blade, which was not the case for tip designs 1 and 3. In the case of designs 1 and 3, over tip leakage vortices were pushed away from the blade and were detached from the blade wakes. Also, they were positioned at a lower span than the over tip leakage vortex formed in the case of a winglet squealer. This was found to be caused by the larger leakage flow downward momentum, as a result of the suction side squealer shelves. For all three tips, passage vortices were found to be merged with the over tip leakage vortices.

Regarding the flow inside squealer cavities, two vortices were present at winglet squealer and design 1 tips, with only one vortex being present in the case of design 3. Two vortices present in the case of a winglet squealer and a design 1 tip were the cavity vortex and the scrapping vortex. Cavity vortices formed in both cases as a result of flow separation over the pressure side rims. In the front portion of the tip, their size was smaller than in the second half of the tip where they filled the whole cavities. Scrapping vortices of winglet squealer and design 1 tips formed next to the suction side squealer rims, and their sizes were very different. This was found to be directly related to the width of the squealer cavity. Winglet squealer, which had a

wider squealer cavity than the design 1 tip, featured a large scrapping vortex that created a good sealing effect in the front portion of the tip, resulting in low leakage mass flow. On the other hand, because of both pressure side and suction side squealer shelves, design 1 had a much narrower squealer cavity, and its scrapping vortex was much smaller, ending much sooner. Design 3, featuring no pressure side squealer rim in the front half of the tip, had no scrapping vortex at all. In fact, in the case of design 3, no vortical flow was visible at the front portion of the tip before the over tip leakage flow reached the suction side rim. In the second half of the design 3 tip, the flow was separated over the pressure side rim, which caused a single cavity vortex.

Complicated tip leakage flow patterns caused different heat transfer hotspots. These are shown as the contours of heat transfer coefficient. Figure 5.45 presents the pressure side of the analysed tips, and Figure 5.46 presents the heat transfer coefficient on the tips' suction sides.

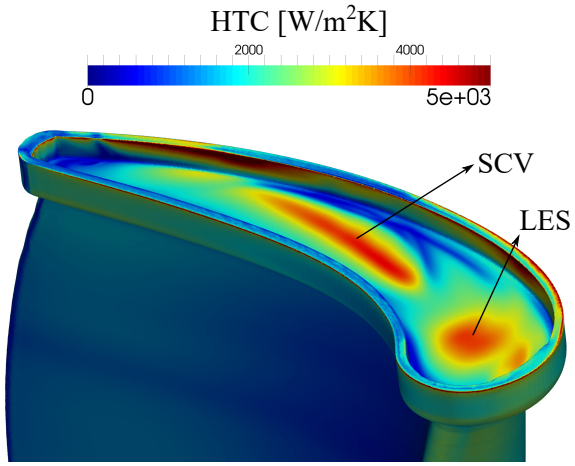

(a) Winglet squealer

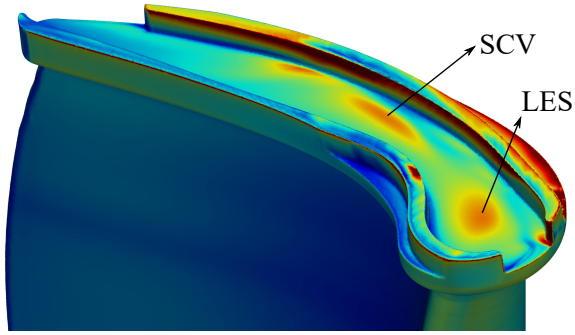

(b) Design 1

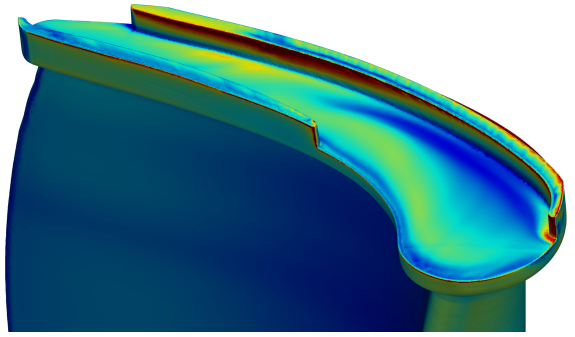

(c) Design 3

Figure 5.45: Contours of heat transfer coefficient at the pressure side of squealer tips

As shown in Figure 5.45, the suction side rim was subjected to a much larger heat load than the pressure side rim in all cases between the two squealer rims. The suction side rims had the highest heat load on their inner sides and on their tops, caused by the rubbing of a highly vortical flow that exited the tip gaps. The higher heat load was present in the aft portions of the tips where most of the flow left the tip gap. Regarding the squealer cavity floor, the highest heat load was caused by

the leading edge area separations (LES), visible in the case of a winglet squealer and design 1 tips, and the scrapping vortex (SCV) rubbing against the cavity floor. The scrapping vortex caused a large stripe of increased heat load across the middle of the winglet squealer tip and a much smaller stripe in the case of design 1. The size of a scrapping vortex hotspot was found to be directly linked to the scrapping vortex size. As design 3 had no leading edge squealer rim, resulting in no leading edge separation and no scrapping vortex, its heat load was much lower in the front portion of the tip compared to winglet squealer and design 1 tips.

Looking at the suction sides of the tips shown in Figure 5.46, it can be seen that the suction side squealer shelves experienced a much larger heat load than the pressure side squealer shelves of design 1 shown in Figure 5.45b. Also, it can be seen that the insides of the pressure side rims were subjected to a much smaller heat load than the insides of the suction side rims, as they did not encounter the leakage flow. The outside of the suction side squealer rim was subjected to a smaller heat load in the case of designs 1 and 3, especially over the squealer shelves. In the case of a winglet squealer, a hotspot stripe was visible at the outside of the suction side rim, starting around the middle of the tip. This was caused by the formation of a passage vortex that rubbed the outside of the blade tip. The passage vortex was effectively eliminated in the case of designs 1 and 3 due to squealer shelves that entrained all of the early leakage and a portion of the passage flow close to the casing. Also, it is worth noting that a hotspot visible at the beginning of the suction side squealer shelve of design 1 was caused by the error in the 3-temperature model, not the flow.

A large part of the overall heat load is generally associated with the proximity of the over tip leakage vortex to the blade suction side. In other words, over tip leakage vortex rubbing was found to increase the heat load on the suction side. This was very significant on the overall heat load. The winglet squealer, which had a strong over tip leakage vortex rubbing against the aft portion of the blade suction side, had a large area of increased heat load in this region. This effect was far less noticeable for designs 1 and 3. Design 1, having a larger suction side squealer shelve, pushed over tip leakage vortex further away from the blade than design 3, resulting in the smallest area of increased heating at the late suction side. On the other hand, the suction side squealer shelve of design 3 produced a smaller amount of heating but resulted in the over tip leakage vortex being slightly closer to the blade suction side compared to design 1. This caused some higher level of rubbing on the late suction side, however still much lower than in the case of a winglet squealer. Considering

these observations, it can be concluded that the use of suction side squealer shelves for heat transfer is a trade-off.

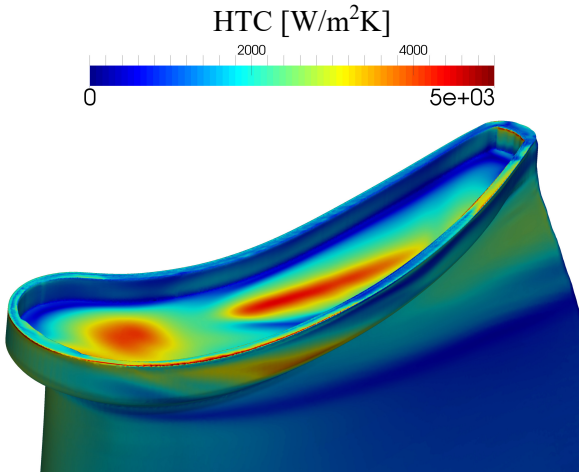

(a) Winglet squealer

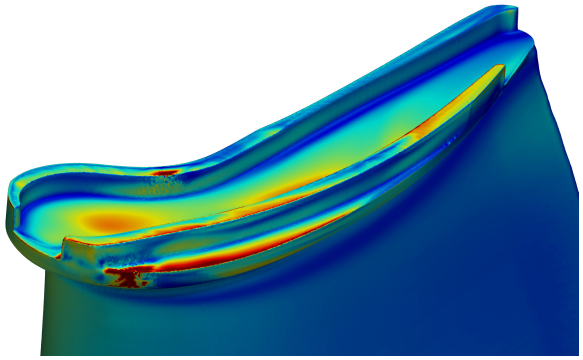

(b) Design 1

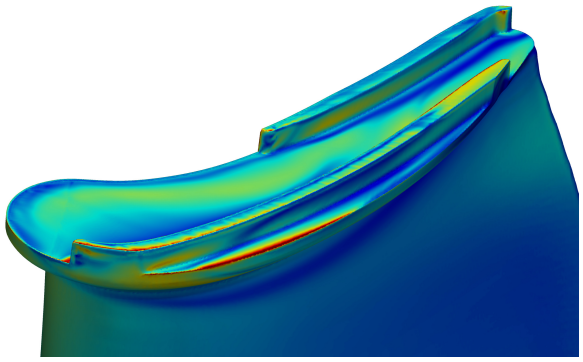

(c) Design 3

Figure 5.46: Contours of heat transfer coefficient at suction side of squealer tips

Finally, to assess the impact of different designs on entropy generation, radially averaged entropy is plotted at 0.5 of the axial chord downstream of the trailing edges for all three tips in Figure 5.47.

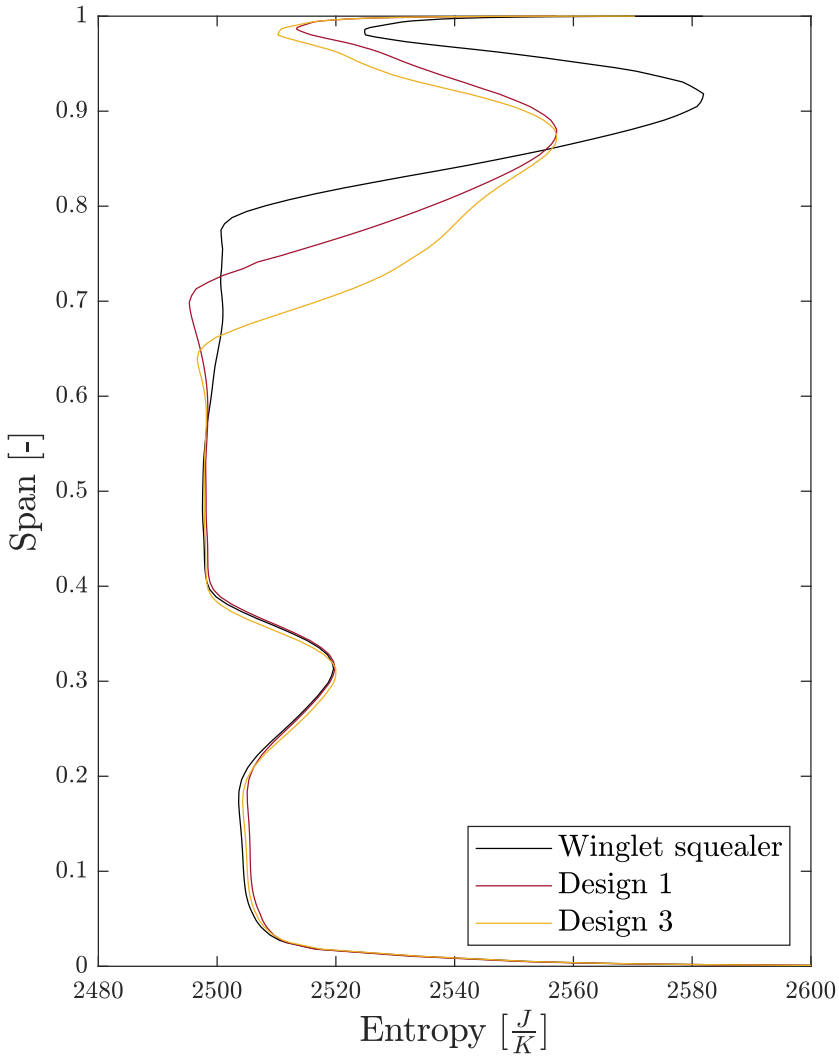

Figure 5.47: Circumferentially averaged entropy field at 0.5 axial chord downstream of the trailing edge

Starting from the casing (span=1), it can be seen that above 0.95 of the span, the winglet squealer had the highest entropy production followed by designs 1 and 3. This region is associated with losses in the squealer cavity, and as the winglet squealer had no squealer openings, its flow had the largest entropy production as a result of the largest over tip leakage flow separations. Design 3 had the smallest entropy production in this region as a result of no separation over the pressure side in the front portion of the tip. Spikes of increased entropy for all three tips visible around 0.85-0.9 of the span are associated with the losses caused by the over tip leakage vortex. As shown in Figure 5.44a, the winglet squealer had the strongest over

tip leakage vortex, resulting in much higher entropy production compared to designs 1 and 3. Both designs 1 and 3 had similar peak values of entropy production, but as in the case of design 3, the over tip leakage vortex covered a larger area at a lower span, resulting in larger entropy production compared to design 1. Between 0.65 and 0.8 of the span, both designs 1 and 3 had larger entropy production than the winglet squealer, with design 3's entropy being considerably higher. Below 0.6 of the span, the flow was found not to be influenced by the leakage flow since all designs were found to have the same flow conditions, resulting in the same entropy levels.

5.3.5 Final remarks on squealer topology optimisation

Considering the results shown above, it can be concluded that this approach showed good potential for optimising between different topologies. Despite the use of a small number of design parameters (16), various squealer topologies were created and chosen between. This shows good potential for this kind of parametrisation since novel squealer tips with rims that feature openings and cuts were shown to have benefits over more traditional shapes. Out of the analysed tip shapes, it has been shown that there is a clear benefit of using suction side squealer shelves when designing a squealer tip. This kind of squealer tip could not be possible with more traditional squealer parametrisation. However, the benefit of the suction side squealer shelve was found to be mostly aerodynamic since the suction side squealer shelve was prone to increased heating. Considering winglet optimisations, these topology squealer optimisations are difficult to directly compare. But they are shown to pave the way for another approach beside the winglet. The next step could be combining winglet and squealer parametrisations under single optimisation to extract the best of both approaches. Thus, this kind of optimisation should be considered only as a first step in the overall tip design approach.

Chapter 6

Conclusions and Future Work

6.1 Conclusions

This work focuses on exploring and performing aerothermal optimisations for high pressure turbine blade tips. Previous studies, up to this date, have primarily focused on shape optimisations the of the turbine tip, with rotor blade heat transfer being modelled under the assumption of a blade with constant temperature. In this work, both the optimisation approach and the heat transfer modelling approach have been further investigated.

In terms of modelling turbine heat transfer, the heat load on the turbine blade was expressed using the locally corrected heat transfer coefficient. This approach was then used for the first time to optimise the turbine tip, effectively eliminating the introduction of flow field errors caused by the use of a constant wall temperature on the optimised surface. By assuming non-linear heat transfer, the flow field was consistently evaluated at the same operating point, resulting in a more reliable calculation of heat load. This approach was found closely follow the more traditional approach of heat load modelling by imposing a constant blade wall temperature. Considering it is computationally more expensive, its real use in the preliminary design stages, as was the one in these optimisations, needs to be further investigated.

For the case of a winglet tip, aerodynamic and aerothermal optimisations were carried out with constraints. In particular, turbine mass flow and stage reaction were expressed as turbine inlet capacity and the stage reaction and constrained. Two methods of constraining an optimised design were successfully implemented and used. In the case of aerodynamic optimisation, it was shown that handling the constraints inside the optimisation process is more efficient and has an effect on a final design. However, a method of separately matching the turbine stage mass flow and expansion

for the unconstrained optimised design proved to be robust for the case of a winglet tip.

Turbine mass flow and stage reaction were expressed as turbine inlet capacity and stage reaction, respectively, and constrained. Two methods of constraining an optimised design were successfully implemented and utilised. Both of them used the rotor blade skew parametrisation, with only one design parameter. During the aerodynamic optimisation, it was demonstrated that handling the constraints within the optimisation process is more efficient and has an impact on the final design. However, a method of separately matching the turbine stage mass flow and expansion for the unconstrained optimised design proved to be robust in the case of a winglet tip.

These findings were then applied to a case of constrained aerothermal optimisation, which was performed using a gradient-based method. The optimisation objective, which consisted of turbine stage efficiency and heat load, was expressed as a surface-integrated heat transfer coefficient. The heat transfer coefficient on the blade surface was calculated using a 3-temperature method that was applied to a realistic blade temperature operating range. The accuracy of the 3-temperature method was demonstrated to be valid on the winglet tip using the shown methodology. Additionally, in aerothermal optimisation, combining the optimisation objectives through the use of a weighting factor enabled exploration of different parts of the Pareto front.

Different topology optimisations were conducted next, starting with a simple topology optimisation for a single squealer rim tip to test the methodology. By using a simple and flexible definition of the design space, capable of quickly exploring a full range of possible squealer topologies, the parametrisation proved to be quick and robust, showing the potential for more complex tip shapes. Parametrisation included radial basis function surface iso-cut implemented in software called mimic. It has been proved to be a good and efficient approach for topology parametrisations using small number of design parameters. Due to the simplicity of the design space, the optimisation for a single squealer rim tip was carried out using a gradient-based optimiser, quickly converging to the most efficient topology. This topology featured a thin squealer rim at the blade pressure side, matching the results found in the literature.

Using the findings from a single squealer rim optimisation, the design space was expanded to a highly complex design space capable of generating a large number of different squealer topologies with flexible numbers and positions of squealer rims.

During preliminary investigations, this parametrisation was found to be largely discontinuous, making it impossible to use a gradient-based optimiser. Additionally, because of similar reasons, regressing the design space using a Kriging response surface was found to be inaccurate and very expensive, despite the small number of design parameters. Consequently, a method for optimising in the most promising design subspace was suggested and successfully executed. The most promising design subspace was identified through data sampling, and the initial design space was reduced to target a smaller number of possible topologies. It was demonstrated that using this method, successful optimisation can also be performed using a gradient-based optimiser.

Also, it was found that focusing on the most promising design subspace allowed for both topology and shape optimisation within a particular topology to be performed simultaneously. This was a clear benefit of the novel parametrisation approach.

Finally, to explore the relationship between efficiency and heat load, genetic algorithm-based optimisation with and without a surrogate model was performed on the previously identified most promising design subspace. To regress the design space used, a surrogate model was constructed using a novel response surface that utilised artificial neural networks coupled with active design subspaces. It was shown that using this approach, a response surface of very good accuracy could be generated, even for highly discontinuous design spaces. By optimising on the response surface with a genetic algorithm, improvements on the Pareto front were found. However, despite good accuracy of those response surfaces, they were mostly found to be inadequate to find optimums without updating them. In direct genetic algorithm optimisation, novel topologies that showed a considerable increase in efficiency with a decrease in heat load, compared to the tip with a full perimeter squealer, were identified. The most interesting topologies were then further analysed, and some key geometric features were explained. This approach was found to be computationally more expensive than the surrogate model based approach. However, with slightly larger benefits in terms of optimisation accuracy.

6.2 Future Work

In regards to the modelling of the heat load using the 3-temperature method, there are still some concerns about the accuracy in the tip region that have not been addressed. It has been shown that the accuracy worsens in regions with flow separation,

recirculation, and large pressure gradients, all of which are typically found in the tip region. Therefore, further work is needed to improve the accuracy of this approach.

The majority of the optimisation work in this thesis was focused on the most promising topology. However, to fully analyse the entire design space, a genetic algorithm optimisation could be performed using the full range of potential design parameters. However, this would probably be computationally expensive.

Moreover, in this work, the design space was successfully regressed using a novel response surface method and active design subspaces. However, active design subspaces were found to be almost ineffective for this particular example. Further investigation would be useful to determine if additional parametrisation savings could be achieved by tuning active design subspaces, thus simplifying and lowering the computational cost of the optimisation process.

Lastly, a method for simultaneously optimising the tip squealer topology and the tip cooling holes topology has only recently been presented in the literature. This method provides an interesting approach for handling topologies characterised by heat transfer hotspots through an arbitrary number of cooling holes. In this work, certain topologies were found to have far lower heat loads than others, indicating potential for simpler and less extensive cooling. Future work focusing on the coupling of the tip geometry with cooling arrangements would be beneficial.

Bibliography

[1] Advance and Ultrafan, 2016. Available at :"https://www.rolls-royce.com/media/our-stories/innovation/2016/advance-and-ultrafan", last accessed 20th September 2021.

[2] H. I. H. Saravanamuttoo, H. Cohen, and G. F. C. Rogers. *Gas Turbine Theory*. Pearson, 5th edition, 2001.

[3] R. Robins. Enterprise and innovation. *Aerospace*, pages 8–13, February 1994.

[4] T. Povey, M. Sharpe, and A. Rawlinson. Experimental Measurements of Gas Turbine Flow Capacity Using a Novel Transient Technique. *Journal of Turbomachinery*, 133(1), January 2011.

[5] S. L. Dixon and C. A. Hall. *Fluid Mechanics and Thermodynamics of Turbomachinery*. Elsevier, 7th edition, 2014.

[6] J. D. Denton. The 1993 IGTI Scholar Lecture: Loss Mechanisms in Turbomachines. *Journal of Turbomachinery*, 115(4):621–656, October 1993.

[7] H. Hoheisel, R. Kiock, H. J. Lichtfuss, and L. Fottner. Influence of Free-Stream Turbulence and Blade Pressure Gradient on Boundary Layer and Loss Behavior of Turbine Cascades. *Journal of Turbomachinery*, 109(2):210–219, April 1987.

[8] James E. Kopriva, Gregory M. Laskowski, and M. Reza H. Sheikhi. Computational Assessment of Inlet Turbulence on Boundary Layer Development and Momentum/Thermal Wakes for High Pressure Turbine Nozzle and Blade. volume Volume 8B: Heat Transfer and Thermal Engineering of *ASME International Mechanical Engineering Congress and Exposition*, November 2014.

[9] Ronald S. Bunker. A Review of Shaped Hole Turbine Film-Cooling Technology . *Journal of Heat Transfer*, 127(4):441–453, March 2005.

[10] L. Xu and J. D. Denton. The Base Pressure and Loss of a Family of Four Turbine Blades. *Journal of Turbomachinery*, 110(1):9–17, January 1988.

[11] A. P. Melzer and G. Pullan. The Role of Vortex Shedding in the Trailing Edge Loss of Transonic Turbine Blades. *Journal of Turbomachinery*, 141(4), January 2019.

[12] C. H. Sieverding, H. Richard, and J. Desse. Turbine Blade Trailing Edge Flow Characteristics at High Subsonic Outlet Mach Number. *Journal of Turbomachinery*, 125(2):298–309, April 2003.

[13] H. Sauer, R. Schmidt, and K. Vogeler. Influence of Chord Length and Inlet Boundary Layer on the Secondary Losses of Turbine Blades. *Journal of Turbomachinery*, 134(1), January 2012.

[14] M. Pátý and S. Lavagnoli. A Novel Vortex Identification Technique Applied to the 3D Flow Field of a High-Pressure Turbine. *Journal of Turbomachinery*, 142(3), 02 2020.

[15] J. P. Bindon. The Measurement and Formation of Tip Clearance Loss. *Journal of Turbomachinery*, 111(3):257–263, July 1989.

[16] J. Moore and J. S. Tilton. Tip Leakage Flow in a Linear Turbine Cascade. *Journal of Turbomachinery*, 110(1):18–26, January 1988.

[17] F. J. G. Heyes, H. P. Hodson, and G. M. Dailey. The Effect of Blade Tip Geometry on the Tip Leakage Flow in Axial Turbine Cascades. *Journal of Turbomachinery*, 114(3):643–651, July 1992.

[18] M. I. Yaras and S. A. Sjolander. Effects of Simulated Rotation on Tip Leakage in a Planar Cascade of Turbine Blades: Part I-Tip Gap Flow. *Journal of Turbomachinery*, 114(3):652–659, July 1992.

[19] M. I. Yaras, S. A. Sjolander, and R. J. Kind. Effects of Simulated Rotation on Tip Leakage in a Planar Cascade of Turbine Blades: Part II-Downstream Flow Field and Blade Loading. *Journal of Turbomachinery*, 114(3):660–667, July 1992.

[20] J. Moore, J. G. Moore, G. S. Henry, and U. Chaudhry. Flow and Heat Transfer in Turbine Tip Gaps. *Journal of Turbomachinery*, 111(3):301–309, July 1989.

[21] M. K. Chyu, H. K. Moon, and D. E. Metzger. Heat Transfer in the Tip Region of Grooved Turbine Blades. *Journal of Turbomachinery*, 111(2):131–138, April 1989.

[22] R. S. Bunker, J. C. Bailey, and A. A. Ameri. Heat Transfer and Flow on the First-Stage Blade Tip of a Power Generation Gas Turbine: Part 1-Experimental Results . *Journal of Turbomachinery*, 122(2):263–271, April 2000.

[23] G. S. Azad, J. Han, S. Teng, and R. J. Boyle. Heat Transfer and Pressure Distributions on a Gas Turbine Blade Tip. *Journal of Turbomachinery*, 122(4):717–724, October 2000.

[24] A. J Jackson, A. P. S Wheeler, and R. W. Ainsworth. An experimental and computational study of tip clearance effects on a transonic turbine stage. *International Journal of Heat and Fluid Flow*, 56:335–343, 2015.

[25] R. Maffulli and L. He. Impact of Wall Temperature on Heat Transfer Coefficient and Aerodynamics for Three-Dimensional Turbine Blade Passage. *Journal of Thermal Science and Engineering Applications*, 9(4), December 2017.

[26] Q. Zhang and L. He. Impact of Wall Temperature on Turbine Blade Tip Aerothermal Performance. *Journal of Engineering for Gas Turbines and Power*, 136(5), May 2014.

[27] A. A. Ameri, E. Steinthorsson, and D. L. Rigby. Effect of Squealer Tip on Rotor Heat Transfer and Efficiency. *Journal of Turbomachinery*, 120(4):753–759, October 1998.

[28] P. J. Newton, G. D. Lock, S. K. Krishnababu, H. P. Hodson, W. N. Dawes, J. Hannis, and C. Whitney. Heat Transfer and Aerodynamics of Turbine Blade Tips in a Linear Cascade. *Journal of Turbomachinery*, 128(2):300–309, April 2006.

[29] N. L. Key and T. Arts. Comparison of Turbine Tip Leakage Flow for Flat Tip and Squealer Tip Geometries at High-Speed Conditions. *Journal of Turbomachinery*, 128(2):213–220, April 2006.

[30] S. E. Lee and Lee S. W. Over-tip leakage flow and loss in a turbine cascade equipped with suction-side partial squealers. *International Journal of Heat and Fluid Flow*, 61:575–584, 2016.

[31] K. Du, Z. Li, J. Li, and B. Sunden. Influences of a multi-cavity tip on the blade tip and the over tip casing aerothermal performance in a high pressure turbine cascade. *Applied Thermal Engineering*, 147:347–360, 2019.

[32] B. Mischo, T. Behr, and R. S. Abhari. Flow Physics and Profiling of Recessed Blade Tips: Impact on Performance and Heat Load. *Journal of Turbomachinery*, 130(2), April 2008.

[33] S. K. Krishnababu, P. J. Newton, W. N. Dawes, G. D. Lock, H. P. Hodson, J. Hannis, and C. Whitney. Aerothermal Investigations of Tip Leakage Flow in Axial Flow Turbines-Part I: Effect of Tip Geometry and Tip Clearance Gap. *Journal of Turbomachinery*, 131(1), January 2009.

[34] S. K. Krishnababu, W. N. Dawes, H. P. Hodson, G. D. Lock, J. Hannis, and C. Whitney. Aerothermal Investigations of Tip Leakage Flow in Axial Flow Turbines-Part II: Effect of Relative Casing Motion. *Journal of Turbomachinery*, 131(1), January 2009.

[35] Z. Schabowski and H. Hodson. The Reduction of Over Tip Leakage Loss in Unshrouded Axial Turbines Using Winglets and Squealers. *Journal of Turbomachinery*, 136(4), April 2014.

[36] C.B. Senel, H. Maral, L.A. Kavurmacioglu, and C. Camci. An aerothermal study of the influence of squealer width and height near a hp turbine blade. *International Journal of Heat and Mass Transfer*, 120:18–32, 2018.

[37] J. H Kim, S. Y. Lee, and J. T. Chung. Numerical analysis of the aerodynamic performance & heat transfer of a transonic turbine with a partial squealer tip. *Applied Thermal Engineering*, 152:878–889, 2019.

[38] J. D. Coull, N. R. Atkins, and H. P. Hodson. Winglets for Improved Aerothermal Performance of High Pressure Turbines. *Journal of Turbomachinery*, 136(9), September 2014.

[39] J. H Cheon and S. W. Lee. Tip leakage aerodynamics over the cavity squealer tip equipped with full coverage winglets in a turbine cascade. *International Journal of Heat and Fluid Flow*, 56:60–70, 2015.

[40] X. Yan, Y. Huang, K. He, J. Li, and Z. Feng. Numerical investigations into the effect of squealer–winglet blade tip modifications on aerodynamic and

heat transfer performance. *International Journal of Heat and Mass Transfer*, 103:242–253, 2016.

[41] Q. Zhang and L. He. Overtip choking and its implications on turbine blade-tip aerodynamic performance. *Journal of Propulsion and Power*, 27(5):1008–1014, 2011.

[42] Q. Zhang, D. O. O'Dowd, L. He, A. P. S. Wheeler, P. M. Ligrani, and B. C. Y. Cheong. Overtip Shock Wave Structure and Its Impact on Turbine Blade Tip Heat Transfer. *Journal of Turbomachinery*, 133(4), October 2011.

[43] D. O. O'Dowd, Q. Zhang, L. He, M. L. G. Oldfield, P. M. Ligrani, B. C. Y. Cheong, and I. Tibbott. Aerothermal Performance of a Winglet at Engine Representative Mach and Reynolds Numbers. *Journal of Turbomachinery*, 133(4), October 2011.

[44] Z. Zou, L. Xuan, Y. Chen, and F. Shao. Effects of flow structure on heat transfer of squealer tip in a turbine rotor blade. *International Communications in Heat and Mass Transfer*, 114:104588, 2020.

[45] Q. Zhang and L. He. Tip-Shaping for HP Turbine Blade Aerothermal Performance Management. *Journal of Turbomachinery*, 135(5), September 2013.

[46] C. De Maesschalck, S. Lavagnoli, and G. Paniagua. Blade Tip Carving Effects on the Aerothermal Performance of a Transonic Turbine. *Journal of Turbomachinery*, 137(2), February 2015.

[47] C. De Maesschalck, S. Lavagnoli, and G. Paniagua. Blade Tip Shape Optimization for Enhanced Turbine Aerothermal Performance. *Journal of Turbomachinery*, 136(4), April 2014.

[48] S. Caloni, S. Shahpar, and J. D. Coull. Numerical investigations of different tip designs for shroudless turbine blades. *Proceedings of the Institution of Mechanical Engineers, Part A: Journal of Power and Energy*, 230(7):709–720, 2016.

[49] C. De Maesschalck, S. Lavagnoli, G. Paniagua, T. Verstraete, R. Olive, and P. Picot. Heterogeneous Optimization Strategies for Carved and Squealer-Like Turbine Blade Tips. *Journal of Turbomachinery*, 138(12), December 2016.

[50] V. Andreoli, J. Braun, G. Paniagua, C. De Maesschalck, M. Bloxham, W. Cummings, and L. Langford. Aerothermal Optimization of Fully Cooled Turbine Blade Tips. *Journal of Turbomachinery*, 141(6), June 2019.

[51] C. De Maesschalck, V. Andreoli, G. Paniagua, T. Gillen, and B. Barker. Aerothermal Optimization of Turbine Squealer Tip Geometries With Arbitrary Cooling Injection. *Journal of Turbomachinery*, 143(11), June 2021.

[52] L. Baert, E. Chérière, C. Sainvitu, I. Lepot, A. Nouvellon, and V. Leonardon. Aerodynamic Optimization of the Low-Pressure Turbine Module: Exploiting Surrogate Models in a High-Dimensional Design Space. *Journal of Turbomachinery*, 142(3), February 2020.

[53] S. Shahpar, S. Caloni, and L. de Prieelle. Automatic Design Optimization of Profiled Endwalls Including Real Geometrical Effects to Minimize Turbine Secondary Flows. *Journal of Turbomachinery*, 139(7), July 2017.

[54] L. Lapworth. HYDRA-CFD: A Framework for Collaborative CFD Development. International Conference on Scientific & Engineering Computation (ICSEC), Singapore, July 2004.

[55] L. Lapworth and S. Shahpar. Design of gas turbine engines using CFD. European Congress on Computational Methods in Applied Sciences and Engineering ECCOMAS, pages 24–28, August 2004.

[56] O. Reynolds. Iv. on the dynamical theory of incompressible viscous fluids and the determination of the criterion. *Philosophical Transactions of the Royal Society of London. (A.)*, 186:123–164, 1895.

[57] P. R. Spalart and S. R. Allmaras. A one-equation turbulence model for aerodynamic flows. volume AIAA 1992-439 of *30th Aerospace Sciences Meeting and Exhibit*, 1992.

[58] F. R. Menter. Zonal two equation k-w turbulence models for aerodynamic flows. volume AlAA 93-2906 of *24th Fluid Dynamics Conference*, July 1993.

[59] F. R. Menter. Two-equation eddy-viscosity turbulence models for engineering applications. *AIAA Journal*, 32(8):1598–1605, 1994.

[60] P. Moinier. *Algorithm developments for an unstructured viscous flow solver*. PhD dissertation, University of Oxford, 1999.

[61] P. L. Roe. Approximate Riemann solvers, parameter vectors, and difference schemes. *Journal of Computational Physics*, 43(2):357–372, 1981.

[62] H. Luo, J. D. Baum, and R. Lohner. Edge-based finite element scheme for the Euler equations. *AIAA Journal*, 32(6):1183–1190, 1994.

[63] P. Moinier, J. Muller, and M. B. Giles. Edge-based multigrid and preconditioning for hybrid grids. *AIAA Journal*, 40(10):1954–1960, 2002.

[64] A. Jameson. Transonic aerofoil calculations using the Euler equations. IMA Conference on Numerical Methods in Aeronautical Fluid Dynamics, pages 289–308, 1982. London, Academic Press.

[65] P. I. Crumpton, J. A. Mackenzie, and K. W. Morton. Cell Vertex Algorithms for the Compressible Navier-Stokes Equations. *Journal of Computational Physics*, 109(1):1–15, 1993.

[66] L. Martinelli. *Calculations of viscous flows with a multigrid method*. PhD dissertation, Princeton Univ., NJ., 1987.

[67] Kam S. Chana and Terry V. Jones. An Investigation on Turbine Tip and Shroud Heat Transfer . *Journal of Turbomachinery*, 125(3):513–520, August 2003.

[68] C. Hirsch. *Numerical Computation of Internal and External Flows*. Butterworth-Heinemann, 2nd edition, 2007.

[69] J. D. Denton and U. K. Singh. Time marching methods for turbomachinery flow calculation: application of numerical methods to flow calculations in turbomachichines. von Karman Institute for Fluid Dynamics Lecture Series, April 1979.

[70] F. Montomoli, H. P. Hodson, and L. Lapworth. RANS–URANS in axial compressor, a design methodology. *Proceedings of the Institution of Mechanical Engineers, Part A: Journal of Power and Energy*, 225(3):363–374, 2011.

[71] T. R. Palmer, C. S. Tan, H. Zuniga, D. Little, M. Montgomery, and A. Malandra. Quantifying Loss Mechanisms in Turbine Tip Shroud Cavity Flows. *Journal of Turbomachinery*, 138(9), September 2016.

[72] S. Jiang, Z. Li, and J. Li. Effects of the squealer winglet structures on the heat transfer characteristics and aerodynamic performance of turbine blade tip. *International Journal of Heat and Mass Transfer*, 139:860–872, 2019.

[73] A. Milli and S. Shahpar. PADRAM: Parametric Design and Rapid Meshing System for Complex Turbomachinery Configurations. volume 8: Turbomachinery, Parts A, B, and C of *Turbo Expo: Power for Land, Sea, and Air*, pages 2135–2148, June 2012.

[74] S. Shahpar and L. Lapworth. PADRAM: Parametric Design and Rapid Meshing System for Turbomachinery Optimisation. volume 6: Turbo Expo 2003, Parts A and B of *Turbo Expo: Power for Land, Sea, and Air*, pages 579–590, June 2003.

[75] A. A. Demargne, R. Evans, P. Tiller, and W. N. Dawes. Practical and reliable mesh generation for complex, real-world geometries. 52nd Aerospace Sciences Meeting, January 2014.

[76] J. S. Kwak, J. Ahn, J. Han, C. P. Lee, R. S. Bunker, R. Boyle, and R. Gaugler. Heat Transfer Coefficients on the Squealer Tip and Near-Tip Regions of a Gas Turbine Blade With Single or Double Squealer . *Journal of Turbomachinery*, 125(4):778–787, October 2003.

[77] J. Jung, I. Kim, J. S. Joo, and S. W. Lee. Experimental Study on Aerodynamic Loss and Heat Transfer for Various Squealer Tips. *Journal of Turbomachinery*, 143(5), May 2021.

[78] mimic - Computer Aided surface manipulation and mesh morphing. Available at :"http://www.optimad.it/products/mimic/", last accessed 1st October 2021.

[79] V. V. Toropov, A. A. Filatov, and A. A. Polynkin. Multiparameter structural optimization using FEM and multipoint explicit approximations. *Structural optimization*, 6:7–14, 1993.

[80] Andrey Polynkin and Vassili Toropov. Mid-range metamodel assembly building based on linear regression for large scale optimization problems. *Structural and Multidisciplinary Optimization*, 45, 04 2012.

[81] A. A. Polynkin, F. Van Keulen, and V. V. Toropov. Optimization of geometrically non-linear structures based on a multi-point approximation method and adaptivity. *Engineering Computations*, 13(2/3/4):76–97, 1996.

[82] S. Caloni, S. Shahpar, and V. V. Toropov. Multi-disciplinary design optimisation of the cooled squealer tip for high pressure turbines. *Aerospace*, 5(4), 2018.

[83] J. R. R. A. Martins and A. Ning. *Engineering Design Optimization*. Cambridge University Press, January 2022.

[84] D. Jones. A taxonomy of global optimization methods based on response surfaces. *Journal of Global Optimization*, 21:345–383, December 2001.

[85] M. D. McKay, R. J. Beckman, and W. J. Conover. A comparison of three methods for selecting values of input variables in the analysis of output from a computer code. *Technometrics*, 21(2):239–245, 1979.

[86] D. I. Lopez, T. Ghisu, and S. Shahpar. Global Optimization of a Transonic Fan Blade Through AI-Enabled Active Subspaces. *Journal of Turbomachinery*, 144(1), January 2022.

[87] J. S. Arora. Chapter 17 - Nature-Inspired Search Methods. In *Introduction to Optimum Design (Fourth Edition)*, pages 739–769. Academic Press, 2017.

[88] M. Arakawa and I. Hagiwara. Development of Adaptive Real Range (ARRange) Genetic Algorithms. *JSME International Journal*, 41(4):969–977, 1998.

[89] A. Oyama, S. Obayashi, and T. Nakamura. Real-Coded Adaptive Range Genetic Algorithm Applied to Transonic Wing Optimization. *Parallel Problem Solving from Nature PPSN VI*, pages 712–721, 2000.

[90] D. Sasaki, M. Morikawa, S. Obayashi, and K. Nakahashi. Aerodynamic Shape Optimization of Supersonic Wings by Adaptive Range Multiobjective Genetic Algorithms. *Evolutionary Multi-Criterion Optimization*, pages 639–652, 2001.

[91] D. Sasaki and S. Obayashi. Efficient search for trade-offs by adaptive range multi-objective genetic algorithms. *Journal of Aerospace Computing, Information, and Communication*, 2(1):44–64, 2005.

[92] S. Obayashi and D. Sasaki. Multi-objective optimization for aerodynamic designs by using ARMOGAs. Proceedings of the Seventh International Conference on High Performance Computing and Grid in Asia Pacific Region (HPCAsia'04), pages 396– 403, August 2004.

[93] R. Maffulli and L. He. Wall Temperature Effects on Heat Transfer Coefficient. volume 3C: Heat Transfer of *Turbo Expo: Power for Land, Sea, and Air*, June 2013.

[94] R. Maffulli and L. He. Dependence of External Heat Transfer Coefficient and Aerodynamics on Wall Temperature for 3-D Turbine Blade Passage. volume 2C: Turbomachinery of *Turbo Expo: Power for Land, Sea, and Air*, June 2014.

[95] S. Shahpar, Rolls-Royce, 2019. Private communication.

[96] R. Maffulli. *Conjugate heat transfer in high pressure turbines*. PhD dissertation, University of Oxford, 2016.

[97] W. C. Reynolds, W. M. Kays, and S. J. Kline. Heat Transfer in the Turbulent Incompressible Boundary Layer. I. Constant Wall Temperature. December 1958. https://www.osti.gov/biblio/4272879.

[98] S. Simone, F. Montomoli, F. Martelli, K. S. Chana, I. Qureshi, and T. Povey. Analysis on the Effect of a Nonuniform Inlet Profile on Heat Transfer and Fluid Flow in Turbine Stages. *Journal of Turbomachinery*, 134(1), January 2012.

[99] S. Salvadori, F. Montomoli, F. Martelli, P. Adami, K. S. Chana, and L. Castillon. Aerothermal Study of the Unsteady Flow Field in a Transonic Gas Turbine With Inlet Temperature Distortions. *Journal of Turbomachinery*, 133(3), July 2011.

[100] P. F. Beard, A. D. Smith, and T. Povey. Experimental and computational fluid dynamics investigation of the efficiency of an unshrouded transonic high pressure turbine. *Proceedings of the Institution of Mechanical Engineers, Part A: Journal of Power and Energy*, 225(8):1166–1179, 2011.

[101] Q. Zhang, D. O. O'Dowd, L. He, M. L. G. Oldfield, and P. M. Ligrani. Transonic Turbine Blade Tip Aerothermal Performance With Different Tip Gaps—Part I: Tip Heat Transfer. *Journal of Turbomachinery*, 133(4), October 2011.

[102] S. Shahpar and S. Caloni. Aerodynamic Optimization of High-Pressure Turbines for Lean-Burn Combustion System. *Journal of Engineering for Gas Turbines and Power*, 135(5), May 2013.

[103] Chao Zhou and Fangpan Zhong. A Novel Suction-Side Winglet Design Philosophy for High-Pressure Turbine Rotor Tips. *Journal of Turbomachinery*, 139(11), July 2017.

[104] C. De Maesschalck, V. Andreoli, G. Paniagua, T. Gillen, and B. Barker. Aerothermal Optimization of Turbine Squealer Tip Geometries With Arbitrary Cooling Injection. *Journal of Turbomachinery*, 143(11), November 2021.

[105] A. J. Saul, P. T. Ireland, J. D. Coull, T. H. Wong, H. Li, and E. Romero. An Experimental Investigation of Adiabatic Film Cooling Effectiveness and Heat Transfer Coefficient on a Transonic Squealer Tip. *Journal of Turbomachinery*, 141(9), September 2019.

[106] J. Vieira, J. Coull, P. Ireland, and E. Romero. Aerothermal Effect of Cavity Welding Beads on a Transonic Squealer Tip. *Journal of Turbomachinery*, 143(11), November 2021.

[107] PyKrige 1.6.1, 2021. Available at: "https://pypi.org/project/PyKrige".